NASA Technical Paper 2628

1986

Forward-Swept-Wing Configuration Designed for High Maneuverability by Use of a Transonic Computational Method

Michael J. Mann and
Charles E. Mercer

Langley Research Center
Hampton, Virginia

National Aeronautics
and Space Administration

**Scientific and Technical
Information Branch**

SUMMARY

A transonic computational analysis method and a transonic design procedure have been used to design the wing and the canard of a forward-swept-wing fighter configuration for good transonic maneuver performance. A model of this configuration was tested in the Langley 16-Foot Transonic Tunnel. The computational method calculates the transonic flow over a canard-wing-fuselage combination so that the strong transonic induced-flow effects of the canard on the wing are taken into account. The transonic theory gave a reasonably good estimate of the wing pressure distributions at transonic maneuver conditions. Comparison of the forward-swept-wing configuration with an equivalent aft-swept-wing configuration showed that, at a Mach number of 0.90 and a lift coefficient of 0.9, the two configurations have the same trimmed drag. The forward-swept-wing configuration was also found to have trimmed drag levels at transonic maneuver conditions which are comparable to those of the HiMAT (highly maneuverable aircraft technology) configuration and the X-29 forward-swept-wing research configuration. The configuration of this study was also tested with a forebody strake in order to examine the effects of a vortex on a forward-swept wing at subsonic and transonic maneuver conditions.

INTRODUCTION

Recent developments in composite structures have opened the possibility of forward-swept wings which exhibit good static divergence characteristics with acceptable levels of structural mass (refs. 1 to 3). These developments have led to several studies of the application of forward sweep to highly maneuverable aircraft (refs. 4 to 13). These studies have examined the various structural and aerodynamic design requirements for a practical fighter aircraft that uses a forward-swept wing. Part of these efforts has culminated in the design and flight test of the X-29 forward-swept-wing technology demonstrator aircraft.

Recent studies have examined the application of supercritical technology to the improved maneuver performance of wings with moderately sweptback leading edges (ref. 14). The primary purpose of the present investigation has been to study the application of supercritical technology to a forward-swept-wing fighter configuration and to make an assessment of the relative performance of forward sweep and aft sweep. The wing and canard for this forward-swept-wing configuration were designed for transonic maneuver with a transonic computational analysis method and a transonic design procedure. The computational method calculates the transonic flow over a canard-wing-fuselage combination so that the strong transonic induced-flow effects of the canard on the wing are taken into account. This study has also included tests to examine the effects of a forebody strake on the maneuver performance of a forward-swept wing.

A model of this forward-swept-wing configuration was tested in the Langley 16-Foot Transonic Tunnel. The wing pressure distributions were measured and have been compared with the theoretical calculations. The lift and drag characteristics of this configuration have been compared with the characteristics of an equivalent aft-swept-wing configuration, the highly maneuverable aircraft technology (HiMAT) configuration, and the X-29 forward-swept-wing research configuration.

A tabulation of the experimental run schedule for the tests in the Langley 16-Foot Transonic Tunnel is presented in a "Supplement to NASA TP-2628." Also presented in the supplement are the tabulated force and pressure data for the configurations tested. The supplement is available upon request, and a request form is included at the back of this paper.

SYMBOLS

Wing geometric parameters A, $\bar{c}$, S, and λ are for the basic trapezoidal wing extended to the model centerline.

A	wing aspect ratio
b	wing span, ft
b_c	canard span, ft
C_D	drag coefficient, D/qS
$C_{D,o}$	zero-lift turbulent skin-friction drag coefficient
$C_{D,trim}$	drag coefficient at $C_m = 0$
C_L	total lift coefficient, L/qS
$C_{L,th}$	theoretical lift coefficient of wing and canard (if present) in the presence of an infinite cylinder
C_m	pitching-moment coefficient (referred to a moment center 23.9 in. from fuselage nose for FSW), $\frac{\text{Pitching moment}}{qS\bar{c}}$
C_p	pressure coefficient, $\frac{p_l - p}{q}$
c	local chord of wing or canard, parallel to plane of symmetry, in.
$\bar{c}$	wing mean aerodynamic chord, in.
D	drag, lbf
e	correction factor for induced drag term in equation $C_D = C_{D,o} + \frac{C_L^2}{e\pi A}$
L	total lift, lbf
M	free-stream Mach number
p	free-stream static pressure, lbf/ft^2
p_l	local static pressure, lbf/ft^2
q	free-stream dynamic pressure, lbf/ft^2
$R_{\bar{c}}$	Reynolds number based on $\bar{c}$

S wing reference area, ft^2

$S_{c,exp}$ exposed canard area, ft^2

$S_{t,exp}$ exposed horizontal-tail area, ft^2

t/c ratio of maximum wing-section thickness at a given spanwise station to the local wing chord parallel to plane of symmetry

x local chordwise distance from wing or canard leading edge, parallel to plane of symmetry, in.

x' distance from apex of strake measured parallel to plane of symmetry, in.

x_{cg} center of gravity (moment reference) measured from fuselage nose, in.

y spanwise distance from plane of symmetry, ft

y' spanwise distance measured from apex of strake, in.

z_u, z_l upper and lower airfoil vertical ordinates, measured from FRP, in.

α angle of attack, deg

α' = α + Constant; constant is selected to make $\alpha' = 0°$ when $C_L = 0$, deg

δ_c canard deflection, positive with leading edge up, deg

$\delta_{f,LE}$ leading-edge flap deflection measured chordwise, positive with leading edge down, deg

$\delta_{f,TE}$ trailing-edge flap deflection measured chordwise, positive with trailing edge down, deg

δ_t horizontal-tail deflection, positive with leading edge up, deg

$\Delta C_{p,sh}$ change in C_p across shock wave

η semispan location, $\frac{y}{b/2}$

η_c canard semispan location, $\frac{y}{b_c/2}$

λ wing taper ratio, $\frac{\text{Tip chord}}{\text{Root chord}}$

Abbreviations:

FRP fuselage reference plane (see fig. 1(a))

FS fuselage station (distance from nose) of wing or canard leading edge, in.

FSW forward-swept wing

HiMAT highly maneuverable aircraft technology

SMF supercritical maneuvering fighter

APPARATUS AND TESTS

Model Description

Drawings of the wind-tunnel model are shown in figure 1, and photographs are shown in figure 2. The geometric characteristics are given in table I. The model represents a highly maneuverable fighter configuration equipped with a forward-swept wing and a canard for pitch control (ref. 15). The incidence of the canard can be varied, and the wing leading- and trailing-edge flaps can be deflected (figs. 1(a) and 1(b)).

In order to make an assessment of the relative performance of forward sweep compared with aft sweep, the planform of the forward-swept wing was designed as a counterpart of the planform of the SMF-1 aft-swept wing described in reference 14. As shown in figure 3(a), the wings for these configurations have the same aspect ratio, taper ratio, and wing area. The structural axes for these wings have been assumed to lie along the 40-percent-chord line. The sweep of the 40-percent-chord line on the forward-swept wing is the negative of the sweepback of the 40-percent-chord line on the aft-swept wing. It was assumed for the present study that this would make the structural weights of these wings approximately the same as on an actual aircraft.

The section shapes of the wing and canard for the forward-swept-wing configuration (tables II and III) and the SMF-1 aft-swept wing have been designed for good transonic maneuver performance through the use of current transonic computational methods and the supercritical technology development discussed in reference 14. The forward-swept wing was designed for a range of Mach number from 0.85 to 0.95 and a lift coefficient of 0.9. The SMF-1 was designed for a Mach number of 0.90 and a lift coefficient of 0.9. Table IV includes a comparison of the areas of the canard and the horizontal tail for these configurations. The transonic maneuver drag levels of these configurations are compared.

The canard planform of the forward-swept-wing configuration was chosen to be aft swept because an aft-swept canard would seem to have a more favorable influence on the wing than a forward-swept canard. The flow on the forward-swept wing separates first at the root, and the flow on the aft-swept canard separates first at the tip. Therefore, the downwash from the root region of the canard, where the flow remains attached at maneuver conditions, helps to reduce the flow separation in the root region of the wing.

The fuselage of the forward-swept-wing configuration was area ruled by the use of the supersonic design and analysis method of reference 16 (figs. 1(d) and 1(e)). The area distribution was designed to reduce the zero-lift wave drag subject to certain requirements. These requirements included sufficient internal volume for model instrumentation and external contour lines on the fuselage which are smooth in the streamwise direction and provide a flat side on the canopy for canard rotation. The wave drag was examined for Mach numbers between 1.00 and 1.60. The supersonic code was also used to define the negative trailing-edge flap deflection angle necessary for low drag at a Mach number of 1.20. The model was not configured to provide for propulsion simulation.

The wing and canard twist distributions of the forward-swept-wing configuration are shown in figure 1(c). The vortex-lattice design method of reference 17 was used to calculate the twist of the wing in the presence of the canard. The wing twist shown in figure 1(c) is a compromise between the optimum twist distributions for transonic maneuver and cruise (corresponding to lift coefficients of 0.9 and 0.4, respectively). The canard has the same planform as the transonic wing design of reference 14. Therefore, the twist of that wing was reduced to allow for cruise requirements and was then used as the canard twist for the present study.

The forward-swept-wing configuration was also tested with the forebody strake shown in figure 1(f). The strake was constructed from a flat plate about 1/8 in. thick (zero twist and camber) and had a sharp beveled leading edge, with a radius normal to the leading edge of 0.002 to 0.003 in. The planform coordinates of the strake leading edge are given in table V. The planform shape of the leading edge was designed by the method of reference 18. The method of reference 18 determines the planform shape of a flat isolated strake by the specification of the leading-edge suction distribution in a simplified flow. For a sharp leading-edge strake, it is assumed that there is a relationship between the calculated attached-flow leading-edge suction distribution and the vortex stability which will be realized under experimental conditions. One of the better strakes described in references 18 and 19 is called AD 14. The leading-edge suction distribution of AD 14 was used to design the leading-edge planform shape of the current strake for a Mach number of 0.90 and a strake width of 2.94 in.

Since the strake was designed as an isolated lifting surface and the wing was designed to operate in the presence of a canard, it should be noted that the strake and the wing have not been designed to operate in the presence of each other. However, this strake could be utilized in conjunction with the current forward-swept wing to examine some of the basic characteristics of a strake—forward-swept-wing configuration at high Mach numbers. In addition to the measurement of the overall forces and moments, oil-flow photographs have been used to examine the interaction between the strake vortex and the forward-swept-wing flow field.

Comparison Configurations

The maneuver drag levels of the forward-swept-wing configuration have also been evaluated by comparison with the HiMAT configuration (ref. 20) and the X-29 forward-swept-wing research configuration (refs. 4 to 6). The HiMAT and the X-29 are recently developed configurations for which supercritical technology has been utilized to achieve good transonic maneuver performance at a Mach number of 0.90 and lift coefficients of about 1.0. The version of the X-29 used in the current study is a research configuration (ref. 4) of the X-29 forward-swept-wing technology demonstrator aircraft. Since the research configuration does not have certain geometric characteristics required for the X-29 aircraft, the research configuration provides a more appropriate comparison with the current forward-swept-wing configuration than does the X-29 aircraft. The X-29 research configuration has lower trimmed maneuver drag than does the X-29 airplane configuration for Mach numbers of 0.60, 0.90, and 1.20. Some geometric parameters for both the HiMAT and the X-29 research configurations are given in table IV and drawings of the two configurations are shown in figures 3(b) and 3(c). All the experimental results presented for the HiMAT (and the X-29) are derived from wind-tunnel data.

Tests and Corrections

The major part of this investigation of a forward-swept-wing configuration was conducted in the Langley 16-Foot Transonic Tunnel. Subsequent to these tests, additional tests were run in the Langley 7- by 10-Foot High-Speed Tunnel in order to obtain oil-flow photographs on selected configurations. Both of these facilities are continuous-flow, single-return atmospheric tunnels. The test section of the Langley 16-Foot Transonic Tunnel is octagonal, and the test section of the Langley 7- by 10-Foot High-Speed Tunnel is rectangular. A description of these tunnels is given in references 21 and 22.

The tests were run at Mach numbers from 0.60 to 1.20 and angles of attack between -4° and 17°. The Reynolds number, based on wing mean aerodynamic chord, varied from 2.5×10^6 at a Mach number of 0.60 to 3.0×10^6 at a Mach number of 1.20.

Boundary-layer transition strips were applied to the model according to the method of reference 23. Strips approximately 0.1 in. wide of No. 120 carborundum grains were used. They were applied 0.6 in. streamwise behind the leading edges of the wings, canards, strakes, and vertical tail and 1 in. behind the fuselage nose.

Aerodynamic forces and moments were measured by an internal, six-component, strain-gauge balance. Model angle of attack was obtained by correcting the angle of the model support system for deflections of the sting and balance under aerodynamic load. The force data have been corrected to a condition of free-stream static pressure over the fuselage base. The angle of attack for the 16-foot transonic tunnel tests was corrected for flow angularity. The same sting was used in both wind tunnels to insure that the aft flow conditions on the model were approximately the same in both tunnels.

The wing was instrumented with static-pressure orifices distributed in streamwise rows. The left-hand wing had orifices on the upper surface at semispan stations of η = 0.25, 0.30, 0.35, 0.40, 0.45, 0.50, 0.65, and 0.85. The right-hand wing had upper surface orifices at η = 0.25 and lower surface orifices at η = 0.25, 0.35, 0.50, 0.65, and 0.85. All surface pressures were recorded by the use of differential pressure scanning valves mounted in the nose section of the model.

Tests of the SMF-1 aft-swept-wing model are described in reference 24, which presents both plots and tabulations of the experimental data.

WING AND CANARD DESIGN

Computational and Design Methods

The airfoil sections of the forward-swept wing were designed in the presence of the canard. The configuration was designed for a maneuver lift coefficient of 0.90 over the Mach number range of 0.85 to 0.95. The thin supercritical sections for the wing and the canard were designed by the use of a three-dimensional transonic computational analysis method and a transonic design procedure. The transonic computational analysis method used is called PANDORA (ref. 25). The PANDORA computer code was selected because it calculates the transonic flow over a canard-wing-fuselage configuration and, therefore, accounts for the strong transonic induced-flow effects of the canard on the wing.

Although the PANDORA code was used strictly as a transonic analysis method in the current study, the PANDORA code can also be utilized as an automated design tool through the combined use of the transonic analysis method and numerical optimization. In the present study, however, an alternate design procedure was chosen that seemed to provide a more direct method of achieving the desired type of wing pressure distributions at the selected maneuver design conditions. The transonic design procedure described in reference 26 was utilized along with the PANDORA transonic analysis method for the wing and canard airfoil-section design (ref. 27). This design procedure provides a set of guidelines for the systematic alteration of airfoil-section shape to achieve some desired pressure distribution. Some examples of the application of this design procedure are discussed in reference 14.

Since the forward-swept-wing configuration was designed, additional developments in transonic design methods have taken place. (See, e.g., refs. 28 and 29.) The recently developed method of reference 29 is an improved version of PANDORA called TRO-3D. In TRO-3D, the optimization process has been tailored to transonic aerodynamic design so that better designs should result (more reliable optimums) and the computational run times should be greatly reduced.

The flow equation used in the analysis by the PANDORA code (refs. 25 and 29) is an "extended" transonic small disturbance equation. It is solved by the use of finite-difference approximations in a global crude Cartesian mesh system with individual embedded fine grids placed over the wing and the canard. The crude grid has 64 streamwise, 26 spanwise, and 31 vertical grid points. The fine grid is in vertical planes with 133 streamwise and 25 vertical grid points. There are 15 fine grid planes across the wing semispan and 8 fine grid planes on the canard semispan. The fine grid density is reduced at the wing and canard tips. The effects of viscosity on the wing and canard are included by the use of a modified two-dimensional Bradshaw turbulent boundary-layer analysis and infinite swept-wing theory. For the maneuver conditions calculated in this study, the solution was found to be essentially converged with 100 crude grid iterations followed by 160 crude/fine grid iterations. The boundary-layer solution was updated every 20 iterations during the crude/fine grid calculations.

Figure 4 shows a correlation between the theoretical wing pressure distributions of PANDORA and the experimental pressure distributions. The version of PANDORA contained in the TRO-3D code was used to make the calculations. Results are shown with the canard on for Mach numbers of 0.80 to 0.95 and with the canard off for Mach numbers of 0.85 and 0.90. Comparisons have been made at maneuver lift coefficients for which the flow appears to be largely attached. In the calculations, the fuselage was represented by an infinite cylinder. The experimental lift coefficients (given in fig. 4) were chosen to be approximately 0.1 greater than the theoretical lift coefficients in order to account for the lift on the fuselage which is not accounted for by PANDORA in the case of an infinite cylinder. All flap deflection angles and the canard incidence are zero. The measured wing-section coordinates used in the calculations (table II) and the experimental upper-surface pressure distributions are both for the left wing.

The correlation at all Mach numbers in figure 4, for both the canard on and the canard off, is good considering the high levels of lift involved. As indicated by the lack of good upper-surface trailing-edge pressure recovery in the experimental data, the trailing-edge region of the wing has some separation. This separation would tend to push the shock wave forward and therefore explain the differences in

shock location between the theory and the experiment on the inboard region of the wing. The double shock predicted by the theory at $\eta = 0.50$ does not appear in the experimental data; however, at lower angles of attack, the experimental data (see "Supplement to NASA TP-2628") indicate the presence of two flow accelerations on the upper surface at $\eta = 0.50$ (two "peaks" in the pressure). As the experimental angle of attack is increased, the trailing-edge separation has apparently caused a second shock wave to move forward and to merge with the upstream shock wave. The difference in character between theory and experiment on the upper surface at $\eta = 0.85$ may be caused by the reduction in the number of fine grid points in the theory from 70 over most of the wing to 11 at the wingtip. The upturn in the theoretical pressure at the inboard trailing edge for Mach numbers of 0.90 and 0.95 may be caused by some peculiarity in the extrapolation of the boundary layer past the computed separation point.

Design Considerations

The initial efforts of this study to design a forward-swept-wing configuration without a canard indicated that, based on the studies of reference 14, the inboard flow would experience extensive separation due to the presence of a strong inboard shock wave preceded by a strong adverse pressure gradient. Therefore, a canard was added to the configuration in order to utilize the induced downwash from the canard as a means of lowering the local angle of attack on the inboard part of the wing. When the wing sections were redesigned in the presence of the canard, the strong inboard adverse pressure gradient was eliminated and the shock strength was slightly reduced. Based on these theoretical results and the studies of reference 14, it was felt that the wing would develop less flow separation for the case of the canard configuration than for the case of the configuration designed without a canard. The effects of the canard will be examined in the section "Discussion of Results."

The objective of the design process was to reduce the shock strength and the adverse pressure gradients at a lift coefficient of 0.9 over the Mach number range of 0.85 to 0.95. The studies of reference 14 on the maneuver performance of aft-swept wings (without canards) indicated the desirability of designing the wing so that, at Mach numbers from 0.85 to 0.95, the upper surface pressure distribution ahead of the shock wave is flattened or has a gradual compression. An effort was made to design the forward-swept wing with these types of pressure distributions on the outboard part of the wing for Mach numbers from 0.85 to 0.95 at a lift coefficient of 0.9. (See figs. 4(b) to 4(d).) The inboard part of the wing was designed to eliminate strong shocks preceded by strong adverse pressure gradients. The resultant inboard flow tends to have moderately strong shocks preceded by a favorable pressure gradient. (See figs. 4(b) to 4(d).) These inboard pressure distributions are not necessarily optimum; however, they appeared to be a significant improvement over the configuration designed without the canard.[1]

Since the canard has the same planform as the SMF-1 wing, the midspan airfoil section of SMF-1 was modified and was used on the canard. The modifications were based on calculations with PANDORA and resulted in two new sections, one for the root and one for the tip. Only two sections were defined in order to simplify the model construction process.

---

[1]The downstream pressure peak in figure 4 at $\eta = 0.50$ was not so pronounced in the calculations made during the wing design process. Those calculations were made with the early version of PANDORA (ref. 25) and involved a different method for estimation of boundary-layer effects than the Bradshaw method.

PRESENTATION OF RESULTS

The results of this study are presented in the following figures:

DISCUSSION OF RESULTS

First, the separate effects of the flaps, the canard, and the strakes are examined. Then the performance of the forward-swept-wing configuration is evaluated by comparisons with the ideal and zero-suction polars, the equivalent aft-swept-wing configuration, the HiMAT configuration, and the X-29 configuration.

Flap, Canard, and Strake Effects

The force and pressure data of figures 5 to 14 and the oil-flow photographs of figures 15 and 16 are, in general, for untrimmed conditions. These data are used to examine the effects of the wing leading- and trailing-edge flaps, the canards, and the forebody strakes.

Flap effects.- The effects of the trailing-edge and the leading-edge flaps are shown in figures 5 and 6. Figure 5 shows that, at Mach numbers of 0.60 and 0.90 and lift coefficients greater than the design value of 0.9, deflection of the trailing-edge flap substantially reduces drag and increases the lift-drag ratio. At the design lift coefficient itself, the flap deflection has practically no effect. At a Mach number of 1.20, the negative flap deflection of -14° reduces the drag at the low lift coefficients. The selected flap deflection angles have trimmed the configuration for several values of lift (fig. 5(c)).

Deflection of the leading-edge flap reduces the drag at a Mach number of 0.60 for lift coefficients greater than about 1.1 (fig. 6). At a Mach number of 0.90, however, the leading-edge flap deflection causes the drag to increase for all values of the lift coefficient.

Canard effects.- The effects of canard incidence are shown in figure 7. Effects of the canard on longitudinal aerodynamic characteristics, wing pressure distributions, and wing oil-flow patterns are shown in figures 8, 13, and 15, respectively. For these three figures, the canard and flap deflection angles are zero. All the oil-flow photographs were obtained in the Langley 7- by 10-Foot High-Speed Tunnel, with the exception of figures 15(i) and 15(j), which were obtained in the Langley 16-Foot Transonic Tunnel.

The pitching-moment increments generated by deflection of the canard at Mach numbers of 0.60 and 0.90 can be obtained from figure 7(c). The moment increments needed to trim the configuration with the flaps deflected and with a zero canard deflection are shown in figures 5 and 6. The moment increments produced by deflection of the canard in figure 7(c) would be sufficient to trim the canard-wing configuration with appropriate flap deflections (flaps deflected only at high lift coefficient).

The addition of the canard to the configuration (fig. 8) reduced the drag and increased the lift-drag ratio for lift coefficients greater than about 0.7 over the entire range of Mach number from 0.60 to 1.20. For maneuver lift coefficients on the order of 1.0, there was a substantial reduction in drag. This reduction in drag for a given level of lift is apparently caused by two effects, as follows: First, the additional lifting area provided by the canard which lowers the required angle of attack and, second, favorable interference of the canard on the wing.

The lift-drag ratio of an ideal polar with an elliptical span load (100-percent suction) and a zero-suction polar of a thin flat-plate wing are plotted in figure 8(c).[2] For Mach numbers up to 0.95, the configuration with the canard on tends to develop a larger percentage of the available suction although both the canard-on and canard-off configurations are approaching zero suction at the highest lift coefficients. At a Mach number of 1.20, both configurations have lost all the suction. When the canard is added to the configuration, the additional lifting area provided by the canard lowers the angle of attack necessary to produce a given lift coefficient. Since the drag varies as $C_L \tan \alpha'$ when the lifting surfaces are operating close to zero suction, the lower angle of attack due to the additional area results in lower drag. Of course, a reduction in angle of attack at maneuver conditions generally results in less flow separation so that the lifting surfaces will develop more of the available suction and, because of this, achieve a lower level of drag.

The second reason given for a lower drag with the canard on, namely favorable interference of the canard on the wing, has been the subject of numerous experimental and theoretical investigations (refs. 11 and 30 to 34, for example). The studies of references 11, 30, and 33 have measured the interference effects by the use of a dual-balance system which separates the canard-forebody loads from the wing-afterbody loads. Some aspects of canard configurations designed to utilize this interference for improved maneuver performance have been studied in references 32 and 34. For the current study, the wing pressure distributions and the oil-flow photographs of figures 13 and 15 and the computed shock strengths of figure 19 can be used to examine the interference of the canard on the wing.[3]

Figures 19(a) and 19(b) show the spanwise variation of theoretical shock strength on the forward-swept-wing configuration and its aft-swept counterpart (SMF-1). The pressure increase through the shock wave has been computed with the PANDORA code. The fuselage for both configurations was represented by an infinite cylinder. The calculations were made for a theoretical lift coefficient (excluding fuselage lift) of 0.7 at Mach numbers of 0.85 and 0.90. This theoretical lift coefficient would correspond to a total lift coefficient of about 0.8. In places where a double-shock system exists, the stronger shock jump is plotted and these locations are noted in figures 19(a) and 19(b). The shape of the chordwise pressure distribution is shown at selected spanwise stations.

As mentioned earlier, a canard was included on the forward-swept-wing configuration in order to obtain an inboard chordwise pressure distribution which should result in a reasonably attached flow at transonic maneuver conditions. The lower parts of figures 19(a) and 19(b) show the distribution of shock strength on the forward-swept-wing configuration with and without a canard. The calculations were made at a fixed lift coefficient, and the same computational grid was used on

---

[2]The zero-suction drag is computed from $C_D = C_{D,o} + C_L \tan \alpha'$, where $\alpha' = \alpha + \text{Constant}$ and the constant has been selected so that $\alpha' = 0°$ at $C_L = 0$. The ideal polar is computed from $C_D = C_{D,o} + \frac{C_L^2}{\pi A}$.

[3]The addition of the canard will also affect the spanwise distribution of load. This may result in a favorable effect on the induced drag because the wing twist was designed to account for the influence of the canard.

the wing for both cases. These results do not show, of course, the differences that would result if one wing were designed without a canard and the other wing were designed in the presence of a canard. However, the results do graphically illustrate the powerful influence of the canard on the wing flow field by the considerable reduction in shock strength at the wing root. The decrease in shock strength is due to the downwash behind the canard and to the somewhat lower angle of attack necessary to develop the same value of lift (about 1° lower). When the effect of the canard is calculated with the angle of attack fixed at the value for the case with the canard on, the decrease in shock strength is on the order of 80 to 90 percent of that shown in figures 19(a) and 19(b). This result would, therefore, indicate that the majority of the canard effect shown in figures 19(a) and 19(b) is caused by the induced-flow effects from the canard. The addition of the canard also produces a small increase in the strength of the outboard wing shock, apparently due to the upwash induced by the canard outboard of its tip.

A similar reduction in wing shock strength produced by the addition of the canard can be seen in the experimental pressure distributions of figures 13(e) and 13(j). These figures are for Mach numbers of 0.85 and 0.90 at angles of attack of approximately 4° and 6°, respectively (and lift coefficients of 0.65 and 0.85, respectively, with the canard on, from fig. 8(b)). The flow for both configurations at these conditions appears to be predominantly attached. The shock strength has been reduced at $\eta = 0.25$ with the addition of the canard, as previously seen in figure 19. With the canard on, there also appears to be a slightly stronger shock at $\eta = 0.50$ for a Mach number of 0.85 and a small increase in the trailing-edge flow separation at $\eta = 0.50$ for a Mach number of 0.90 (shown by less compression at the trailing edge). These results would correspond to the small increase in the strength of the outboard shock indicated in figure 19.

The oil-flow photographs of figure 15 and the pressure distributions of figure 13 can be used to further examine the influence of the canard on the flow pattern over the wing for lift coefficients up to about 1.0 at Mach numbers of 0.60, 0.85, and 0.90. Comparisons of the canard on with the canard off, shown in figures 13 and 15, are made at approximately constant angle of attack. These figures show the progressive changes at each Mach number as the angle of attack is increased. The angles of attack of the oil flows and the pressure distributions only approximately correspond to each other because the data were obtained in separate tests.

At a Mach number of 0.60, the flow for both the canard on and off at angles of attack from 3.66° to 7.76° appears to be essentially attached (figs. 15(a) and 15(b)). The canard-off configuration at an angle of attack of 7.47° may have a small region of separation at the inboard leading edge. Any leading-edge separation will, of course, strongly contribute to the loss of suction shown in figure 8(c). At an angle of attack of approximately 11° to 12°, the lift coefficient ranges from 0.9 to 1.1 for the canard off and on (figs. 13(c), 15(c), and 8(b)). The flow for the canard-on configuration is largely attached with a small region of trailing-edge separation and with what appears to be some local leading-edge separation on the outboard sections (the latter noticeable in both the oil flow and the pressure distribution at $\eta = 0.65$). This contrasts with the canard-off configuration that has developed a region of separation on the inboard area of the wing although the leading-edge separation on the outboard sections does not appear to be as great. Thus, the downwash from the canard has reduced the separation on the inboard region of the wing. It is expected that this reduced separation would result in significantly lower drag on the wing (ref. 35). However, the aerodynamic forces on the canard and wing cannot, of course, be separately determined without a dual-balance

system. In this study, therefore, it cannot be determined what proportion of the drag reduction with the canard on is due to the interference between the wing and the canard. It is interesting to note that, with the angle of attack fixed at 12°, the lift-drag ratio has increased by only about 0.2 with the addition of the canard (fig. 8(d)). As the angle of attack is increased to the 14° to 15° range (lift coefficient of 1.2 with the canard on), figures 13(d) and 15(d) show that the flow on the wing is separated for both canard on and canard off although the separation appears to be somewhat less severe with the canard on.

Similar results were obtained at a Mach number of 0.85. The flow is attached for both configurations at an angle of attack of approximately 3° to 4° (figs. 13(e) and 15(e)). At an angle of attack of approximately 6° to 7°, the lift coefficient ranges from about 0.7 to 0.9 for the canard off and on (figs. 13(f), 15(f), and 8(b)). The addition of the canard has essentially eliminated a large region of flow separation on the inboard area of the wing. It is interesting to note that, with the canard on, the inboard shock at $x/c \approx 0.35$ and the double or lambda outboard shock are clearly visible in both the oil flow and the pressure distributions. As the angle of attack is increased to approximately 8° and 11° (lift coefficients approximately 1.0 and 1.15 with the canard on), the oil-flow photographs continue to show less inboard separation with the canard on, and the pressure distributions seem to indicate a slightly increased separation at $\eta = 0.50$ with the canard on (figs. 13(g), 13(h), 15(g), and 15(h)). These effects of the canard at an angle of attack of about 8° and 11° correspond with the theoretical results of the lower parts of figures 19(a) and 19(b) which show a weaker shock inboard and a slightly stronger shock outboard with the canard on.

At a Mach number of 0.90 and an angle of attack of approximately 10° (lift coefficient of 0.95 to 1.1 for canard off and on), figures 13(k) and 15(j) also show less separation inboard with the canard on, while figure 13(k) shows increased separation at $\eta = 0.50$ with the canard on.

Strake effects.- The addition of the strake (canard off) with zero wing-flap deflections (fig. 9) reduced the drag and increased L/D at maneuver conditions over the entire Mach number range from 0.60 to 1.20. The L/D curves of figure 9(c) show that there is little difference in suction level between the strake-on and the strake-off configurations. The strake itself would not be expected to produce any suction because it is flat with a sharp leading edge. At the higher Mach numbers, the strake configuration does not produce much suction at maneuver conditions and, as similar to the case of the canard, the suction is close to zero at Mach numbers of 0.95 and 1.20. At the lower Mach numbers (0.60 and 0.80), the strake configuration does not have as high a level of suction for lift coefficients near 1.0 as the canard configuration in figure 8. (Note that the canard-off data of fig. 8 are the same as the strake-off data of fig. 9.)

Comparisons of the canard and strake configurations are shown in figure 12. The canard configurations exhibit substantially lower drag for a wide range of maneuver conditions. At a Mach number of 0.90 (fig. 12(a)), however, the canard configuration has stalled at the highest lift coefficients so that its drag polar crosses over the polar for the strake configuration. The configuration with both the strake and the canard is best because it has the low drag levels of the canard configuration but does not stall at the high-lift coefficients. However, the strake-canard configuration cannot be trimmed with the canard deflection angles of figure 7(c) for the entire range of lift coefficients of figure 12(c).

Figures 10 and 11 show the effects of the strake when the canard is installed and when either the canard or the wing trailing-edge flap is deflected. The results show that the addition of the strake can either increase or decrease the drag, depending upon Mach number, angle of attack, and configuration. With the canard at zero incidence and a trailing-edge flap deflection of 10° (fig. 10), the strake has reduced the drag for lift coefficients greater than 1.0 at Mach numbers of 0.85 and 0.90. With the canard at -10° incidence and zero flap deflections (fig. 11), the strake has significantly increased the drag at a Mach number of 0.60 but has had only a small effect at a Mach number of 0.90.

References 12 and 13 describe the results of tests at very low Mach numbers of forward-swept-wing configurations equipped with forebody strakes. These references have oil-flow photographs which show the effects of the strakes on the wing flow field at low Mach numbers. The pressure distributions and oil-flow photographs of figures 14 and 16 of the current study can be used to examine the interference of the strake on the wing. The conditions examined are lift coefficients up to about 1.0 for Mach numbers of 0.60 and 0.85. As in the case of the canard, the comparisons of strake on with strake off are made with the angle of attack held approximately constant.

As the angle of attack is increased at a Mach number of 0.60, the oil-flow photographs of figures 16(a) to 16(d) show the development of a classical vortex flow from the sharp leading-edge strake. (See, e.g., ref. 36.) At angles of attack of approximately 11° and 14°, the strake has changed the flow on the inboard region of the wing from the usual separated flow into an organized vortex flow. As might be expected, a separate disturbance appears to be emanating from the strake wing juncture (figs. 16(a) and 16(b)) at angles of attack of 3.63° and 7.67° (C_L = 0.52 and 0.82). At an angle of attack of 10.69° (C_L = 1.0), this disturbance has been replaced by two small "eye" structures near the strake-wing juncture (fig. 16(c)). Poll and Qui (ref. 13) observed similar results in their oil-flow studies at low Mach numbers.

Since the shock strength on a forward-swept wing at transonic conditions is greatest at the root, a forward-swept wing equipped with a forebody strake presents a situation in which a strong vortex will interact with a strong shock wave. Figures 16(e) to 16(h) and 14(e) to 14(h) can be used to examine this interaction at a Mach number of 0.85. At an angle of attack of 2.70° (fig. 16(e)), there is no apparent vortex. For angles of attack from 6.71° to 11.37° (figs. 16(f) to 16(h)), the oil-flow photographs again show the existence of a vortex on the strake and the inboard region of the wing. (Compare to fig. 16(c).) For this angle-of-attack range, the lift coefficient with the strake on varies from 0.8 to 1.1 (fig. 9(b)). The pressure distributions at η = 0.50, 0.65, and 0.85 (figs. 14(f) to 14(h)) and the oil flows (figs. 16(f) to 16(h)) show the existence of a system of shock waves on the outboard region of the wing. At an angle of attack of 6.71°, it appears from the oil flow (fig. 16(f)) that a shock wave extending from the outboard region of the wing has passed through the vortex. Evidence of the presence of this shock wave in the region of the vortex flow is also seen in the pressure distribution at η = 0.25 (fig. 14(f)).[4] A similar situation seems to have occurred at an angle of attack of 8.76° (figs. 14(g) and 16(g)). At an angle of attack of 11.37° (figs. 14(h)

[4]The strake-wing juncture is at η = 0.32 so that the row of orifices at η = 0.25 is behind the strake. With the strake on, x/c still refers to x measured from a line along the wing leading edge extended to the fuselage.

and 16(h)), the situation is not so clear with regard to the shock-vortex interaction. The outboard wing panel appears to have a swept-forward lambda shock at the tip, with a sweptback shock farther inboard.

The addition of the strake at an angle of attack of 6.71° (figs. 14(f) and 16(f)) appears to have strengthened the shock wave at $\eta = 0.50$. This may have been caused by the outward induced flow from the vortex (toward the wingtip), which would tend to reduce the effective wing sweep.

Evaluation of Forward-Swept-Wing Configuration

Low Mach number tests of the forward-swept-wing configuration of the present study are reported in reference 15. Those results showed that a center-of-gravity location (moment reference) of 23.9 in. would allow the canard configuration, with the wing flaps deflected, to be trimmed from $\alpha \approx 4°$ to $\alpha \approx 22°$. Because of the small number of flap and canard deflections examined in the present tests, only a limited study of the effect of center of gravity on trim drag could be conducted for the higher Mach numbers. Figure 17(a) shows that, for a lift coefficient of 0.9, small changes in center-of-gravity location from 23.9 in. do not have a large effect on trimmed drag. The center-of-gravity location of 23.9 in. has been used to present the data and to trim the forward-swept-wing configuration in this study. The trim drag points of figure 17(a) are plotted in figure 17(b) as a function of static margin, where the static margin is defined as the negative of $\partial C_m/\partial C_L$.

Comparison of experimental results with ideal and zero-suction polars.- Figure 18 presents drag polars for the forward-swept-wing (FSW) configuration at Mach numbers of 0.60 and 0.90. Since only a few trimmed points are available, figures 18(a) and 18(b) have untrimmed data for a configuration with fixed flap deflections and zero canard incidence. The chosen flap deflection angles reduce the drag above the design lift condition and, of course, increase the drag at the low lift coefficients. Figure 18 also shows the ideal polar corresponding to an elliptic lift distribution (100-percent suction) and the curve of $C_L \tan \alpha'$ that corresponds to a zero-suction condition of a thin flat-plate wing; $C_{D,o}$ is a zero-lift turbulent skin-friction drag coefficient. The skin friction was calculated with the Von Kármán-Schoenherr formula for incompressible turbulent flow on a flat plate at zero incidence (ref. 37). The skin-friction drag was then corrected for compressibility by the Sommer and Short T' method (ref. 38) and corrected for thickness by the method of Hoerner (ref. 39).

At a Mach number of 0.60 and design lift coefficient of 0.9, the FSW configuration has achieved most of the available potential for drag reduction based on the limits indicated by the two calculated curves. However, at a Mach number of 0.90 and the same lift coefficient, the experimental results are only about midway between the theoretical limits. Although the theoretical minimum of this ideal polar cannot be achieved, it would seem that there is potential for further drag reduction at a Mach number of 0.90 and a lift coefficient of 0.9. Any transonic maneuver drag reduction must be done, of course, for the entire range of transonic speeds and not just for a Mach number of 0.90. An improved transonic computational design code such as TRO-3D would appear to offer potential for further improvements.

Comparison of forward and aft sweep.- Figure 19 can also be utilized to examine the effect of wing sweep on the spanwise variation of shock strength. Although flow separation is governed by the presence of various pressure gradients as well as the

shock strength, figure 19 provides a useful means of examining some of the aerodynamic differences between forward and aft sweep. The upper parts of figures 19(a) and 19(b) and both parts of figure 19(c) show the effects of sweep on the pressure increase through the shock wave for wing-body configurations with the wing planforms shown in figure 3(a). The forward-swept wing was designed with a canard, as discussed previously, and the aft-swept wing (SMF-1) was designed without a canard. However, it was found during the forward-swept-wing design study that this type of distribution of shock strength for the forward-swept-wing—body configuration (no canard present) is generally representative of a wing designed with or without a canard. Figures 19(a) and 19(b) show the theoretical distribution of shock strength at Mach numbers of 0.85 and 0.90 for a theoretical lift coefficient of 0.7 or a total lift coefficient, including fuselage effects, of approximately 0.8. Figure 19(c) shows the experimental distribution of shock strength at the same Mach numbers as in figures 19(a) and 19(b) and a lift coefficient of 0.7. The experimental values of pressure jump at the shock wave for a Mach number of 0.90 are substantially lower than the theoretical values in figure 19(b). Although there is some difference in lift coefficient between figures 19(b) and 19(c), this difference in pressure jump is also apparent in figure 4(f) and is probably due to some local separation at the experimental shock location. However, the general trends in the spanwise variation of pressure jump at the shock wave are the same for theory as for experiment.

The results of figure 19 show that the shock strength on the forward-swept wing is greatest on the inboard region. As previously discussed, this result provides the opportunity to include some aerodynamic device on the aircraft which will have a strong favorable interference effect on the region of the wing where the flow first separates. As discussed in the section on canard effects, an example of such a device is a canard with positive lift that will induce a downwash on the inboard part of the wing and, therefore, lower the local angle of attack on that part of the wing. If the wing is designed to operate in the presence of this canard-induced flow field, the lower local angle of attack will reduce the flow separation and should result in improved maneuver performance. The lower parts of figures 19(a) and 19(b) illustrate the effects of the induced flow from the canard on the wing shock strength.

As figure 19 also shows, the shock strength on the aft-swept wing is greatest at the wingtip. In this case, then, the wingtip region is where the flow separation first develops as the angle of attack is increased. (See, e.g., the aft-swept-canard oil-flow patterns in figs. 15(g) and 15(h).) Since the separation first occurs at the wingtip for an aft-swept wing, the favorable interference effects of a canard are not quite so clear as in the case of a forward-swept wing. The downwash from the canard unloads the wing root, which, in turn, produces less upwash at the wingtip. However, the canard itself produces an upwash at the wingtip, which tends to increase the local angle of attack in that region.

The lift and drag characteristics of the forward- and aft-swept configurations are shown in figure 20 for Mach numbers of 0.60 and 0.90. The untrimmed data for FSW are for zero flap deflections. (SMF-1 does not have leading- or trailing-edge flaps.) The aspect ratios of the two configurations are the same, and the test Reynolds numbers are very close. The locations of the center of gravity for SMF-1 were selected to produce minimum trimmed drag at cruise and maneuver conditions for the available tail deflection angles (only negative tail settings being tested). Both configurations are unstable at the chosen center-of-gravity locations; their stability levels in terms of $\partial C_m/\partial C_L$ are listed in figure 20. The values of $\partial C_m/\partial C_L$ were determined at trim conditions for a lift coefficient of 0.9.

Both the SMF-1 and FSW configurations were designed for good performance at a Mach number of 0.90 and a lift coefficient of 0.9. At $M = 0.90$ and $C_L = 0.9$, the two configurations have the same trimmed drag. Oil-flow photographs of these configurations at a Mach number of 0.90 show the SMF-1 to have a small amount of trailing-edge and wingtip separation at $C_L = 0.85$ and the FSW to have some separation in the trailing-edge region at $C_L = 0.83$. (See fig. 15(i).) For conditions somewhat above the design lift coefficient, however, the FSW configuration has lower drag than the aft-swept SMF-1. This lower drag is probably due to less flow separation on the FSW caused by the favorable influence from the canard. Similar results were obtained at a Mach number of 0.60.

The comparisons of figure 20 suggest that additional studies need to be conducted in order to evaluate the influence of the canard on the aft-swept SMF-1 configuration.

Extensive analytical and experimental studies have been conducted by other investigators in order to examine the relative capabilities of forward- and aft-swept wings. A good discussion of some of these results, particularly with regard to highly maneuverable tactical aircraft, is given in references 1, 3 to 5, and 7 to 9. Some experimental tests on forward- and aft-swept wings are reported in references 11 to 13.

Comparison of FSW configuration with HiMAT configuration.- The forward-swept-wing configuration is further evaluated by comparison with the HiMAT configuration. Figure 21 compares wind-tunnel results for the HiMAT with those for the FSW configuration at Mach numbers of 0.60, 0.90, and 1.20. The results for the HiMAT at Mach numbers of 0.60 and 0.90 are for the maneuver configuration, and the results at a Mach number of 1.20 are for the cruise configuration (ref. 20). The maneuver configuration has more camber than the cruise configuration because of the deflection of leading- and trailing-edge devices and also has additional twist built into the wing in order to simulate aeroelastic deformation. The HiMAT data are trimmed and the FSW data are both trimmed and untrimmed. The untrimmed data in figure 21 for FSW at Mach numbers of 0.60 and 0.90 have the same flap deflections as in figure 18. The untrimmed data for FSW at a Mach number of 1.20 are plotted for two flap deflection angles in order to estimate trimmed conditions. The HiMAT data of figures 21(a) to 21(c) have been corrected from an aspect ratio of 3.85 to 3.28 for the FSW (assuming an induced-drag correction factor $e = 1.0$ and assuming $C_{D,o}$ and S are constant). Since fixed transition was utilized on both wind-tunnel models, the difference in Reynolds number shown in figure 21 is expected to have only a minor effect on the drag. This difference in Reynolds number changes the calculated value of $C_{D,o}$ for FSW by less than 20 counts (0.0020). The values of $\partial C_m/\partial C_L$ are again noted in figure 21. Figures 21(a) to 21(c) compare the lift and drag in the form of conventional lift and drag coefficients. Figures 21(d) to 21(f) make the comparison on the basis of $L/(qb^2)$ and $D/(qb^2)$. This method of nondimensionalization has been developed by Harold J. Walker of the Ames-Dryden Flight Research Facility to evaluate the performance of dissimilar aircraft (ref. 40). Since the lift and drag are nondimensionalized with b^2, it is not necessary to correct the HiMAT data for aspect ratio. A lift coefficient of 0.9 corresponds to $\frac{L}{qb^2} = 0.234$ and 0.274 for the HiMAT and the FSW, respectively.

Figures 21(a) and 21(b) show that, at Mach numbers of 0.60 and 0.90, the HiMAT has lower drag than FSW although the drag levels are reasonably close at maneuver conditions. A Mach number of 0.90 and a lift coefficient of 0.9 approximates the

transonic maneuver design point for both configurations. When the actual value of e is used to correct the HiMAT data for aspect ratio and the effect of the winglets on the HiMAT is accounted for, the trimmed drag at a Mach number of 0.90 and a lift coefficient of 0.9 is essentially the same for these two configurations. The high drag for FSW at the low levels of lift is due to the large amount of camber in the wing. This camber is required for maneuver and could be reduced by means of variable geometry, as illustrated in figure 21(c) for $\delta_{f,TE} = -14°$. Figure 21(c) shows that the FSW and the HiMAT have comparable performance at a Mach number of 1.20. At a lift coefficient of 0.082, corresponding to level flight of the HiMAT at an altitude of 30 000 ft with one half fuel load, the two configurations have about the same value of trimmed C_D. In terms of $L/(qb^2)$ and $D/(qb^2)$, the curves of figures 21(d) and 21(e) cross so that at Mach numbers of 0.60 and 0.90 the FSW has lower drag than the HiMAT at the higher levels of lift.

Comparison of FSW configuration with X-29 research configuration.- Comparisons of the FSW configuration with the X-29 forward-swept-wing research configuration are shown in figure 22 for Mach numbers of 0.60, 0.90, and 1.20. The results are again presented in terms of both C_L, C_D and $L/(qb^2)$, $D/(qb^2)$. All the X-29 data are trimmed, and the results shown in figures 22(a) to 22(c) were corrected from an aspect ratio of 4.00 to 3.28 (assuming $e = 1.0$). The FSW data are the same as in figure 21. The difference in test Reynolds number for the two configurations was found to change the value of $C_{D,o}$ for FSW by only 10 to 15 counts (0.0010 to 0.0015). Note that the X-29 is trimmed for an even higher level of instability than the FSW.

At a Mach number of 0.90 and a lift coefficient of 0.9, which again approximates the transonic maneuver design condition for both configurations, figure 22(b) shows that the X-29 and the FSW have the same trimmed drag. At a Mach number of 0.60, the X-29 polar crosses to higher drag levels than the FSW polar at the higher lift coefficients (fig. 22(a)). At a Mach number of 1.20, the drag levels of the two configurations are comparable (fig. 22(c)). Conversion from C_L, C_D to $L/(qb^2)$, $D/(qb^2)$ has slightly rotated the X-29 curves with respect to the FSW curves (figs. 22(d) to 22(f)), as occurred for the HiMAT curves with respect to the FSW curves (figs. 21(d) to 21(f)).

CONCLUSIONS

This study has examined the application of supercritical technology to a forward-swept-wing fighter configuration, and some assessment has been made of the relative performance of forward and aft sweep. The wing and the canard of the forward-swept-wing configuration were designed for transonic maneuver by a transonic computational analysis method and a transonic design procedure. A model of this configuration was tested at Mach numbers from 0.60 to 1.20 and at angles of attack from approximately -4° to 17°. The results of this study may be summarized as follows:

1. The PANDORA transonic computational method predicted wing pressure distributions which showed reasonably good correlation with experimental results for Mach numbers from 0.80 to 0.95 with the canard on and for Mach numbers of 0.85 and 0.90 with the canard off. The correlations were made at maneuver lift coefficients for which the flow appeared to be largely attached.

2. The use of the PANDORA code and the transonic design procedure indicated that, if the forward-swept wing were designed in the presence of the canard, a chordwise pressure distribution could be developed at transonic maneuver conditions which should produce less flow separation than the pressure distribution that results for a wing designed without the canard. Oil-flow photographs at Mach numbers of 0.60, 0.85, and 0.90 and lift coefficients on the order of 1.0 showed that for the wing designed in the presence of a canard, the flow separation was much less at a given angle of attack with the canard on than with the canard off.

3. The canard produces sufficient pitching-moment increments to trim the canard-wing configuration with appropriate flap deflections for the conditions of this study.

4. The addition of the forebody strake to the forward-swept-wing—body configuration significantly reduced the drag at lift coefficients on the order of 1.0 for Mach numbers from 0.60 to 1.20; however, this configuration could not be trimmed with the canard for all conditions.

5. Oil-flow photographs of the strake-wing configuration at Mach numbers of 0.60 and 0.85 showed the presence of a classical vortex flow on the strake and wing, and at a Mach number of 0.85, a wing shock wave appeared to pass through the vortex.

6. Trailing-edge flap deflections reduced the drag of the canard-wing configuration at Mach numbers of 0.60 and 0.90 for lift coefficients above the design value of 0.9. Leading-edge flap deflections reduced drag at a Mach number of 0.60 for lift coefficients greater than 1.1.

7. Comparison of the drag polar for the canard-wing configuration with the ideal polar and the flat-plate wing or zero-suction polar at the design lift coefficient of 0.9 showed that, at a Mach number of 0.60, most of the available potential for drag reduction had been achieved; however, at a Mach number of 0.90 and a lift coefficient of 0.9, there appears to be some potential for further drag reduction.

8. The forward-swept-wing configuration and an equivalent aft-swept-wing configuration were both designed for good maneuver performance at a Mach number of 0.90 and a lift coefficient of 0.9. These two configurations had the same trimmed drag at a Mach number of 0.90 and a lift coefficient of 0.9; however, at higher lift coefficients, the forward-swept-wing configuration had lower drag, probably due to the favorable influence of the canard.

9. The forward-swept-wing configuration (equipped with a canard) showed maneuver performance at Mach numbers of 0.60, 0.90, and 1.20 which was comparable with the maneuver performance of the HiMAT (highly maneuverable aircraft technology) fighter configuration and the X-29 forward-swept-wing research configuration. At a Mach number of 0.90 and a lift coefficient of 0.9, which approximates the transonic maneuver design point for all three configurations, the trimmed drag was essentially the same for all three configurations.

NASA Langley Research Center
Hampton, VA 23665-5225
September 4, 1986

REFERENCES

1. Krone, Norris J., Jr.: Divergence Elimination With Advanced Composites. AIAA-75-1009, Aug. 1975.

2. Ricketts, Rodney H.; and Doggett, Robert V., Jr.: Wind-Tunnel Experiments on Divergence of Forward-Swept Wings. NASA TP-1685, 1980.

3. Burns, B. R. A.: Forward Sweep: The Pros and Cons. Interavia, vol. 40, no. 1, Jan. 1985, pp. 39-41.

4. Uhuad, G. C.; Weeks, T. M.; and Large, R.: Wind Tunnel Investigation of the Transonic Aerodynamic Characteristics of Forward Swept Wings. J. Aircr., vol. 20, no. 3, Mar. 1983, pp. 195-202.

5. Moore, M.; and Frei, D.: X-29 Forward Swept Wing Aerodynamic Overview. AIAA-83-1834, July 1983.

6. Spacht, G.: The Forward Swept Wing: A Unique Design Challenge. AIAA-80-1885, Aug. 1980.

7. Miller, B. D.; and Hadley, S. K.: Application of Forward Swept Wings to an Air Combat Fighter. AIAA-83-1833, July 1983.

8. Hadley, S. K.; and Miller, B. D.: Application of Forward Swept Wings to an Air Combat Fighter. AIAA-80-1883, Aug. 1980.

9. Robinson, Michael R.; and Robinson, Douglas A.: Forward Swept Wing (FSW) Designs: A High Payoff Through Technology Integration. AIAA-80-1884, Aug. 1980.

10. Stanniland, D. R.: Aspects of the Aerodynamic Design of a Thin Supercritical, Forward Swept Wing for a Combat Aircraft. Proceedings - International Conference - Forward Swept Wing Aircraft, R. K. Nangia, ed., Univ. of Bristol (United Kingdom), c.1983, pp. I.13.1 - I.13.13.

11. Huffman, Jarrett K.; and Fox, Charles H., Jr.: Subsonic Longitudinal and Lateral-Directional Static Aerodynamic Characteristics for a Close-Coupled Wing-Canard Model in Both Swept Back and Swept Forward Configurations. NASA TM-74092, 1978.

12. Huffman, Jarrett K.; and Fox, Charles H., Jr.: Subsonic Longitudinal and Lateral-Directional Static Aerodynamic Characteristics for a Model With Swept Back and Swept Forward Wings. NASA TM-74093, 1978.

13. Poll, D. I. A.; and Qui, Cheng-Hao: A Comparison of the Aerodynamic Characteristics of Swept Forward and Swept Back Wings Including the Effect of Strakes. Proceedings - International Conference - Forward Swept Wing Aircraft, R. K. Nangia, ed., Univ. of Bristol (United Kingdom), c.1983, pp. I.20.1 - I.20.15.

14. Mann, Michael J.; Campbell, Richard L.; and Ferris, James C.: Aerodynamic Design for Improved Maneuverability by Use of Three-Dimensional Transonic Theory. NASA TP-2282, 1984.

15. Gainer, Thomas G.; Mann, Michael J.; and Huffman, Jarrett K.: Low-Speed Investigation of Effects of Wing Leading- and Trailing-Edge Flap Deflections and Canard Incidence on a Fighter Configuration Equipped With a Forward-Swept Wing. NASA TM-85795, 1984.

16. Middleton, W. D.; and Lundry, J. L.: A System for Aerodynamic Design and Analysis of Supersonic Aircraft. Part 1 - General Description and Theoretical Development. NASA CR-3351, 1980.

17. Lamar, John E.: A Vortex-Lattice Method for the Mean Camber Shapes of Trimmed Noncoplanar Planforms With Minimum Vortex Drag. NASA TN D-8090, 1976.

18. Frink, Neal T.; and Lamar, John E.: Water-Tunnel and Analytical Investigation of the Effect of Strake Design Variables on Strake Vortex Breakdown Characteristics. NASA TP-1676, 1980.

19. Lamar, John E.; and Frink, Neal T.: Experimental and Analytical Study of the Longitudinal Aerodynamic Characteristics of Analytically and Empirically Designed Strake-Wing Configurations at Subcritical Speeds. NASA TP-1803, 1981.

20. Gingrich, P. B.; Child, R. D.; and Panageas, G. N.: Aerodynamic Configuration Development of the Highly Maneuverable Aircraft Technology Remotely Piloted Research Vehicle. NASA CR-143841, 1977.

21. Corson, Blake W., Jr.; Runckel, Jack F.; and Igoe, William B.: Calibration of the Langley 16-Foot Transonic Tunnel With Test Section Air Removal. NASA TR R-423, 1974.

22. Fox, Charles H., Jr.; and Huffman, Jarrett K.: Calibration and Test Capabilities of the Langley 7- by 10-Foot High Speed Tunnel. NASA TM X-74027, 1977.

23. Braslow, Albert L.; and Knox, Eugene C.: Simplified Method for Determination of Critical Height of Distributed Roughness Particles for Boundary-Layer Transition at Mach Numbers From 0 to 5. NACA TN 4363, 1958.

24. Ferris, James C.: Longitudinal Aerodynamic Characteristics of a Generic Fighter Model With a Wing Designed for Sustained Transonic Maneuver Conditions. NASA TM-87729, 1986.

25. Aidala, P.: Numerical Aircraft Design Using 3-D Transonic Analysis With Optimization. Volume III, Part 2: User's Guide to Fighter Design Computer Program. AFWAL-TR-81-3091, Vol. III, Pt. 2, U.S. Air Force, Aug. 1981. (Available from DTIC as AD A110 037.)

26. Mann, Michael J.: The Design of Supercritical Wings by the Use of Three-Dimensional Transonic Theory. NASA TP-1400, 1979.

27. Mann, Michael J.; and Mercer, Charles E.: A Forward-Swept Wing Configuration Designed for High Maneuverability by Use of Three-Dimensional Transonic Theory. AIAA-85-4069, Oct. 1985.

28. Cosentino, Gary B.; and Holst, Terry L.: Numerical Optimization Design of Advanced Transonic Wing Configurations. AIAA-85-0424, Jan. 1985.

29. Davis, Warren H., Jr.; Aidala, Paul V.; and Mason, William H.: A Study To Develop Improved Methods for the Design of Transonic Fighter Wings by the Use of Numerical Optimization. NASA CR-3995, 1986.

30. Gloss, Blair B.: Effect of Canard Location and Size on Canard-Wing Interference and Aerodynamic-Center Shift Related to Maneuvering Aircraft at Transonic Speeds. NASA TN D-7505, 1974.

31. Gloss, Blair B.; and Washburn, Karen E.: A Study of Canard-Wing Interference Using Experimental Pressure Data at Transonic Speeds. NASA TP-1355, 1979.

32. Butler, G. F.: An Analytical Study of the Induced Drag of Canard-Wing-Tail Aircraft Configurations With Various Levels of Static Stability. Aeronaut. J., vol. 87, no. 868, Oct. 1983, pp. 293-300.

33. McKinney, Linwood W.; and Dollyhigh, Samuel M.: Some Trim Drag Considerations for Maneuvering Aircraft. J. Aircr., vol. 8, no. 8, Aug. 1971, pp. 623-629.

34. Agnew, J. W.; and Hess, J. R., Jr.: Benefits of Aerodynamic Interaction to the Three-Surface Configuration. J. Aircr., vol. 17, no. 11, Nov. 1980, pp. 823-827.

35. Mann, Michael J.; Huffman, Jarrett K.; Fox, Charles H., Jr.; and Campbell, Richard L.: Experimental Study of Wing Leading-Edge Devices for Improved Maneuver Performance of a Supercritical Maneuvering Fighter Configuration. NASA TP-2125, 1983.

36. Luckring, James M.: Flow Visualization Studies of a General Research Fighter Model Employing a Strake-Wing Concept at Subsonic Speeds. NASA TM-80057, 1979.

37. Schlichting, Hermann (J. Kestin, transl.): Boundary Layer Theory, Fourth ed. McGraw-Hill Book Co., Inc., c.1960.

38. Sommer, Simon C.; and Short, Barbara J.: Free-Flight Measurements of Turbulent-Boundary-Layer Skin Friction in the Presence of Severe Aerodynamic Heating at Mach Numbers From 2.8 to 7.0. NACA TN 3391, 1955.

39. Hoerner, Sighard F.: Fluid-Dynamic Drag. Hoerner Fluid Dynamics (Brick Town, N.J.), c.1965.

40. Walker, Harold J.: Performance Evaluation Method for Dissimilar Aircraft Designs. NASA RP-1042, 1979.

TABLE I.- GEOMETRIC CHARACTERISTICS OF MODEL

Wing (based on trapezoid extended to fuselage centerline):	
Aspect ratio	3.28
Forward sweep of leading edge, deg	20.234
Forward sweep of trailing edge, deg	49.184
Forward sweep of quarter-chord line, deg	29.505
Taper ratio	0.2142
Area, ft^2	1.50
Span, in.	26.649
Mean aerodynamic chord, in.	9.259
Wing spanwise station of mean aerodynamic chord, in.	5.225
Fuselage station of 25 percent wing mean aerodynamic chord, in.	23.770
Root chord (at fuselage centerline), in.	13.383
Tip chord, in.	2.867
Dihedral, deg	0
Twist (wash in from root to tip), deg	6.0
Incidence (root), deg	-2.0
Airfoil sections	4.2- to 4.6-percent-thick supercritical
Canard (based on trapezoid extended to fuselage centerline, except as noted):	
Leading-edge sweep, deg	45
Aspect ratio	3.28
Taper ratio	0.2142
Area, in^2	54.122
Span, in.	13.324
Root chord (at fuselage centerline), in.	6.691
Tip chord, in.	1.433
Dihedral, deg	10
Airfoil section	5.1-percent-thick supercritical
Ratio of exposed area to wing reference area	0.156
Fuselage:	
Base cavity area, in^2	5.52
Vertical tail (based on exposed area):	
Leading-edge sweep, deg	54
Aspect ratio	1.02
Taper ratio	0.310
Area, in^2	29.76
Span, in.	5.50
Root chord, in.	8.26
Tip chord, in.	2.56
Airfoil section	4-percent circular-arc biconvex
Strakes (based on exposed area of each strake, except as noted):	
Width, in.	2.94
Root chord, in.	17.7
Slenderness ratio (Length/Width)	6.02
Area, in^2	26.10
Dihedral, deg	3
Ratio of exposed area of both strakes to wing reference area	0.241

TABLE II.- WING SECTION COORDINATES

η	0.20		0.32	
c, in.	11.280		10.018	
FS, in.	23.408		22.818	
x/c	z_u/c	z_l/c	z_u/c	z_l/c
.00000	-.03280	-.03280	-.02846	-.02846
.00250	-.02721	-.03576	-.02360	-.03120
.00500	-.02502	-.03612	-.02132	-.03167
.00750	-.02336	-.03628	-.01939	-.03194
.01000	-.02189	-.03637	-.01780	-.03200
.01500	-.01933	-.03643	-.01529	-.03197
.02500	-.01519	-.03630	-.01137	-.03182
.05000	-.00782	-.03536	-.00409	-.03106
.07500	-.00245	-.03479	.00144	-.03002
.10000	.00217	-.03379	.00585	-.02903
.15000	.01035	-.03041	.01342	-.02697
.20000	.01766	-.02670	.01999	-.02404
.25000	.02373	-.02214	.02554	-.01978
.30000	.02924	-.01651	.03054	-.01490
.35000	.03440	-.01018	.03532	-.00898
.40000	.03893	-.00398	.03971	-.00307
.45000	.04301	.00216	.04330	.00247
.50000	.04594	.00763	.04590	.00765
.55000	.04760	.01278	.04742	.01235
.60000	.04826	.01689	.04768	.01635
.65000	.04773	.01951	.04655	.01839
.70000	.04610	.02088	.04441	.01970
.75000	.04288	.02214	.04133	.02030
.80000	.03811	.02172	.03726	.02003
.85000	.03171	.01956	.03153	.01740
.90000	.02383	.01509	.02344	.01261
.95000	.01354	.00739	.01269	.00465
1.00000	-.00212	-.00652	-.00040	-.00595

TABLE II.- Continued

η	0.42		0.52	
c, in.	8.966		7.914	
FS, in.	22.327		21.836	
x/c	z_u/c	z_l/c	z_u/c	z_l/c
.00000	-.02526	-.02526	-.01930	-.01930
.00250	-.01988	-.02835	-.01410	-.02177
.00500	-.01769	-.02908	-.01212	-.02232
.00750	-.01595	-.02937	-.01050	-.02263
.01000	-.01456	-.02951	-.00914	-.02283
.01500	-.01221	-.02954	-.00659	-.02306
.02500	-.00834	-.02953	-.00254	-.02323
.05000	-.00119	-.02866	.00466	-.02283
.07500	.00439	-.02768	.01015	-.02199
.10000	.00894	-.02640	.01504	-.02107
.15000	.01658	-.02398	.02224	-.01870
.20000	.02290	-.02124	.02860	-.01543
.25000	.02819	-.01724	.03352	-.01144
.30000	.03261	-.01295	.03738	-.00803
.35000	.03648	-.00769	.04043	-.00416
.40000	.03995	-.00241	.04281	-.00056
.45000	.04300	.00286	.04462	.00363
.50000	.04533	.00757	.04579	.00706
.55000	.04678	.01169	.04625	.01048
.60000	.04719	.01519	.04581	.01296
.65000	.04622	.01747	.04442	.01510
.70000	.04370	.01886	.04163	.01630
.75000	.04030	.01914	.03794	.01652
.80000	.03550	.01851	.03282	.01549
.85000	.02930	.01603	.02605	.01277
.90000	.02127	.01086	.01724	.00764
.95000	.01045	.00265	.00683	-.00044
1.00000	-.00310	-.00864	-.00664	-.01203

TABLE II.- Continued

η	0.60		0.70	
c, in.	7.073		6.021	
FS, in.	21.443		20.952	
x/c	z_u/c	z_l/c	z_u/c	z_l/c
.00000	-.00855	-.00855	.01120	.01120
.00250	-.00366	-.01151	.01605	.00882
.00500	-.00186	-.01226	.01795	.00805
.00750	-.00046	-.01266	.01949	.00757
.01000	.00080	-.01296	.02079	.00726
.01500	.00307	-.01326	.02313	.00685
.02500	.00676	-.01376	.02662	.00635
.05000	.01368	-.01402	.03296	.00586
.07500	.01898	-.01317	.03755	.00593
.10000	.02349	-.01197	.04090	.00616
.15000	.03100	-.00947	.04592	.00698
.20000	.03666	-.00699	.05013	.00840
.25000	.04088	-.00394	.05313	.01009
.30000	.04392	-.00161	.05512	.01141
.35000	.04610	.00165	.05629	.01319
.40000	.04753	.00420	.05677	.01470
.45000	.04841	.00744	.05649	.01684
.50000	.04866	.01016	.05566	.01855
.55000	.04833	.01294	.05425	.02014
.60000	.04720	.01494	.05209	.02112
.65000	.04509	.01647	.04905	.02094
.70000	.04196	.01710	.04440	.02009
.75000	.03805	.01692	.03928	.01948
.80000	.03240	.01523	.03240	.01635
.85000	.02527	.01163	.02394	.01171
.90000	.01613	.00611	.01363	.00494
.95000	.00418	-.00231	.00074	-.00515
1.00000	-.01065	-.01479	-.01646	-.02074

TABLE II.- Concluded

η	0.80		0.90	
c, in.	4.970		3.918	
FS, in.	20.461		19.970	
x/c	z_u/c	z_l/c	z_u/c	z_l/c
.00000	.02621	.02621	.03736	.03736
.00250	.03125	.02390	.04150	.03548
.00500	.03278	.02319	.04320	.03515
.00750	.03421	.02273	.04465	.03494
.01000	.03542	.02241	.04590	.03476
.01500	.03748	.02202	.04828	.03443
.02500	.04112	.02148	.05207	.03403
.05000	.04733	.02132	.05919	.03367
.07500	.05184	.02081	.06399	.03375
.10000	.05553	.02087	.06760	.03410
.15000	.06061	.02160	.07245	.03494
.20000	.06375	.02210	.07515	.03535
.25000	.06544	.02315	.07665	.03537
.30000	.06607	.02317	.07657	.03510
.35000	.06597	.02400	.07606	.03438
.40000	.06532	.02412	.07403	.03329
.45000	.06417	.02498	.07103	.03177
.50000	.06226	.02539	.06712	.02958
.55000	.05960	.02535	.06244	.02714
.60000	.05605	.02494	.05705	.02470
.65000	.05146	.02357	.05075	.02201
.70000	.04546	.02134	.04338	.01863
.75000	.03913	.01805	.03504	.01421
.80000	.03173	.01457	.02534	.00849
.85000	.02259	.00826	.01418	.00071
.90000	.01102	-.00101	.00112	-.01065
.95000	-.00286	-.01284	-.01423	-.02389
1.00000	-.01946	-.02760	-.03095	-.03858

TABLE III.- CANARD SECTION COORDINATES

η_c	0.30		0.90	
c, in.	5.113		1.956	
FS, in.	13.000		17.000	
x/c	z_u/c	z_l/c	z_u/c	z_l/c
.00000	.29019	.29019	1.10125	1.10125
.01000	.30129	.28498	1.11285	1.09602
.02500	.30509	.28365	1.11890	1.09488
.05000	.31047	.28281	1.12527	1.09499
.07500	.31544	.28272	1.13012	1.09553
.10000	.32012	.28287	1.13459	1.09619
.20000	.33340	.28456	1.14962	1.10229
.30000	.33689	.28632	1.16171	1.11084
.40000	.33562	.28761	1.16966	1.11923
.50000	.33175	.28840	1.17413	1.12789
.60000	.32658	.28908	1.17582	1.13508
.70000	.31964	.28991	1.17478	1.14074
.80000	.31102	.28979	1.17130	1.14521
.90000	.30073	.28765	1.16514	1.14788
.95000	.29423	.28464	1.16100	1.14837
1.00000	.28722	.28008	1.15632	1.14581

TABLE IV.- COMPARISON OF CONFIGURATIONS

[All wing quantities refer to basic trapezoidal wing extended to model centerline]

Configuration	A	λ	$\frac{S_{c,exp}}{S}$	$\frac{S_{t,exp}}{S}$
FSW	3.28	0.2142	0.156	0.245
SMF-1	3.28	.2142		
HiMAT	3.85	.25	.301	
X-29 research model	4.0	.4	.191	

TABLE V.- STRAKE PLANFORM LEADING-EDGE COORDINATES

x', in.	y', in.
0	0
.058	.052
.132	.104
.220	.156
.318	.208
.428	.261
.744	.395
1.114	.529
1.535	.665
2.004	.803
2.520	.941
3.083	1.081
3.695	1.222
4.356	1.364
5.070	1.508
5.840	1.653
6.673	1.800
7.577	1.949
8.568	2.100
9.662	2.254
10.889	2.411
12.304	2.573
14.039	2.743
16.803	2.941

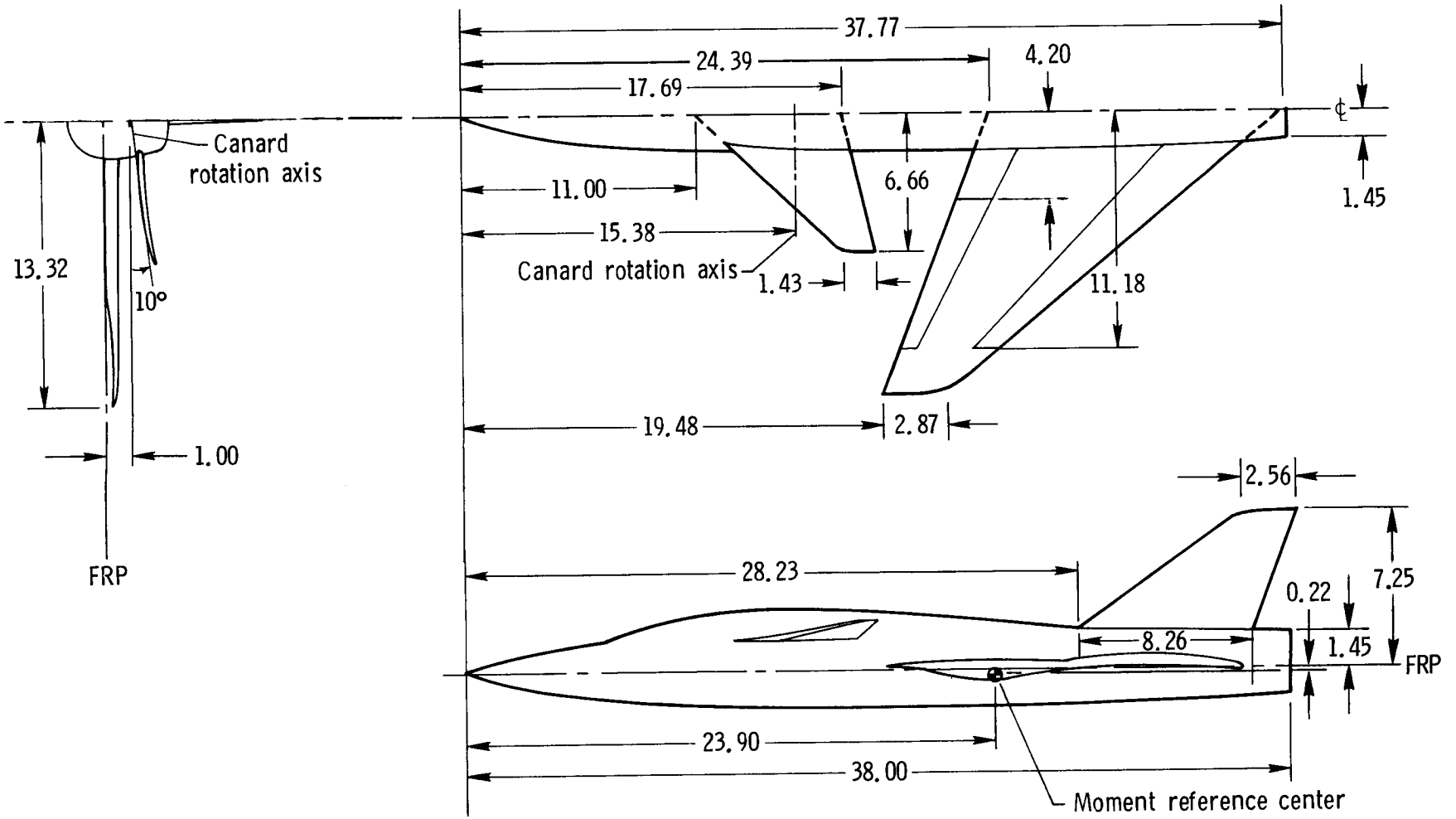

(a) General arrangement of model.

Figure 1.- Geometric characteristics of model. Dimensions are in inches unless otherwise indicated.

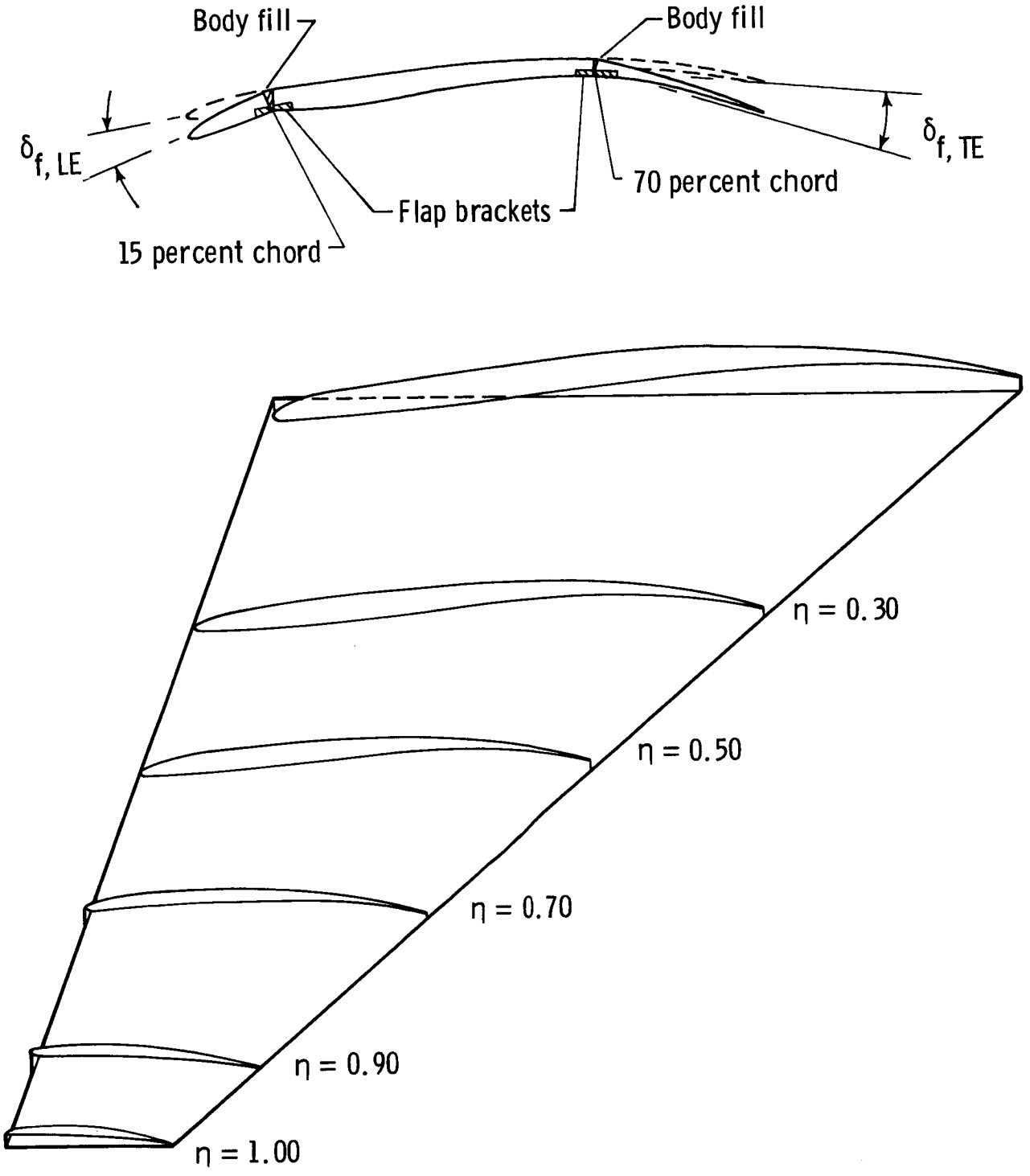

(b) Wing sections and flap locations.

Figure 1.- Continued.

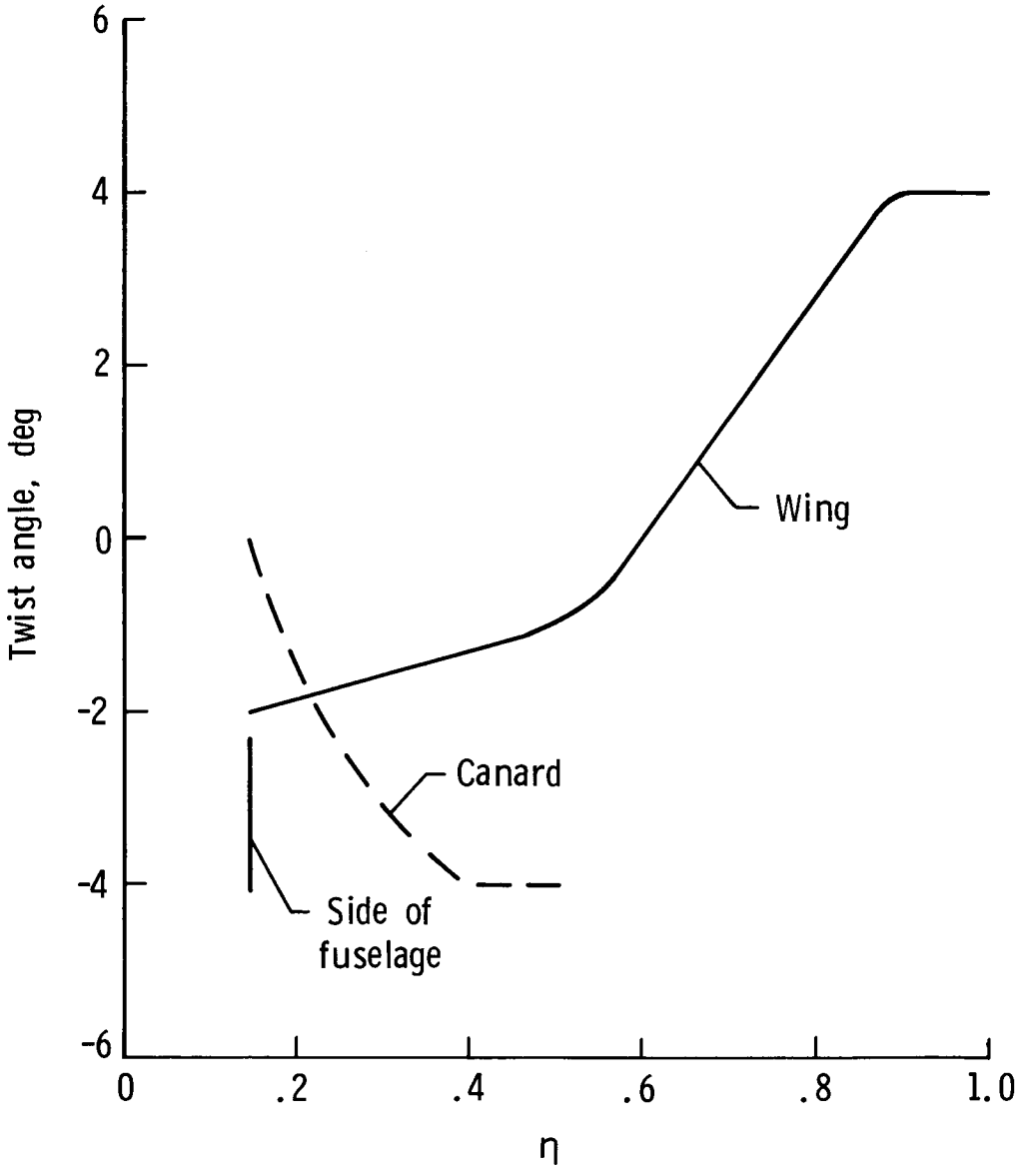

(c) Twist distributions for wing and canard.

Figure 1.- Continued.

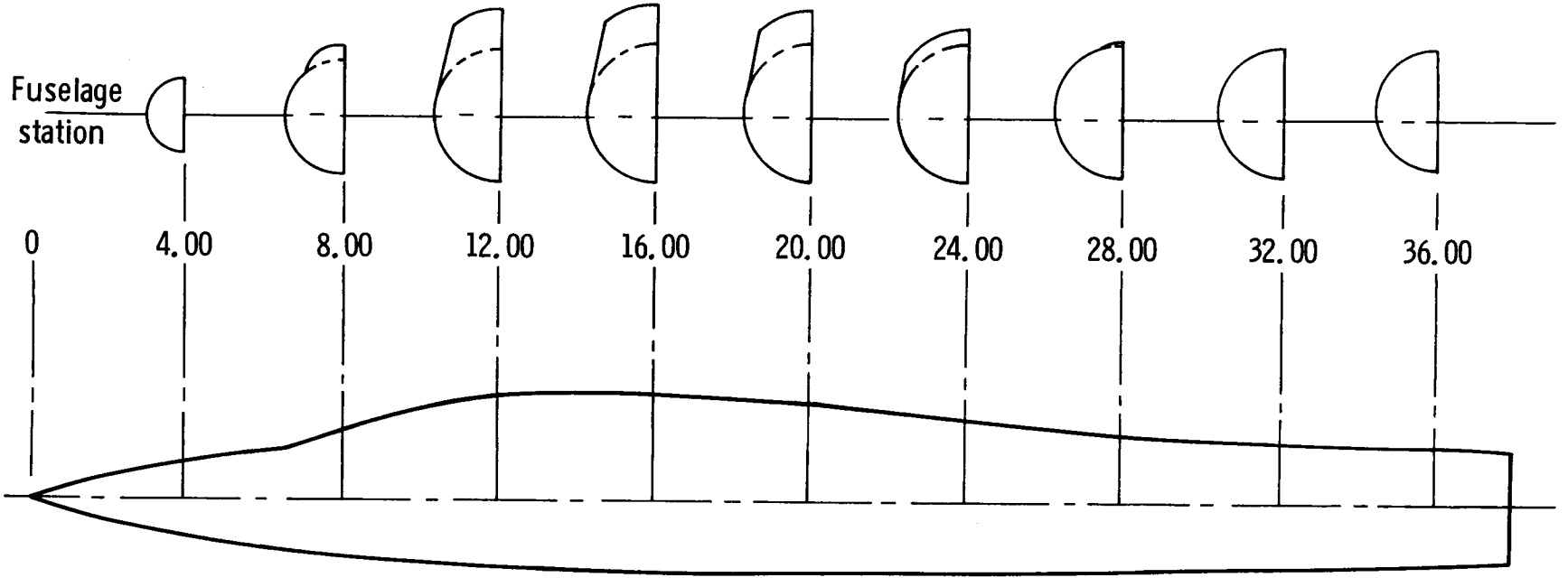

(d) Fuselage external contours.

Figure 1.- Continued.

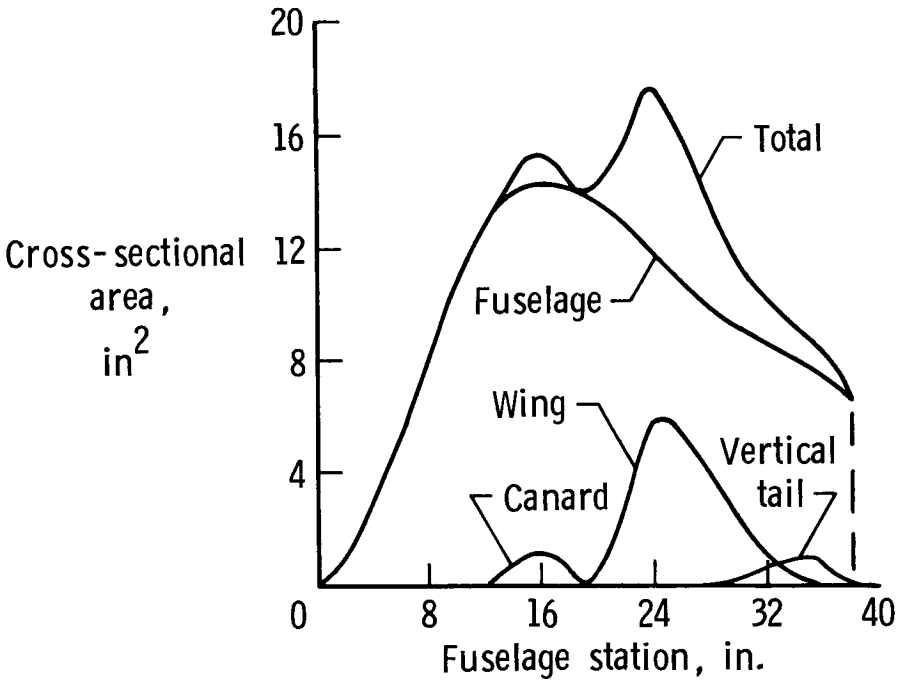

(e) Longitudinal variation of cross-sectional areas.

Figure 1.- Continued.

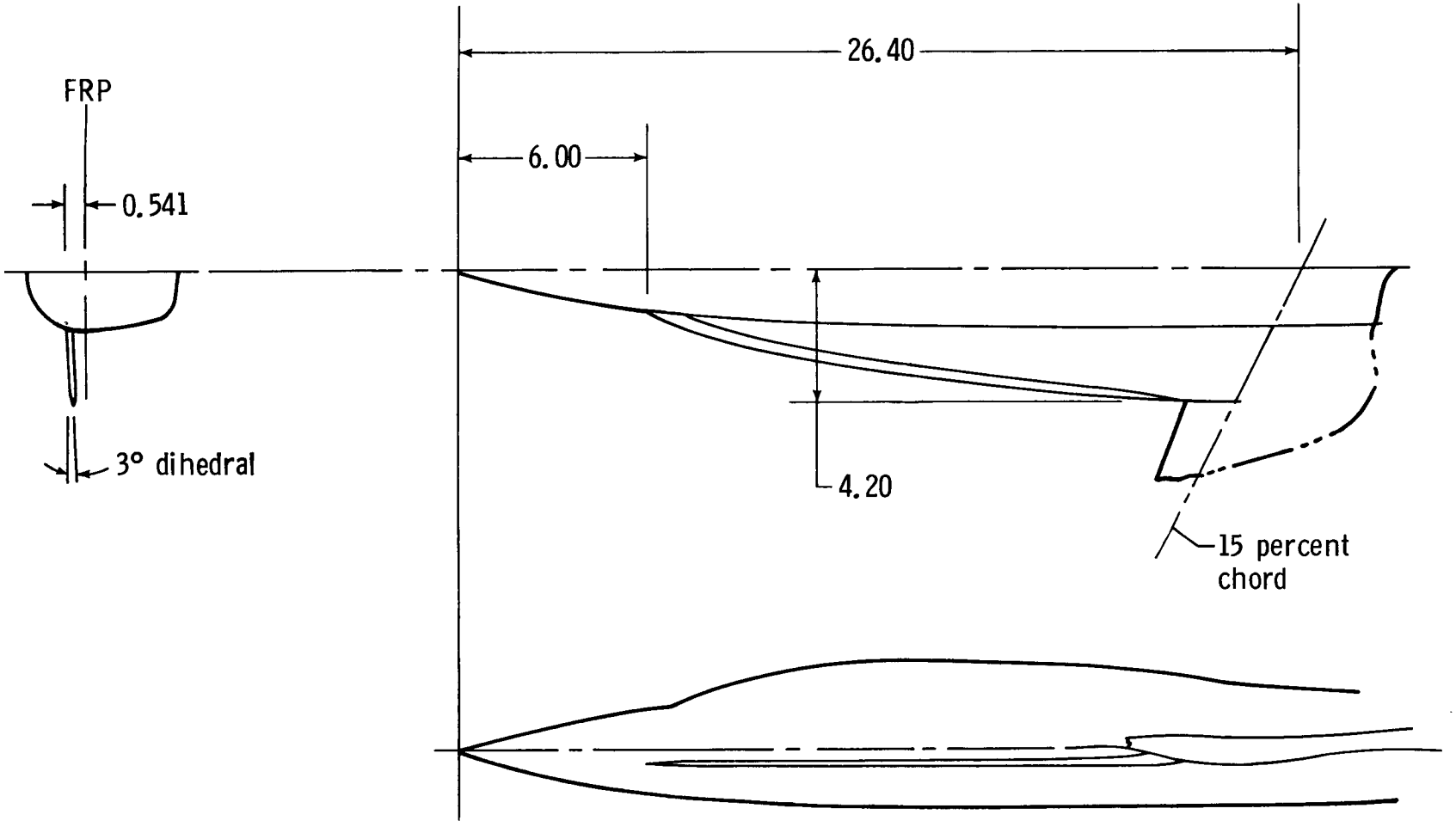

(f) Forebody strakes.

Figure 1.- Concluded.

L-83-6659

(a) Three-quarter front top view of canard-wing configuration in Langley 16-Foot Transonic Tunnel.

Figure 2.- Model mounted in Langley 16-Foot Transonic Tunnel and Langley 7- by 10-Foot High-Speed Tunnel.

L-83-6657

(b) Three-quarter front bottom view of canard-wing configuration in Langley 16-Foot Transonic Tunnel.

Figure 2.- Continued.

L-84-6614

(c) Three-quarter rear top view of strake-wing configuration in Langley 7- by 10-Foot High-Speed Tunnel.

Figure 2.- Concluded.

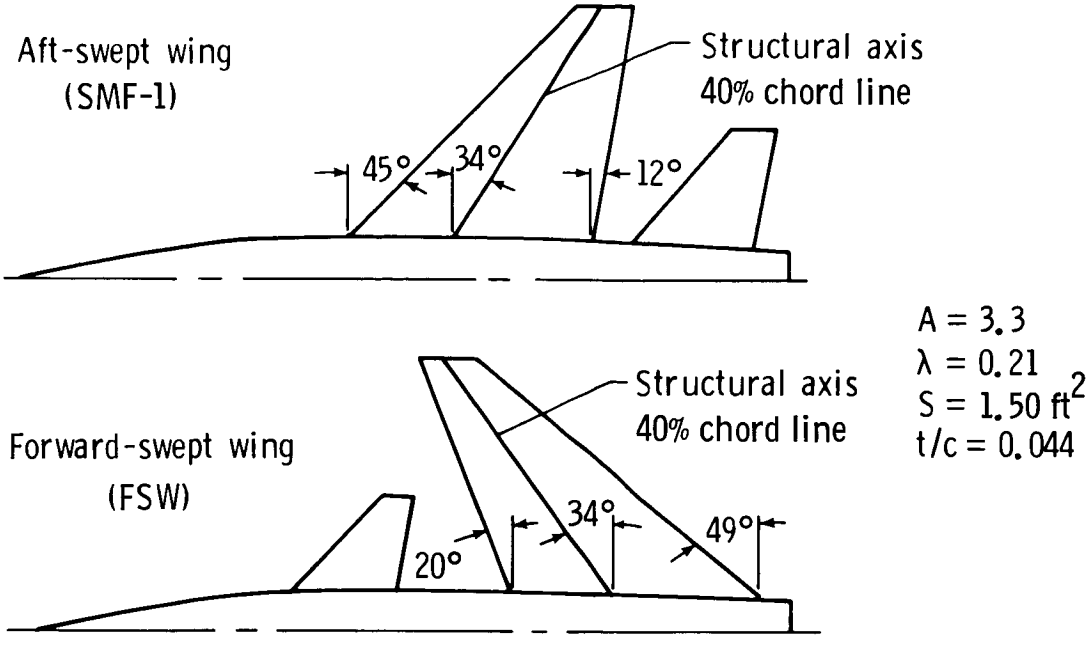

(a) Comparison of forward-swept-wing configuration with an equivalent aft-swept-wing configuration (SMF-1).

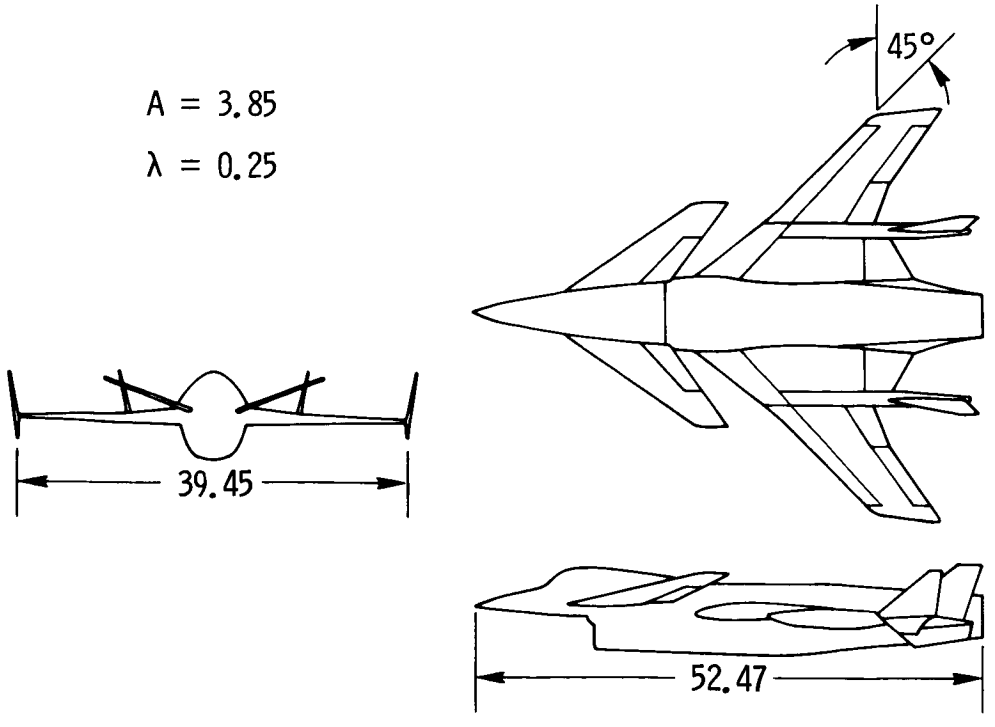

(b) HiMAT configuration.

Figure 3.- General arrangement of configurations examined. Dimensions are in inches unless otherwise indicated.

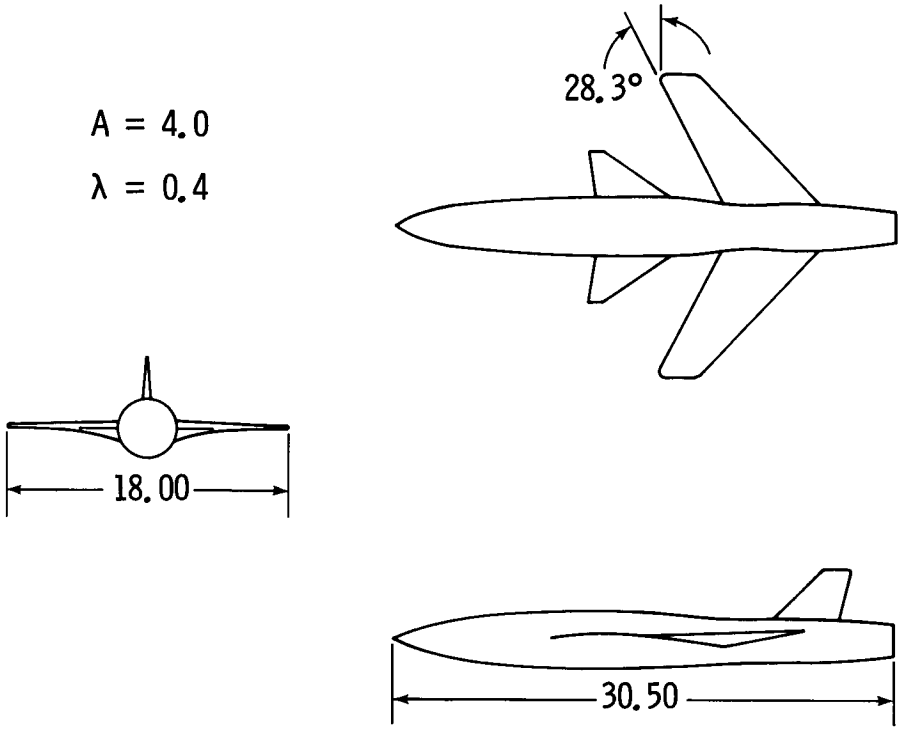

(c) X-29 research configuration.

Figure 3.- Concluded.

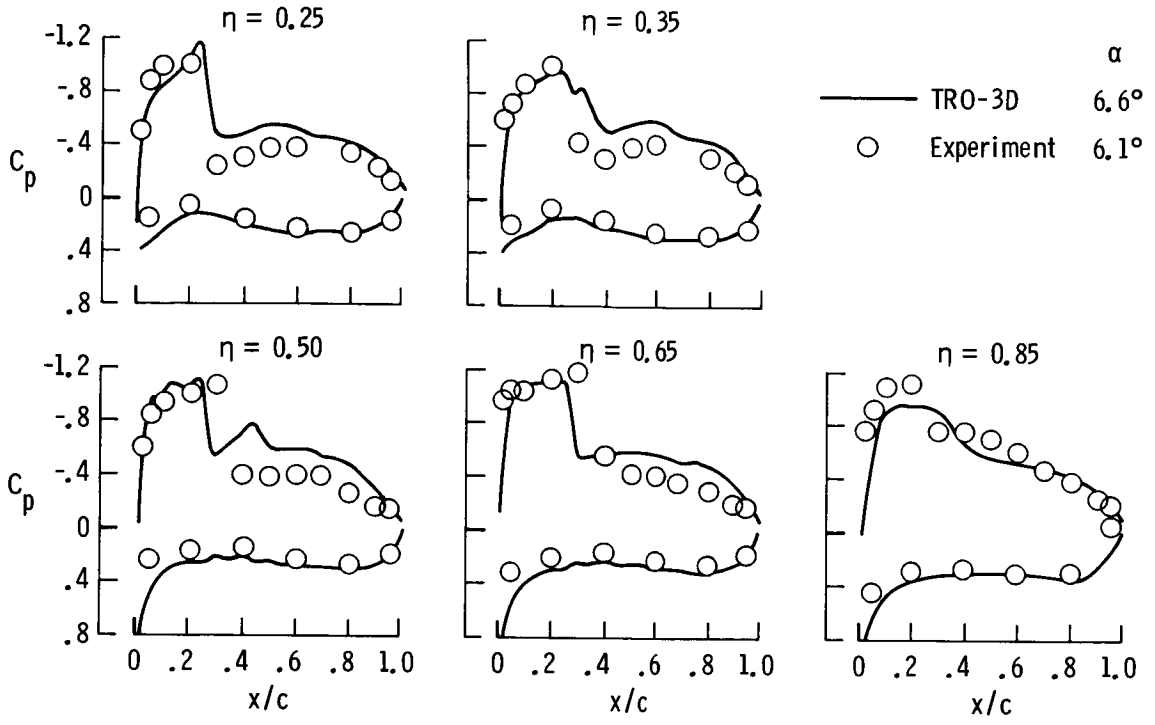

(a) Canard on; M = 0.80; C_L = 0.81.

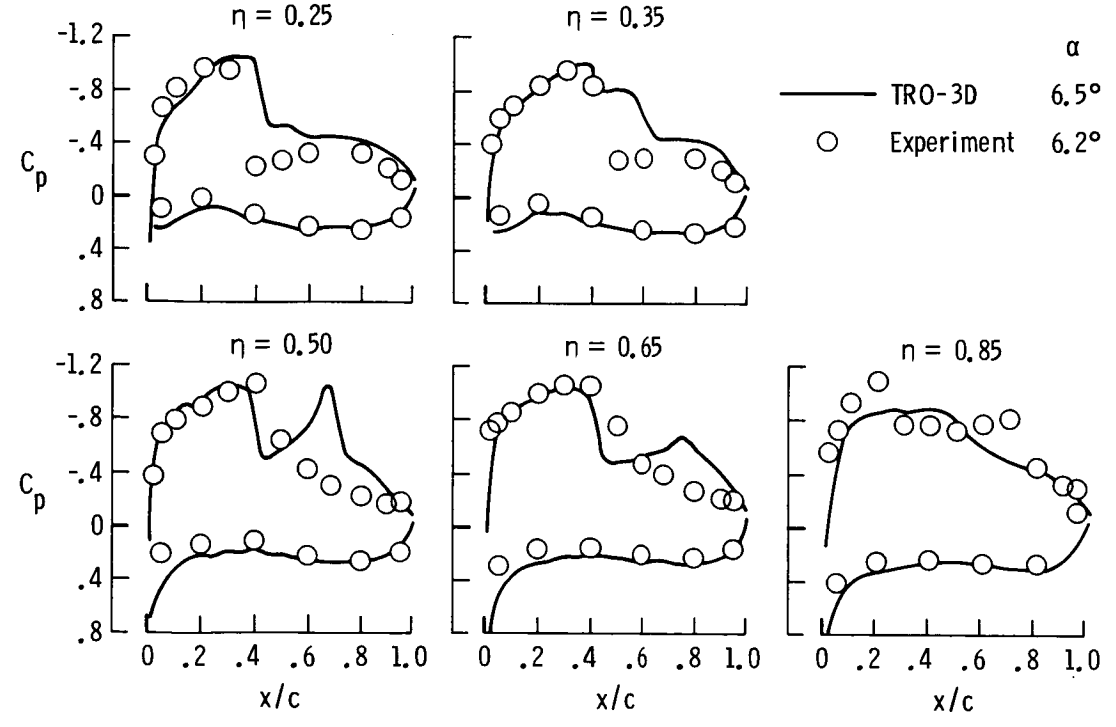

(b) Canard on; M = 0.85; C_L = 0.83.

Figure 4.- Comparison of theoretical and experimental wing pressure distributions. Strakes off; $\delta_c = 0°$; $\delta_{f,TE} = \delta_{f,LE} = 0°$.

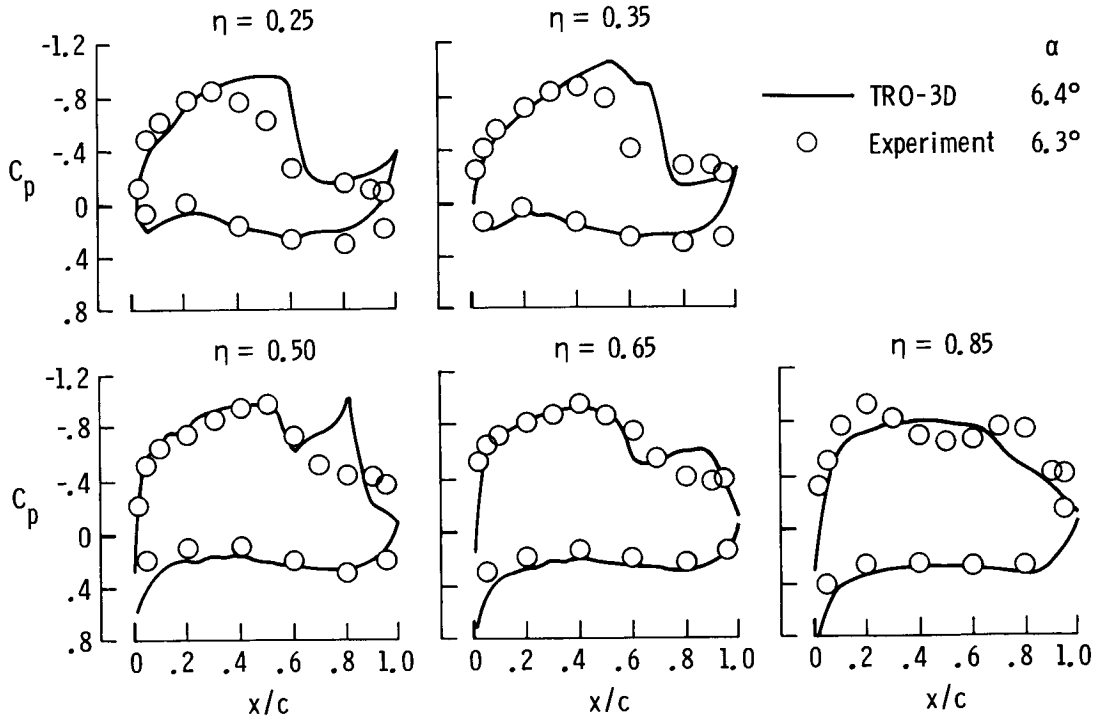

(c) Canard on; M = 0.90; C_L = 0.85.

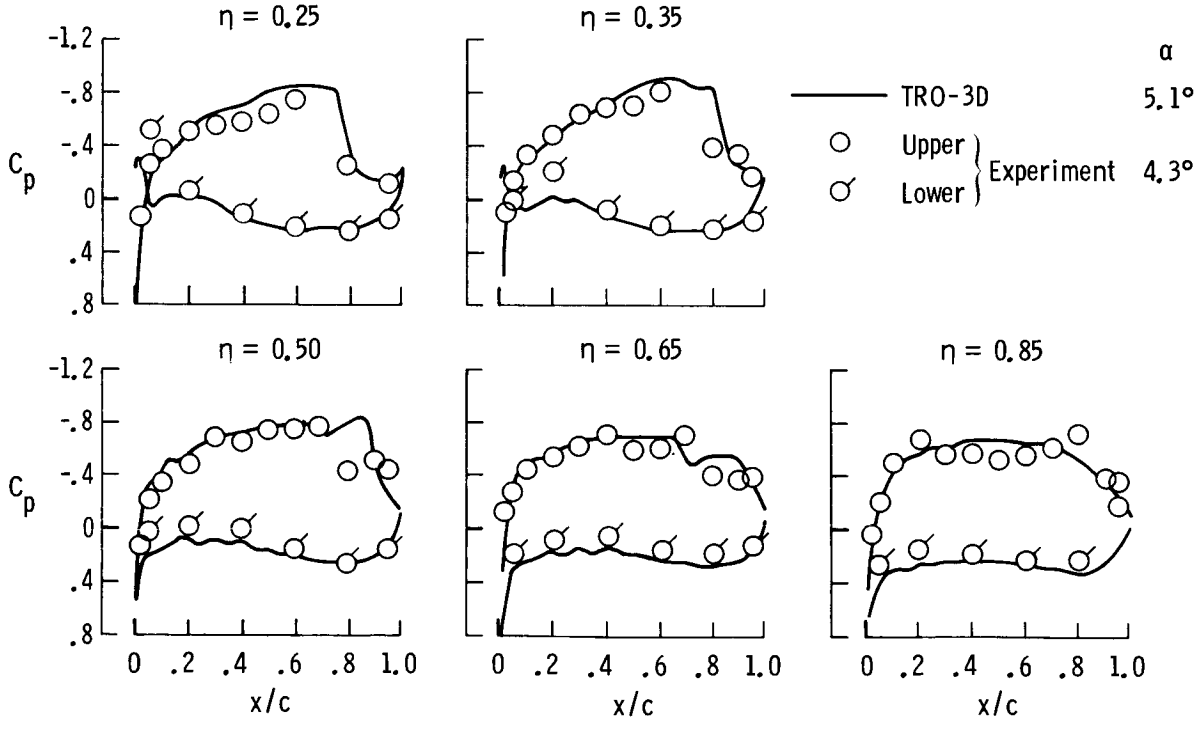

(d) Canard on; M = 0.95; C_L = 0.65.

Figure 4.- Continued.

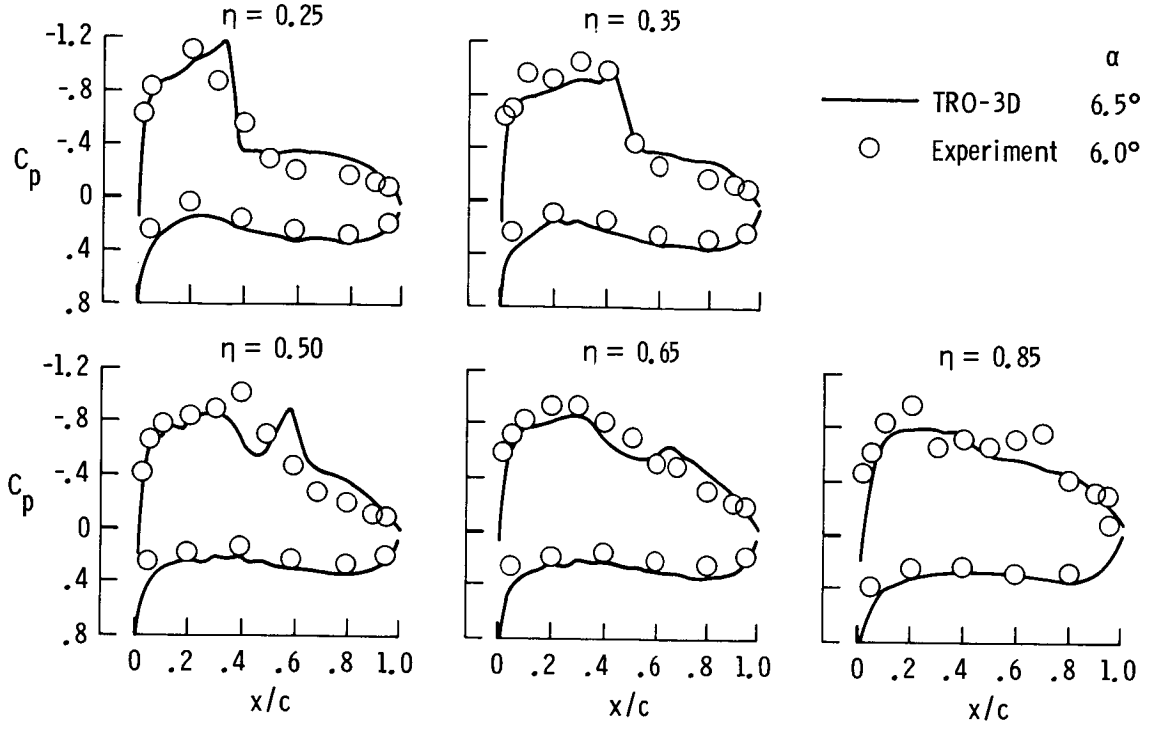

(e) Canard off; M = 0.85; C_L = 0.75.

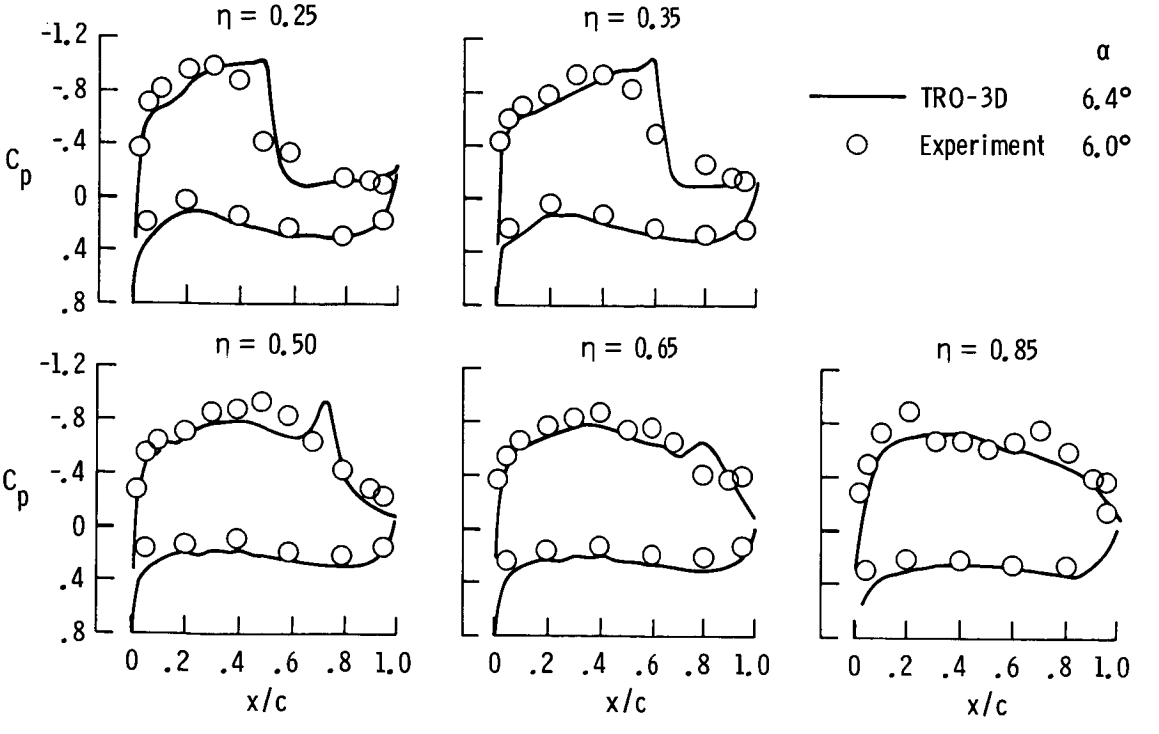

(f) Canard off; M = 0.90; C_L = 0.73.

Figure 4.- Concluded.

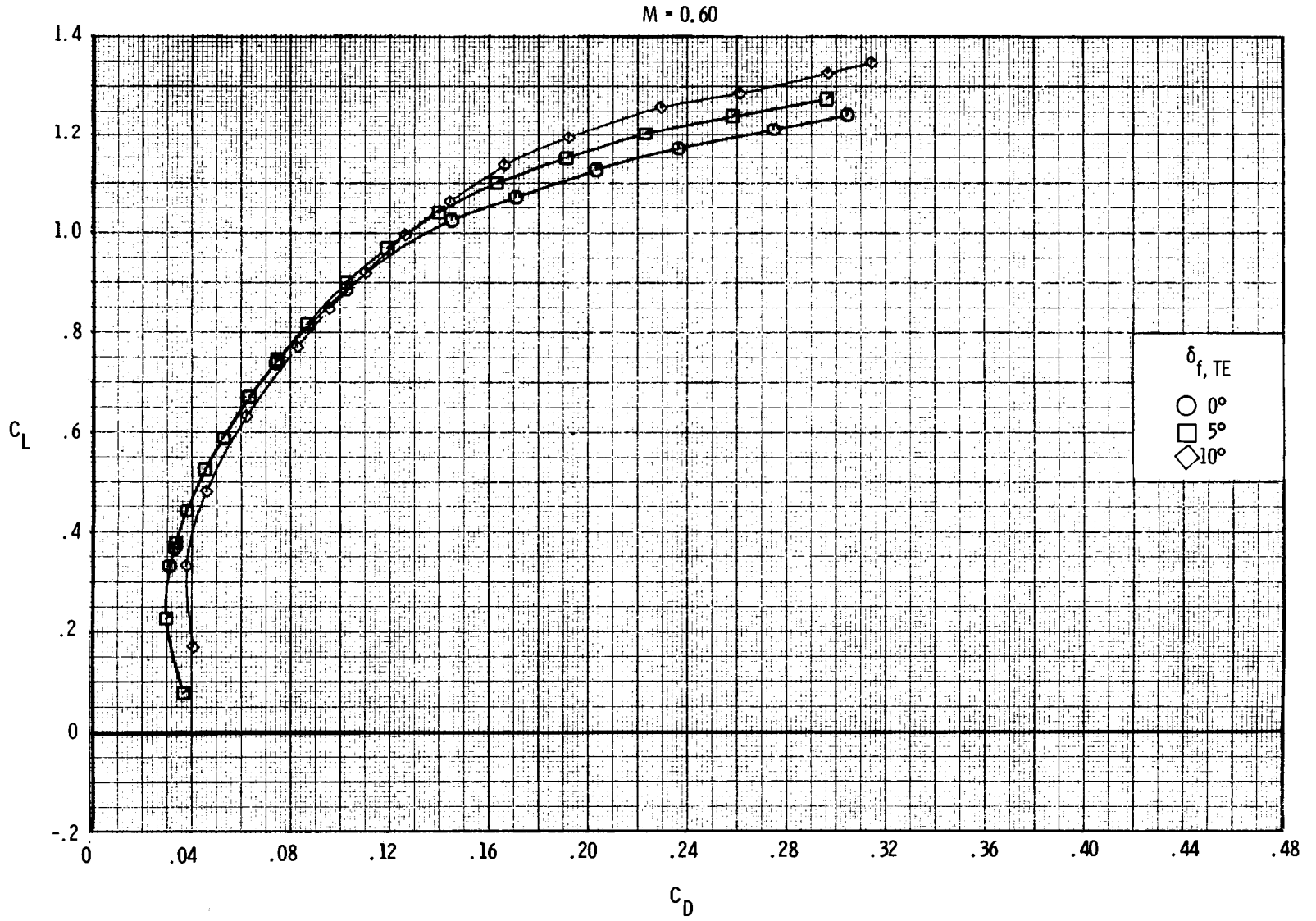

(a) Variation of C_L with C_D.

Figure 5.- Effect of trailing-edge flaps on longitudinal aerodynamic characteristics. Strakes off; $\delta_c = 0°$; $\delta_{f,LE} = 0°$.

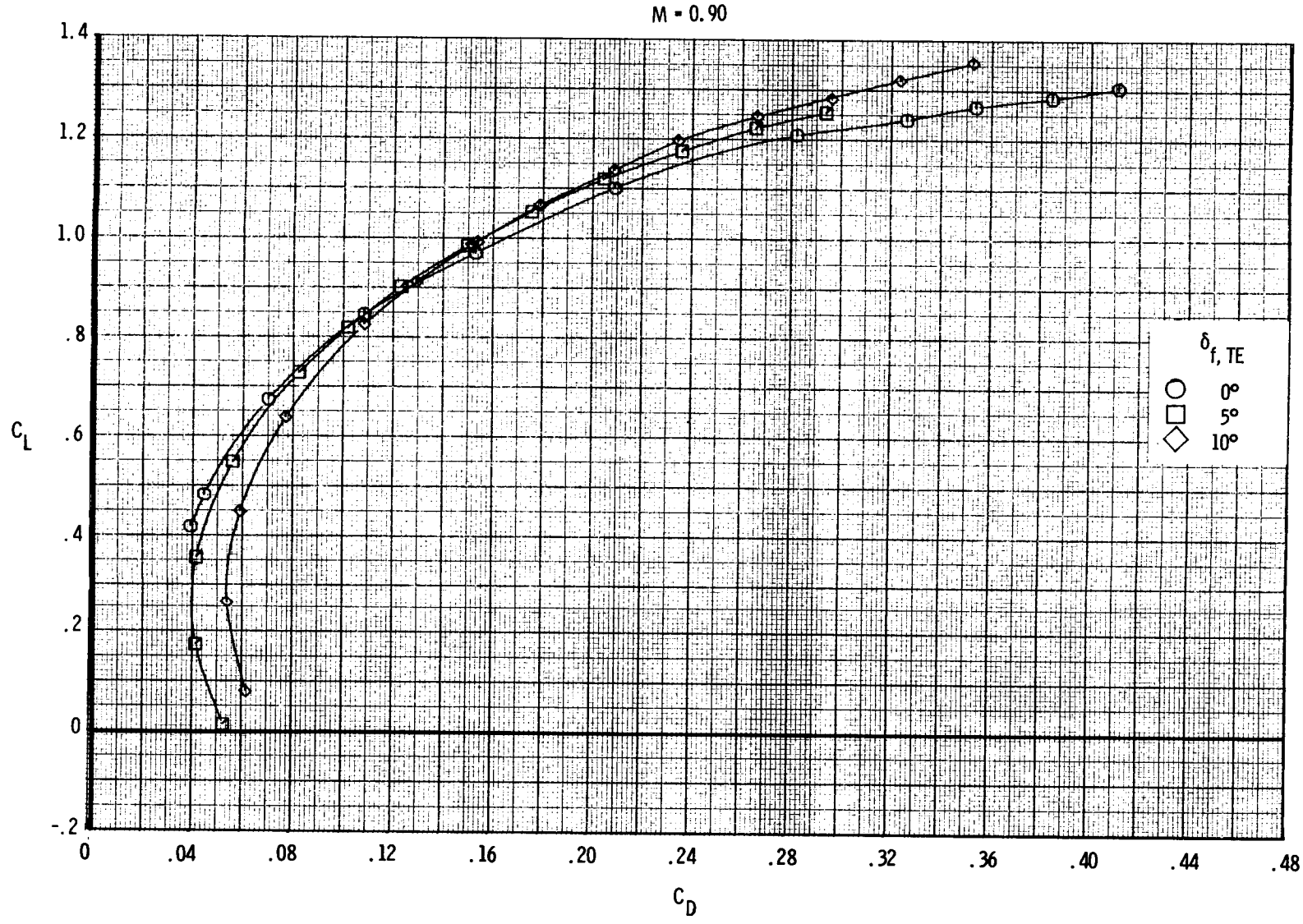

(a) Continued.

Figure 5.- Continued.

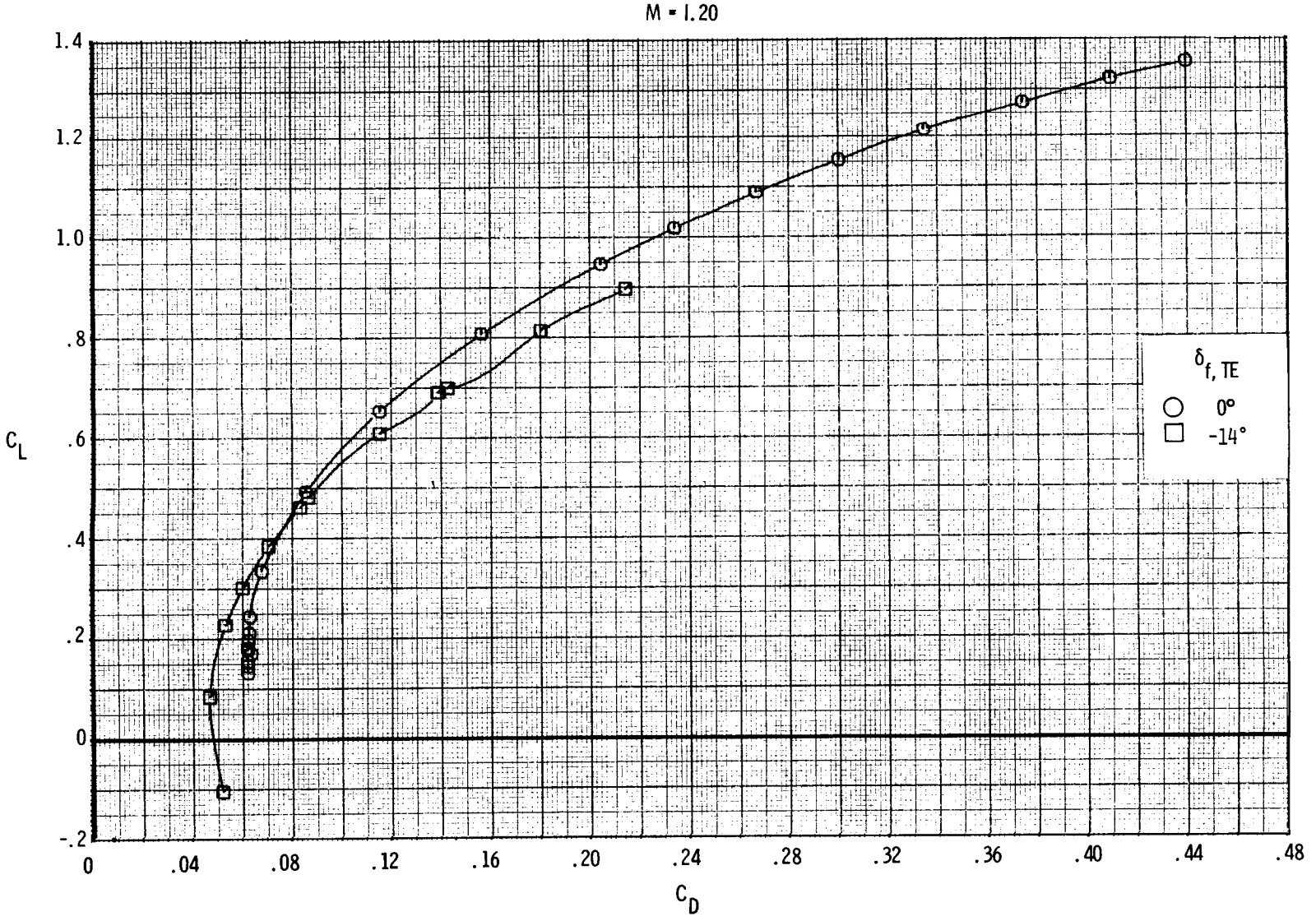

(a) Concluded.

Figure 5.- Continued.

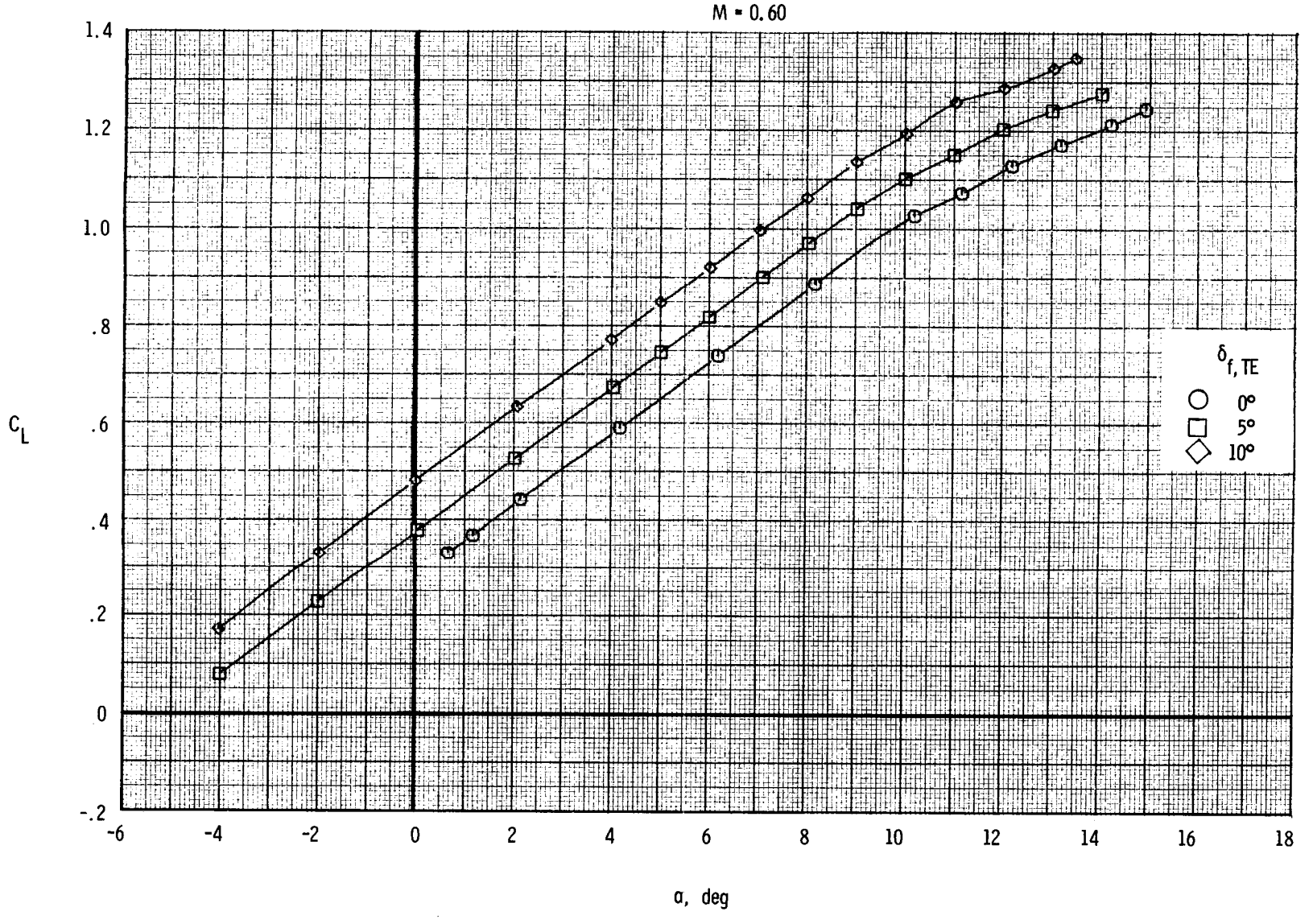

(b) Variation of C_L with α.

Figure 5.- Continued.

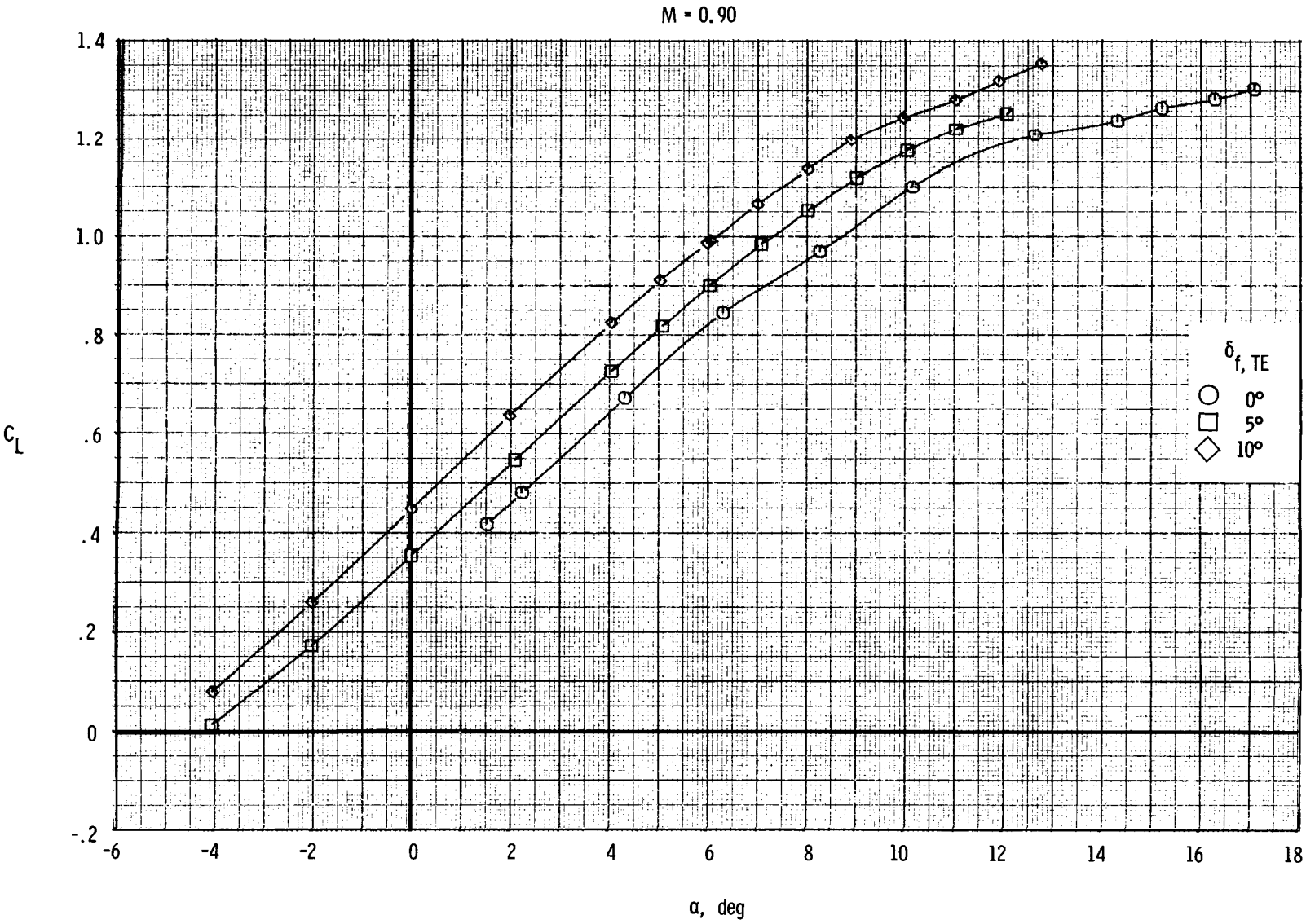

(b) Continued.

Figure 5.- Continued.

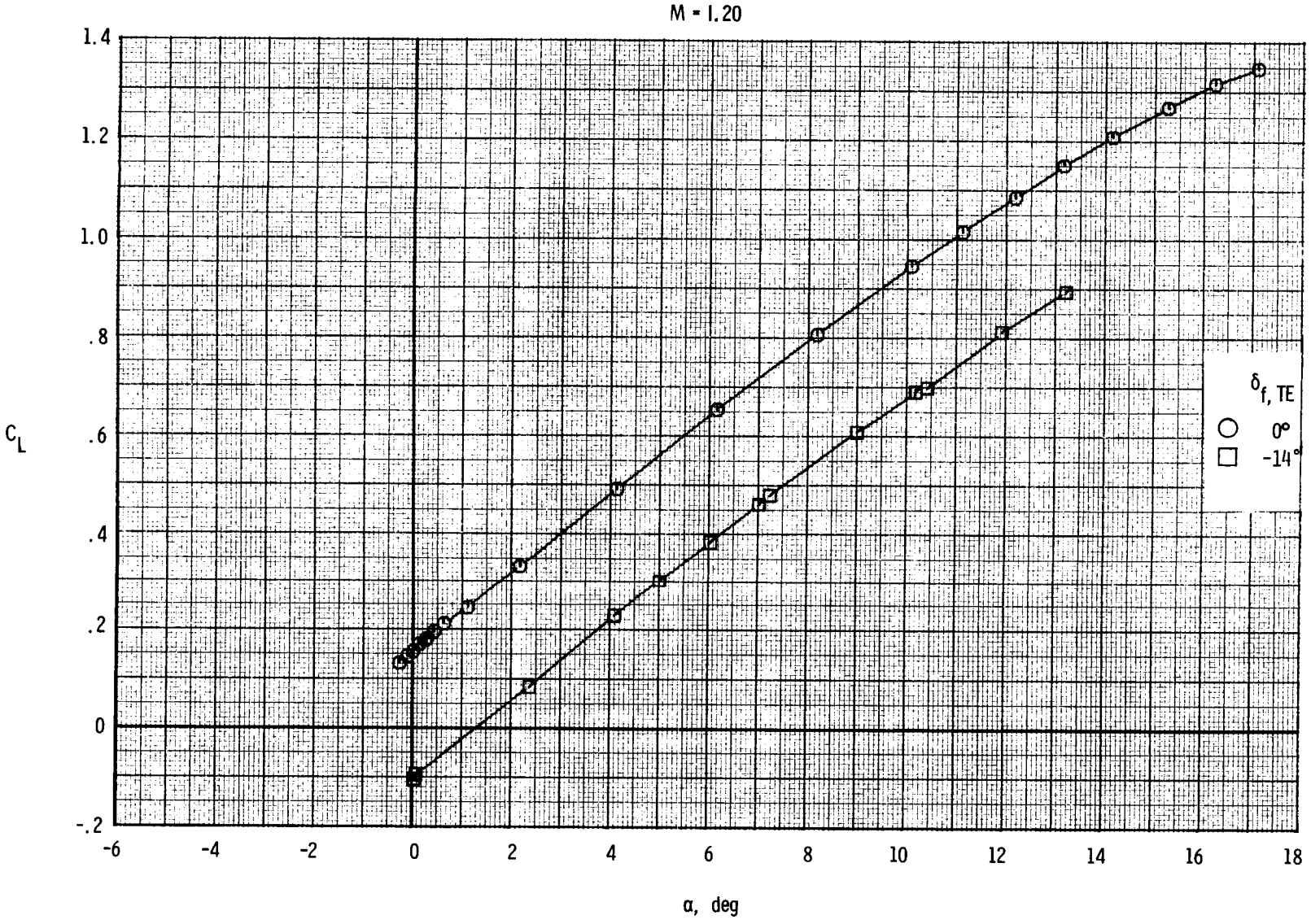

(b) Concluded.

Figure 5.- Continued.

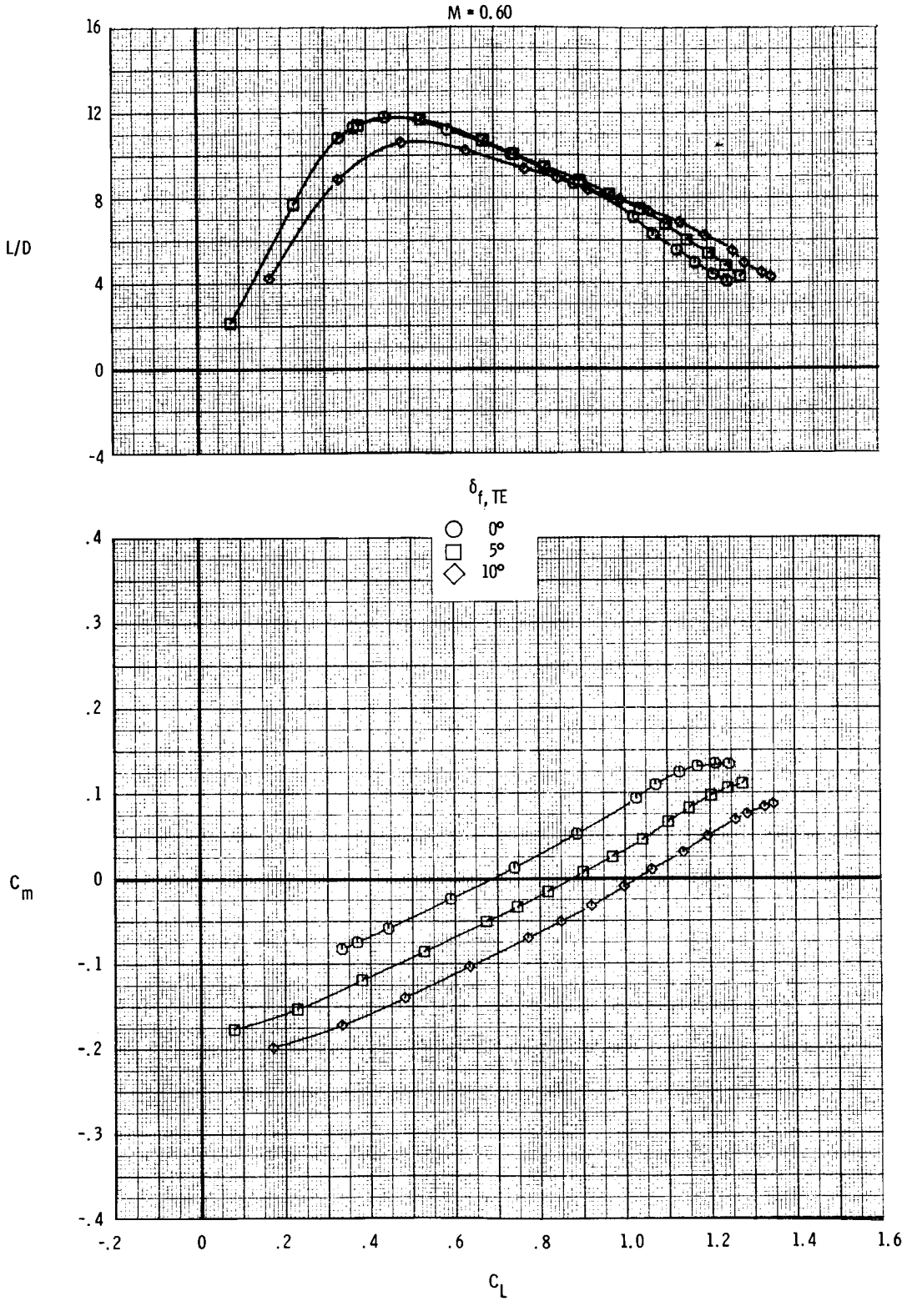

(c) Variation of L/D and C_m with C_L.

Figure 5.- Continued.

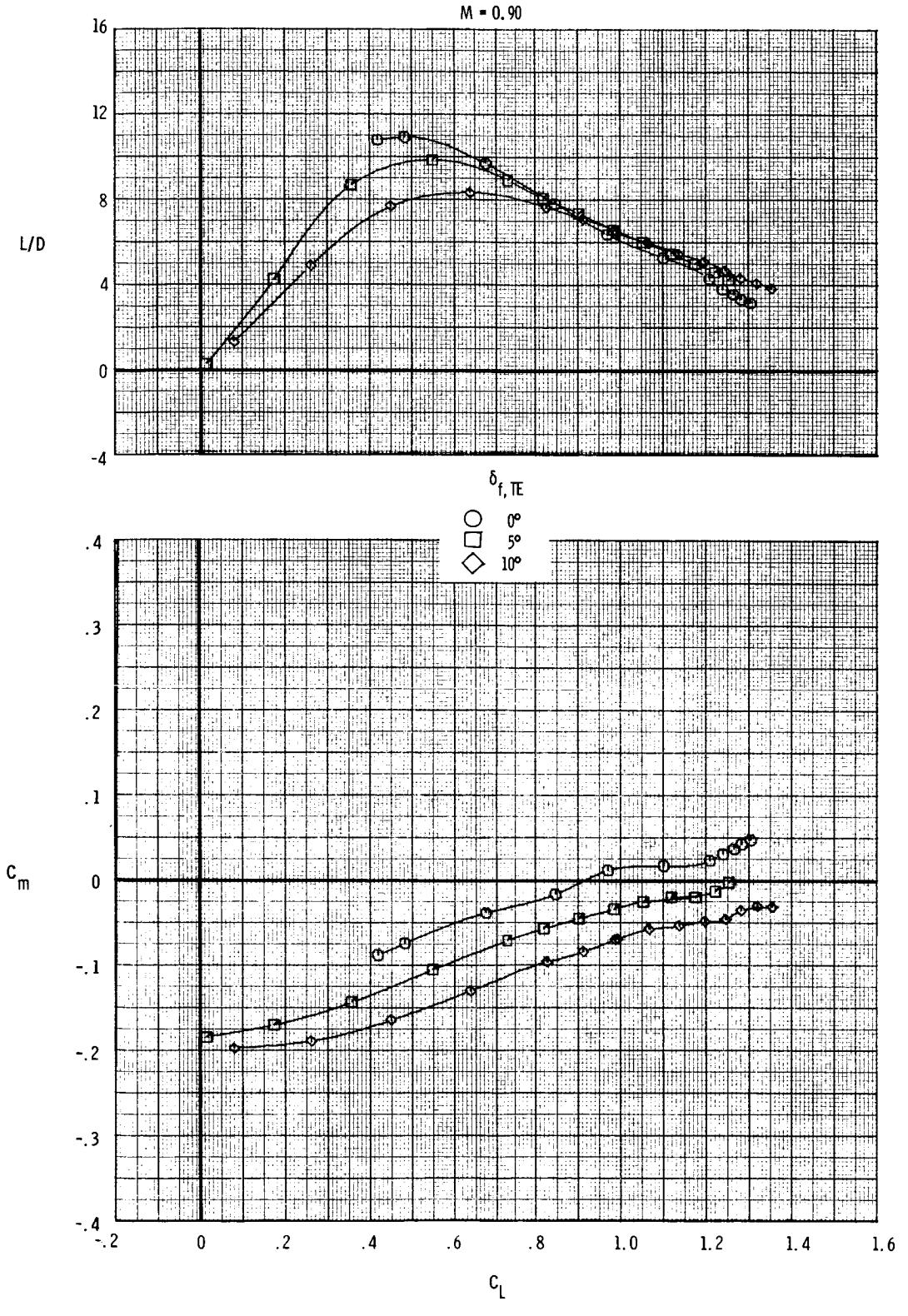

(c) Continued.

Figure 5.- Continued.

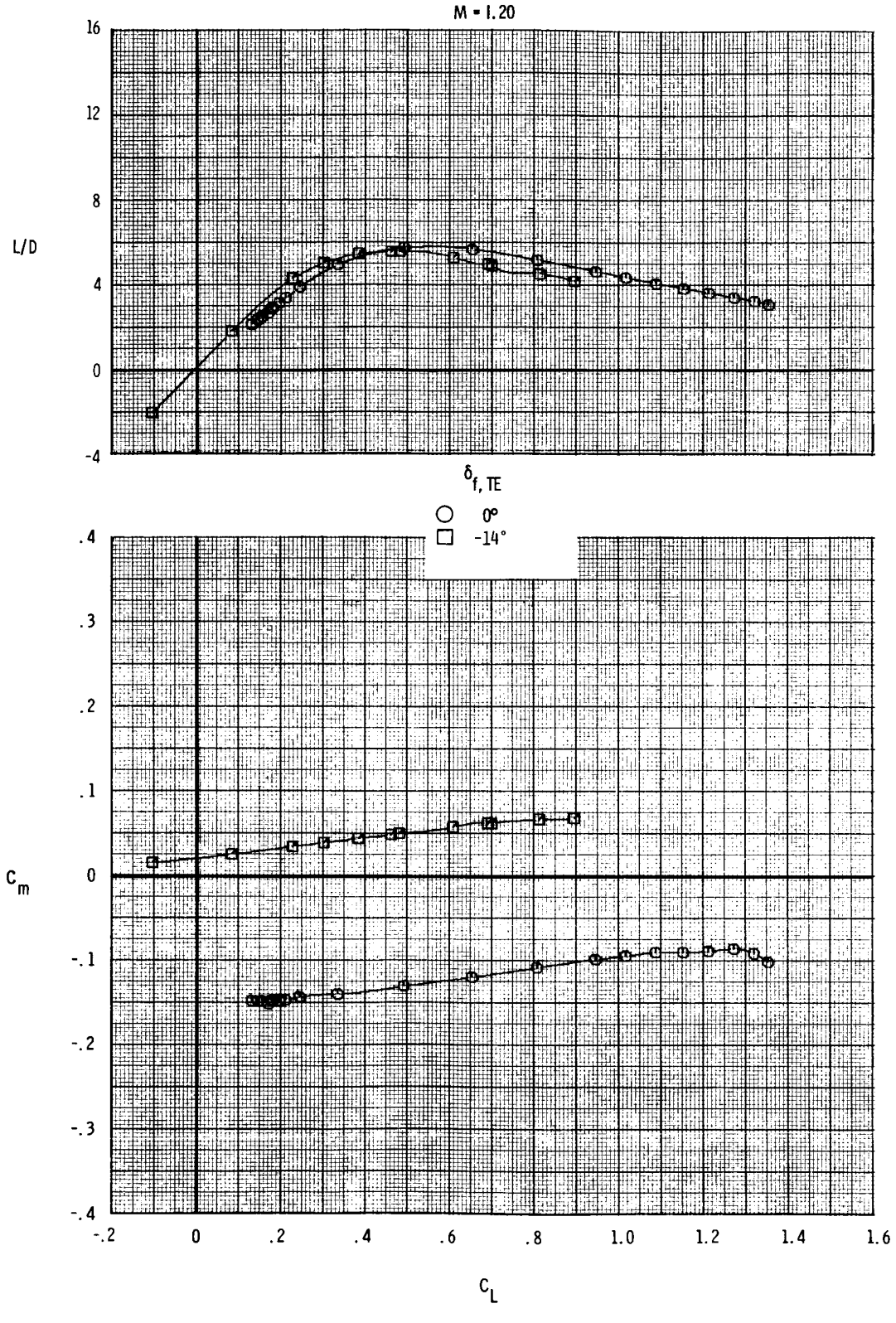

(c) Concluded.

Figure 5.- Concluded.

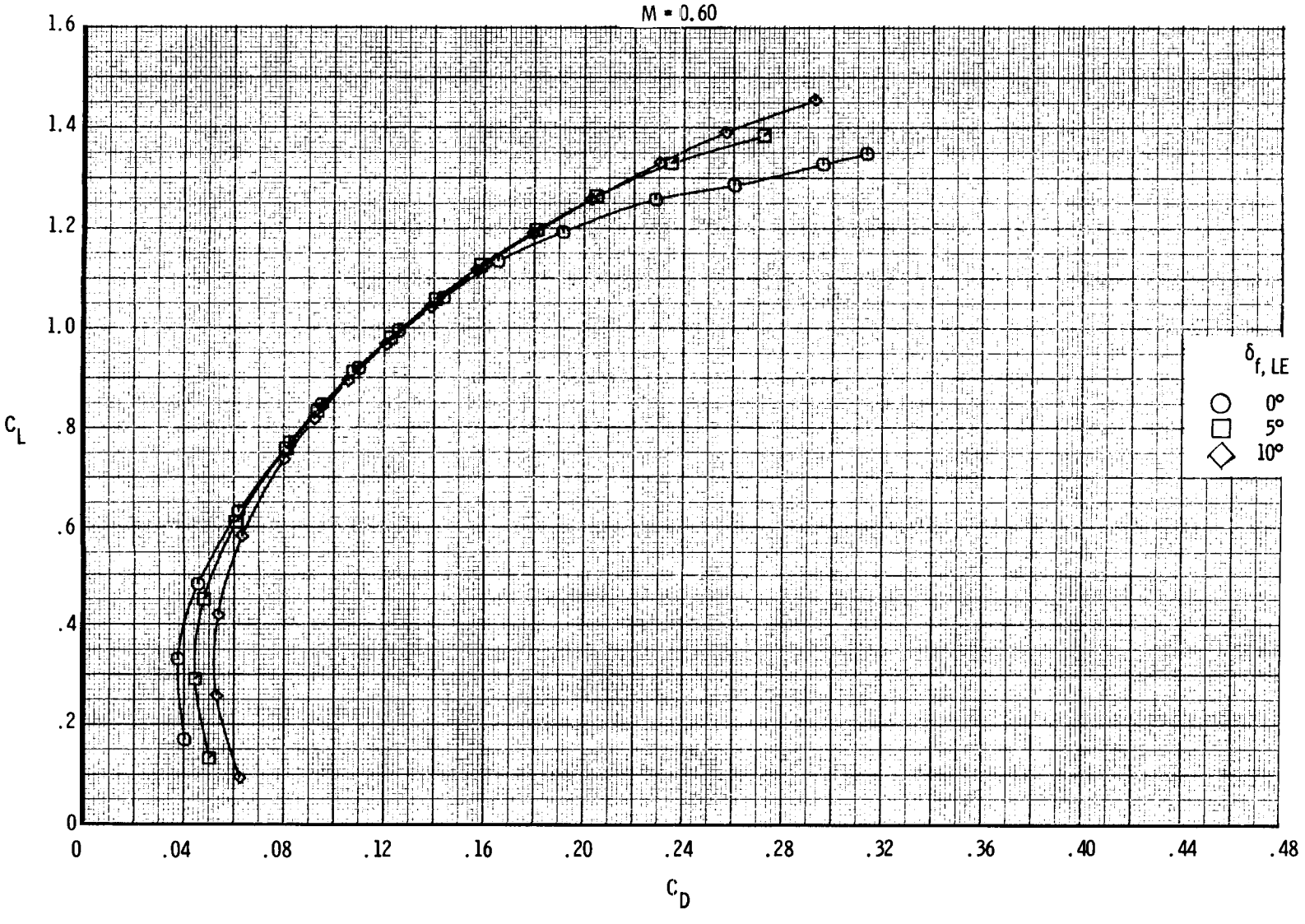

(a) Variation of C_L with C_D.

Figure 6.- Effect of leading-edge flaps on longitudinal aerodynamic characteristics for Mach numbers of 0.60 and 0.90. Strakes off; $\delta_c = 0°$; $\delta_{f,TE} = 10°$.

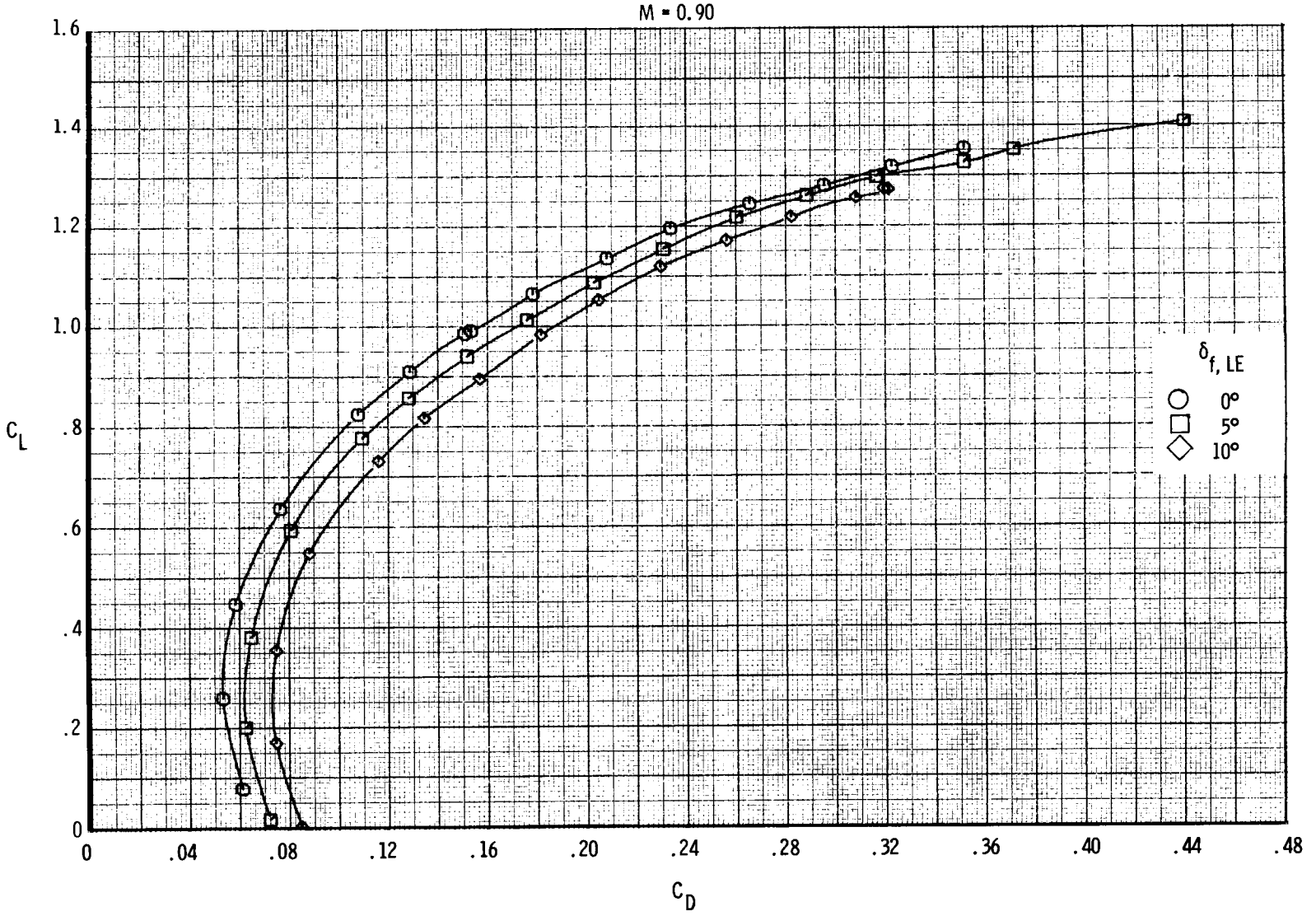

(a) Concluded.

Figure 6.- Continued.

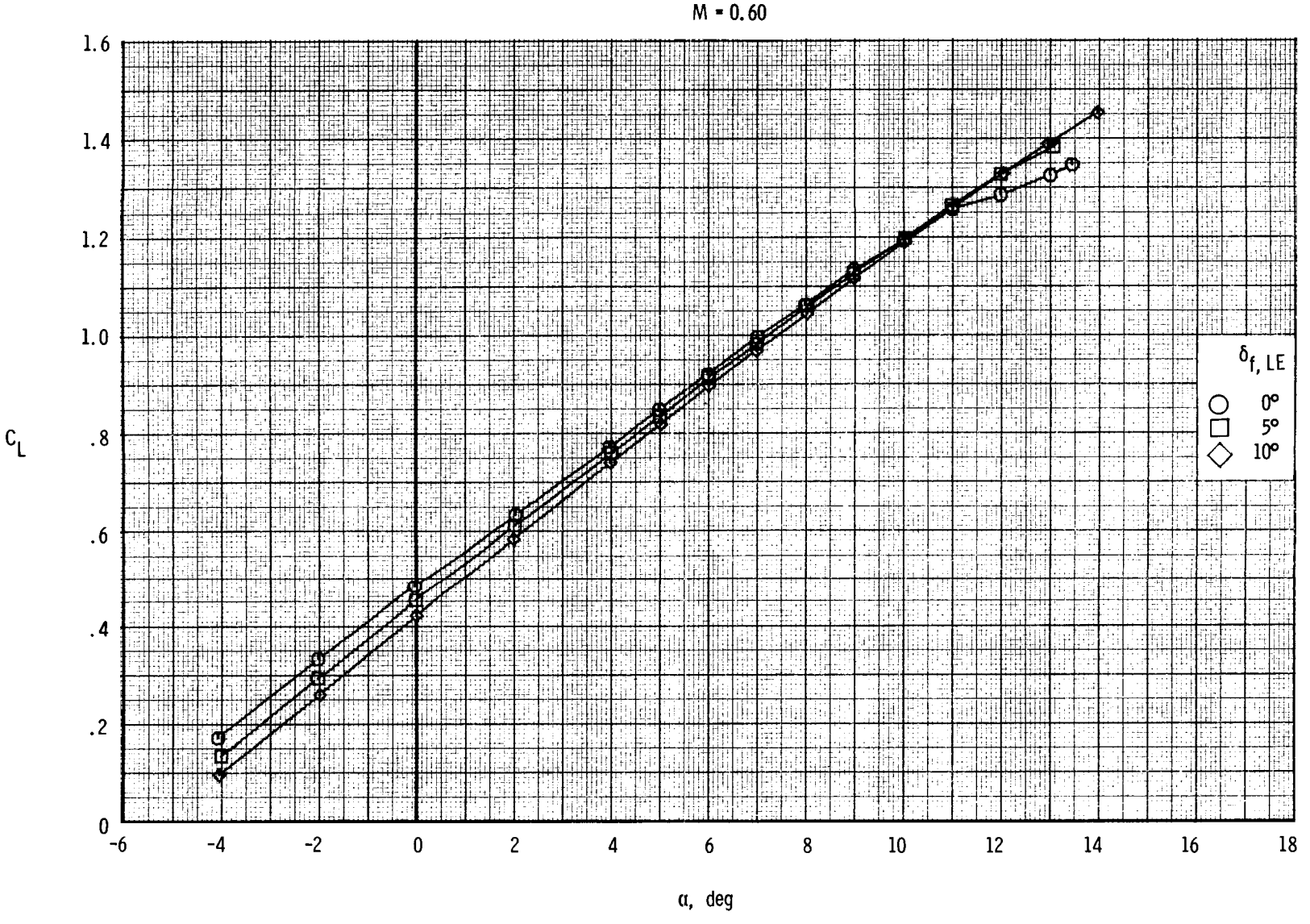

(b) Variation of C_L with α.

Figure 6.- Continued.

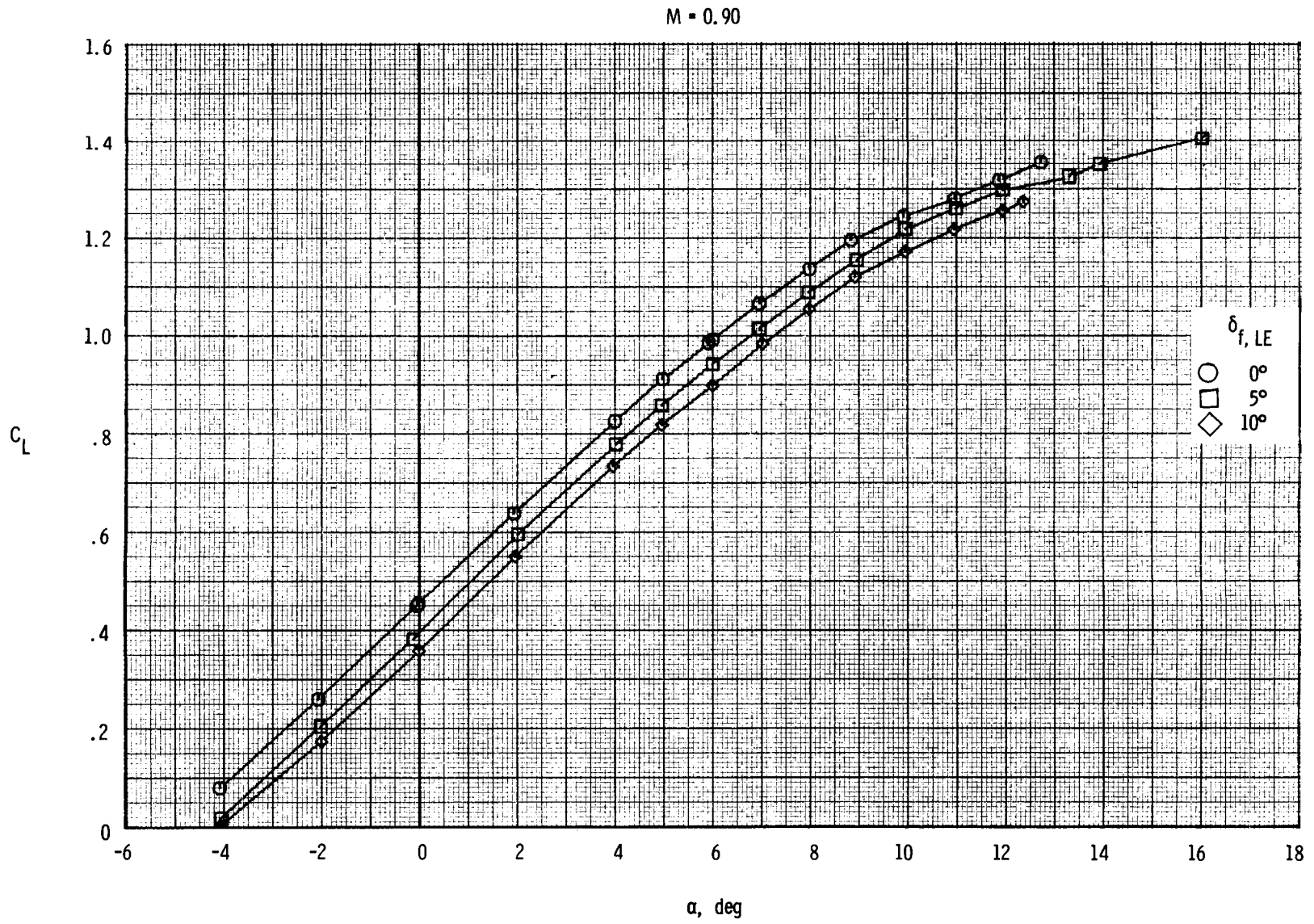

(b) Concluded.

Figure 6.- Continued.

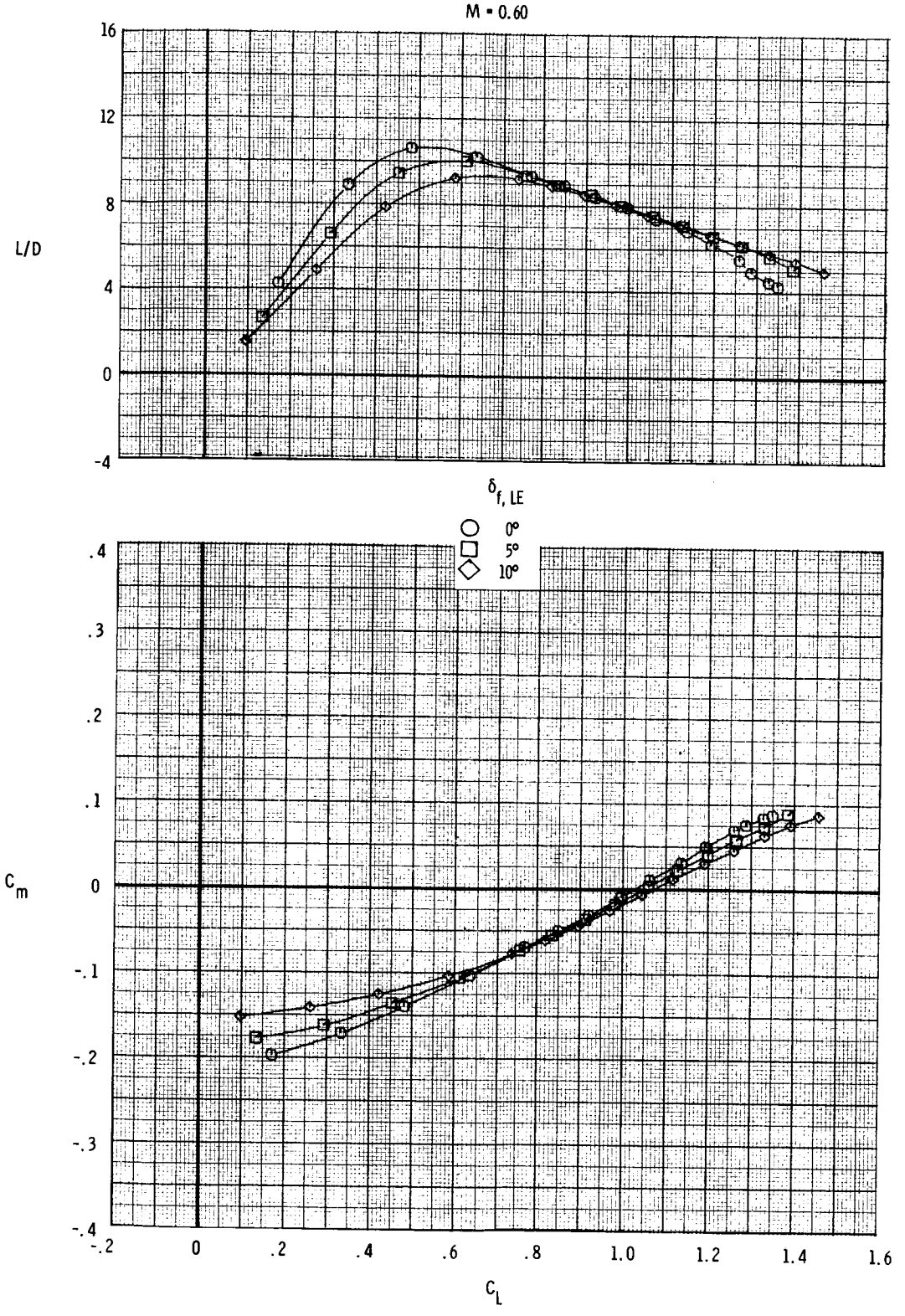

(c) Variation of L/D and C_m with C_L.

Figure 6.- Continued.

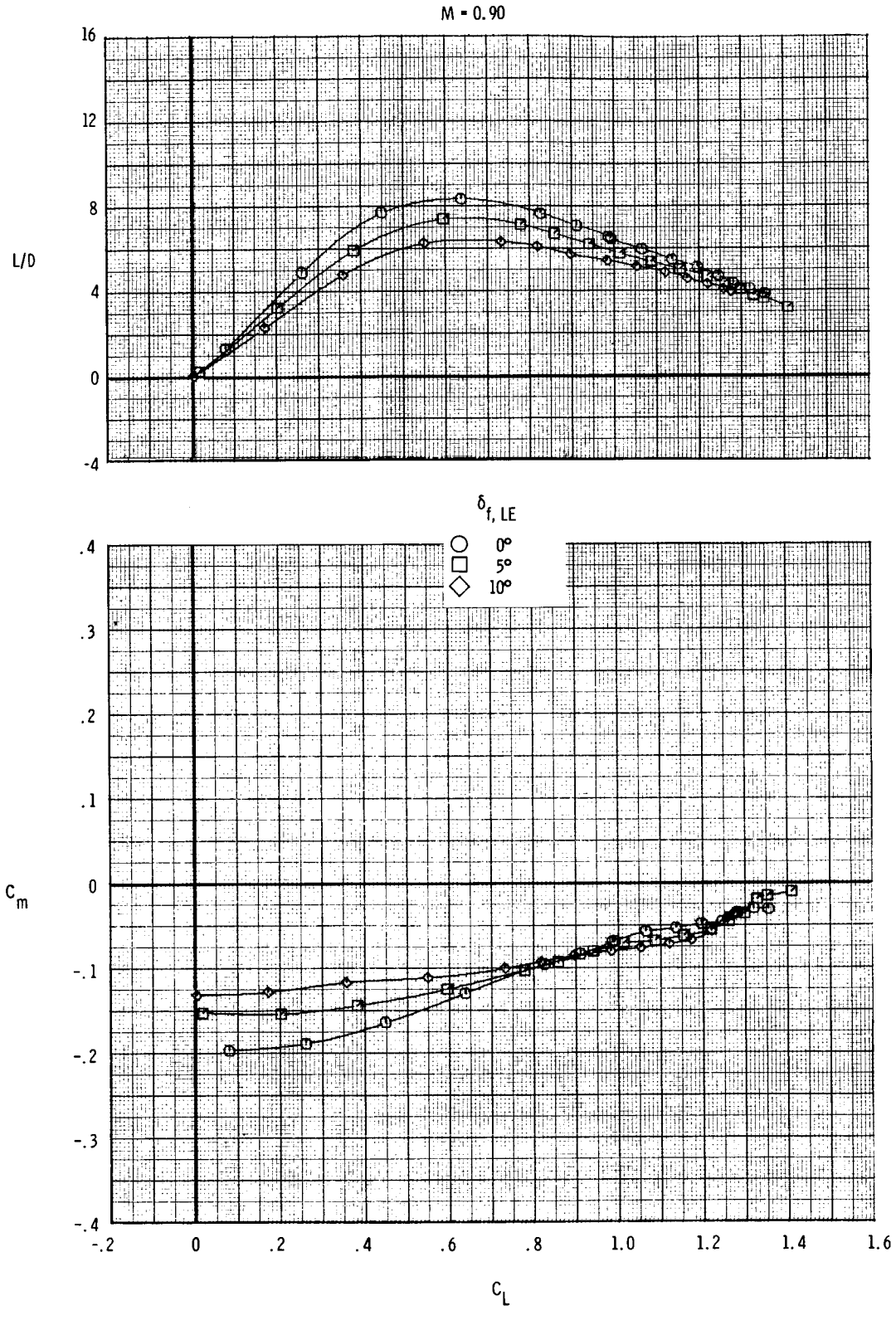

(c) Concluded.

Figure 6.- Concluded.

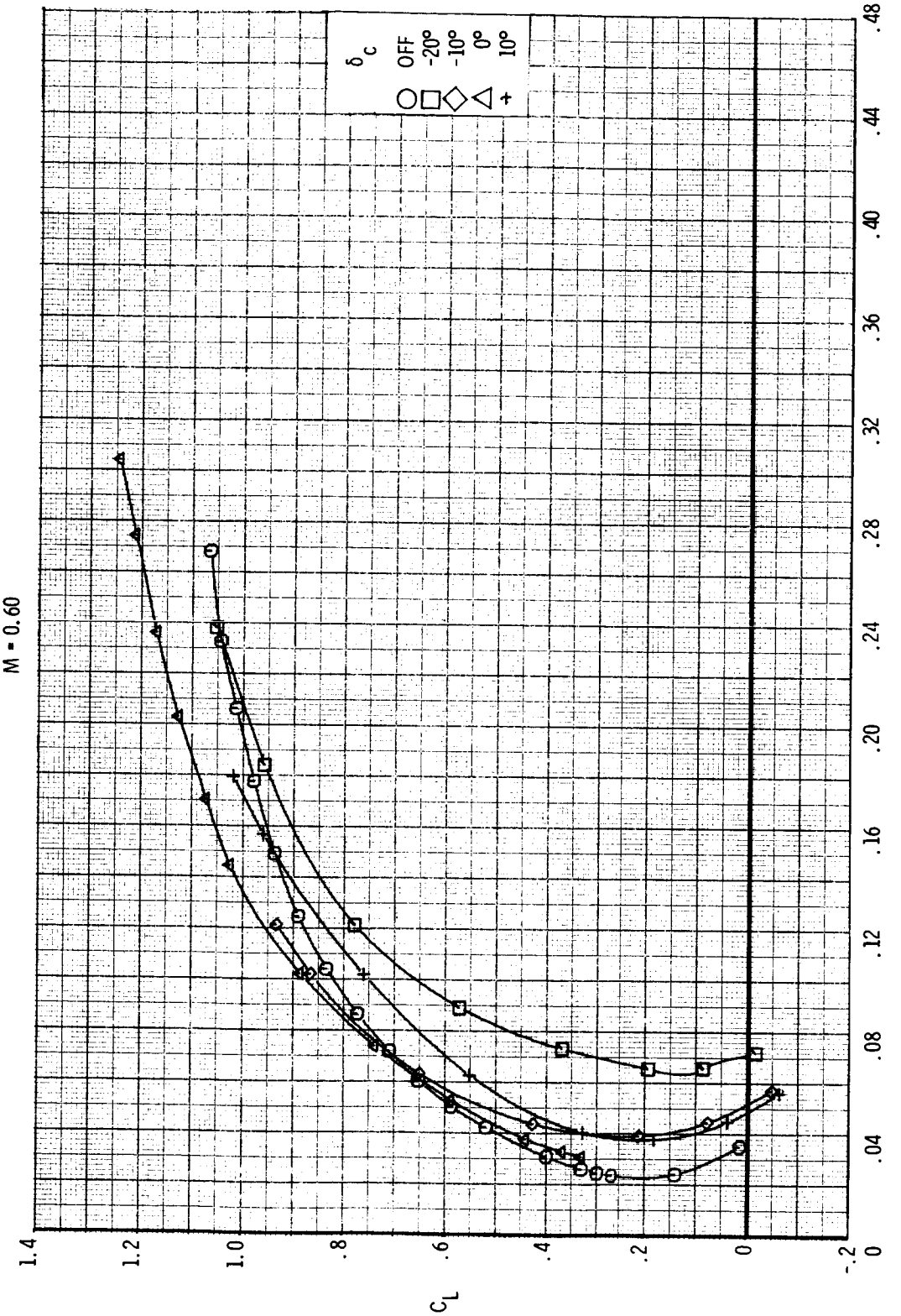

(a) Variation of C_L with C_D.

Figure 7.- Effect of canard incidence on longitudinal aerodynamic characteristics for Mach numbers of 0.60 and 0.90. Strakes off; $\delta_{f,TE} = \delta_{f,LE} = 0°$.

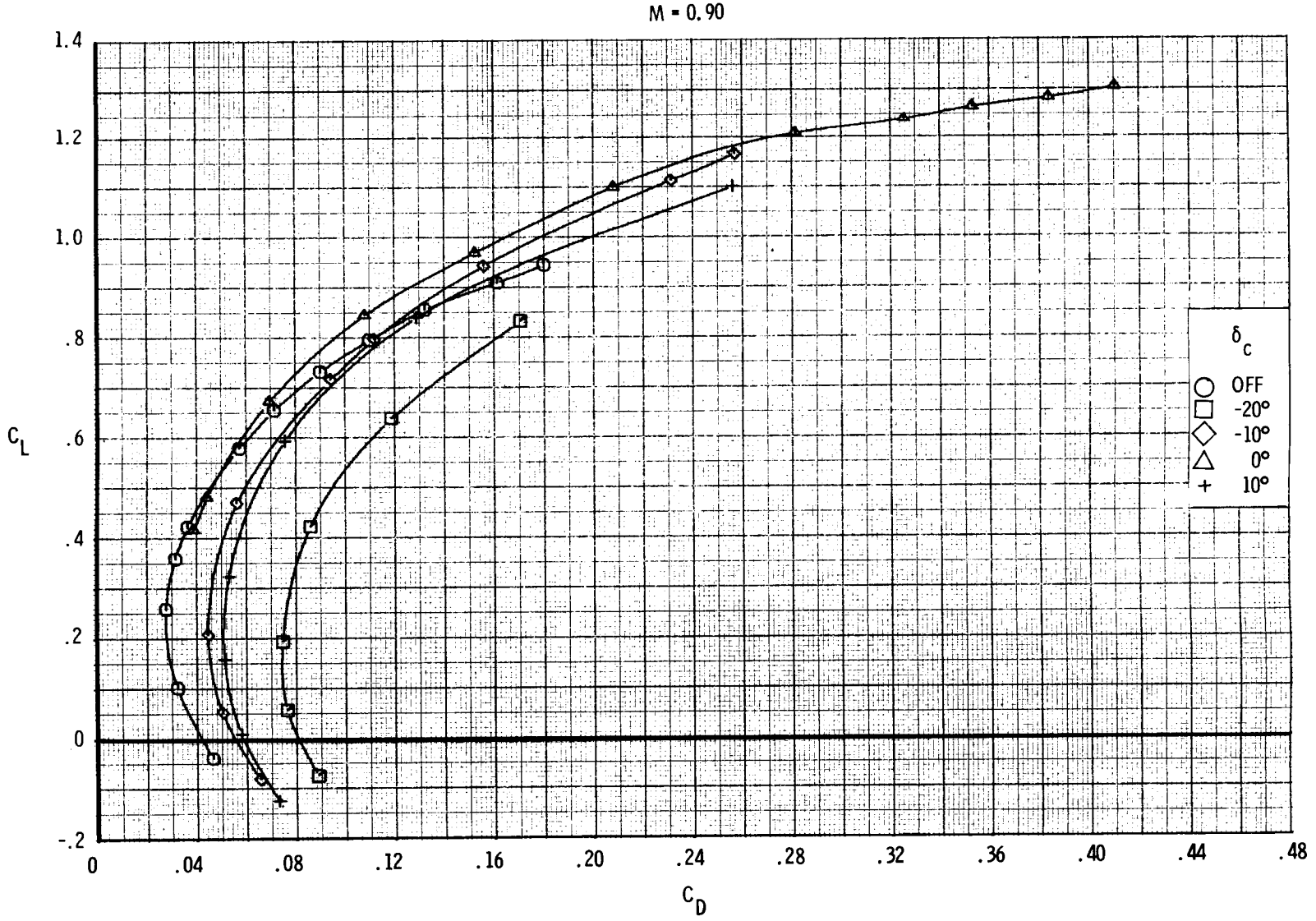

(a) Concluded.

Figure 7.- Continued.

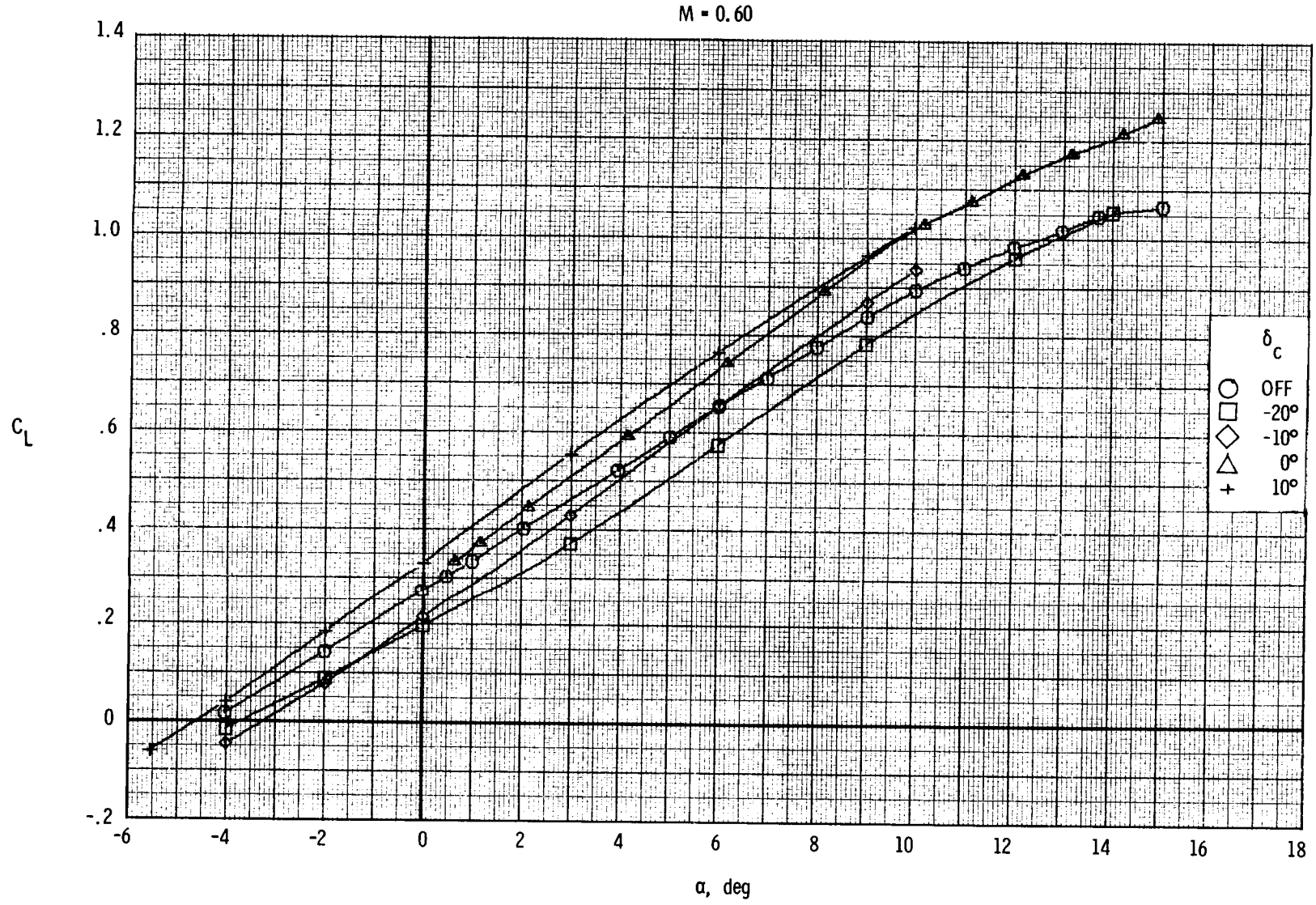

(b) Variation of C_L with α.

Figure 7.- Continued.

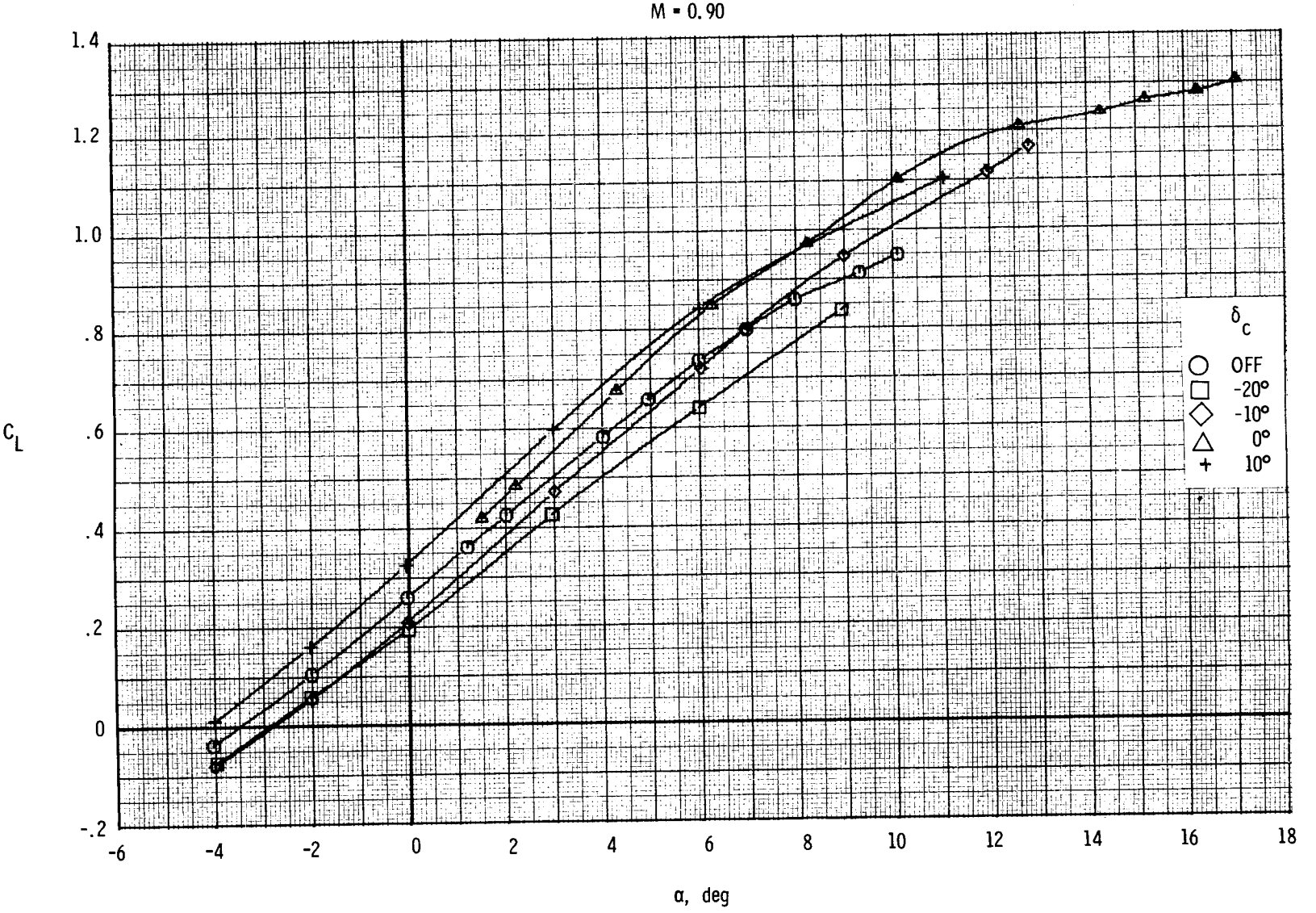

(b) Concluded.

Figure 7.- Continued.

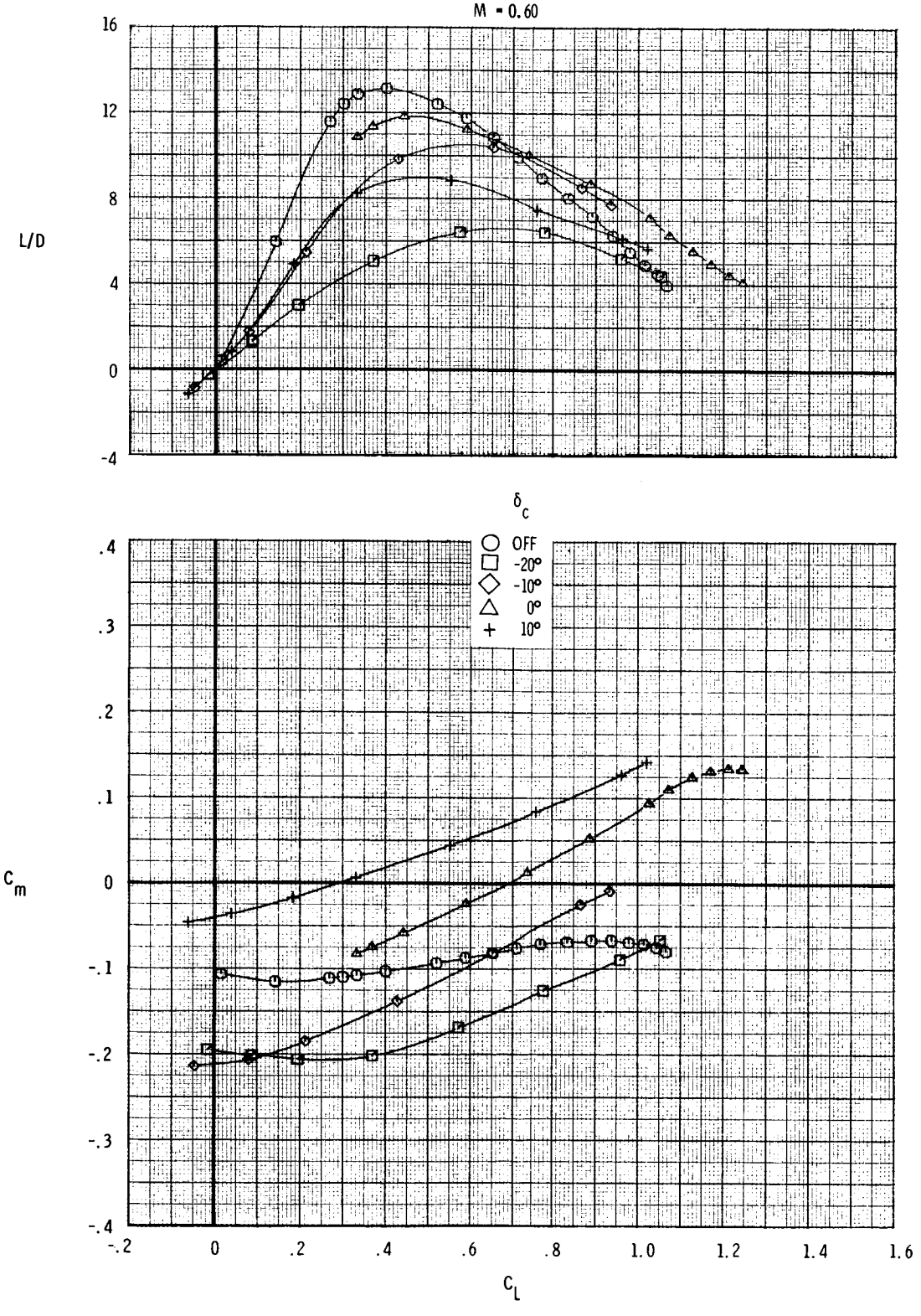

(c) Variation of L/D and C_m with C_L.

Figure 7.- Continued.

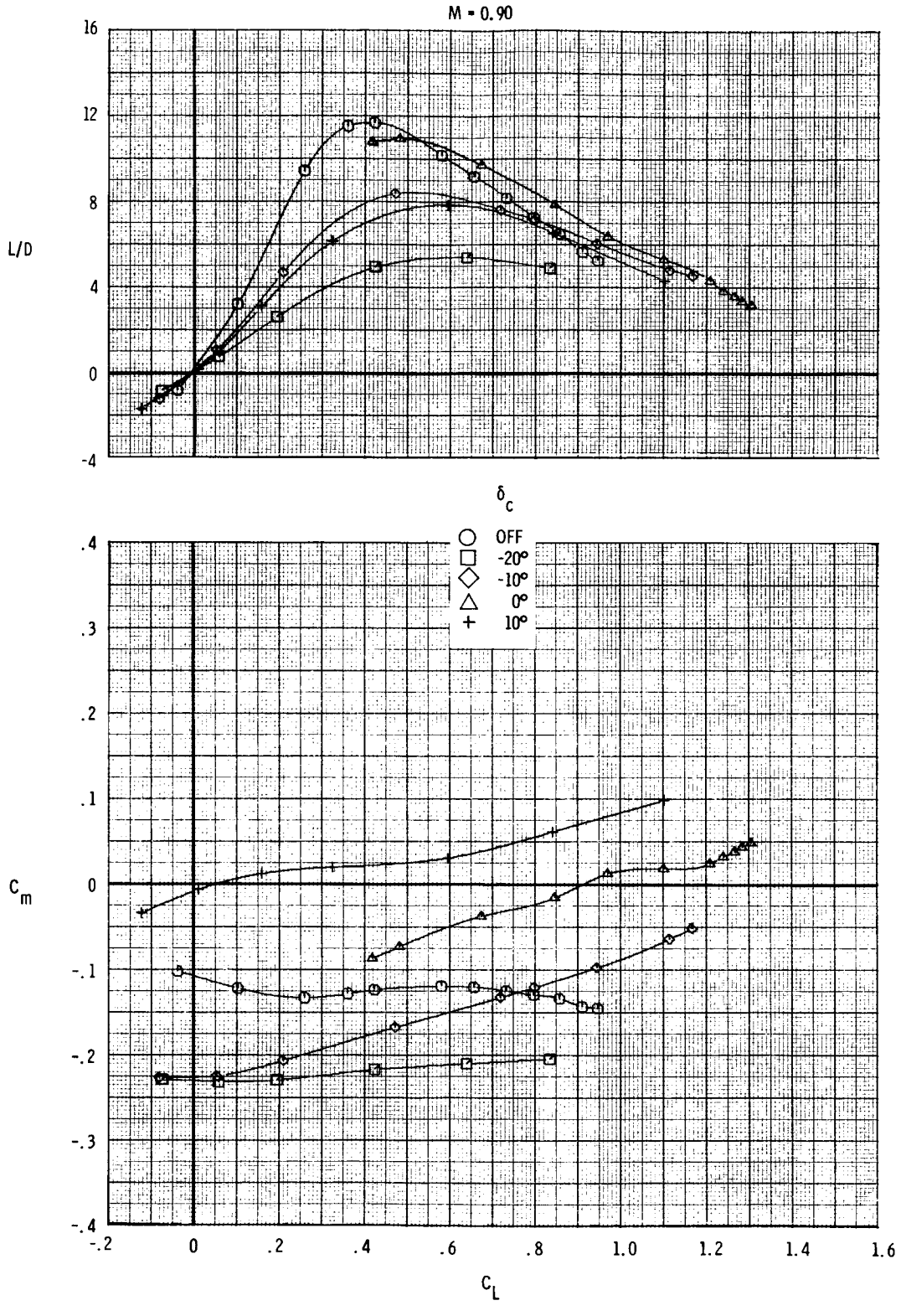

(c) Concluded.

Figure 7.- Concluded.

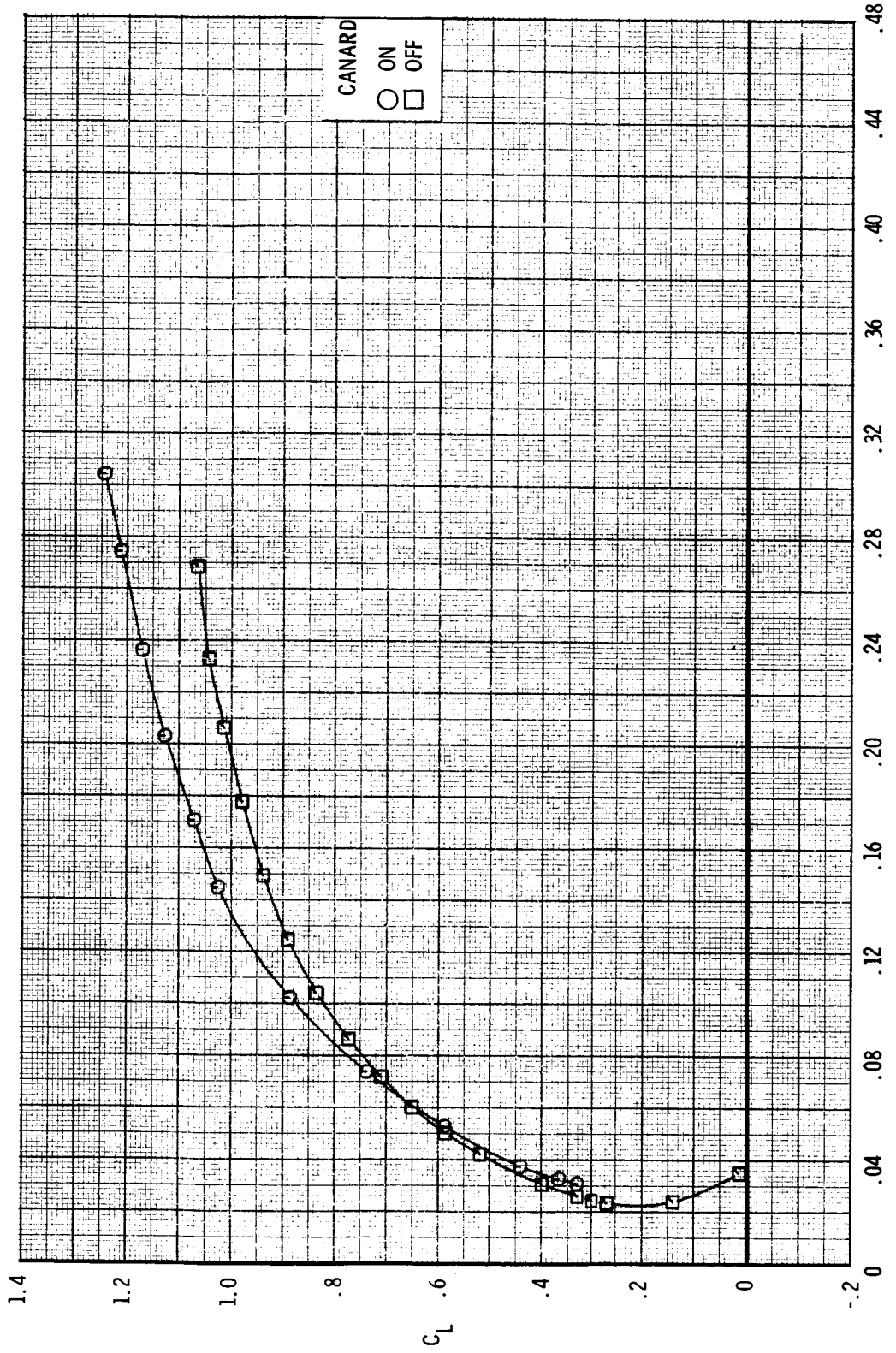

(a) Variation of C_L with C_D.

Figure 8.- Effect of canards on longitudinal aerodynamic characteristics. Strakes off; $\delta_c = 0°$; $\delta_{f,TE} = \delta_{f,LE} = 0°$.

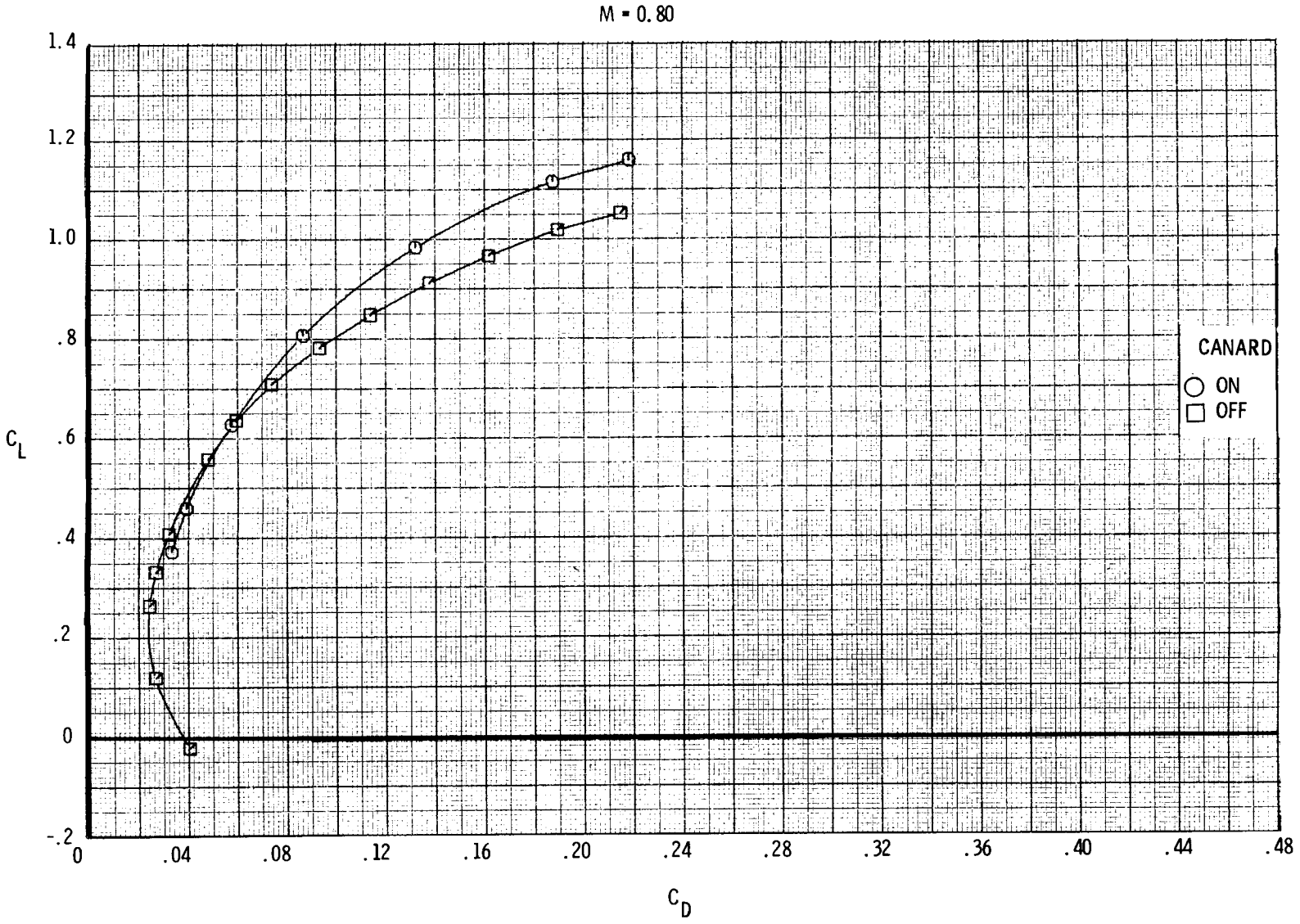

(a) Continued.

Figure 8.- Continued.

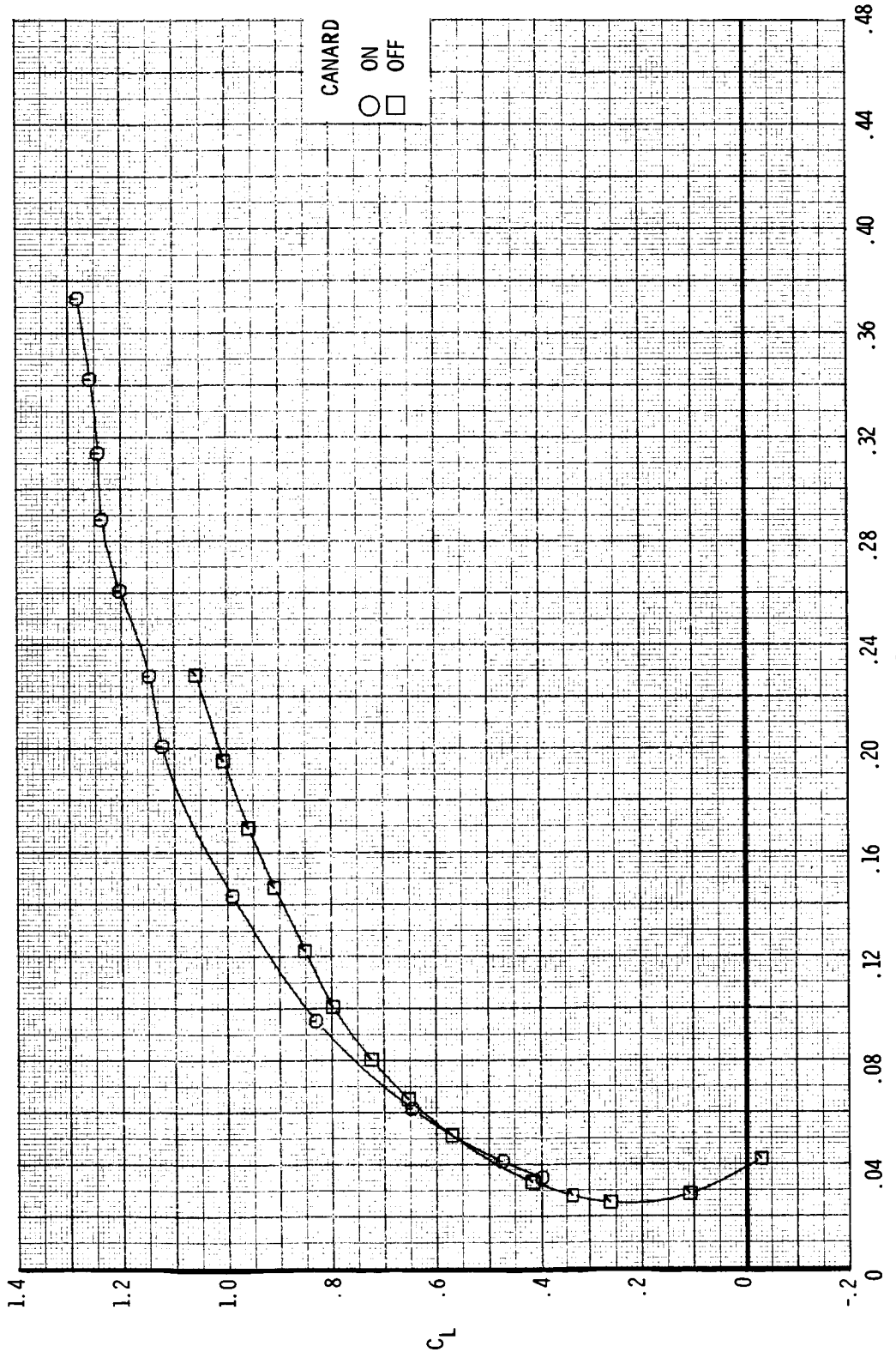

(a) Continued.

Figure 8.- Continued.

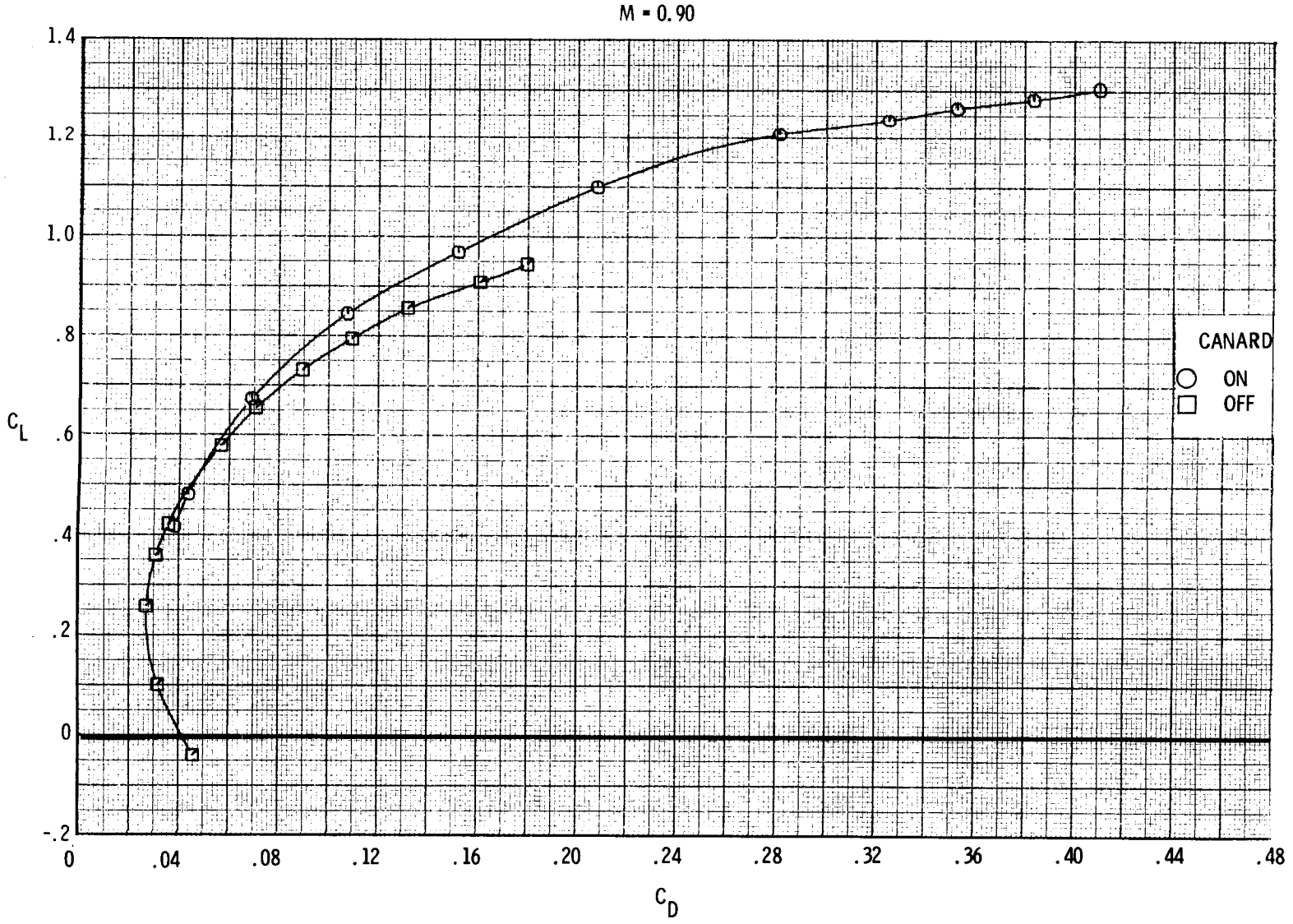

(a) Continued.

Figure 8.- Continued.

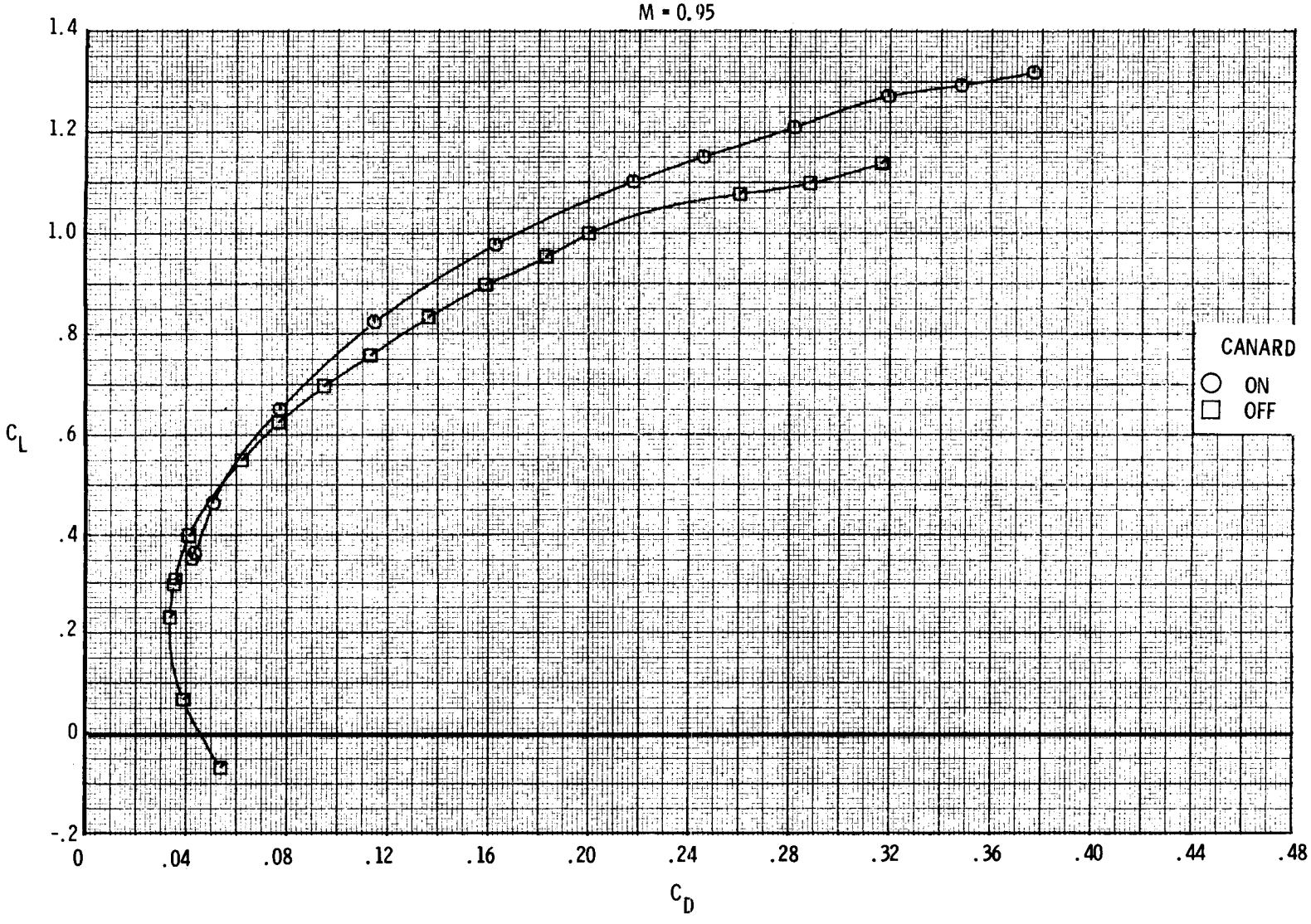

(a) Continued.

Figure 8.- Continued.

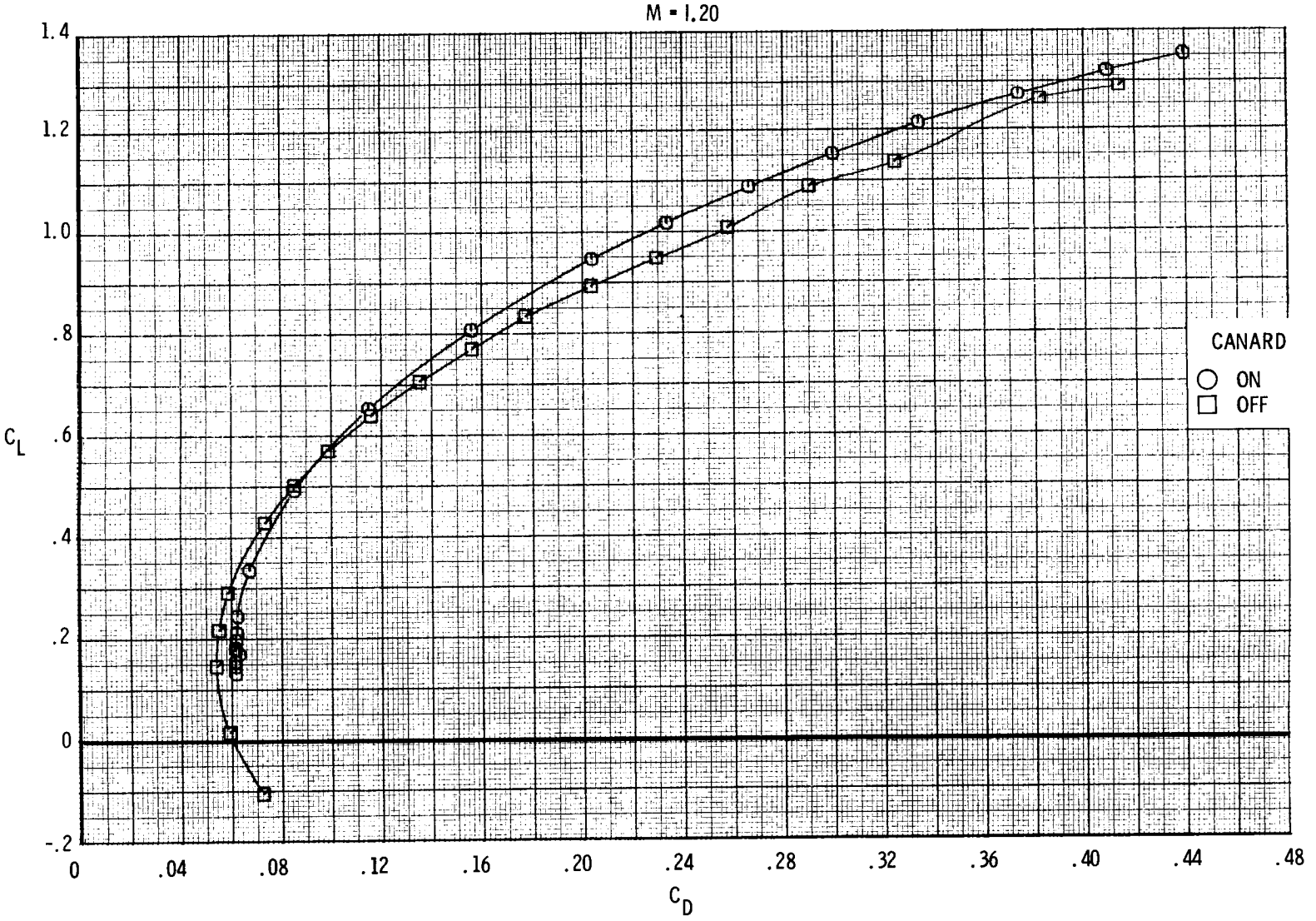

(a) Concluded.

Figure 8.- Continued.

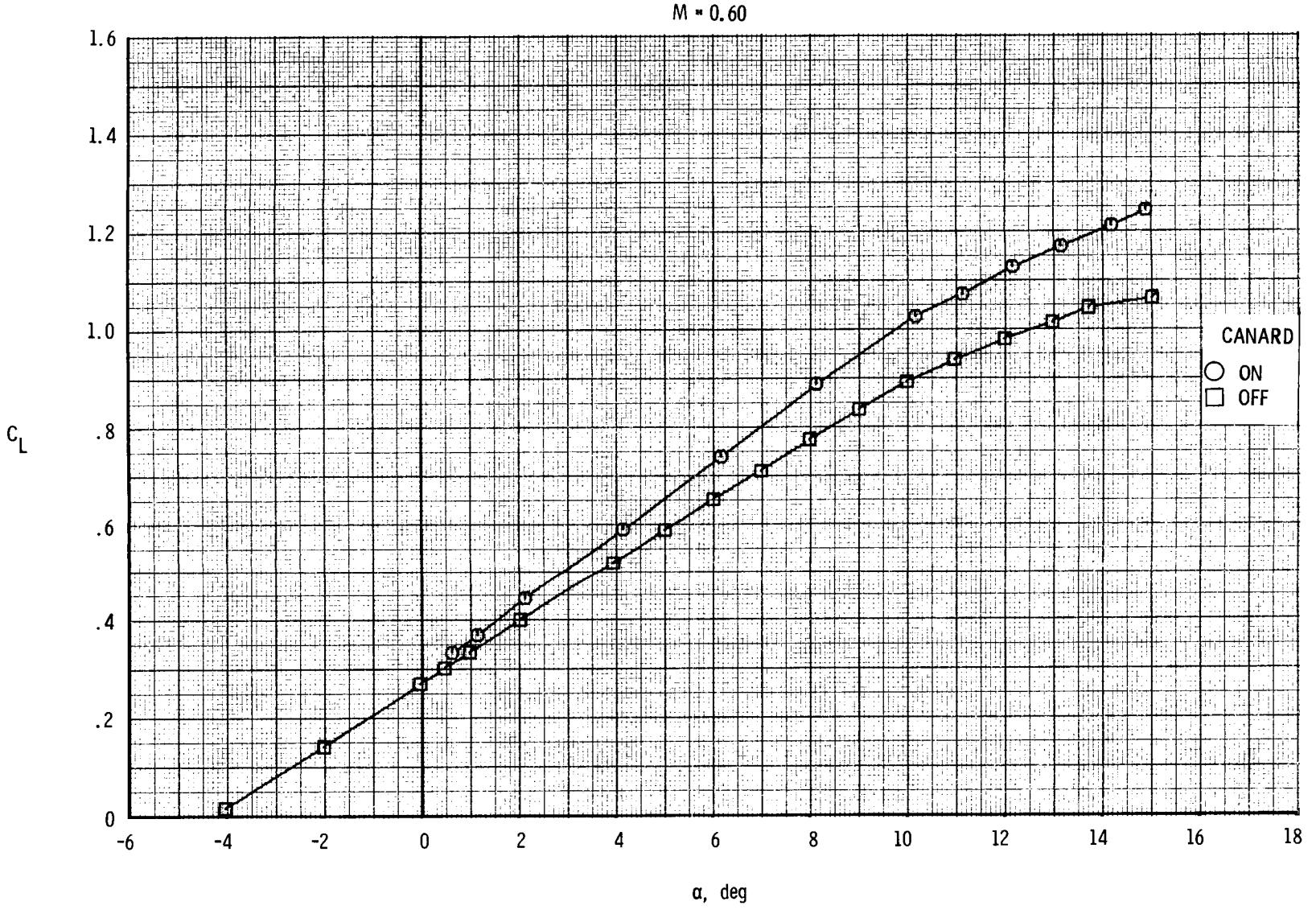

(b) Variation of C_L with α.

Figure 8.- Continued.

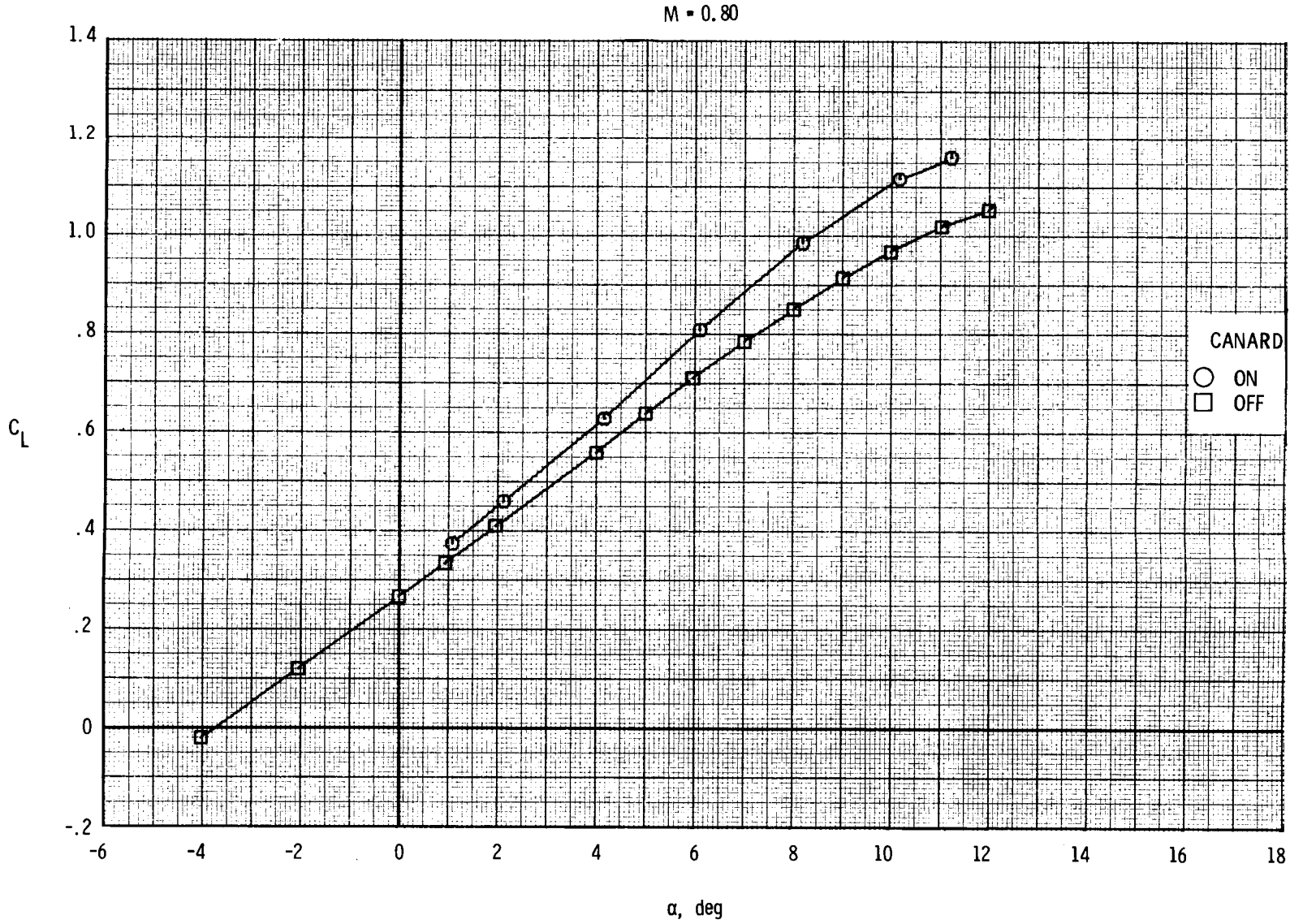

(b) Continued.

Figure 8.- Continued.

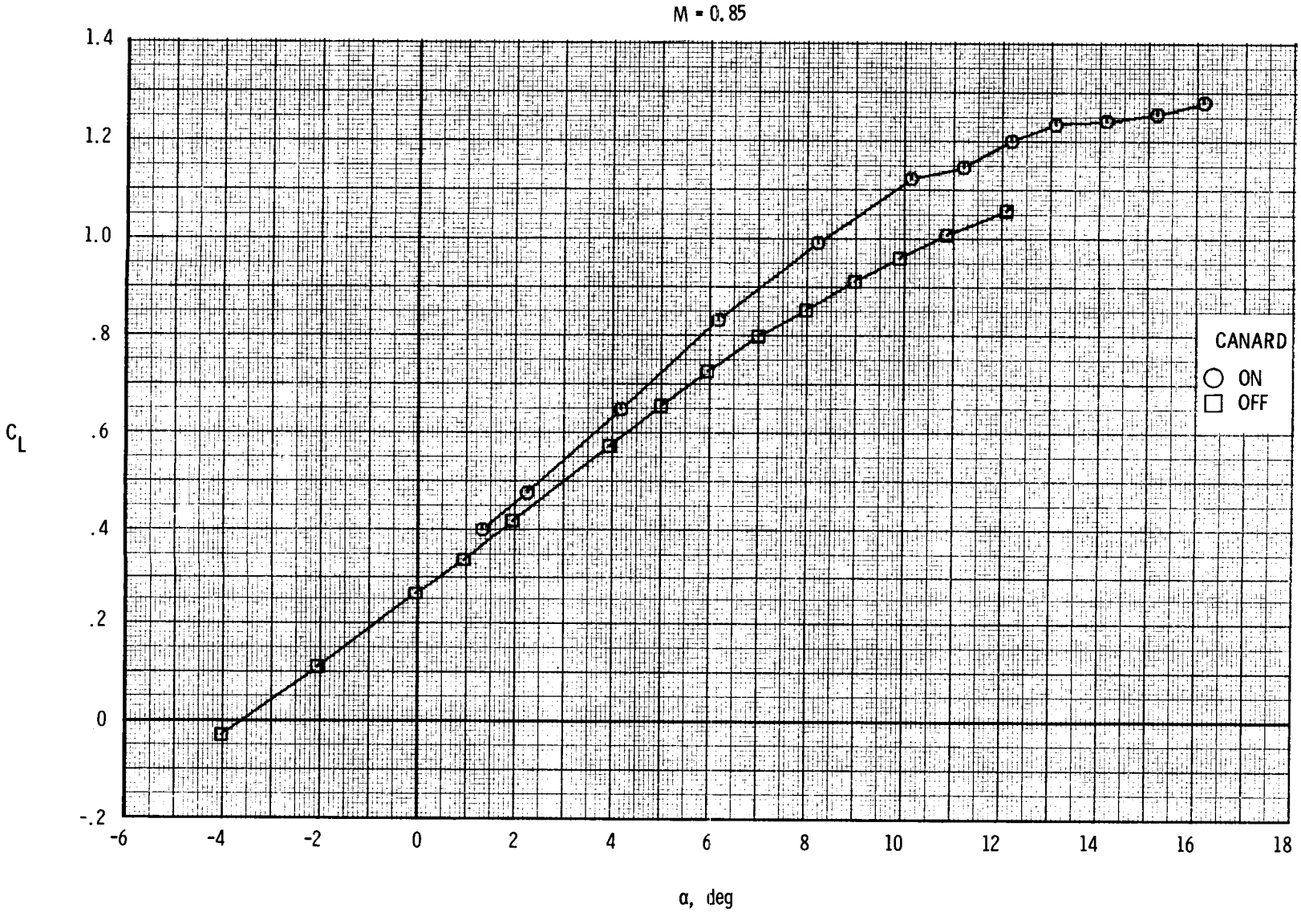

(b) Continued.

Figure 8.- Continued.

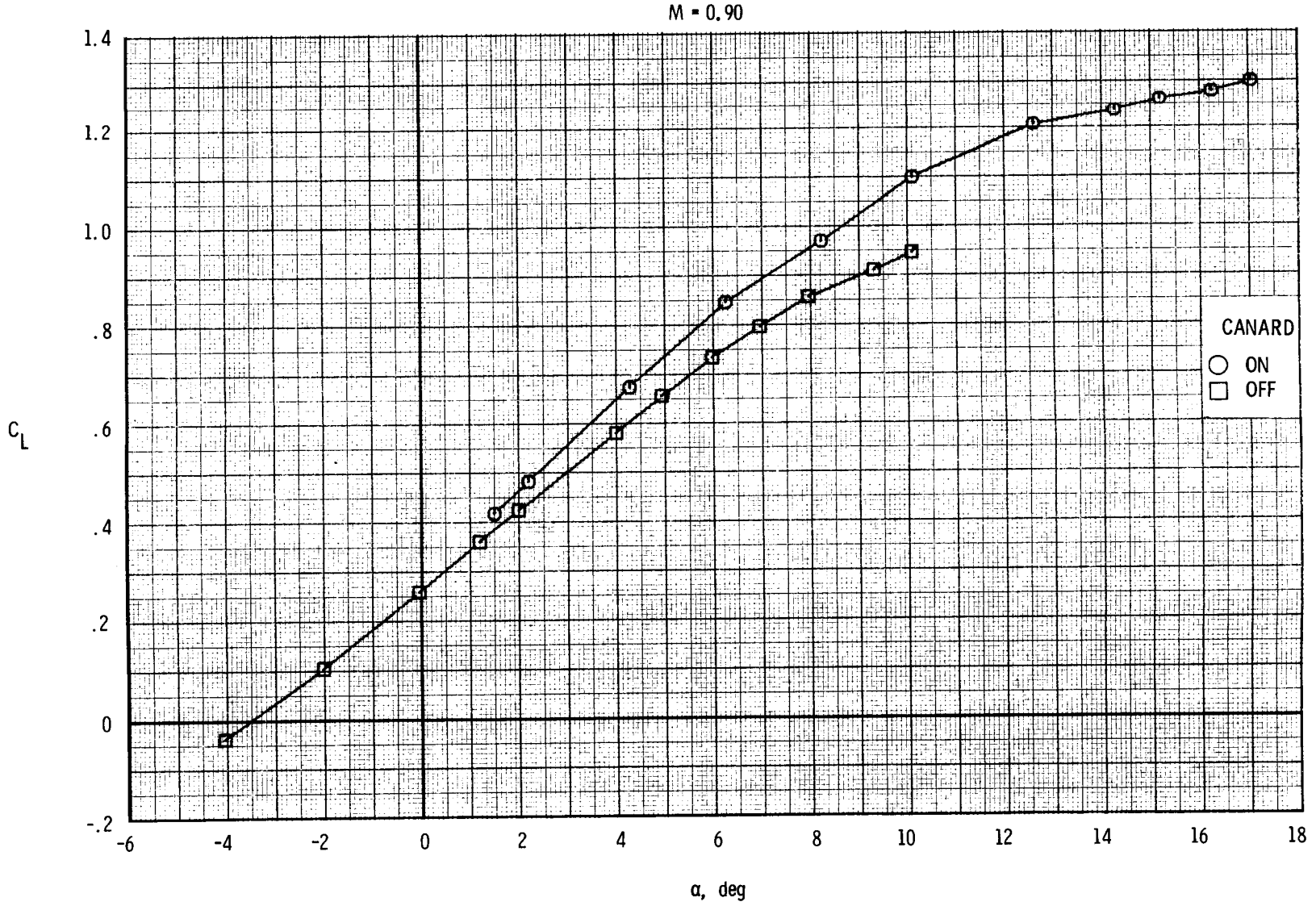

(b) Continued.

Figure 8.- Continued.

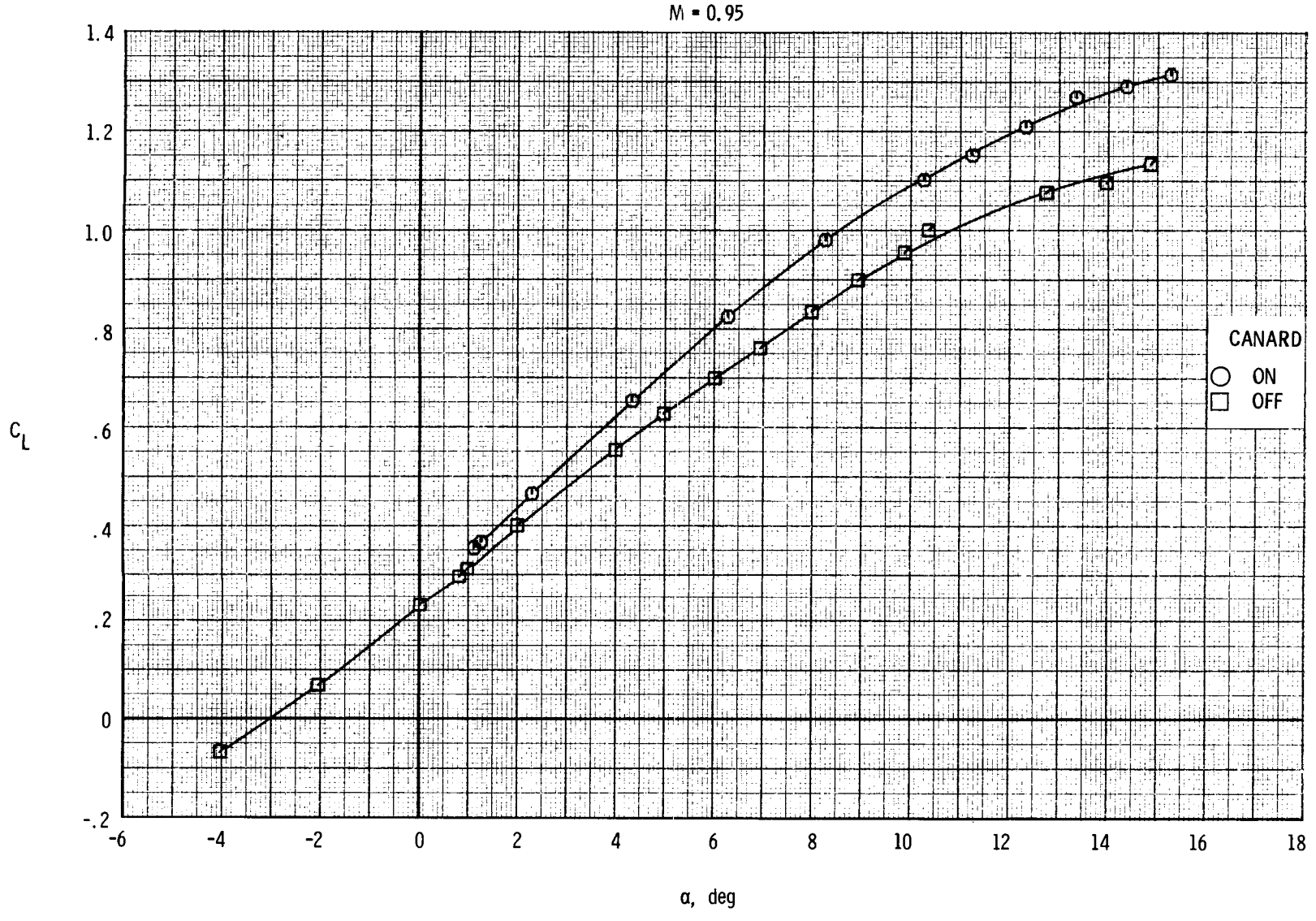

(b) Continued.

Figure 8.- Continued.

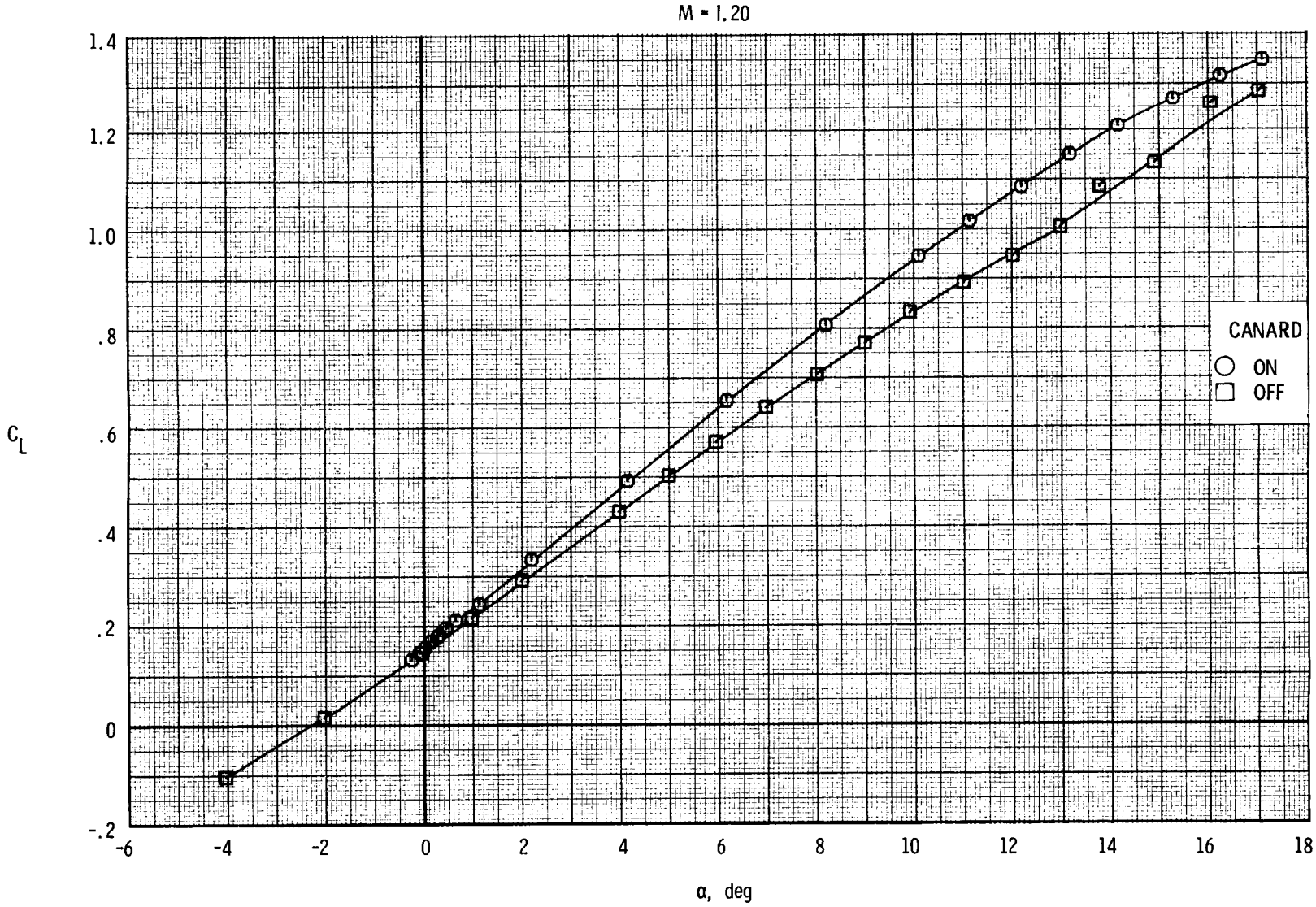

(b) Concluded.

Figure 8.- Continued.

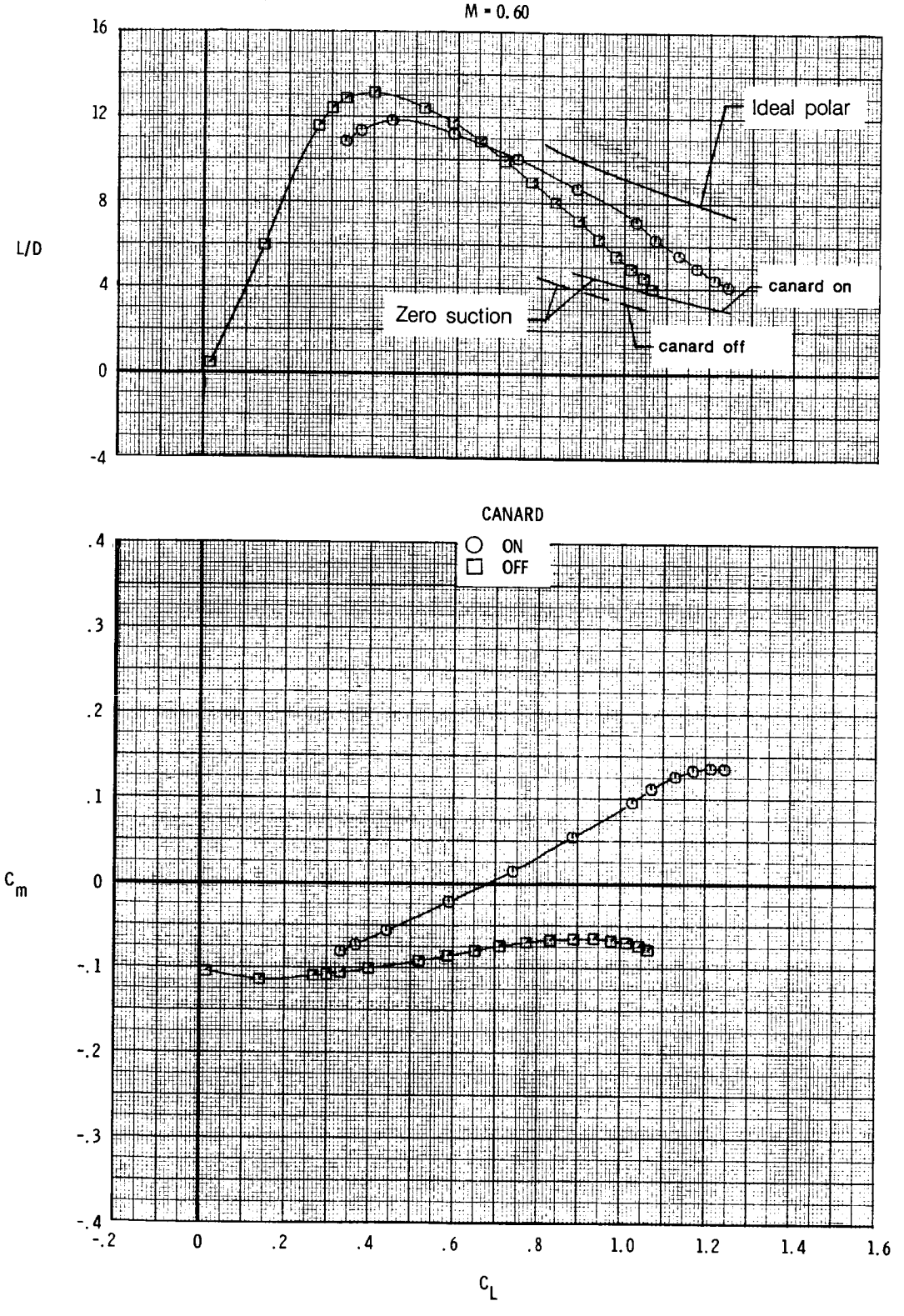

(c) Variation of L/D and C_m with C_L.

Figure 8.- Continued.

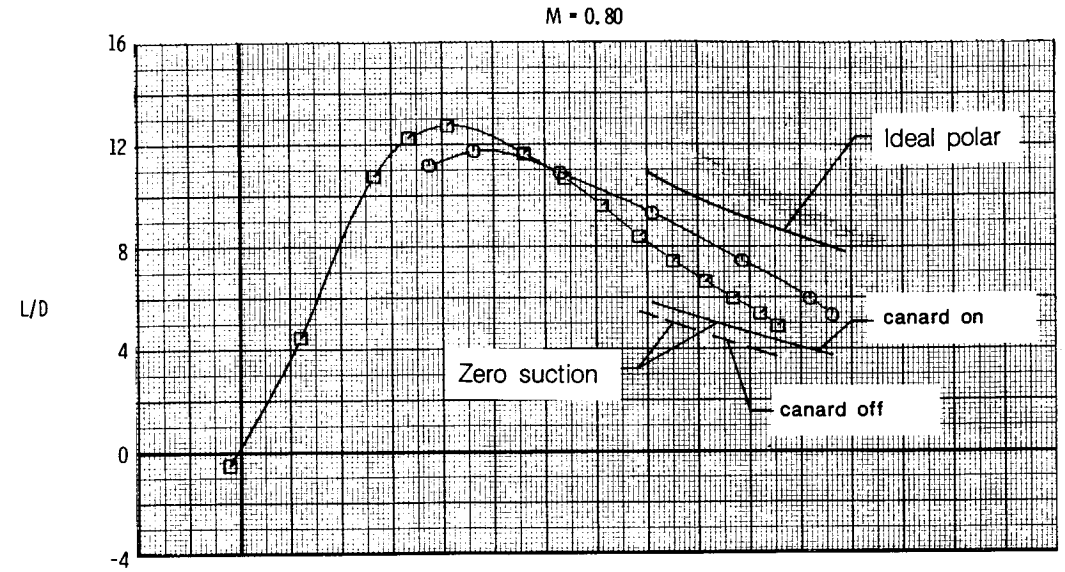

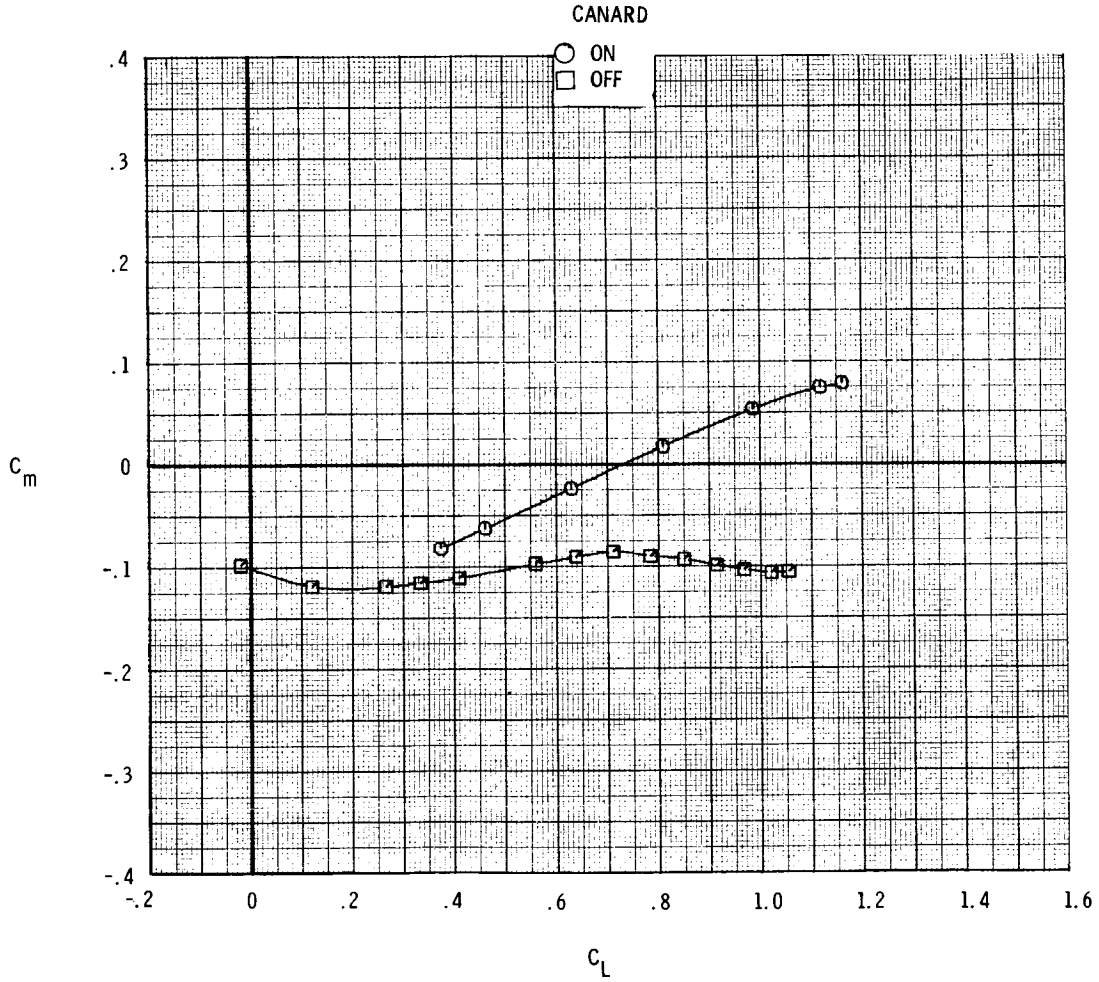

(c) Continued.

Figure 8.- Continued.

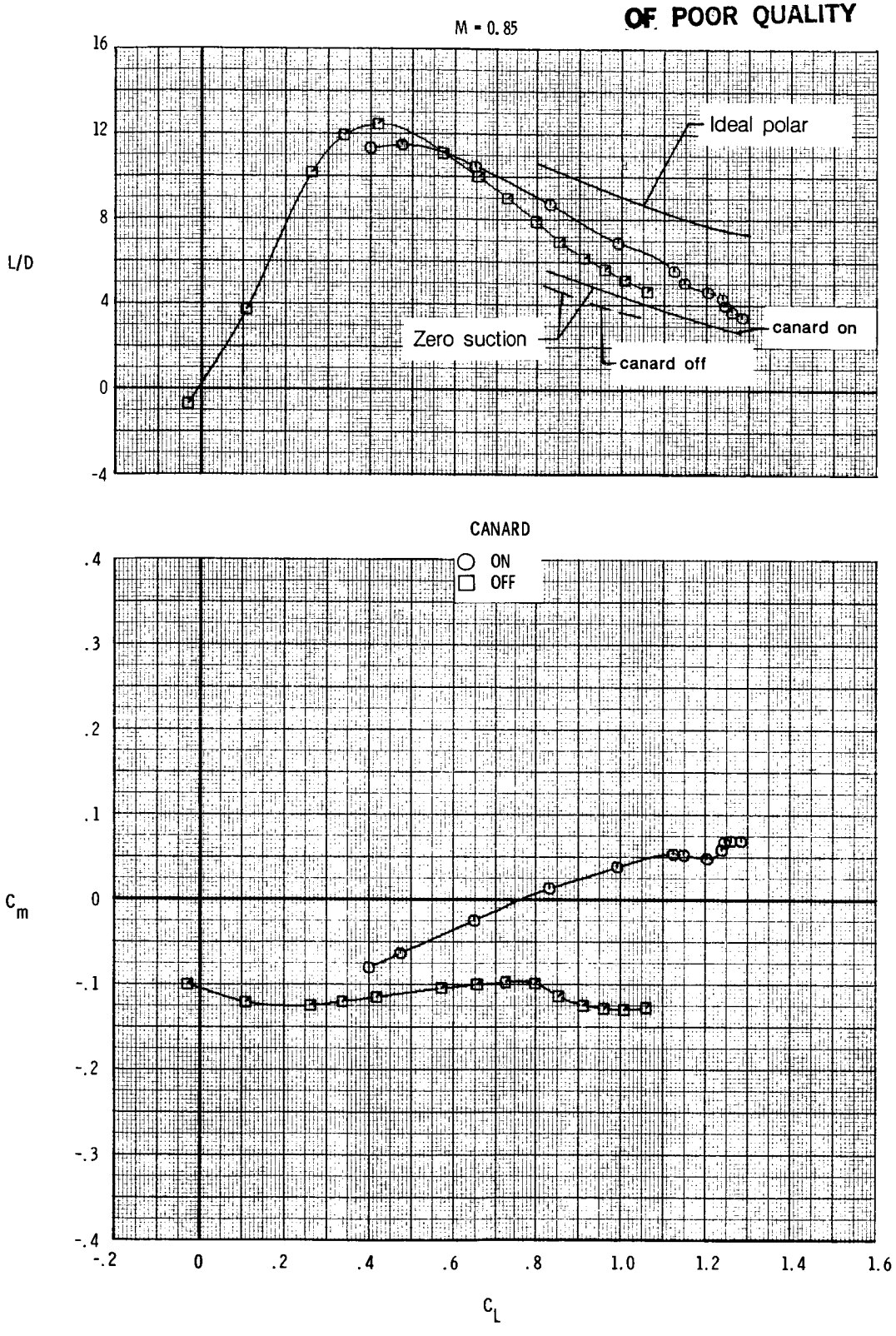

(c) Continued.

Figure 8.- Continued.

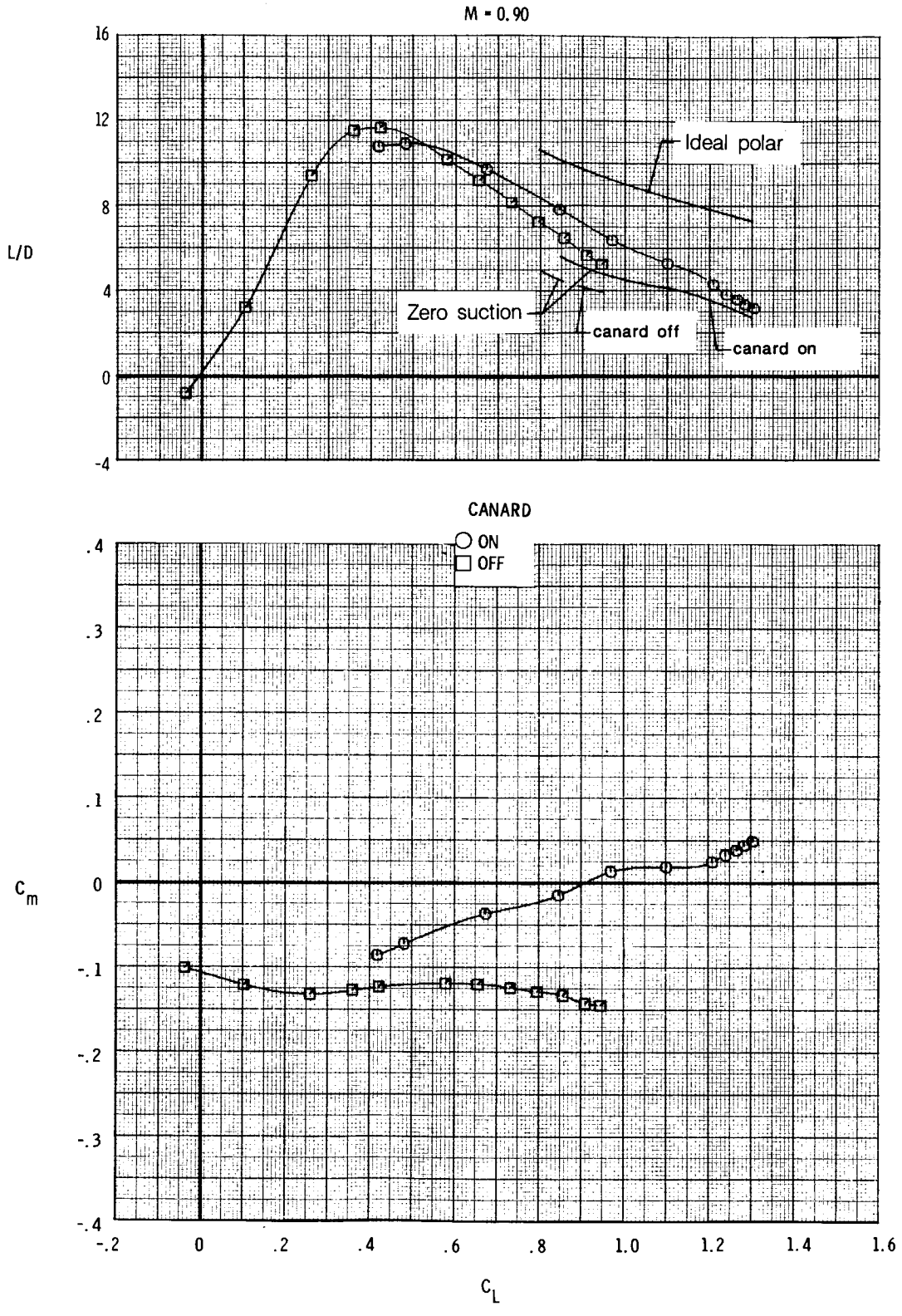

(c) Continued.

Figure 8.- Continued.

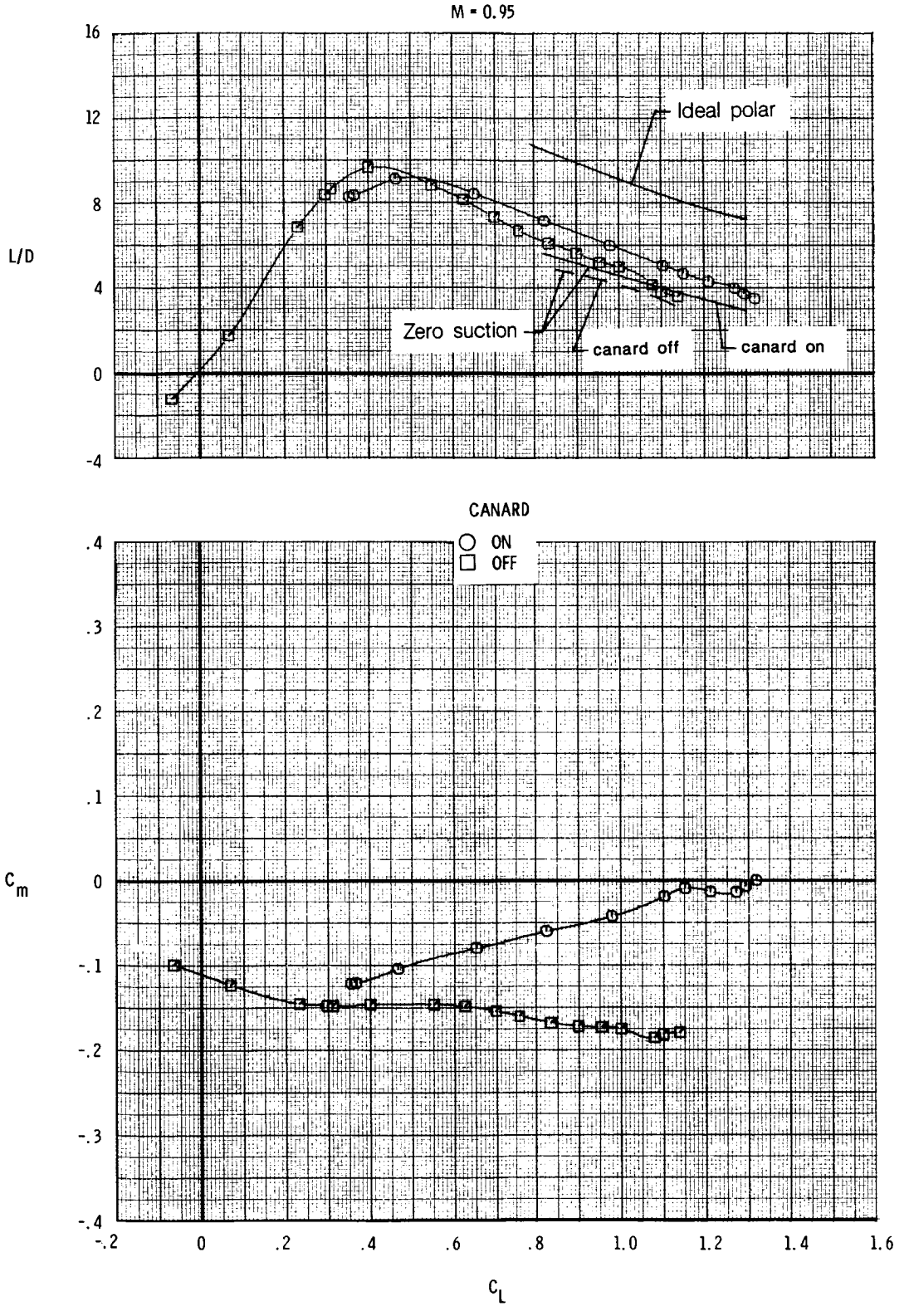

(c) Continued.

Figure 8.- Continued.

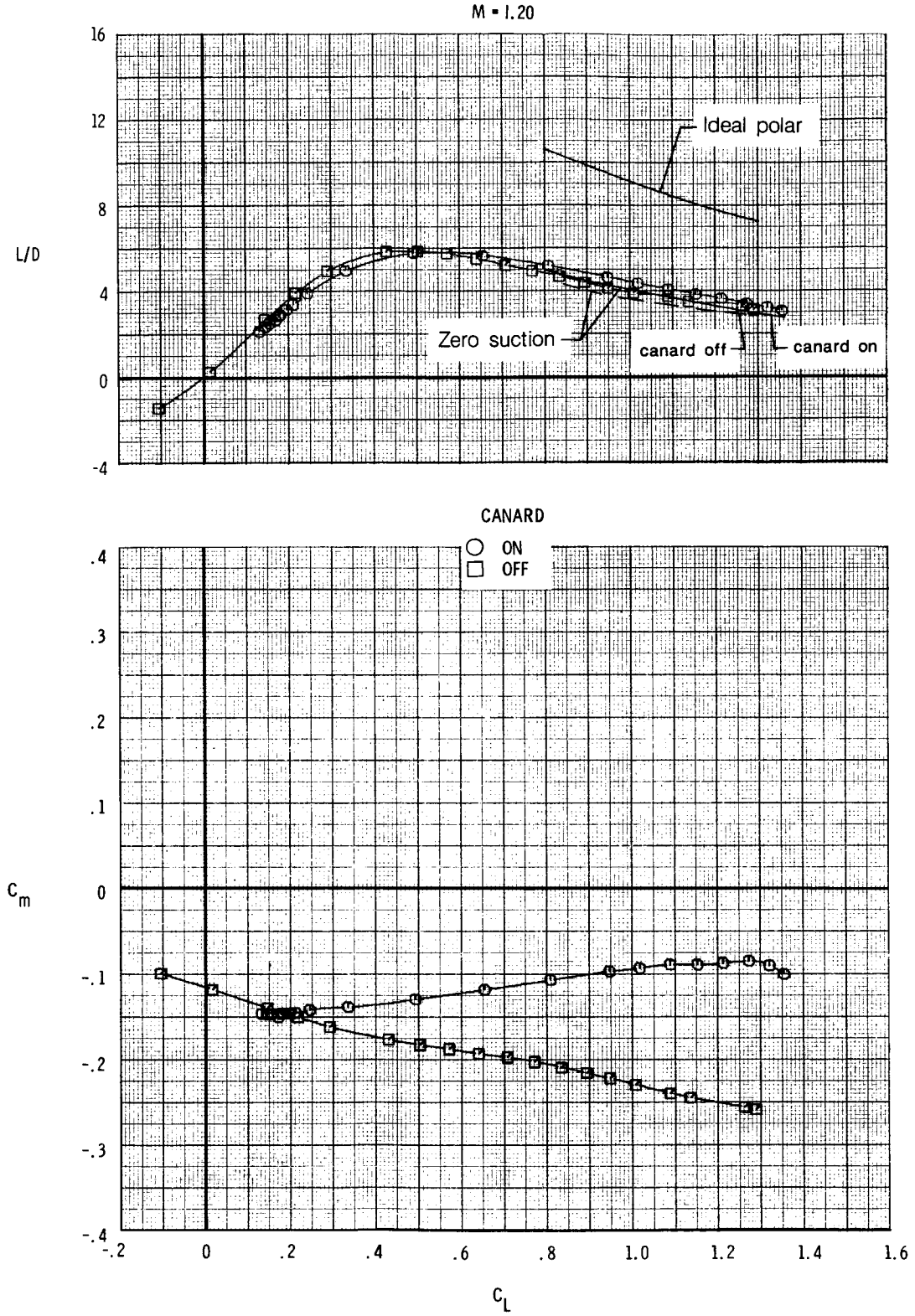

(c) Concluded.

Figure 8.- Continued.

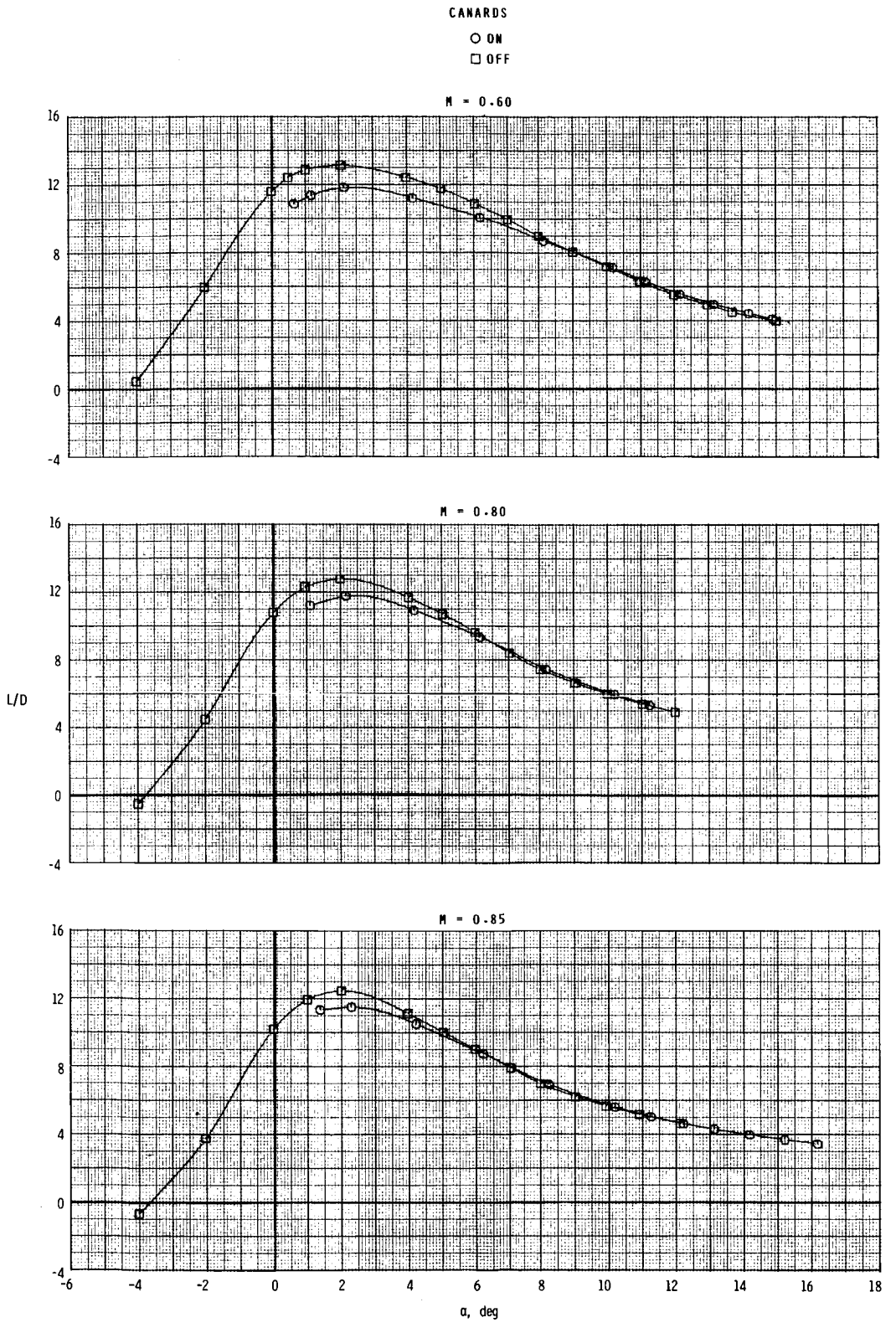

(d) Variation of L/D with α.

Figure 8.- Continued.

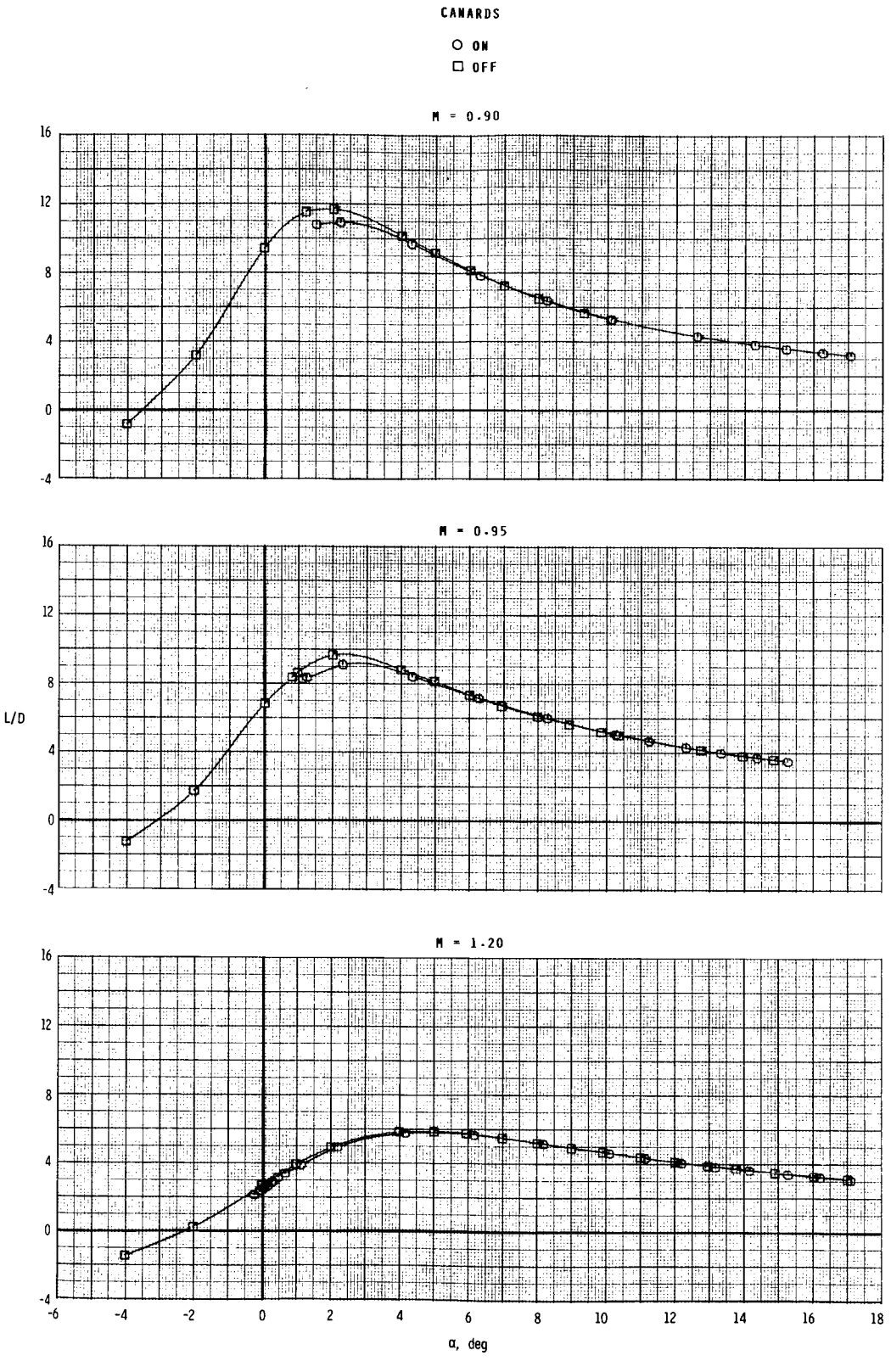

(d) Concluded.

Figure 8.- Concluded.

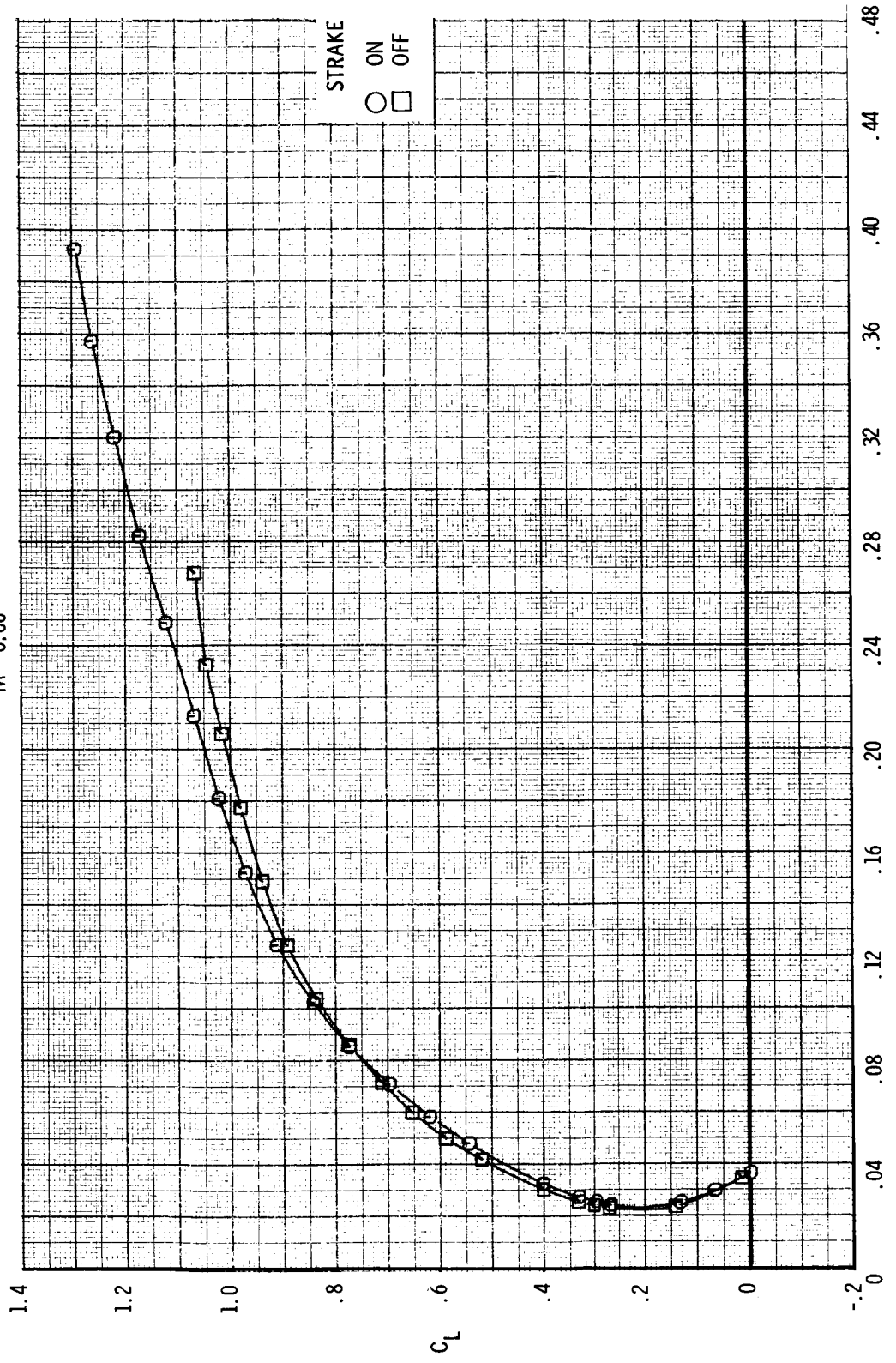

(a) Variation of C_L with C_D.

Figure 9.- Effect of strakes on longitudinal aerodynamic characteristics. Canards off; $\delta_{f,TE} = \delta_{f,LE} = 0°$.

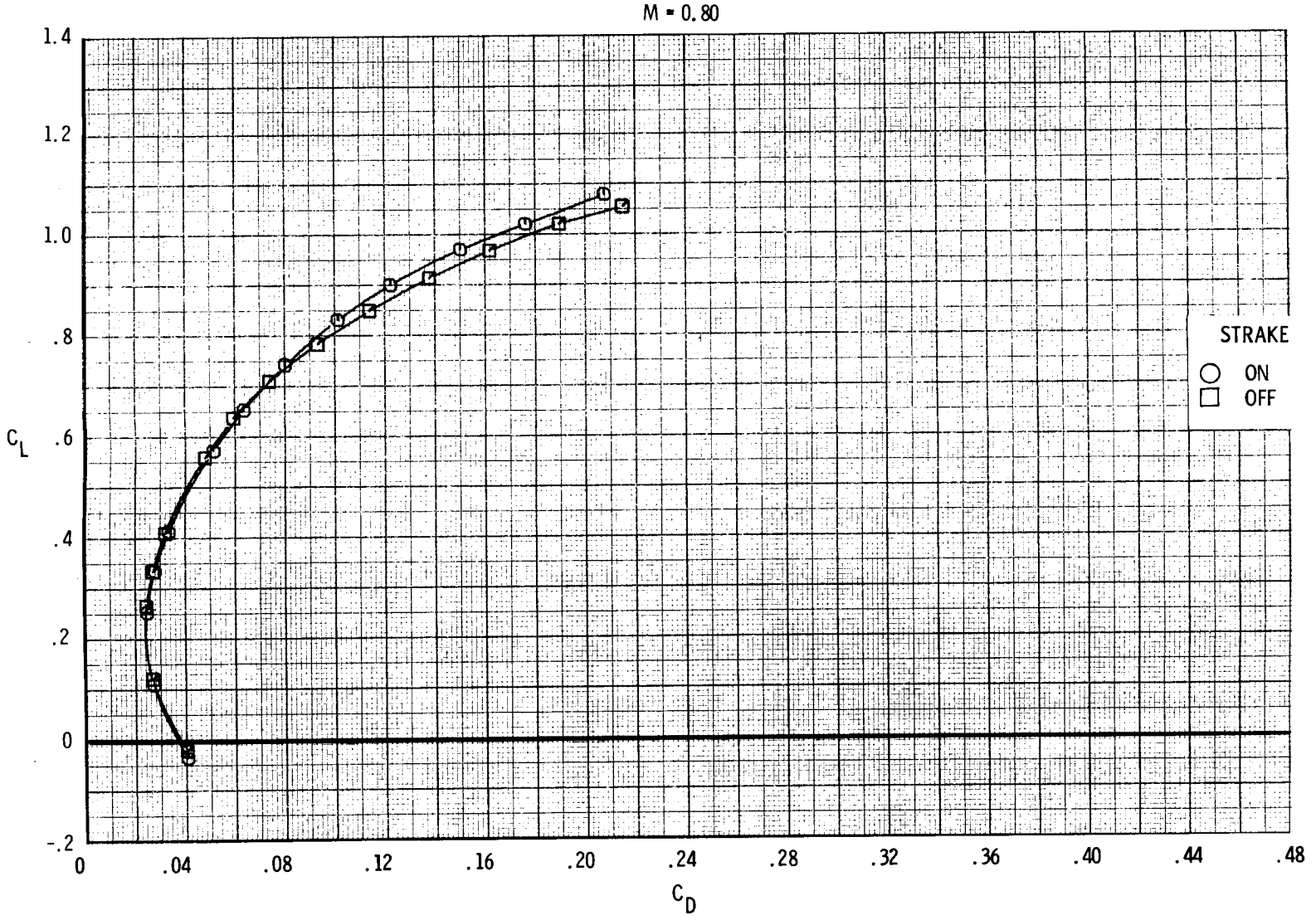

(a) Continued.

Figure 9.- Continued.

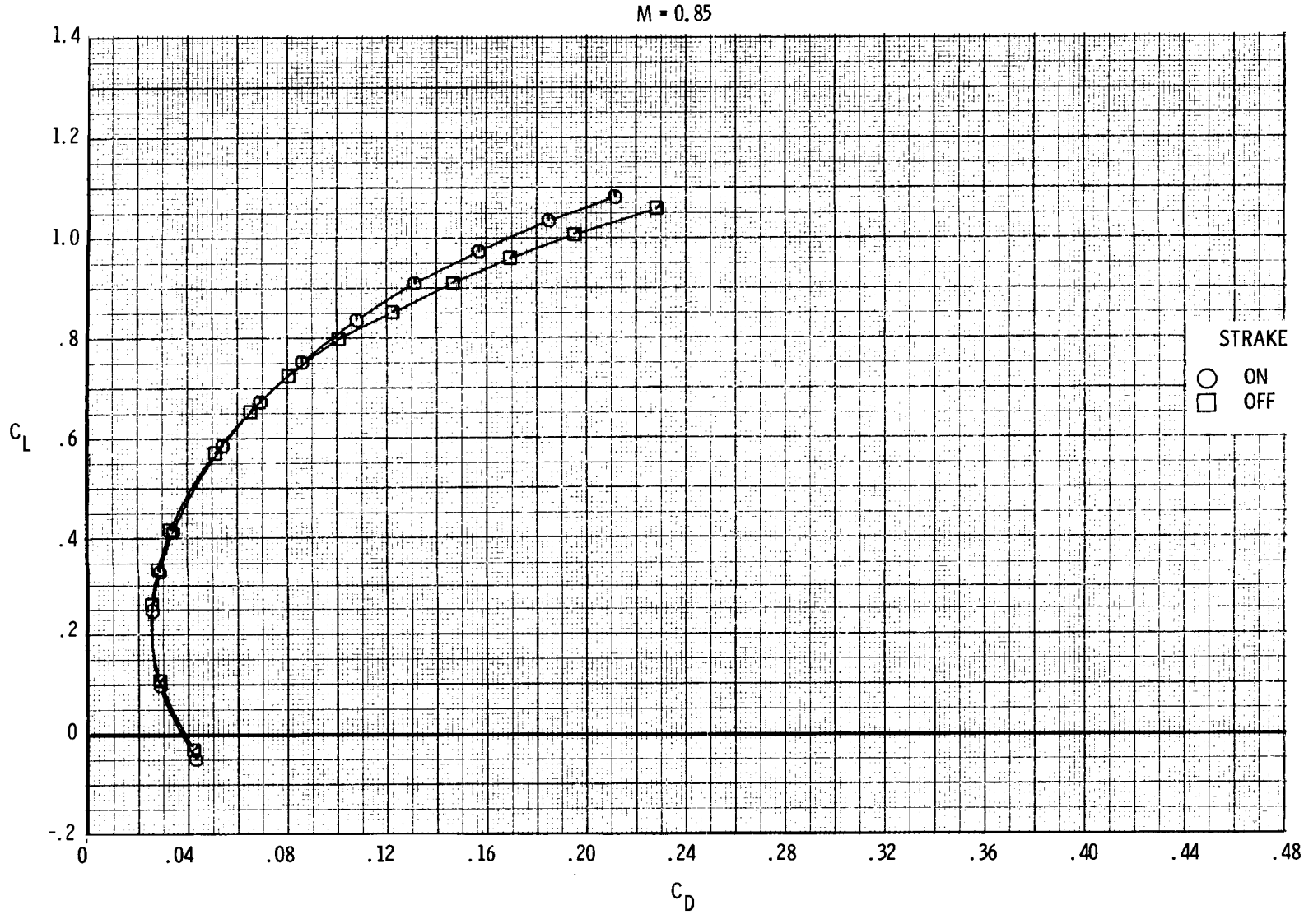

(a) Continued.

Figure 9.- Continued.

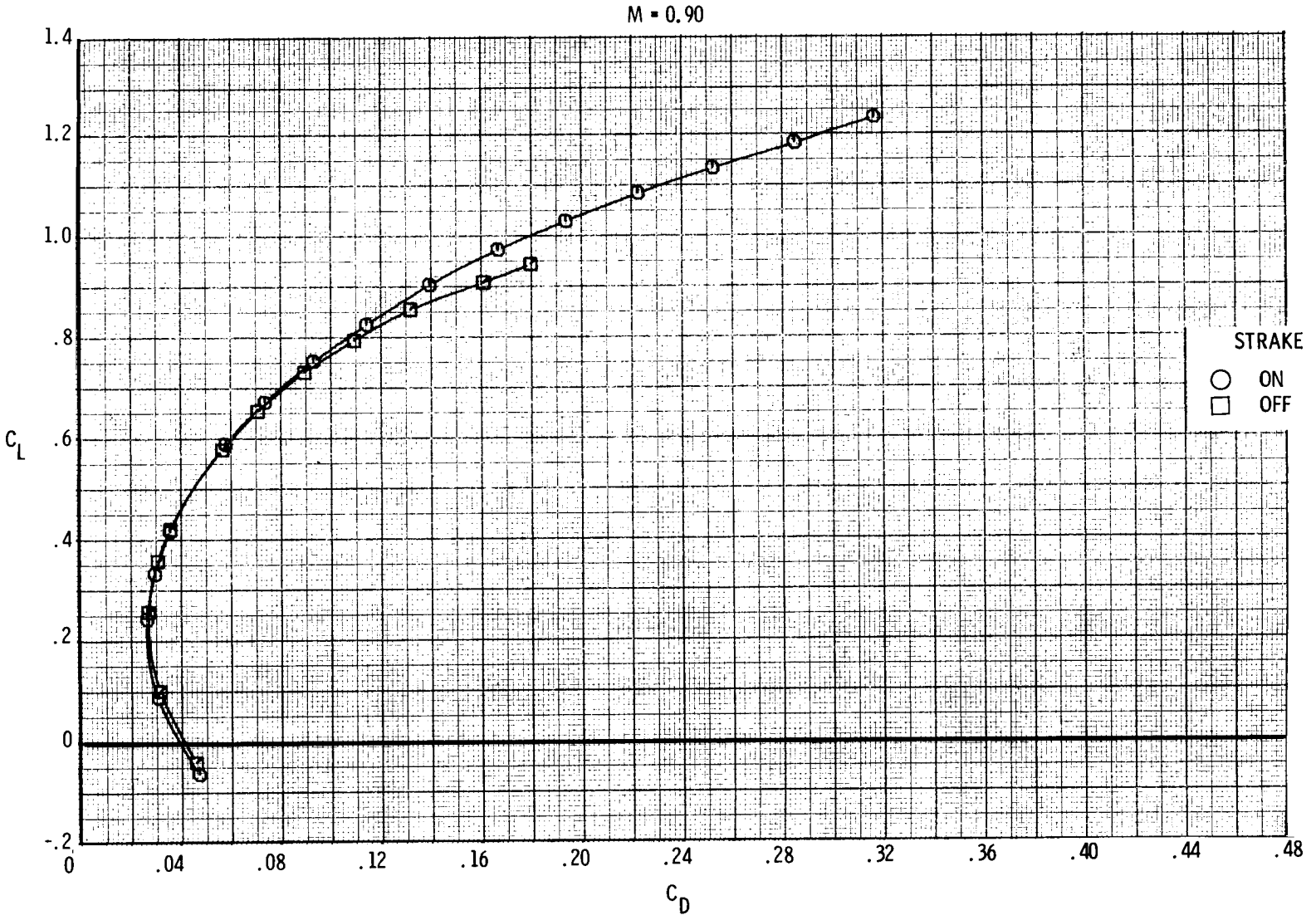

(a) Continued.

Figure 9.- Continued.

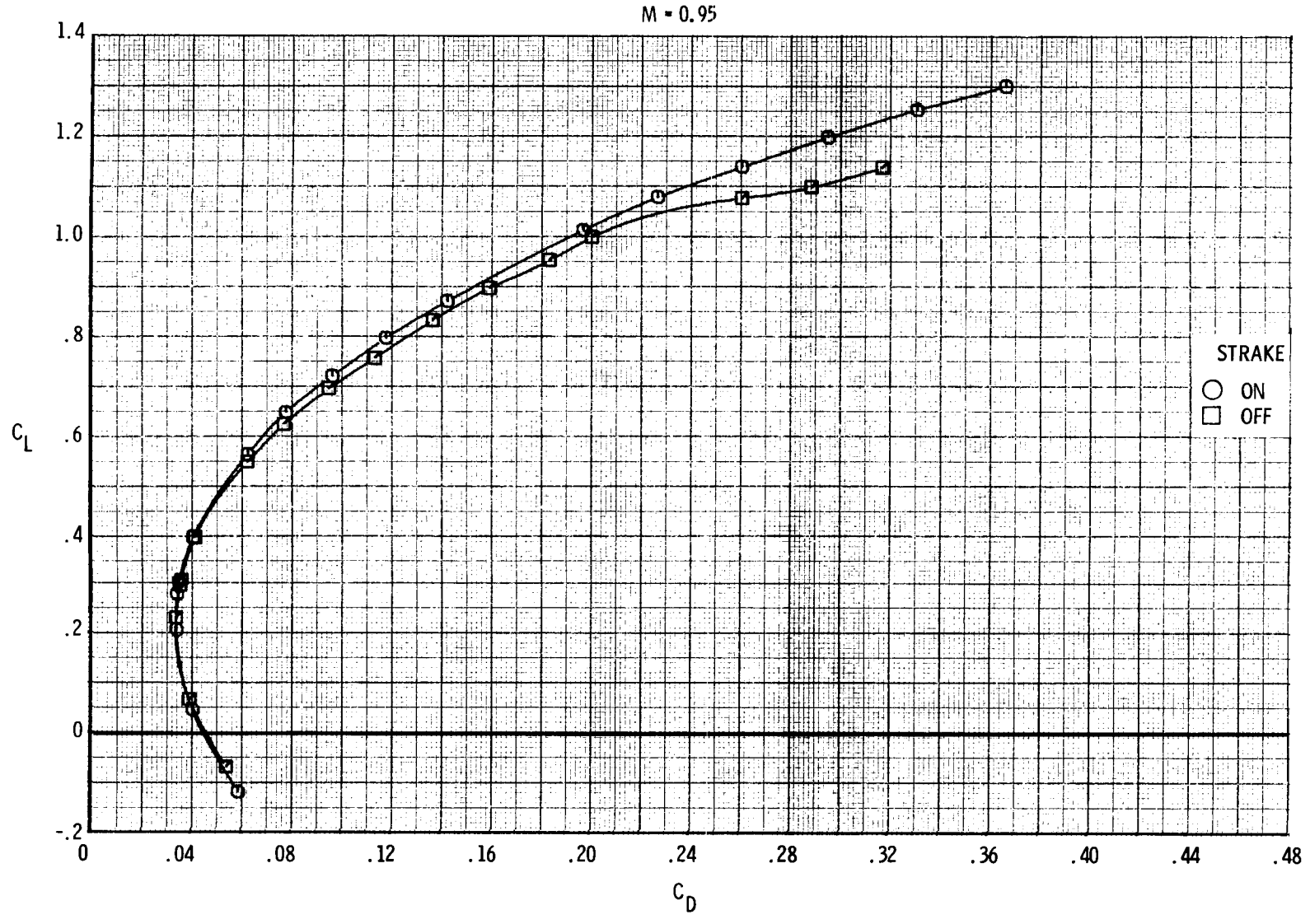

(a) Continued.

Figure 9.- Continued.

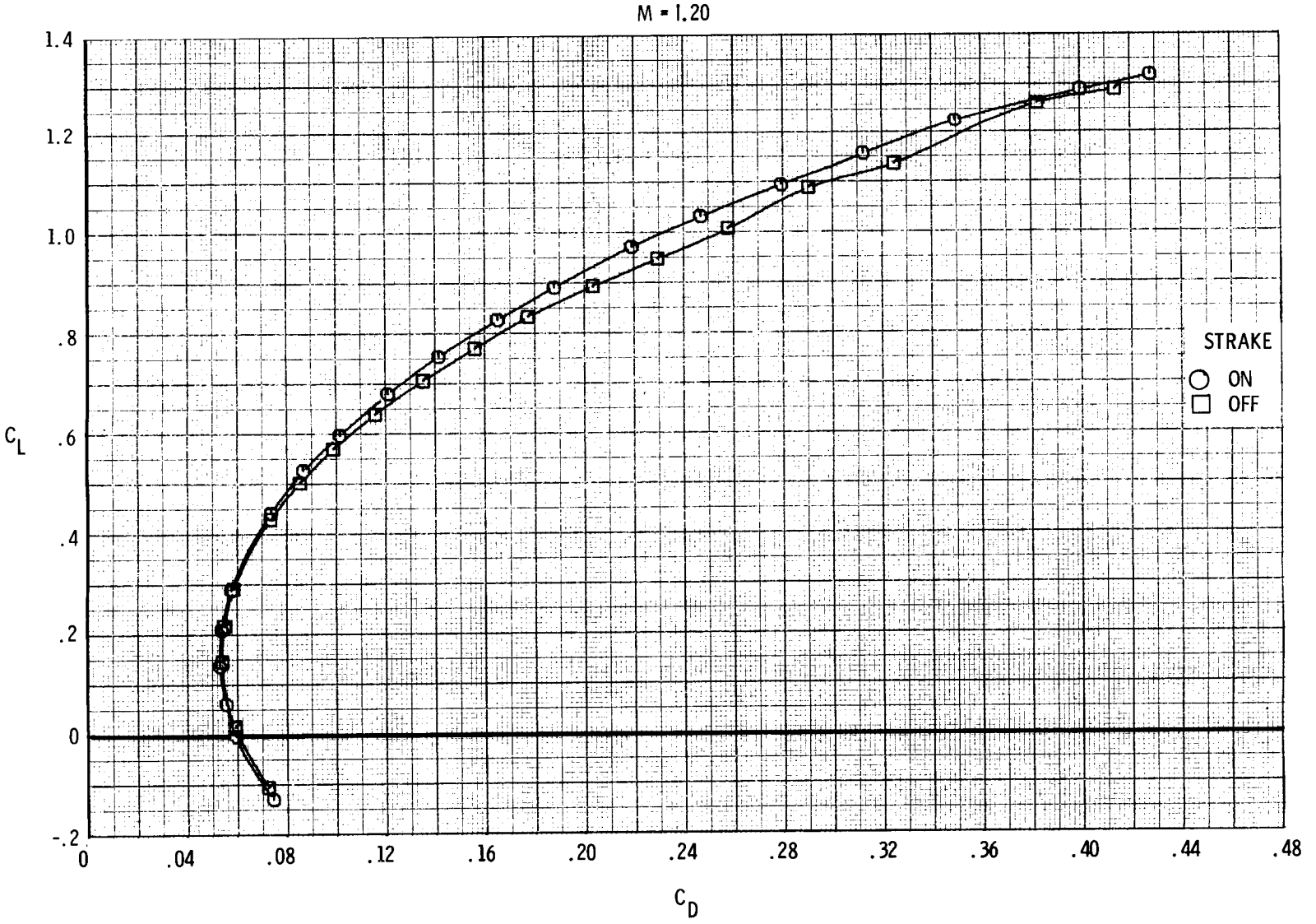

(a) Concluded.

Figure 9.- Continued.

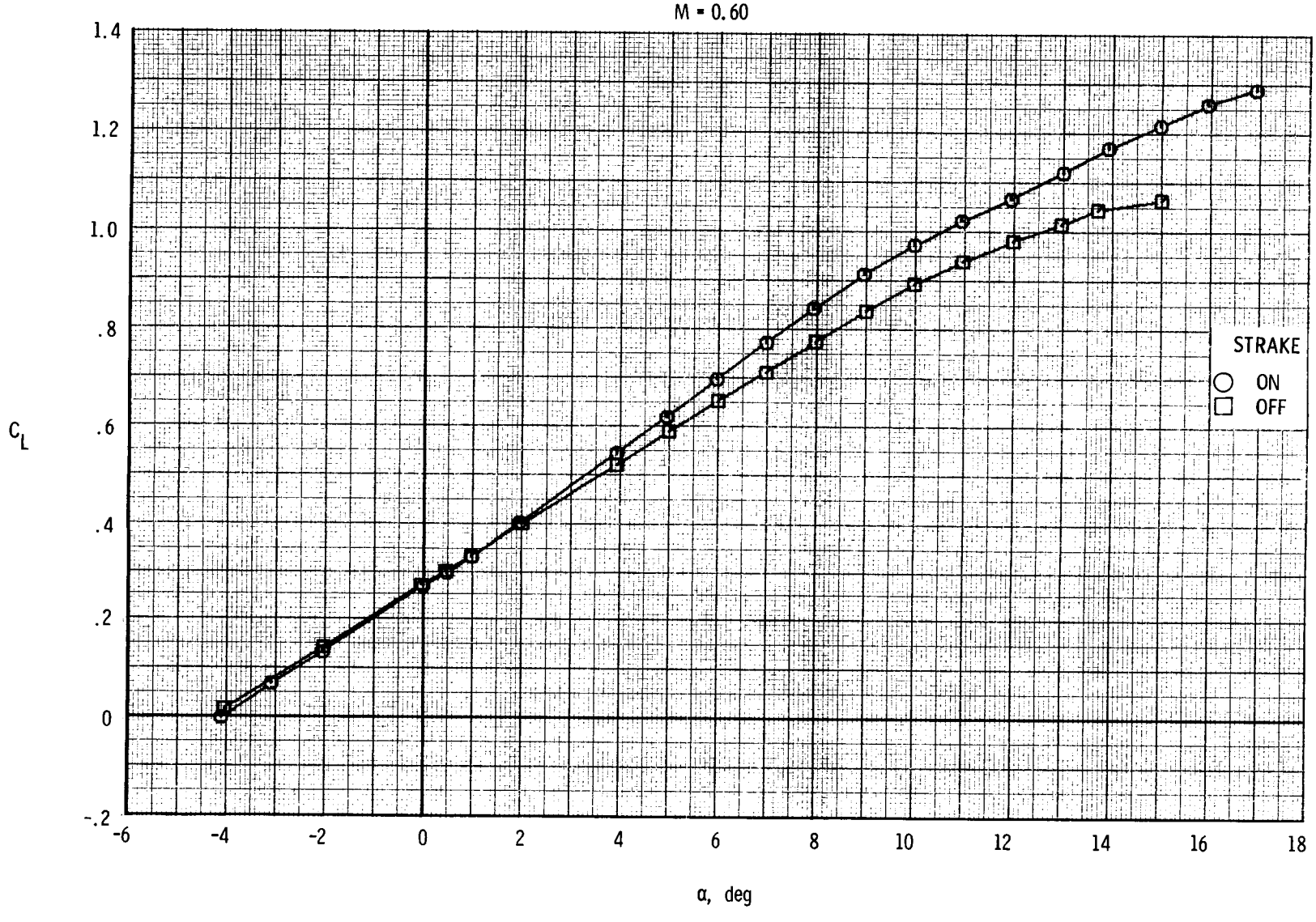

(b) Variation of C_L with α.

Figure 9.- Continued.

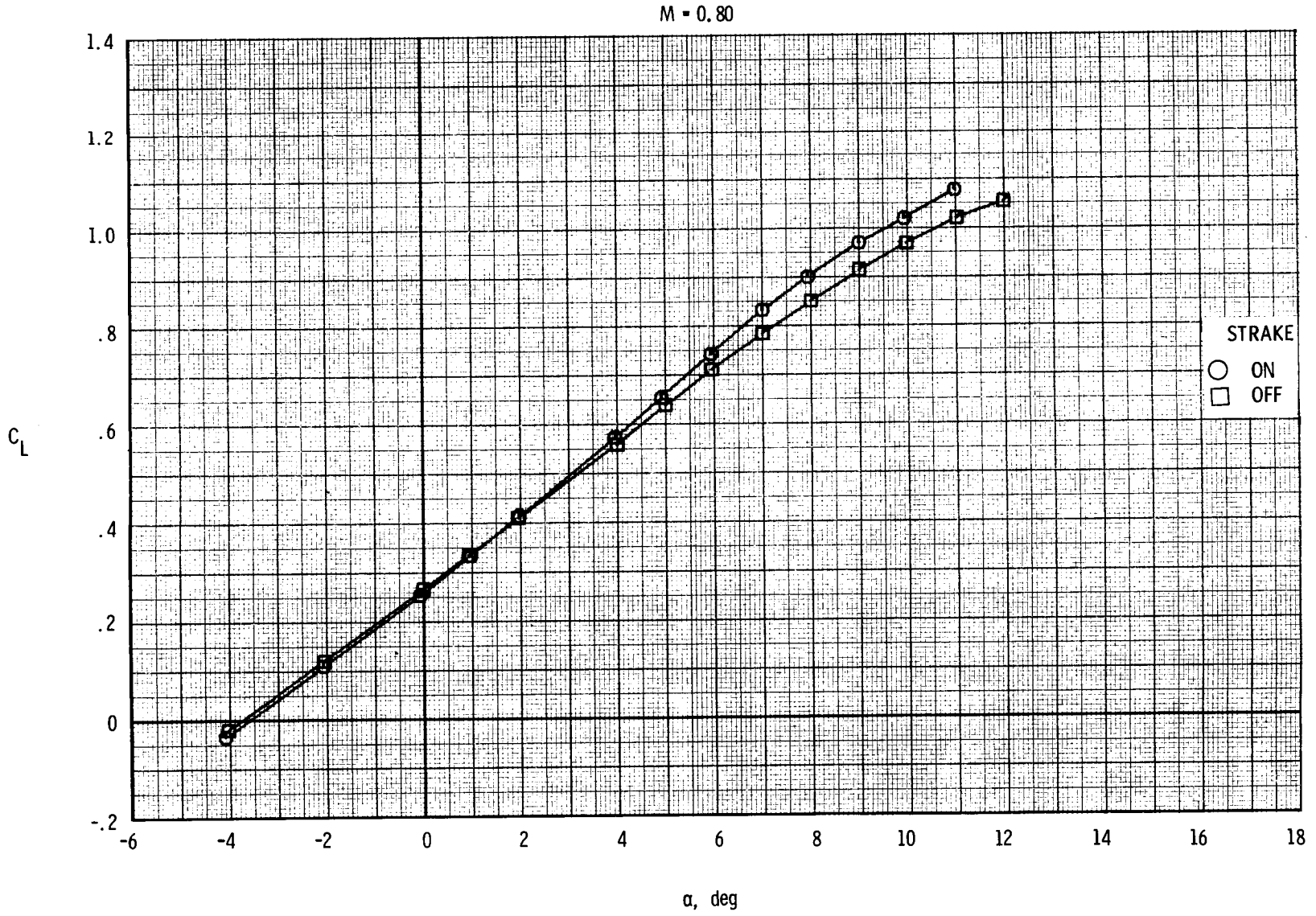

(b) Continued.

Figure 9.- Continued.

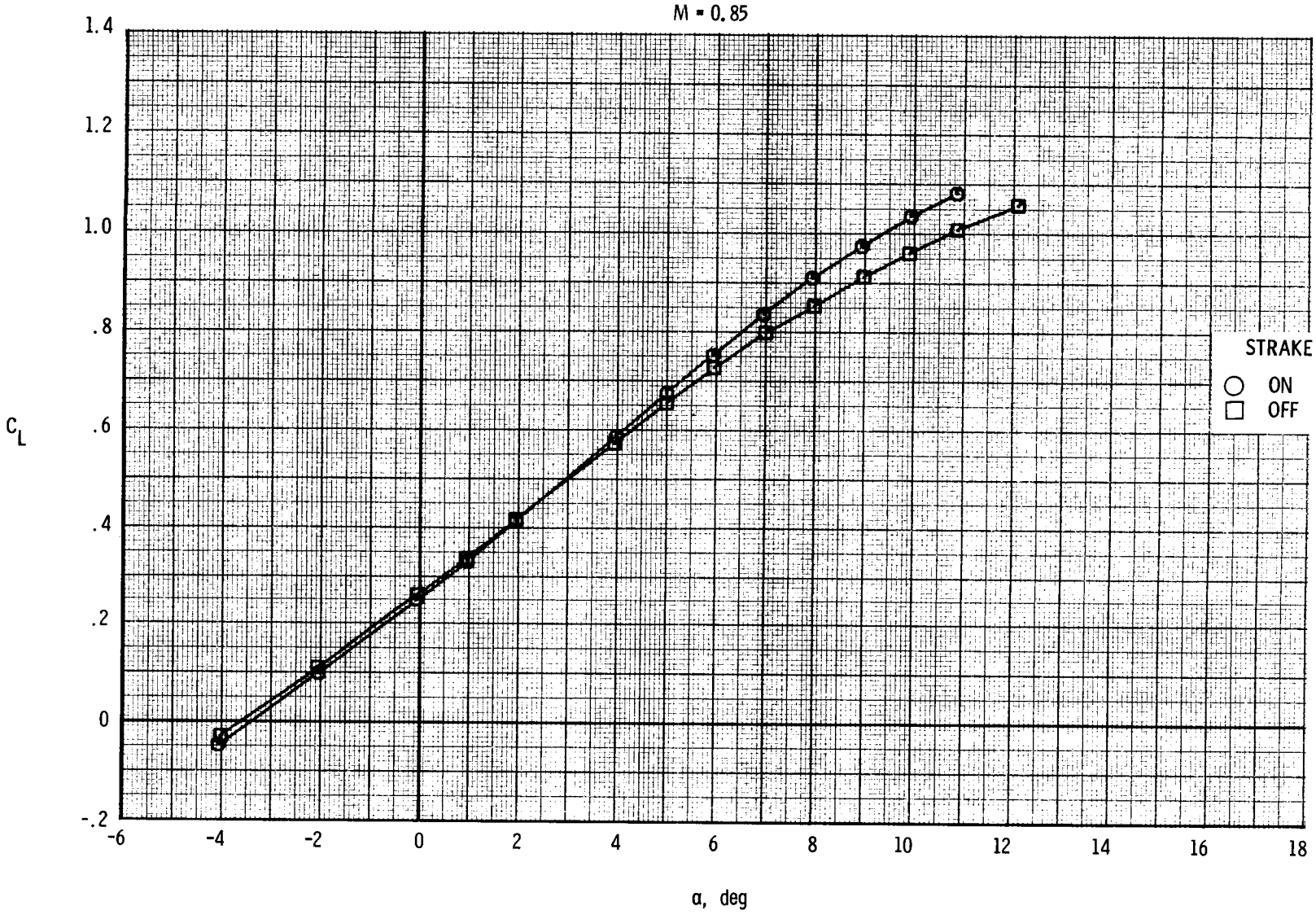

(b) Continued.

Figure 9.- Continued.

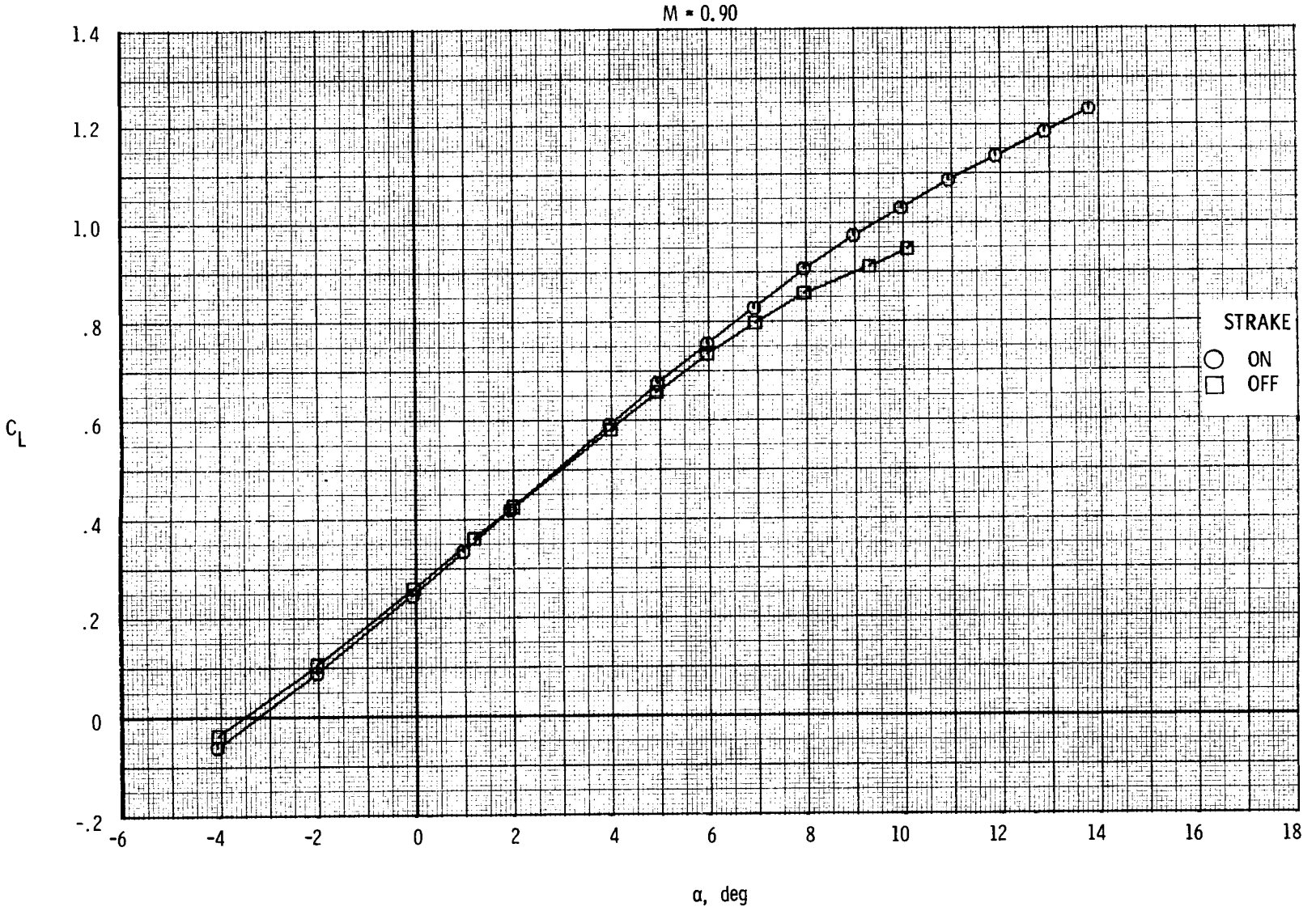

(b) Continued.

Figure 9.- Continued.

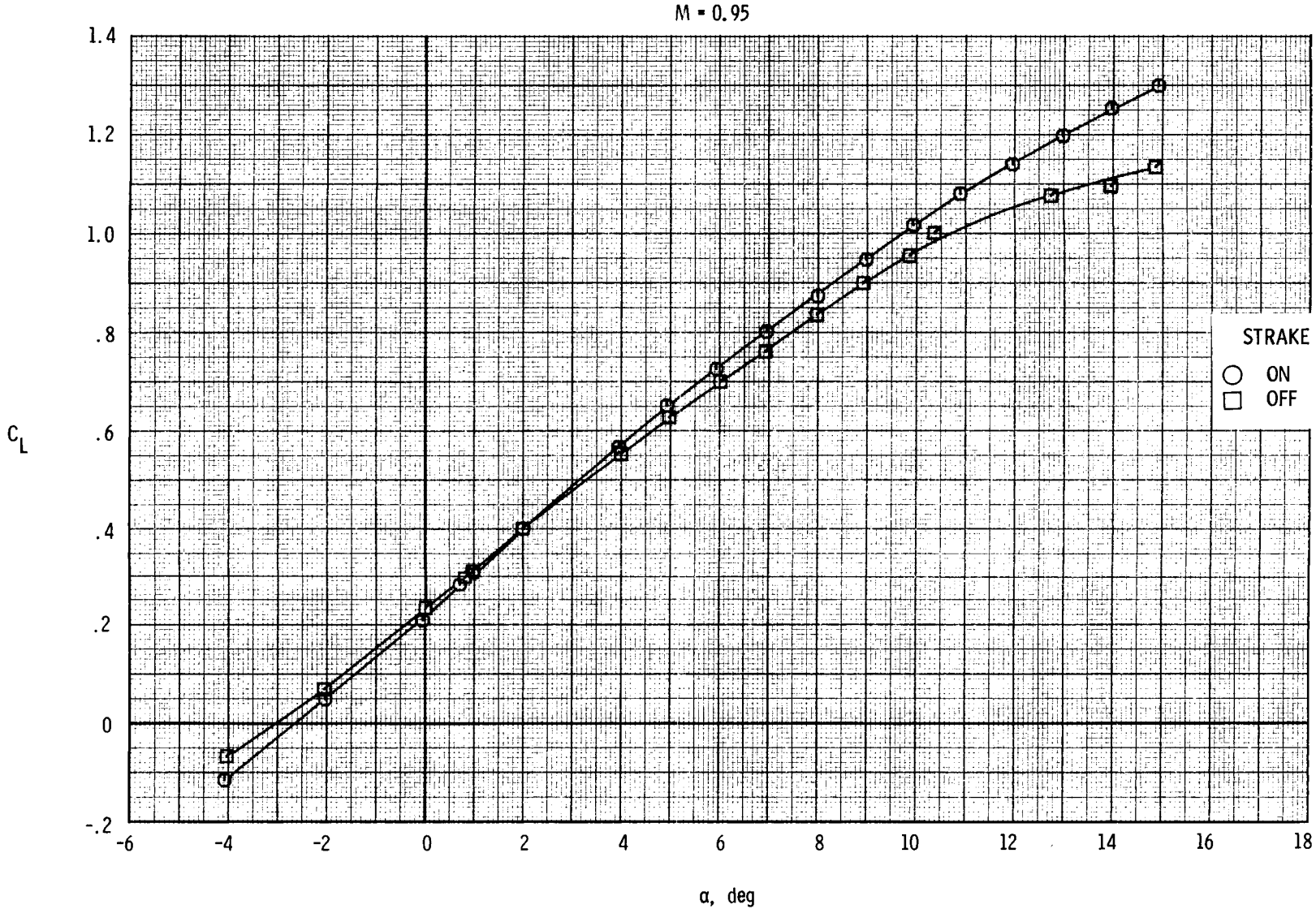

(b) Continued.

Figure 9.- Continued.

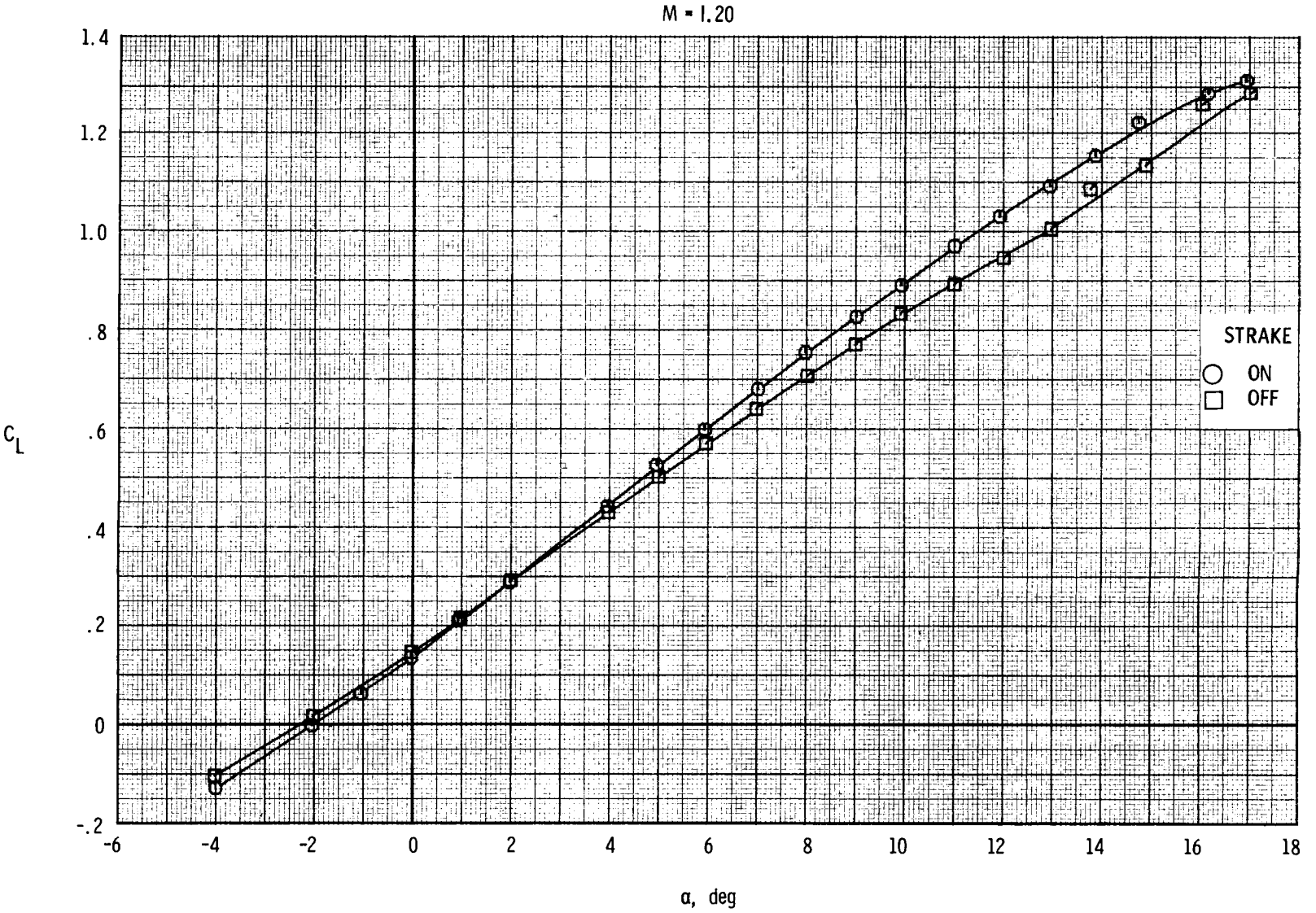

(b) Concluded.

Figure 9.- Continued.

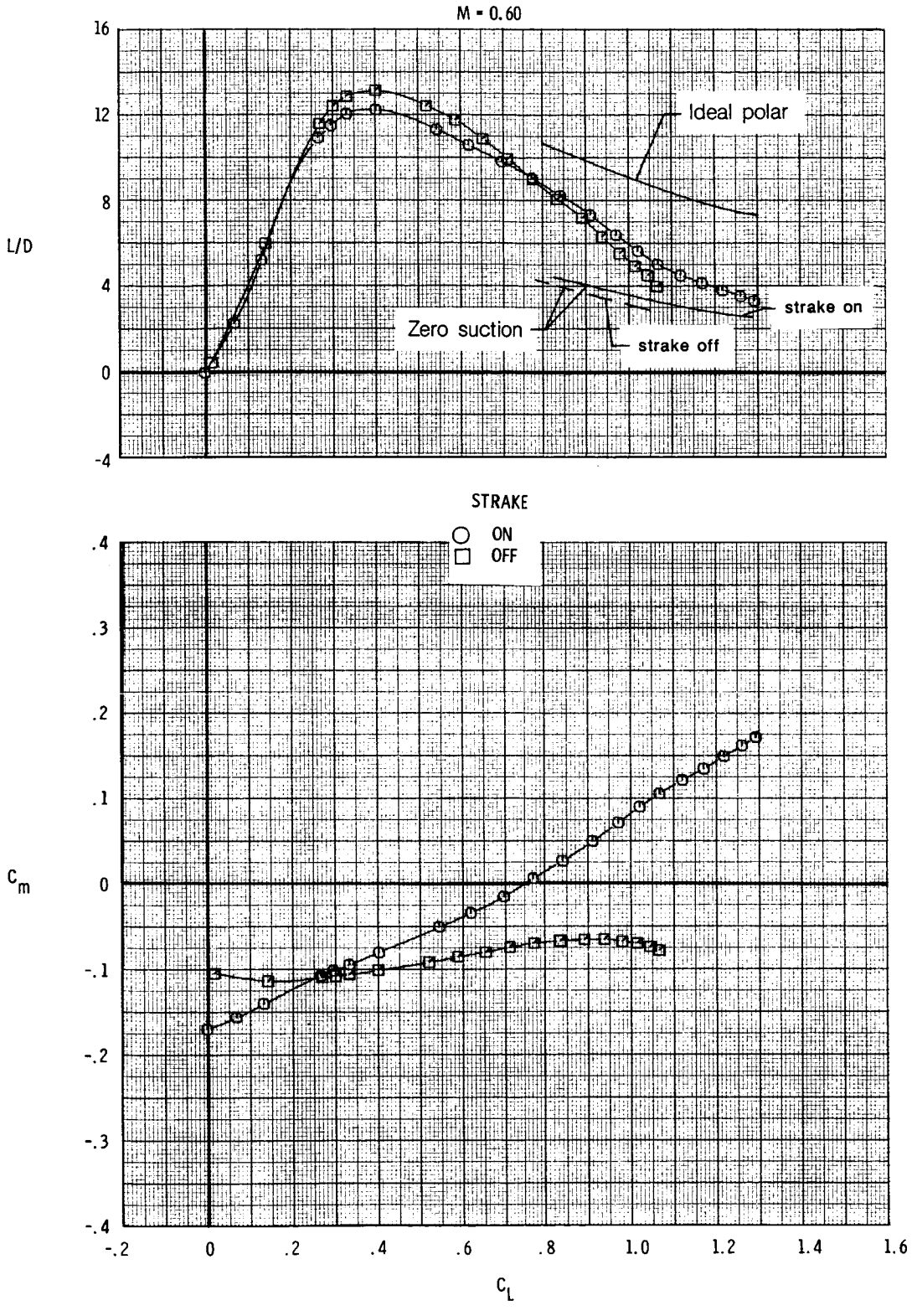

(c) Variation of L/D and C_m with C_L.

Figure 9.- Continued.

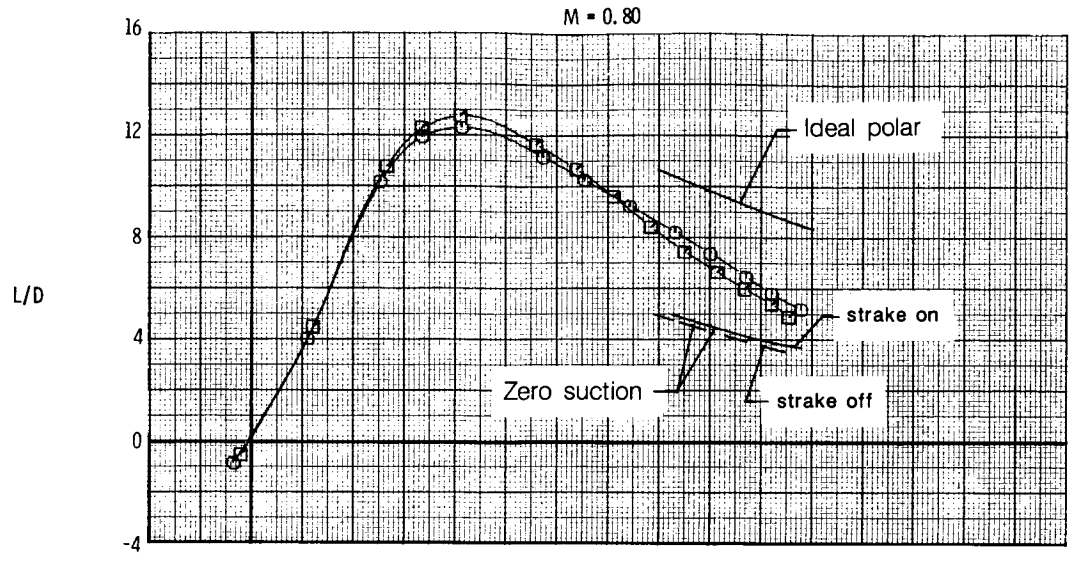

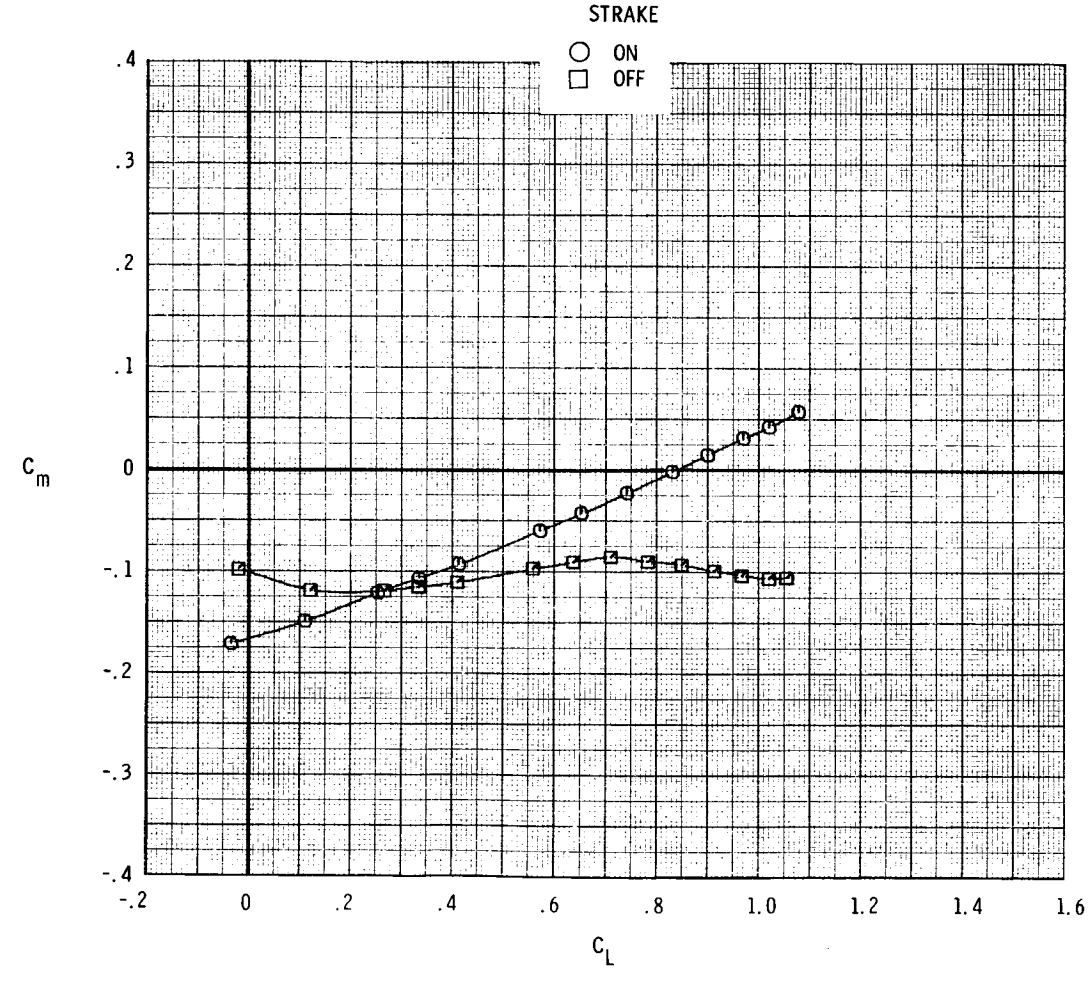

(c) Continued.

Figure 9.- Continued.

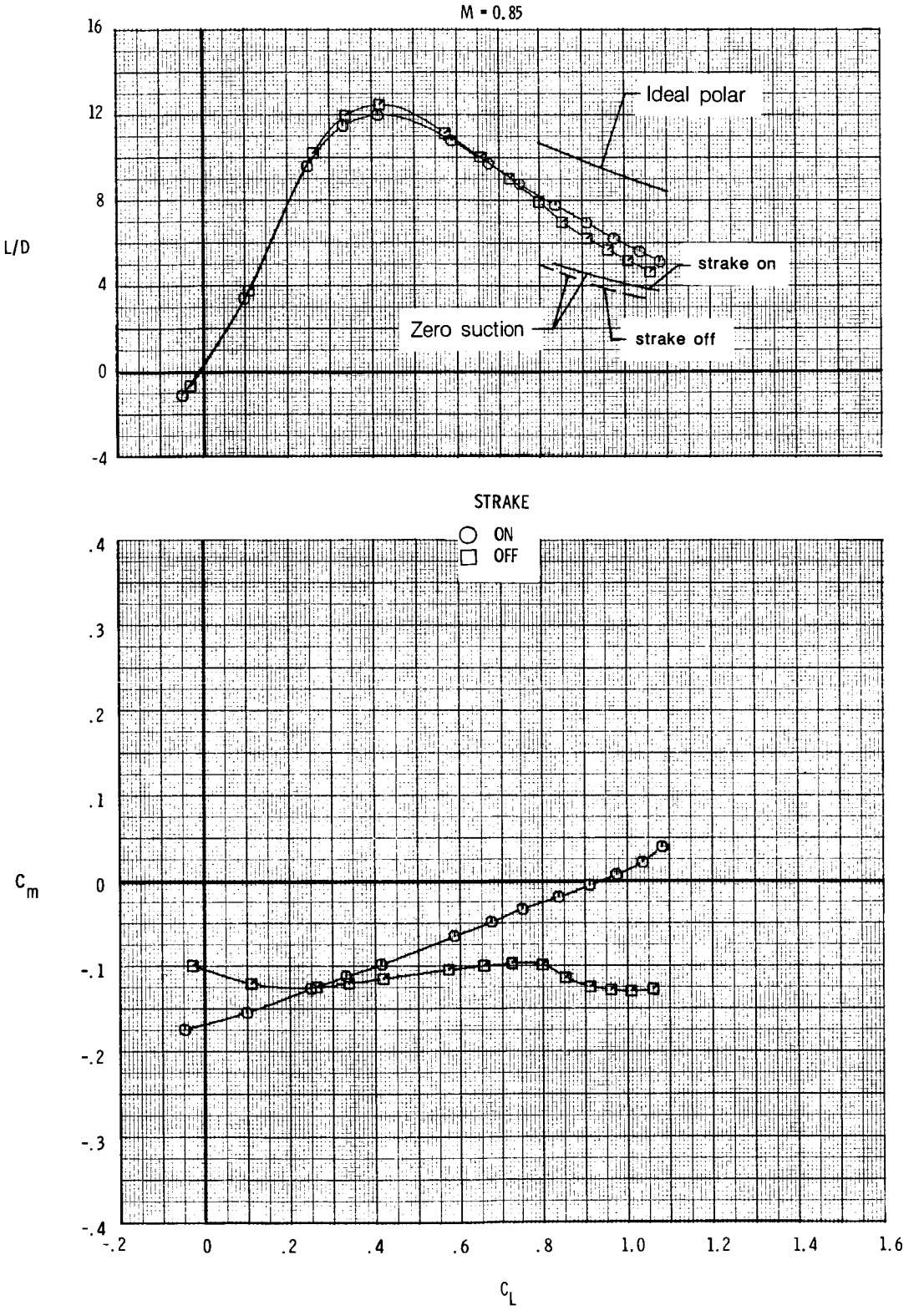

(c) Continued.

Figure 9.- Continued.

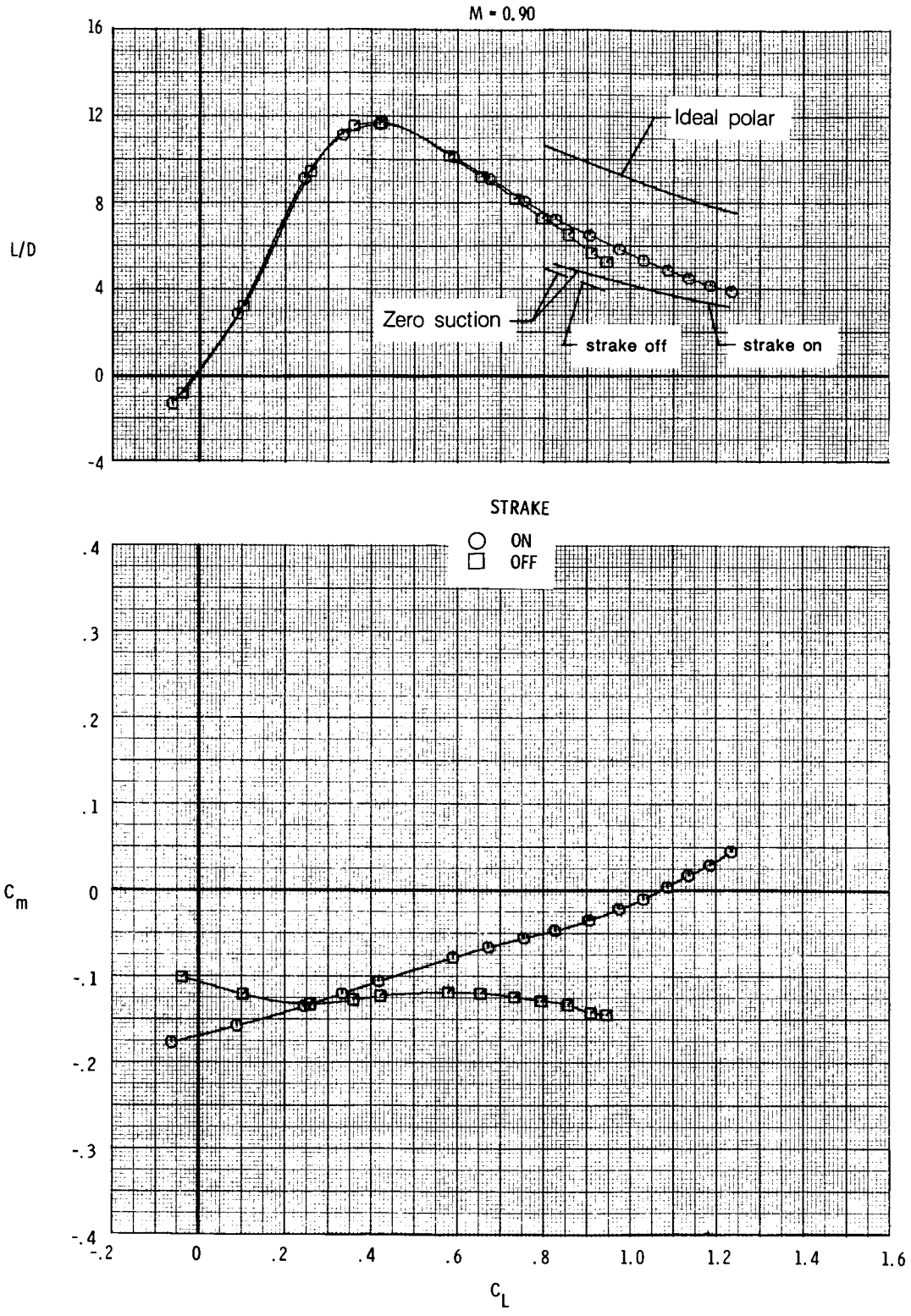

(c) Continued.

Figure 9.- Continued.

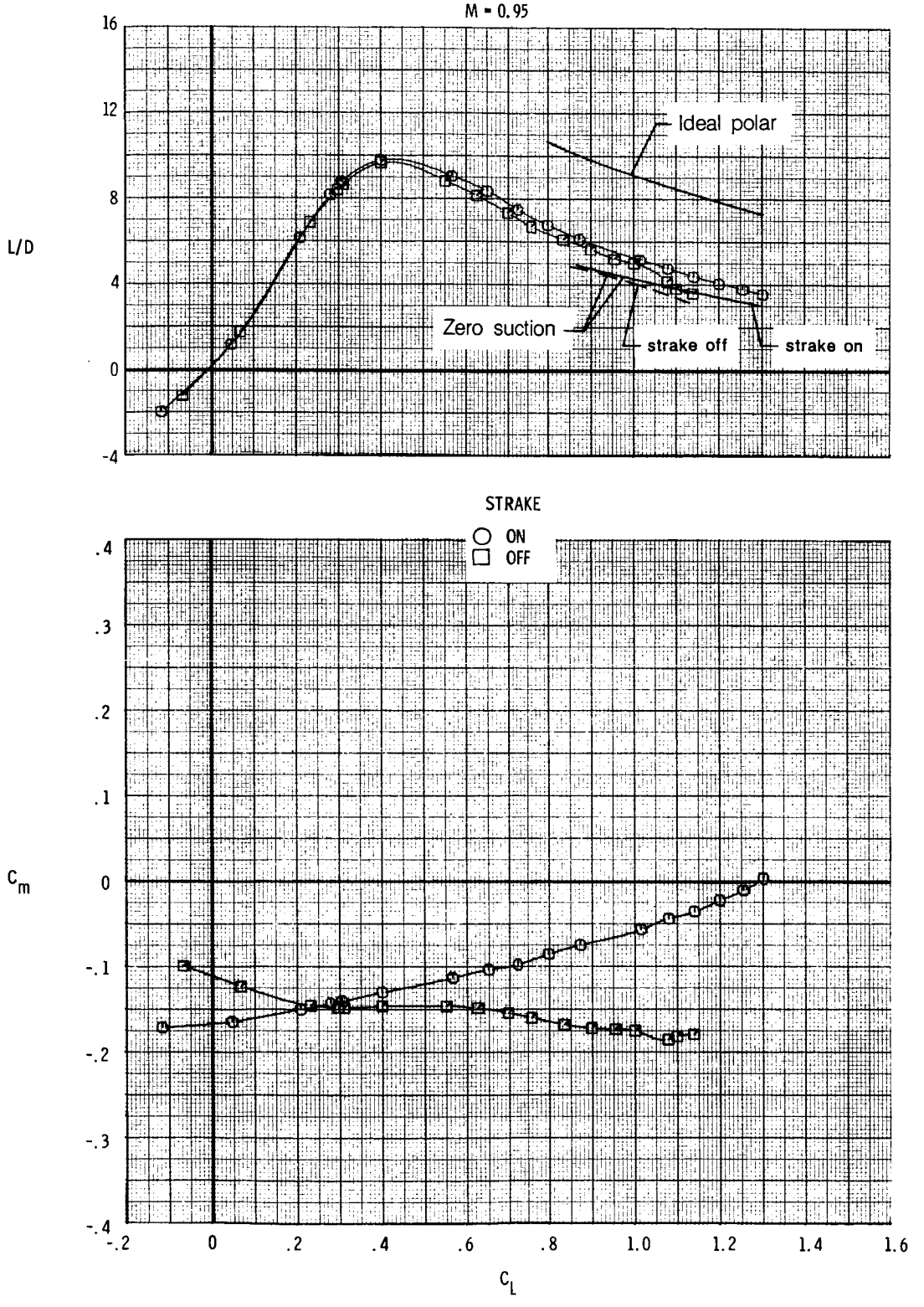

(c) Continued.

Figure 9.- Continued.

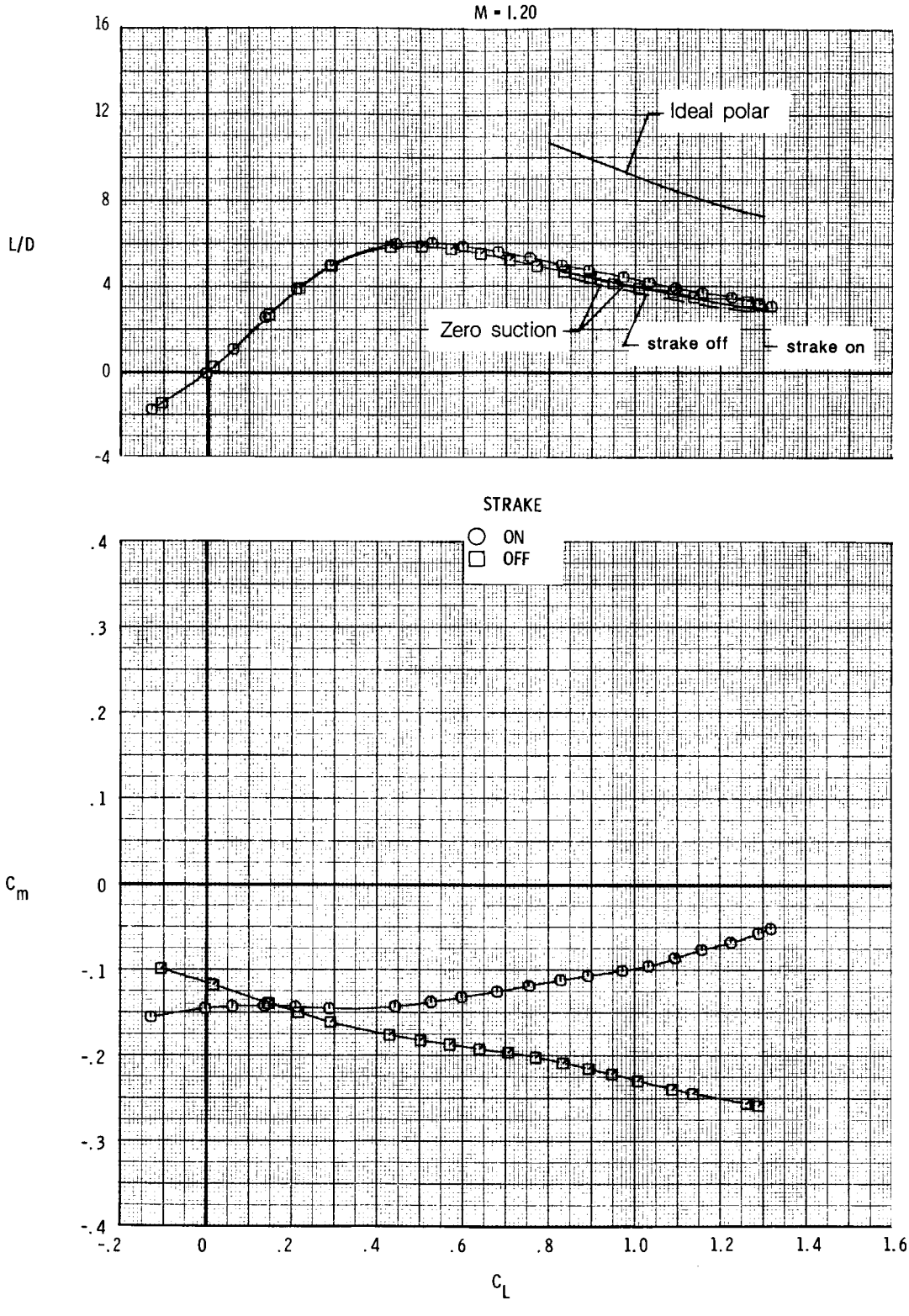

(c) Concluded.

Figure 9.- Continued.

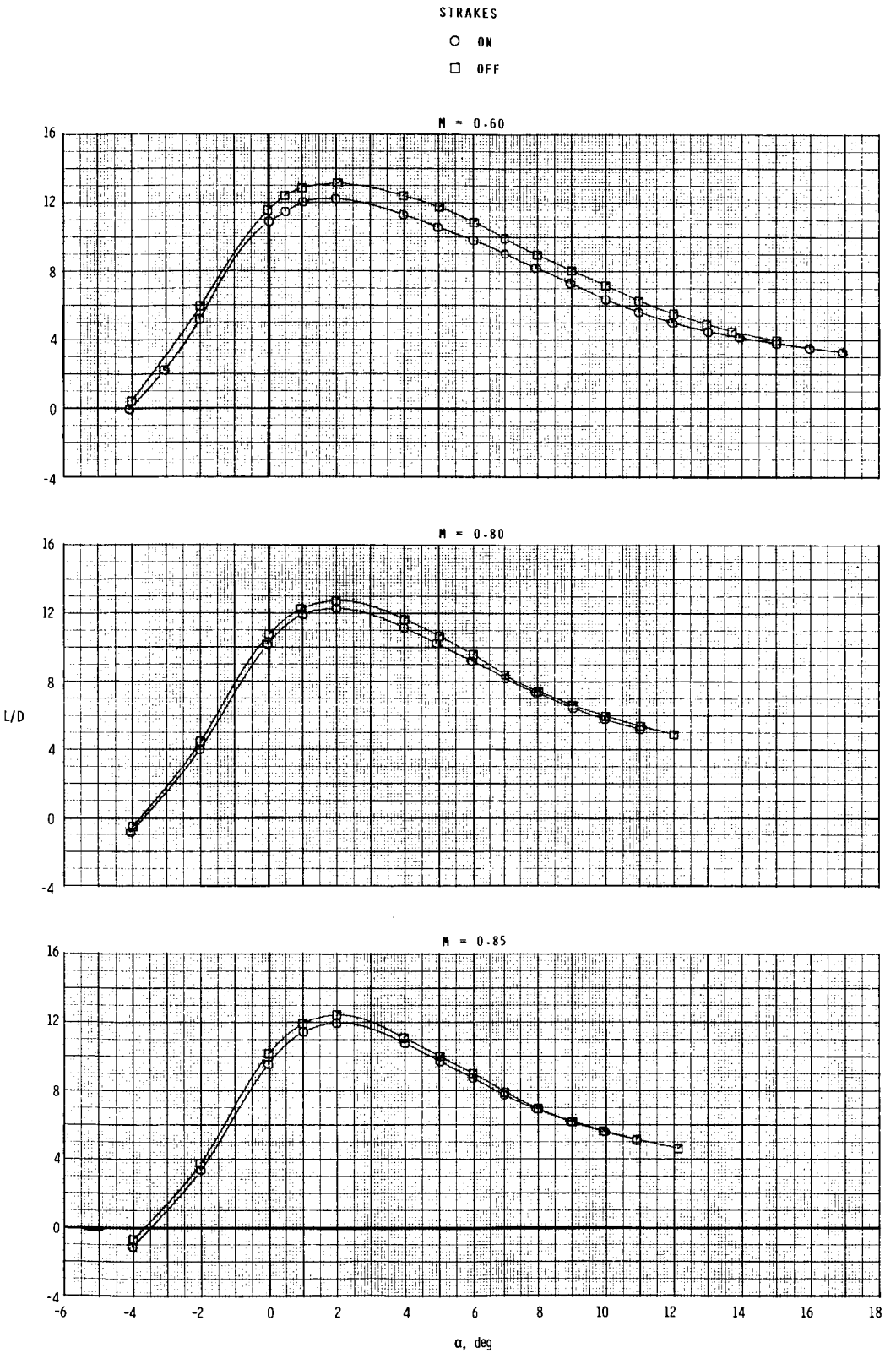

(d) Variation of L/D with α.

Figure 9.- Continued.

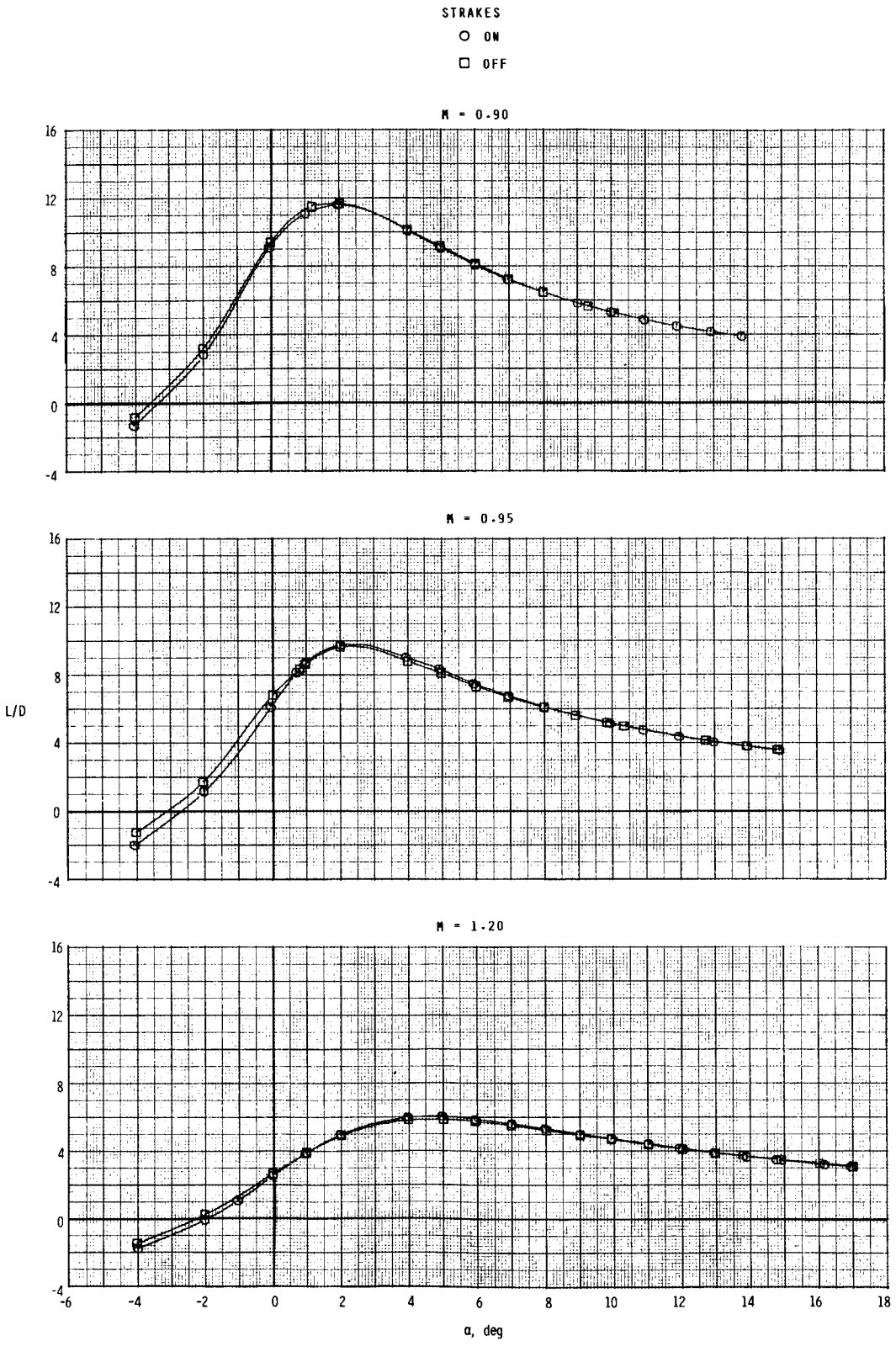

(d) Concluded.

Figure 9.- Concluded.

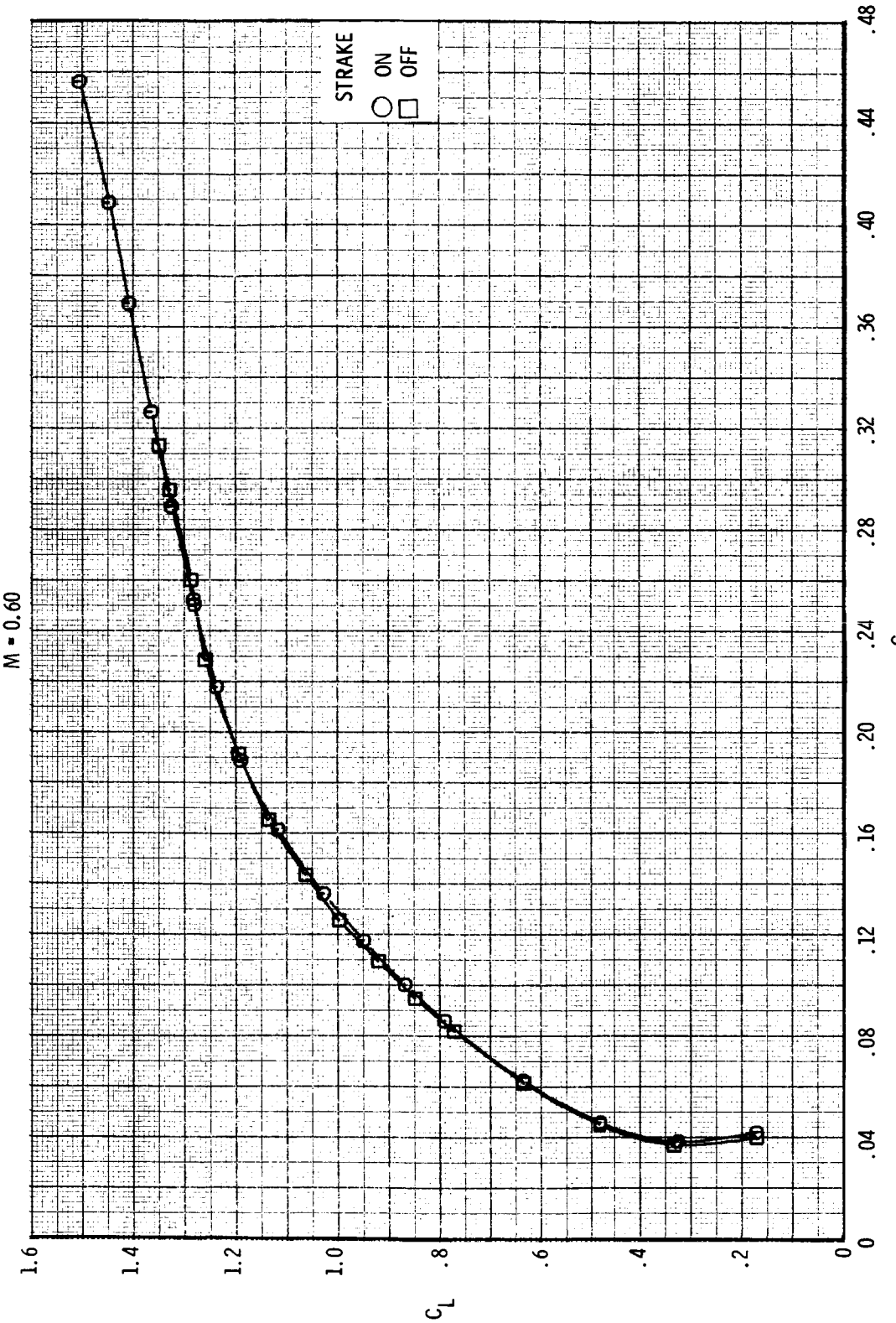

(a) Variation of C_L with C_D.

Figure 10.- Effect of strakes in combination with canards and trailing-edge flaps on longitudinal aerodynamic characteristics. $\delta_c = 0°$; $\delta_{f,LE} = 0°$; $\delta_{f,TE} = 10°$.

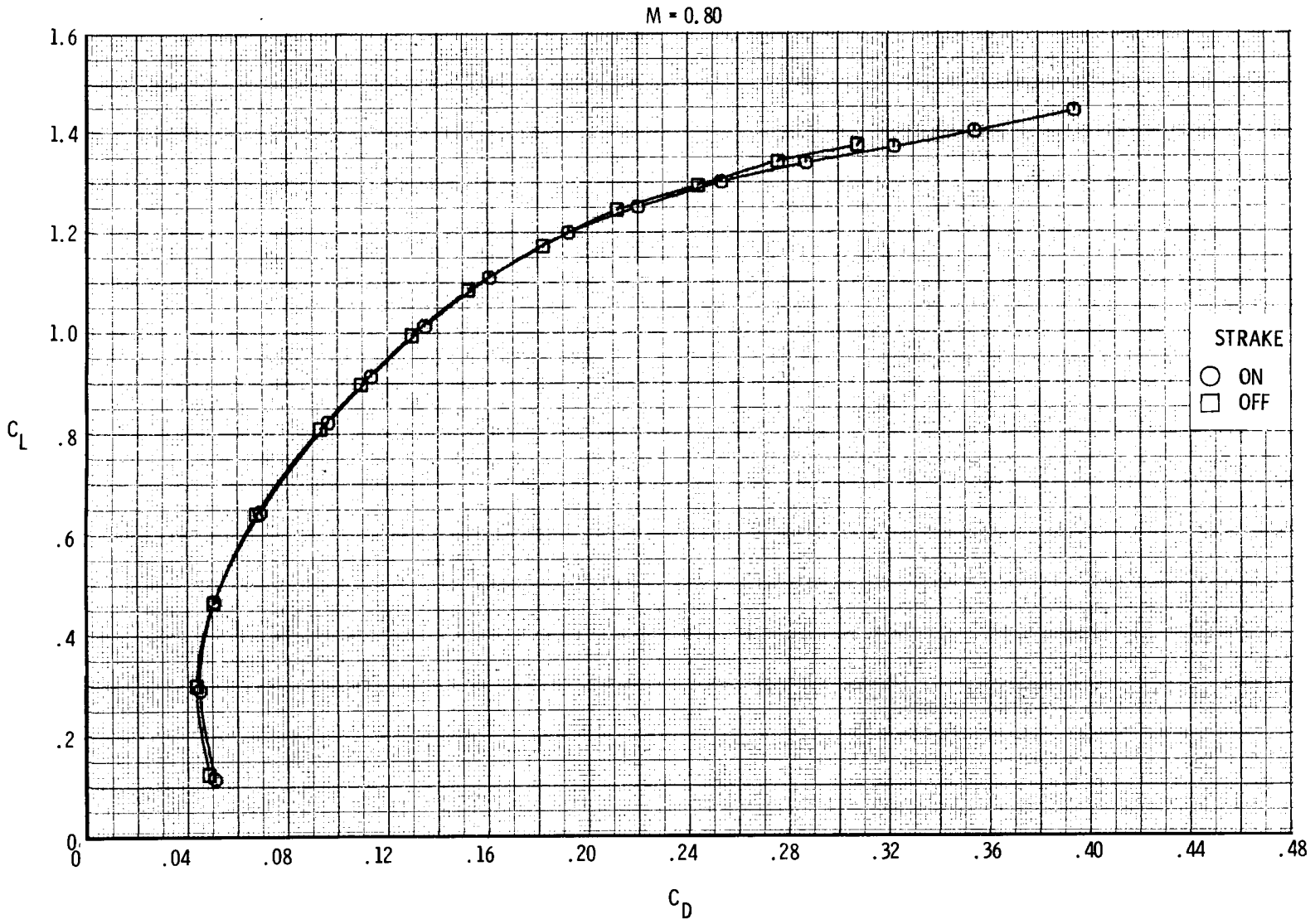

(a) Continued.

Figure 10.- Continued.

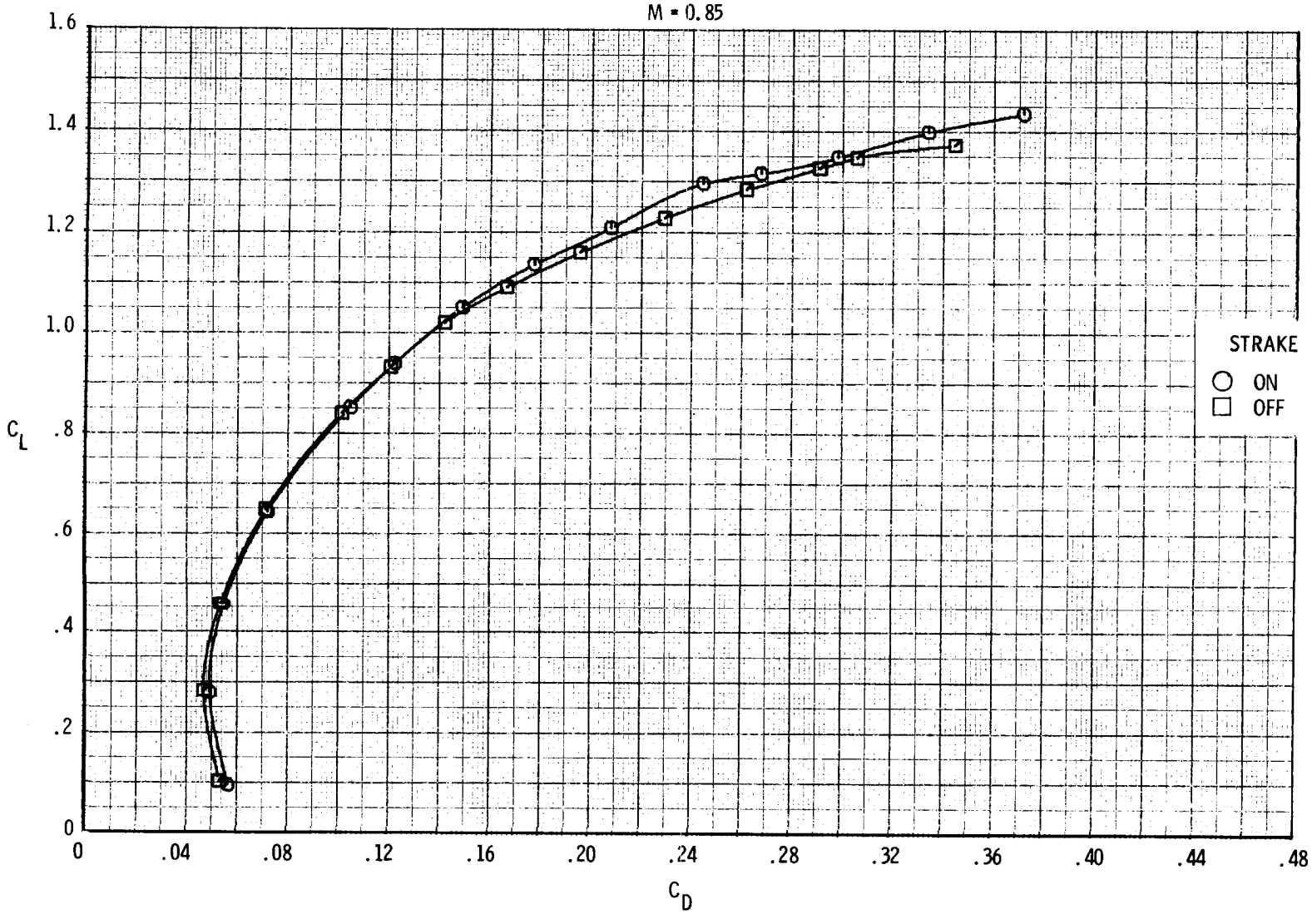

(a) Continued.

Figure 10.- Continued.

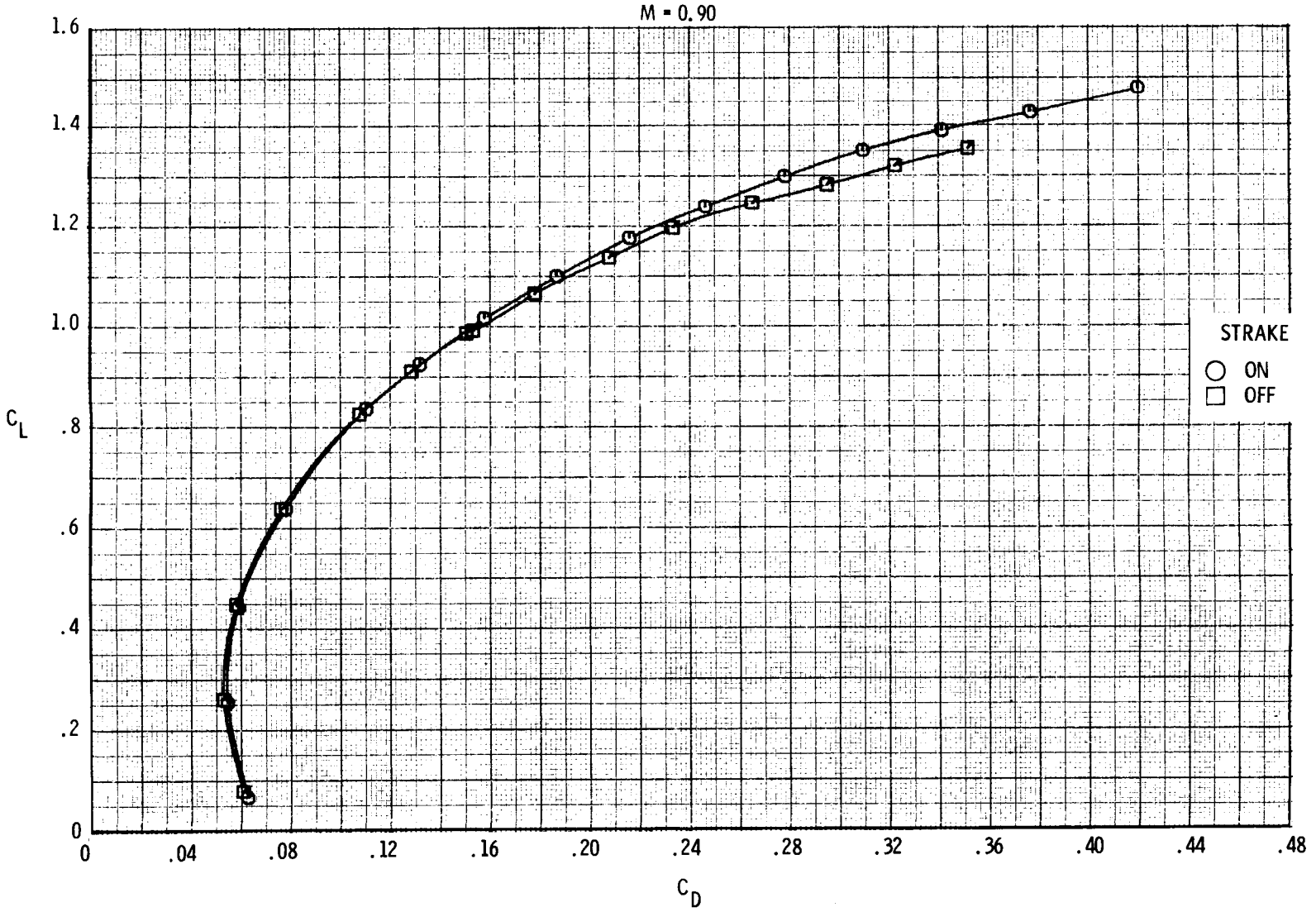

(a) Concluded.

Figure 10.- Continued.

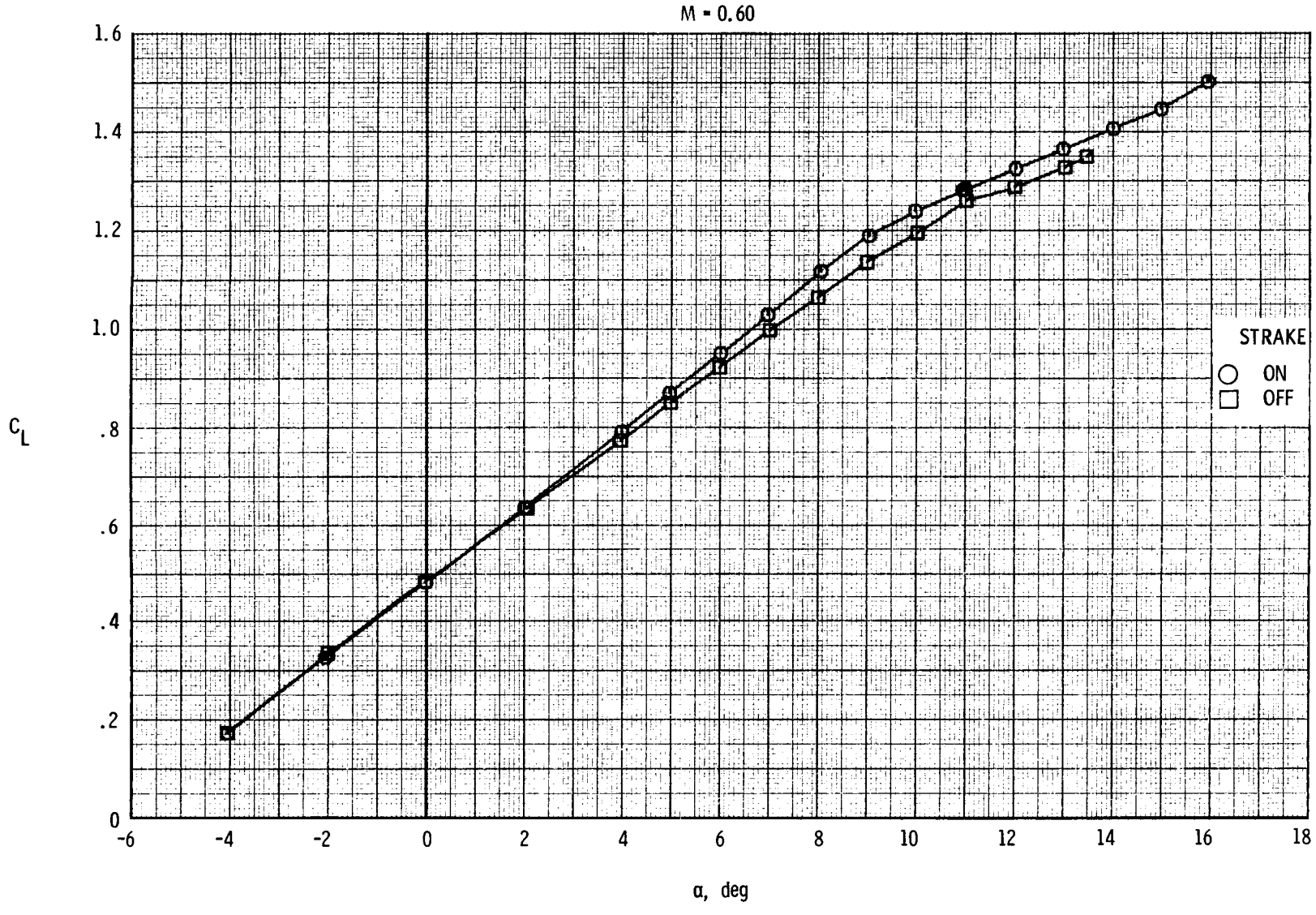

(b) Variation of C_L with α.

Figure 10.- Continued.

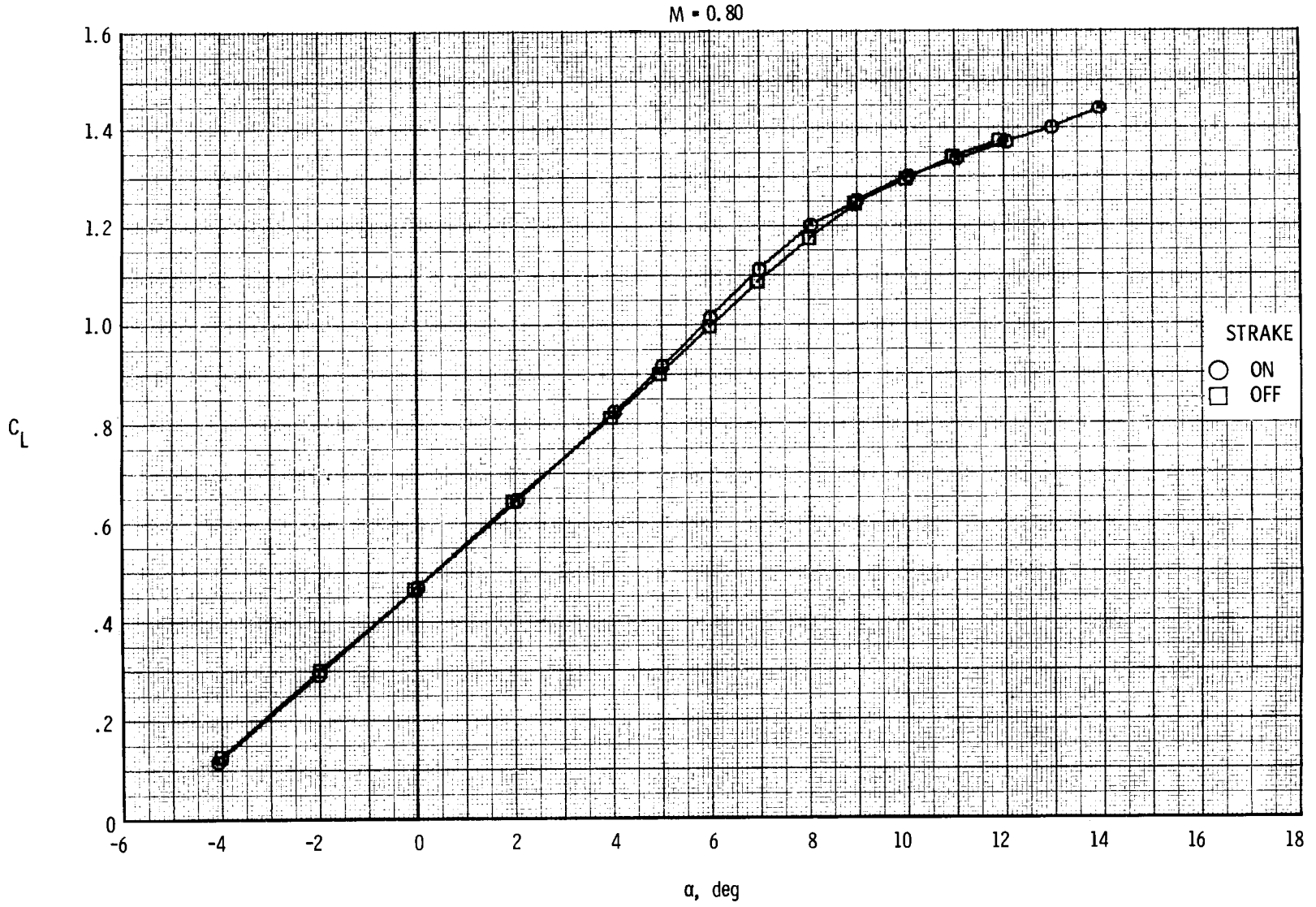

(b) Continued.

Figure 10.- Continued.

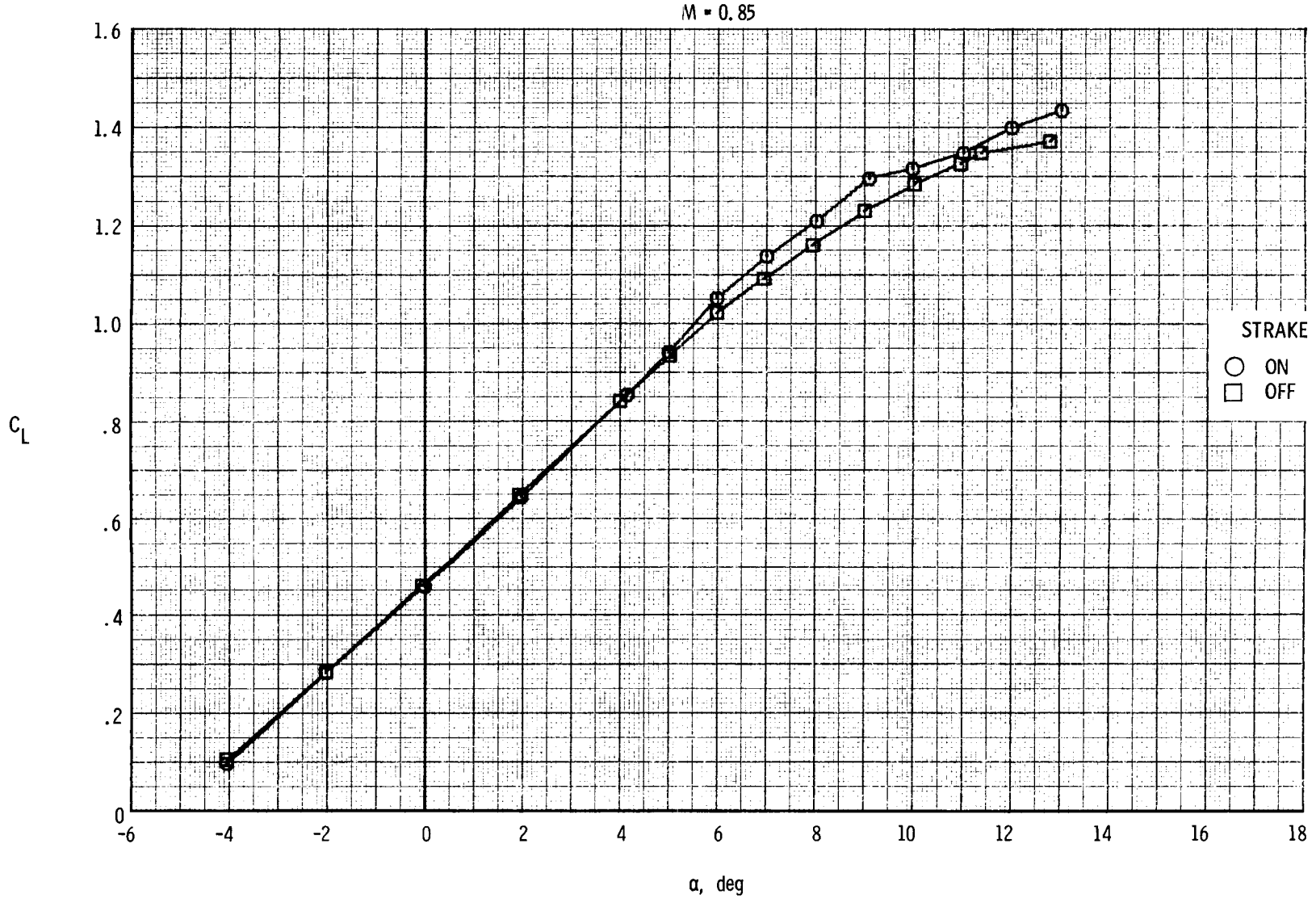

(b) Continued.

Figure 10.- Continued.

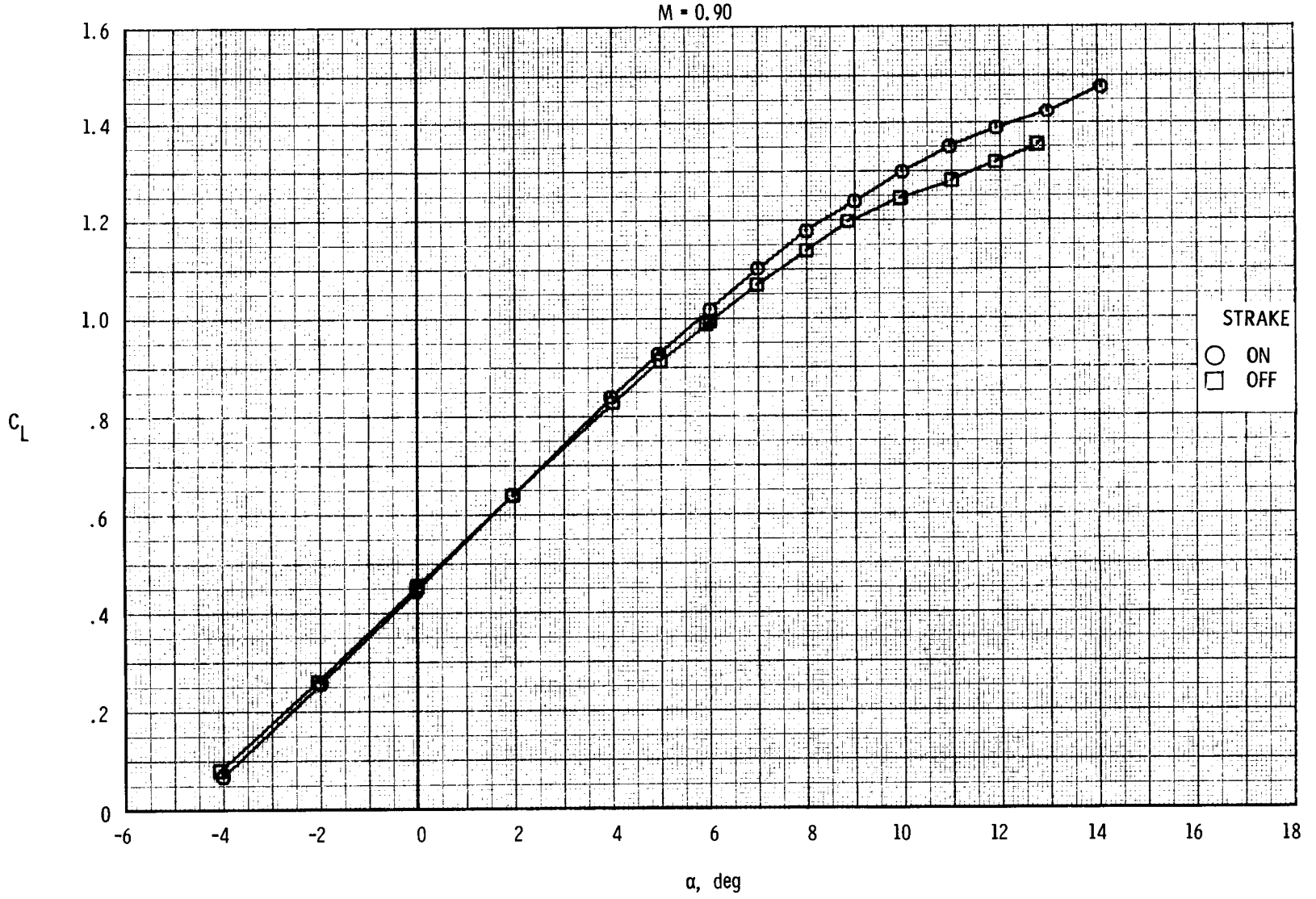

(b) Concluded.

Figure 10.- Continued.

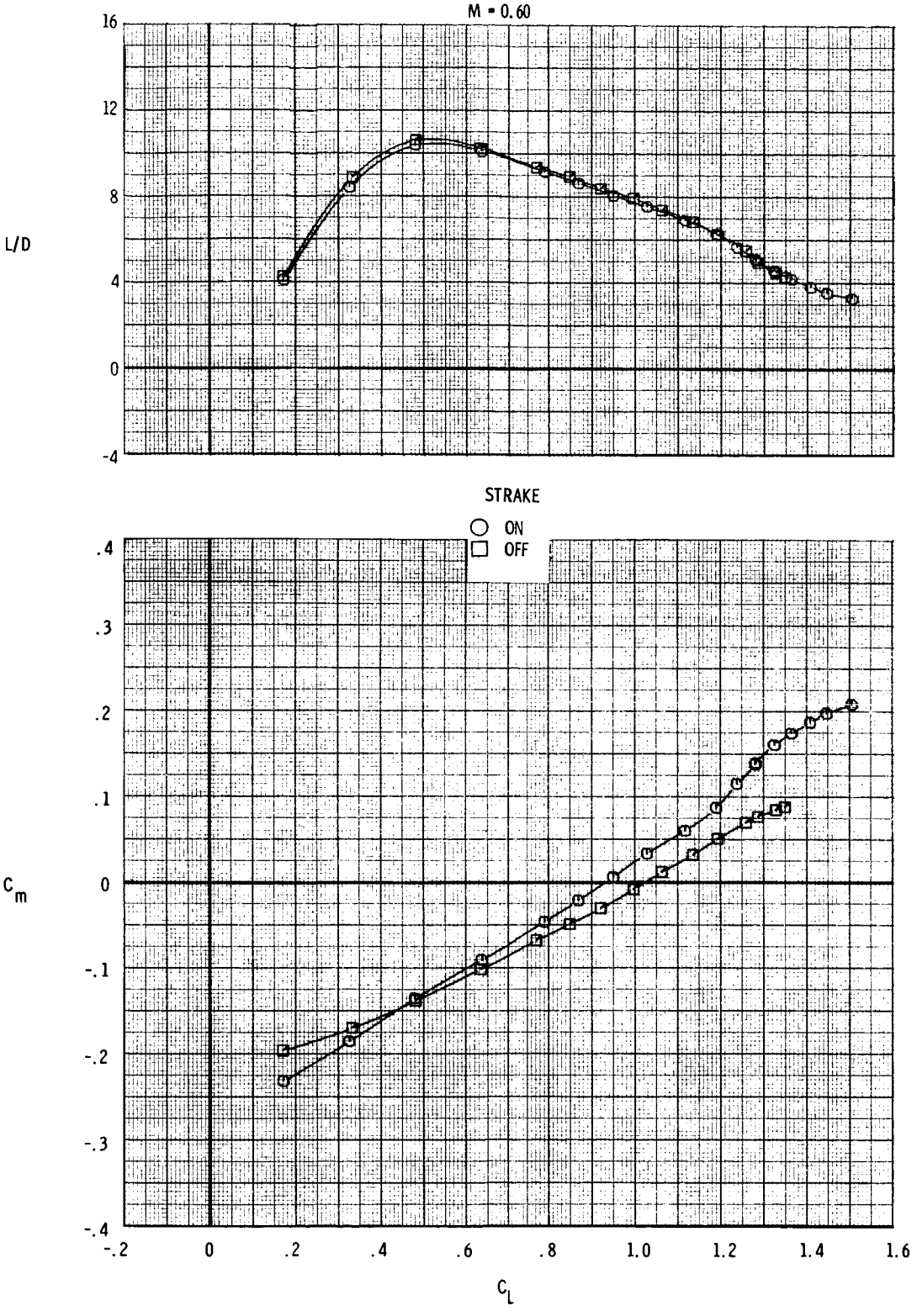

(c) Variation of L/D and C_m with C_L.

Figure 10.- Continued.

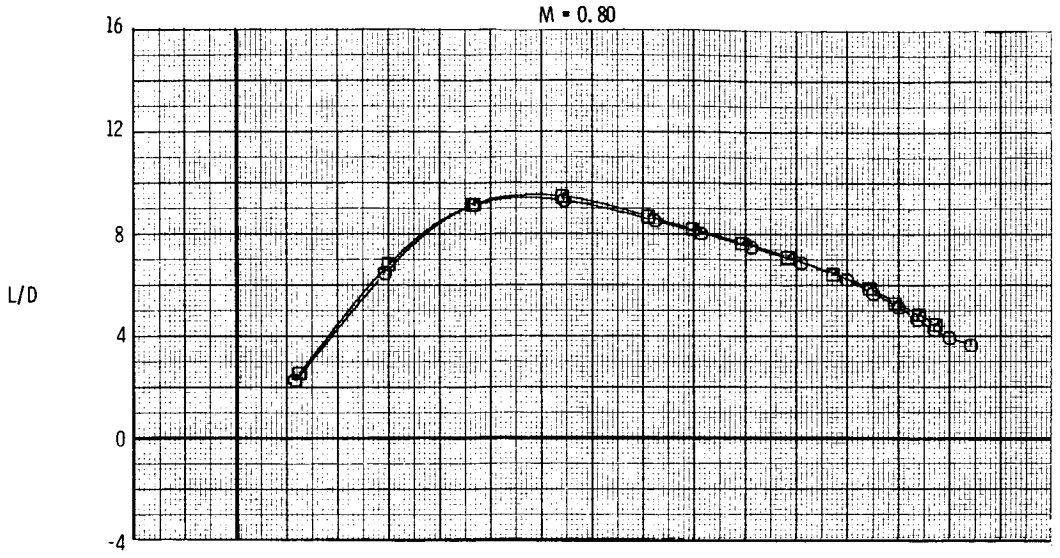

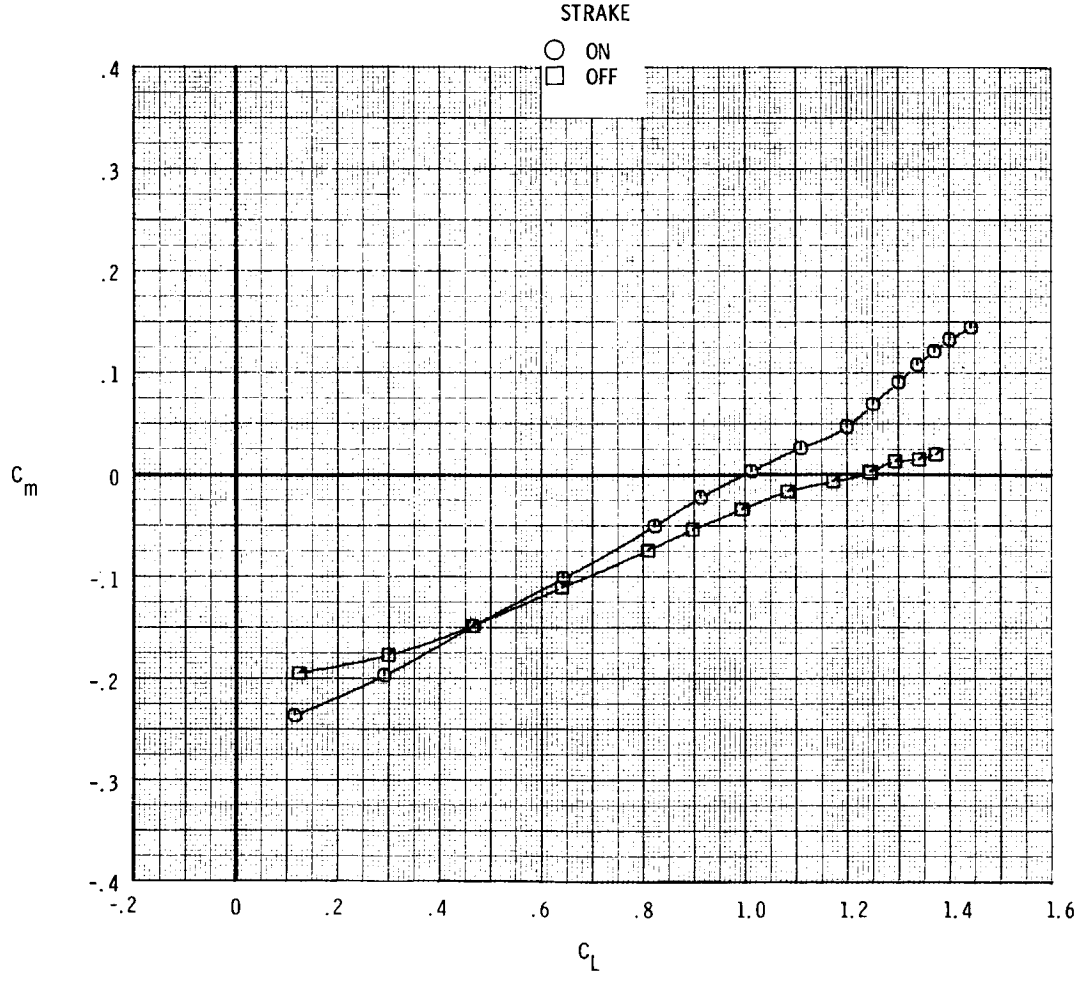

(c) Continued.

Figure 10.- Continued.

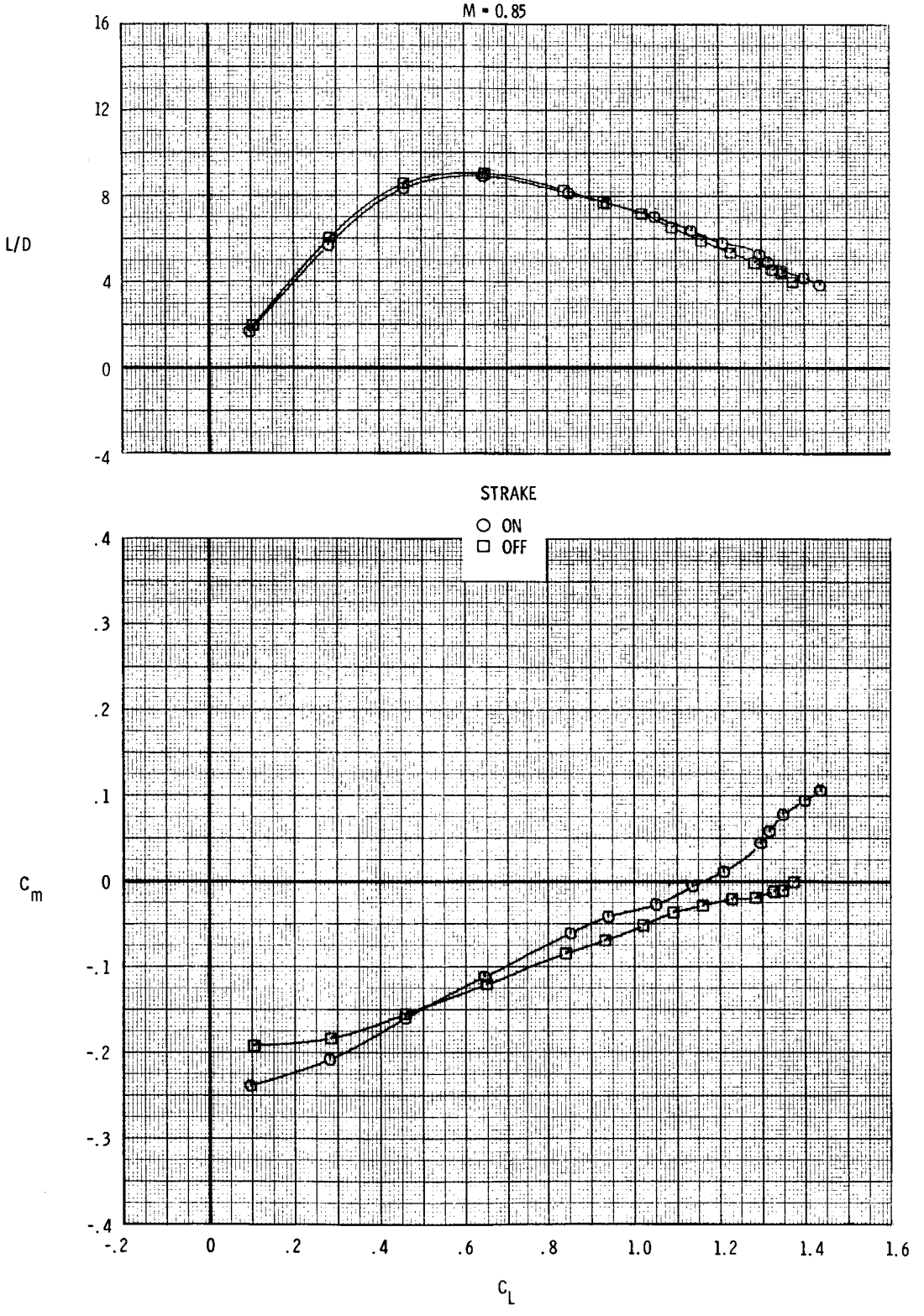

(c) Continued.

Figure 10.- Continued.

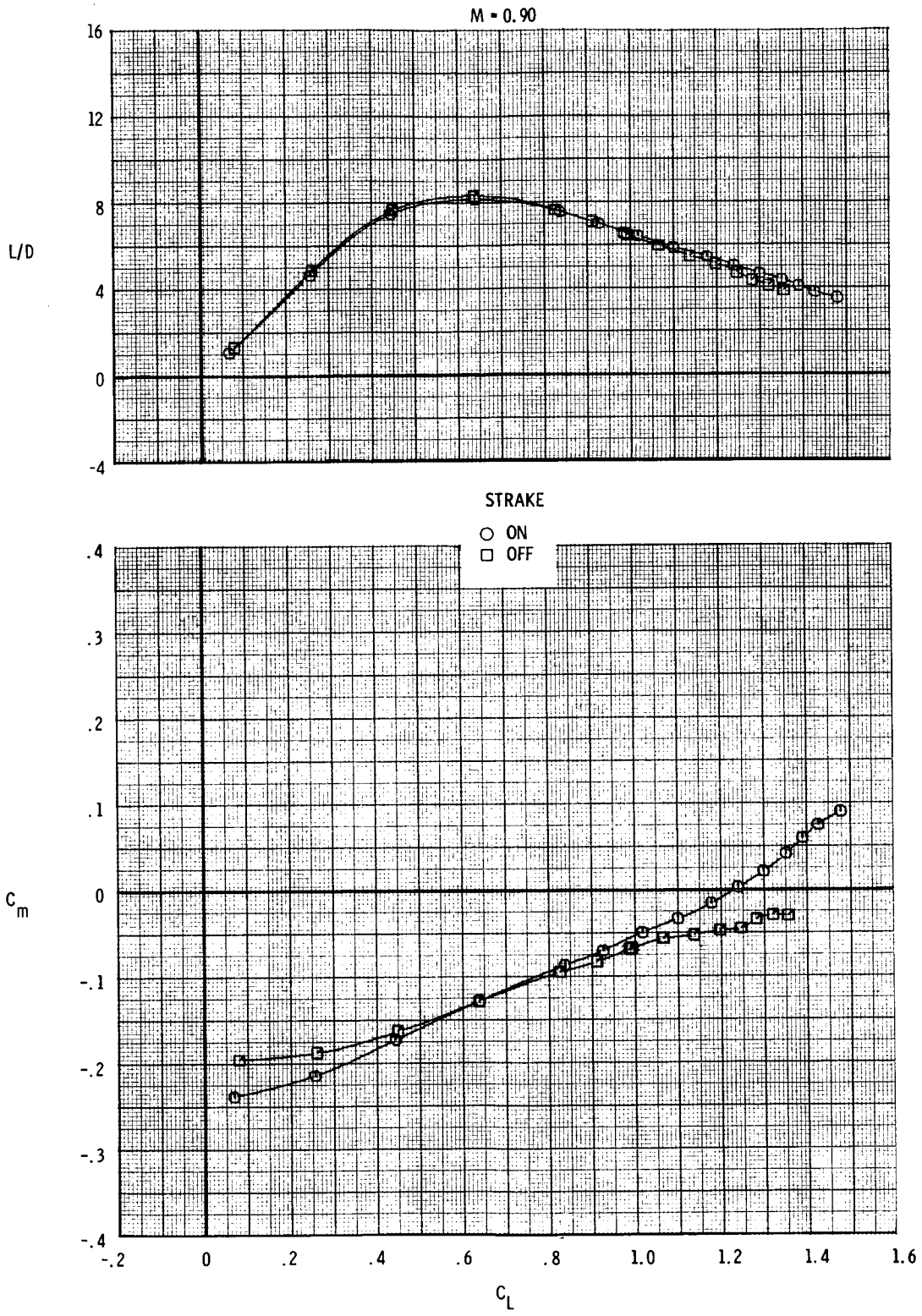

(c) Concluded.

Figure 10.- Concluded.

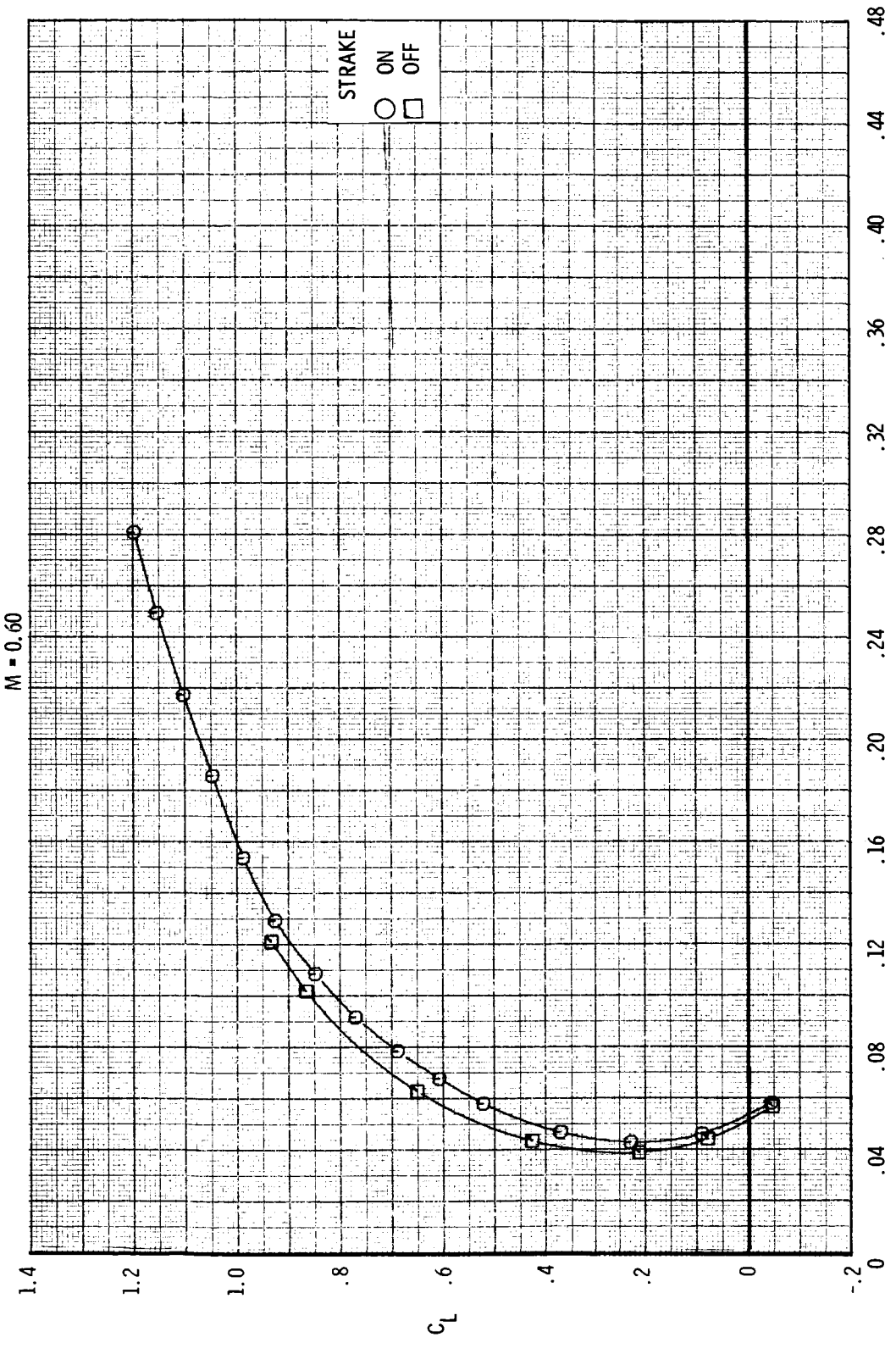

(a) Variation of C_L with C_D.

Figure 11.- Effect of strakes in combination with canards on longitudinal aerodynamic characteristics for Mach numbers of 0.60 and 0.90. $\delta_c = -10°$; $\delta_{f,TE} = \delta_{f,LE} = 0°$.

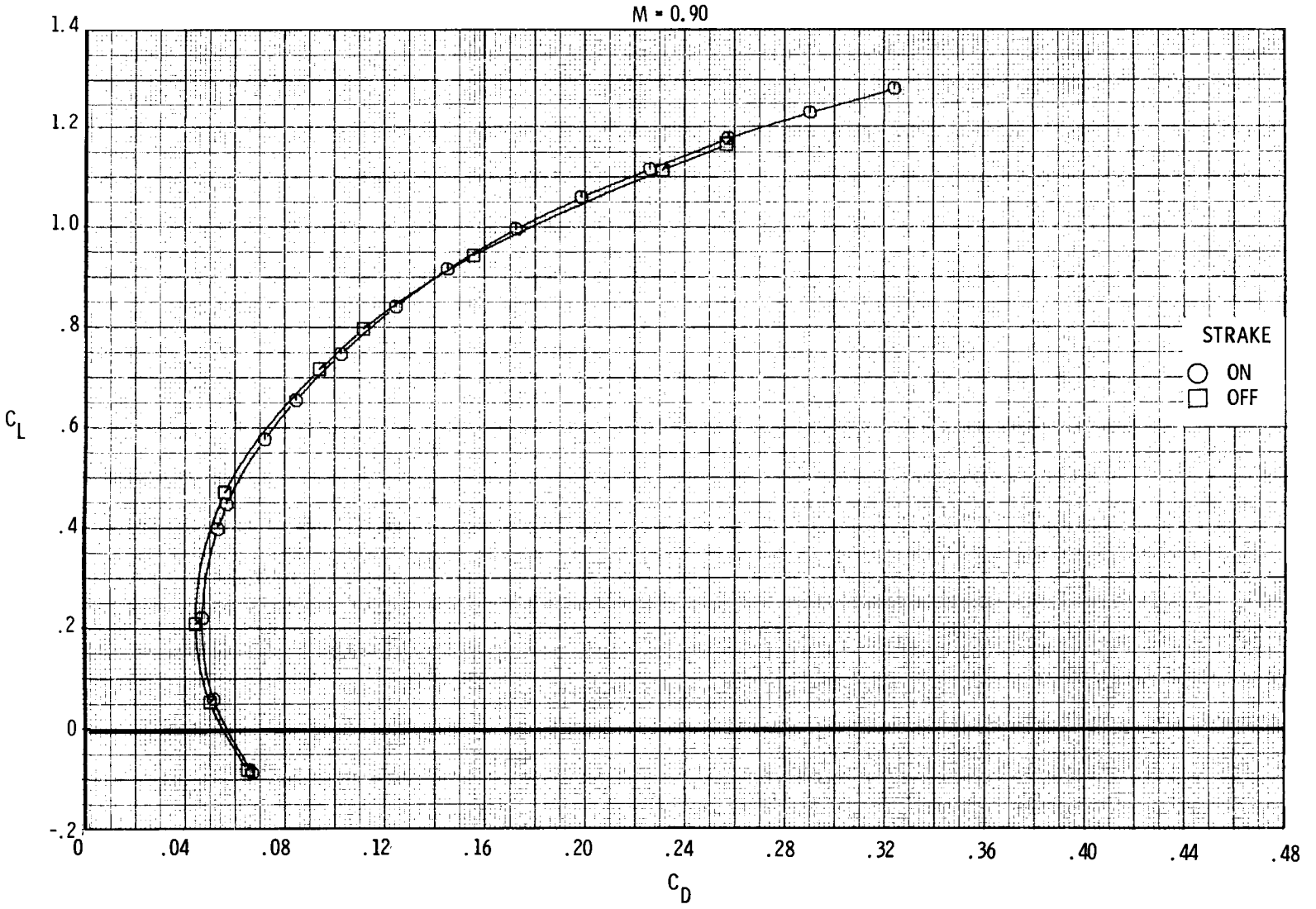

(a) Concluded.

Figure 11.- Continued.

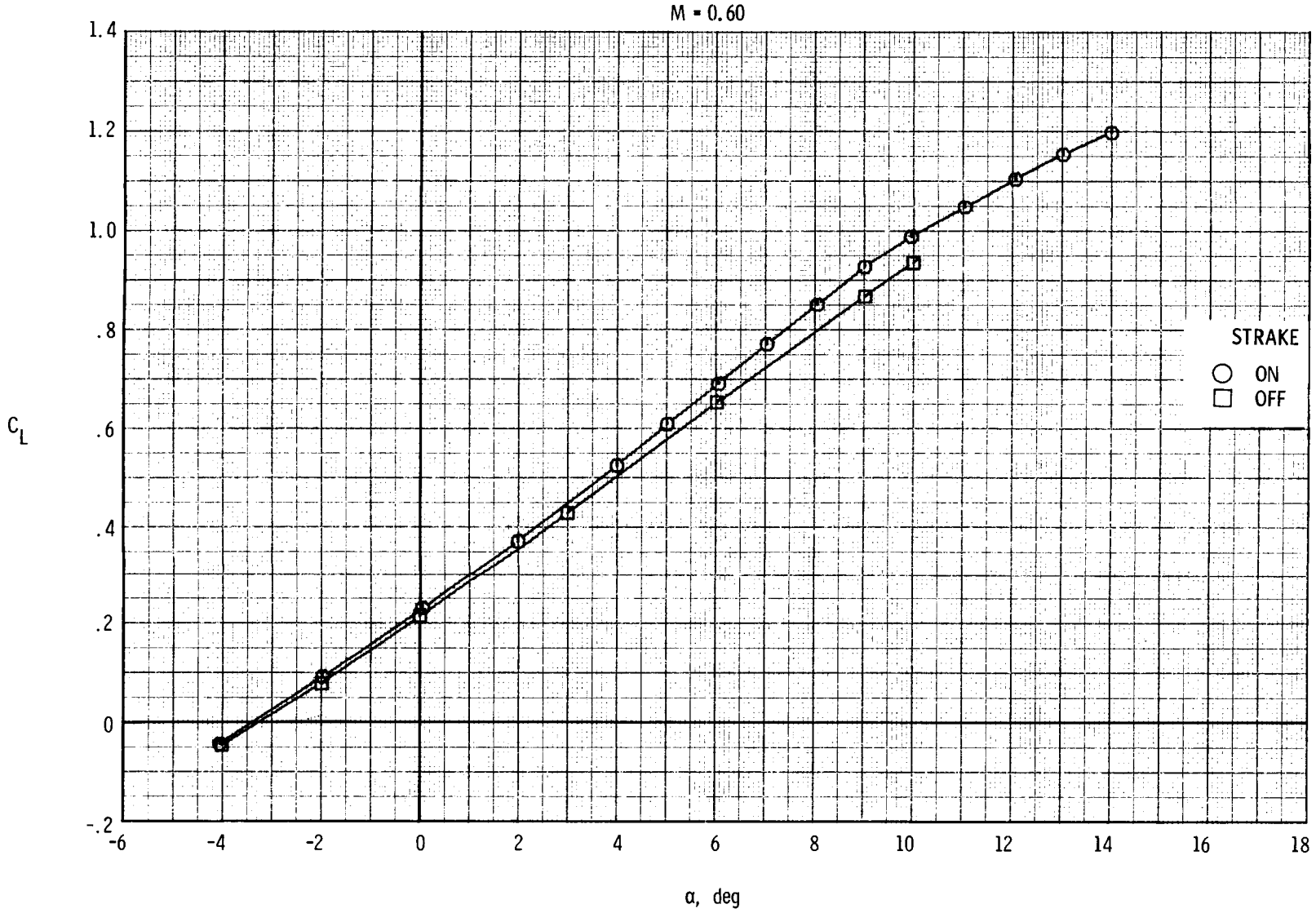

(b) Variation of C_L with α.

Figure 11.- Continued.

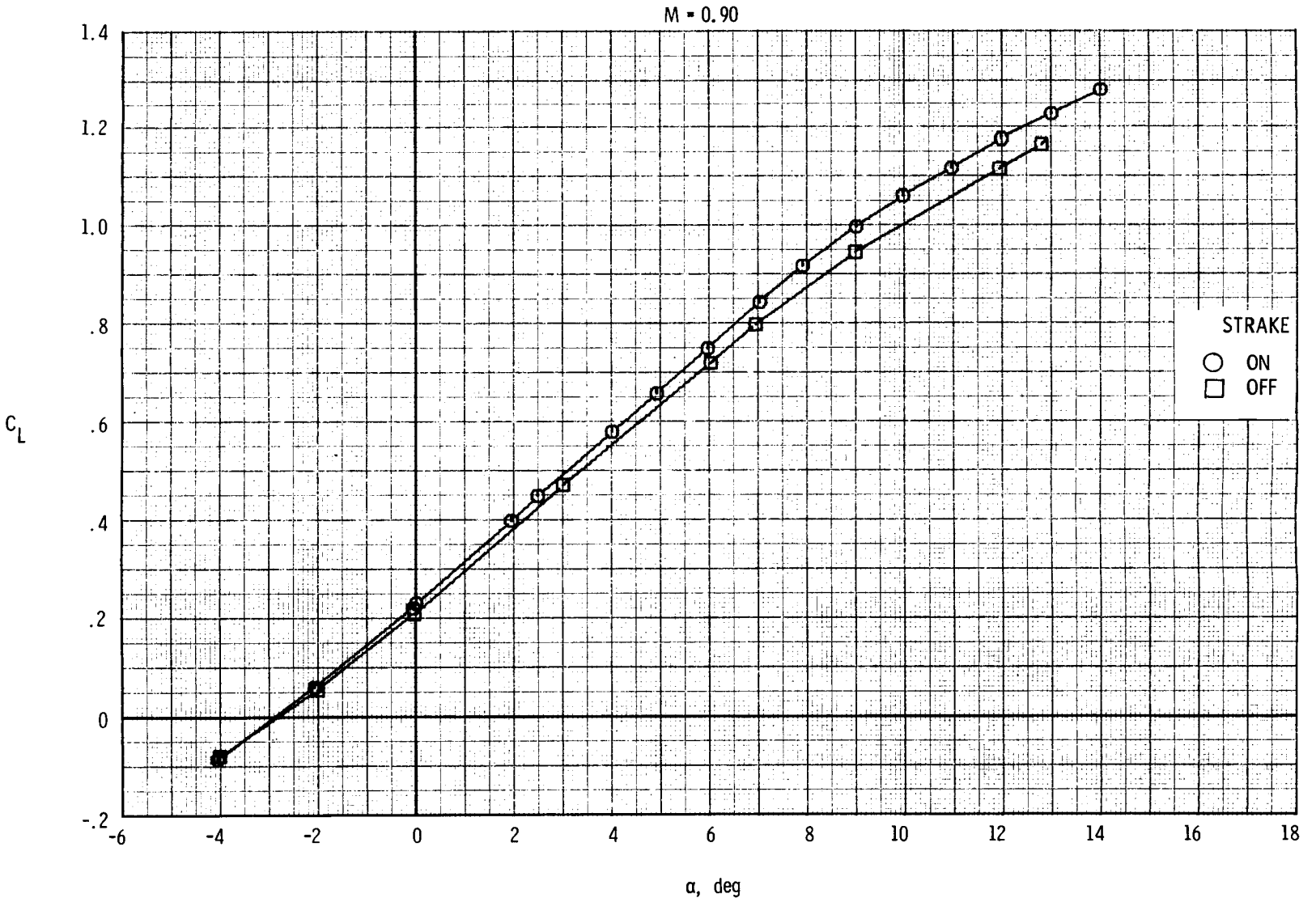

(b) Concluded.

Figure 11.- Continued.

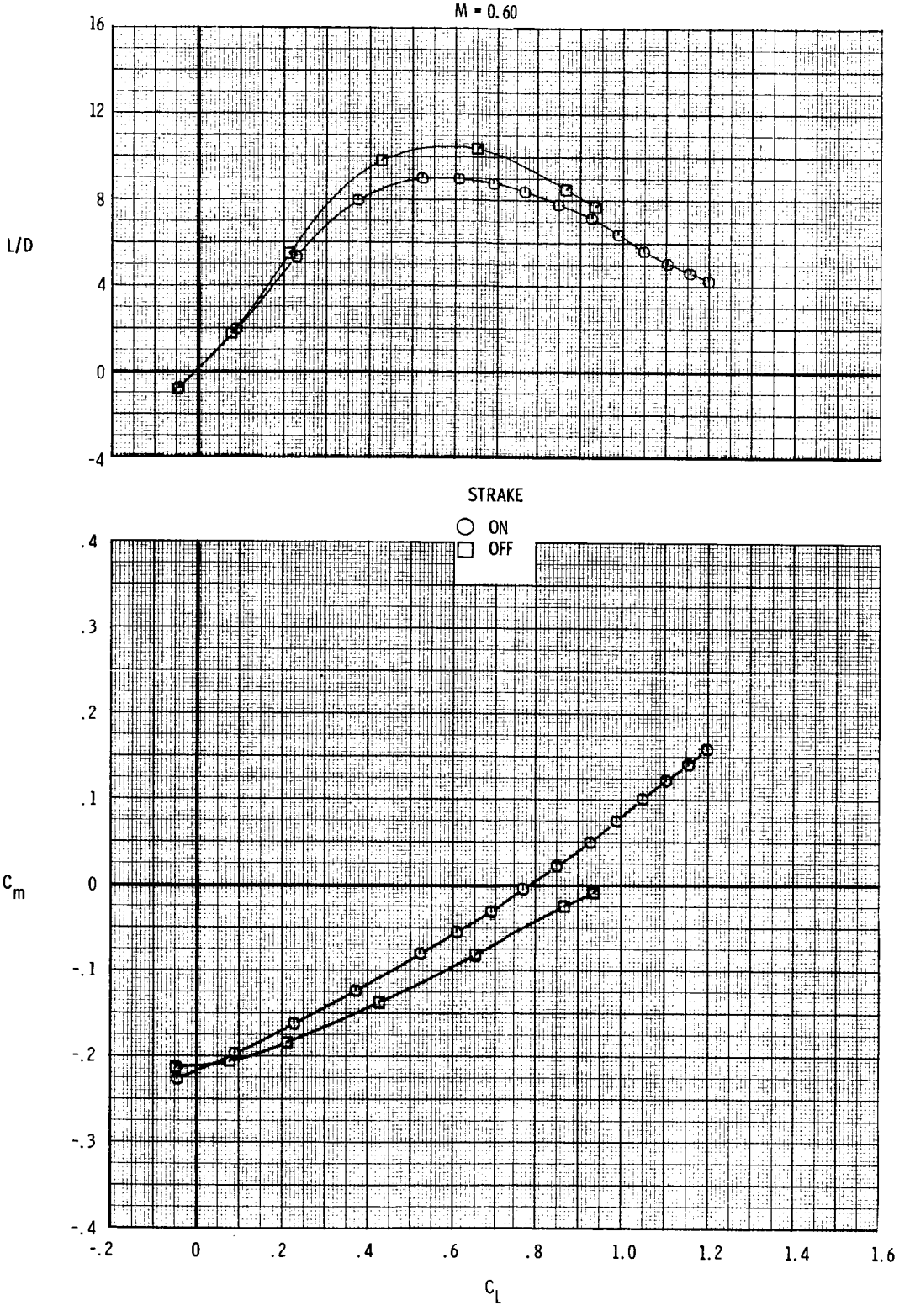

(c) Variation of L/D and C_m with C_L.

Figure 11.- Continued.

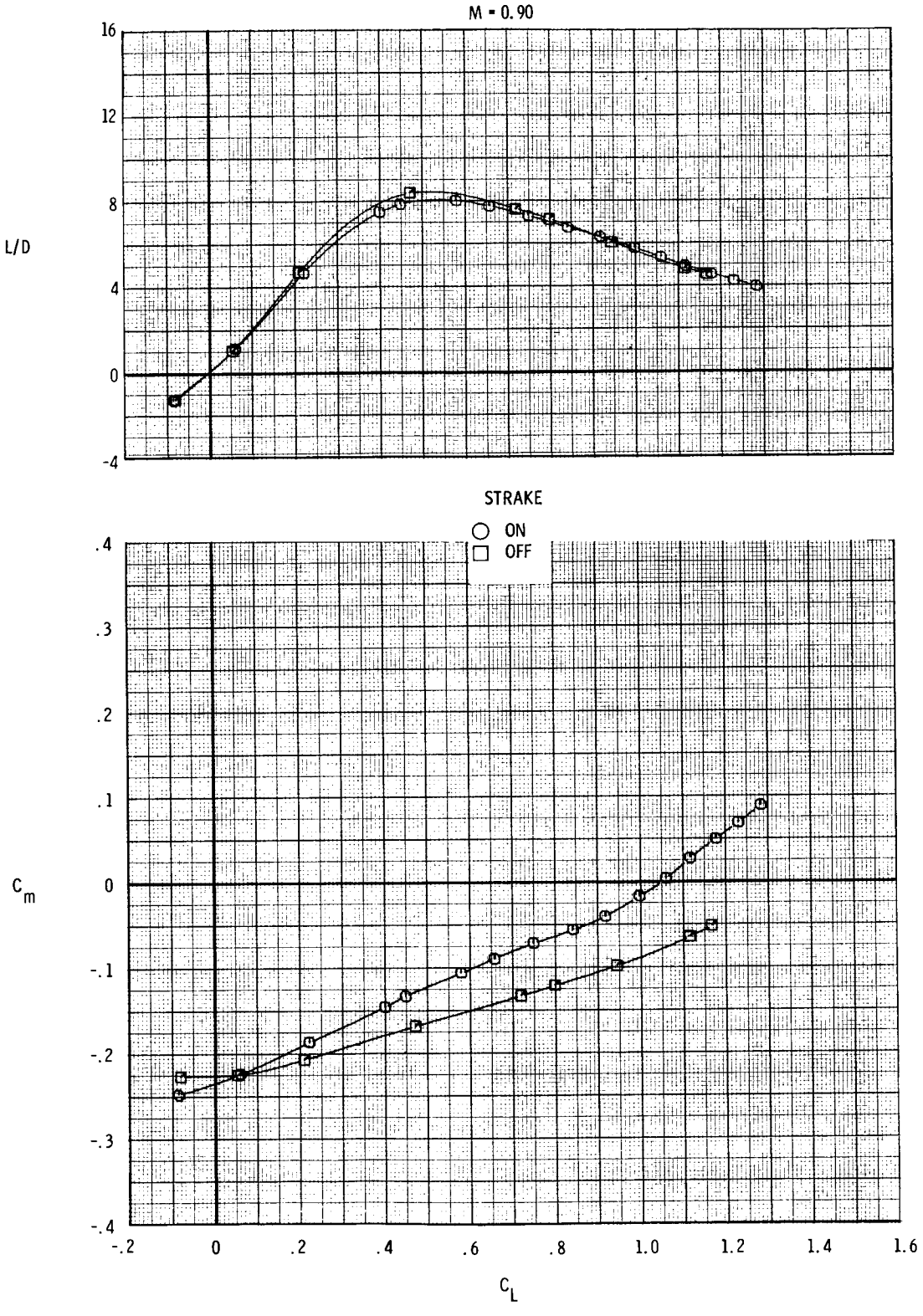

(c) Concluded.

Figure 11.- Concluded.

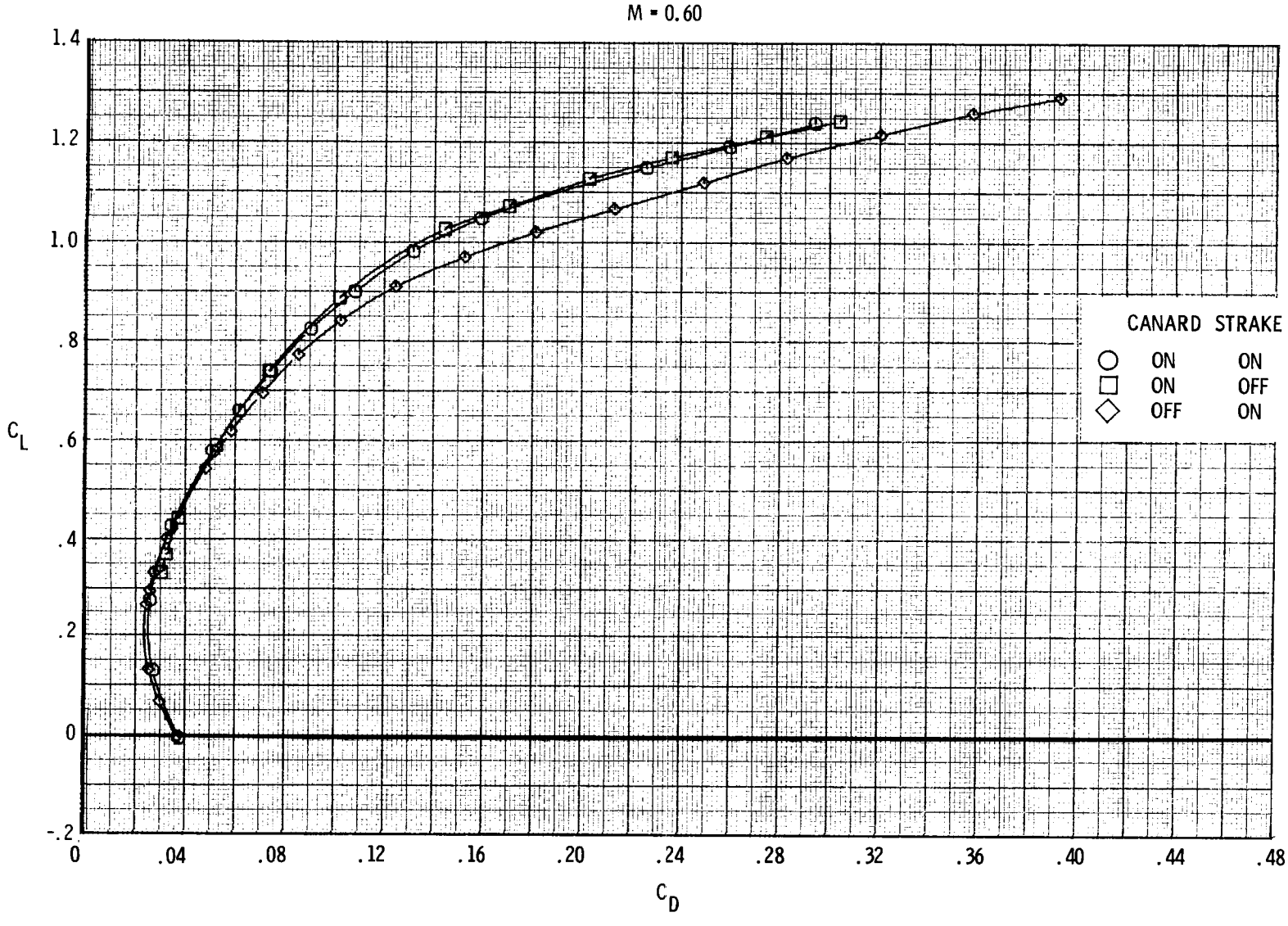

(a) Variation of C_L with C_D.

Figure 12.- Effect of strakes and canards on longitudinal aerodynamic characteristics for Mach numbers of 0.60 and 0.90. $\delta_c = 0°$; $\delta_{f,TE} = \delta_{f,LE} = 0°$.

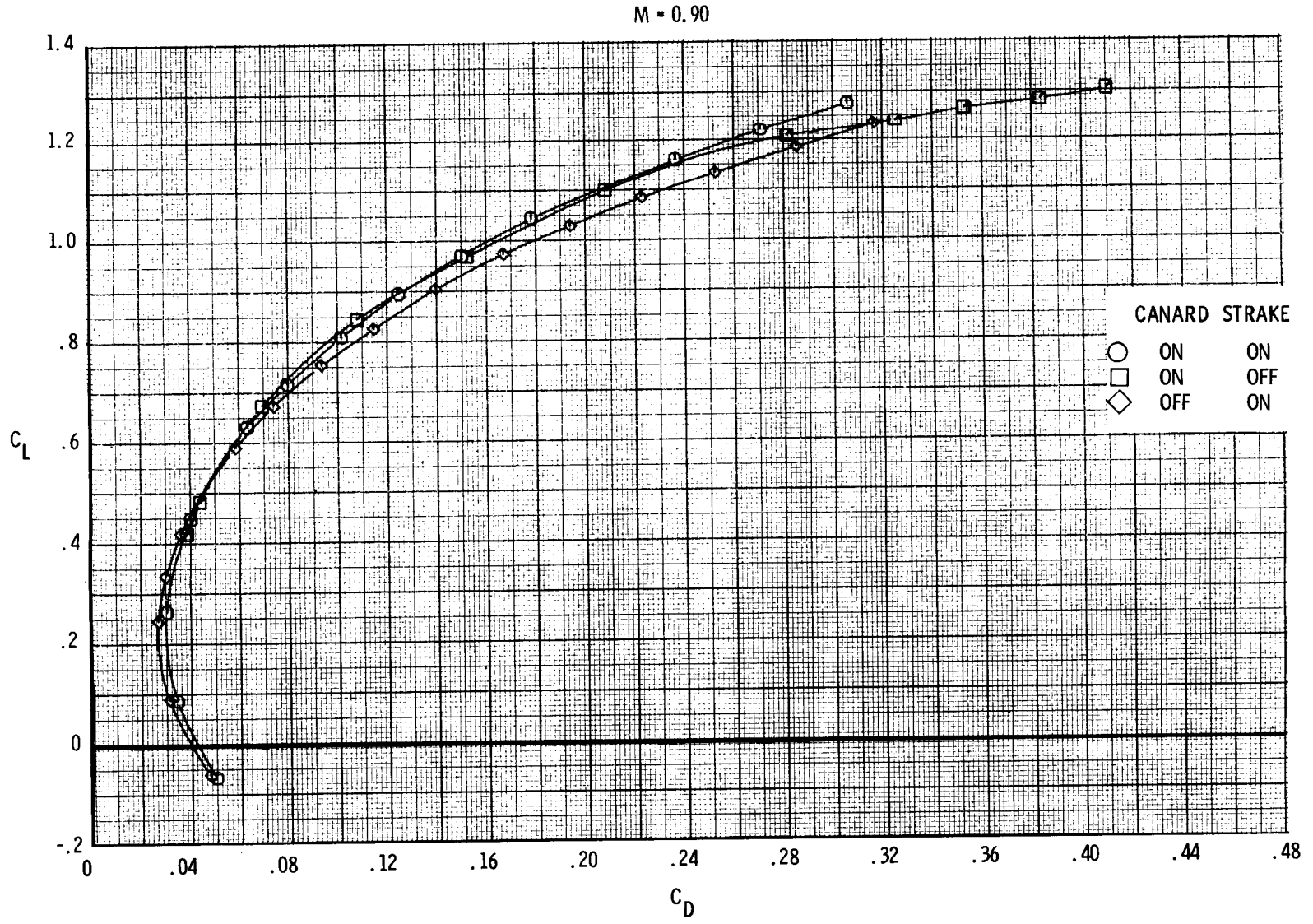

(a) Concluded.

Figure 12.- Continued.

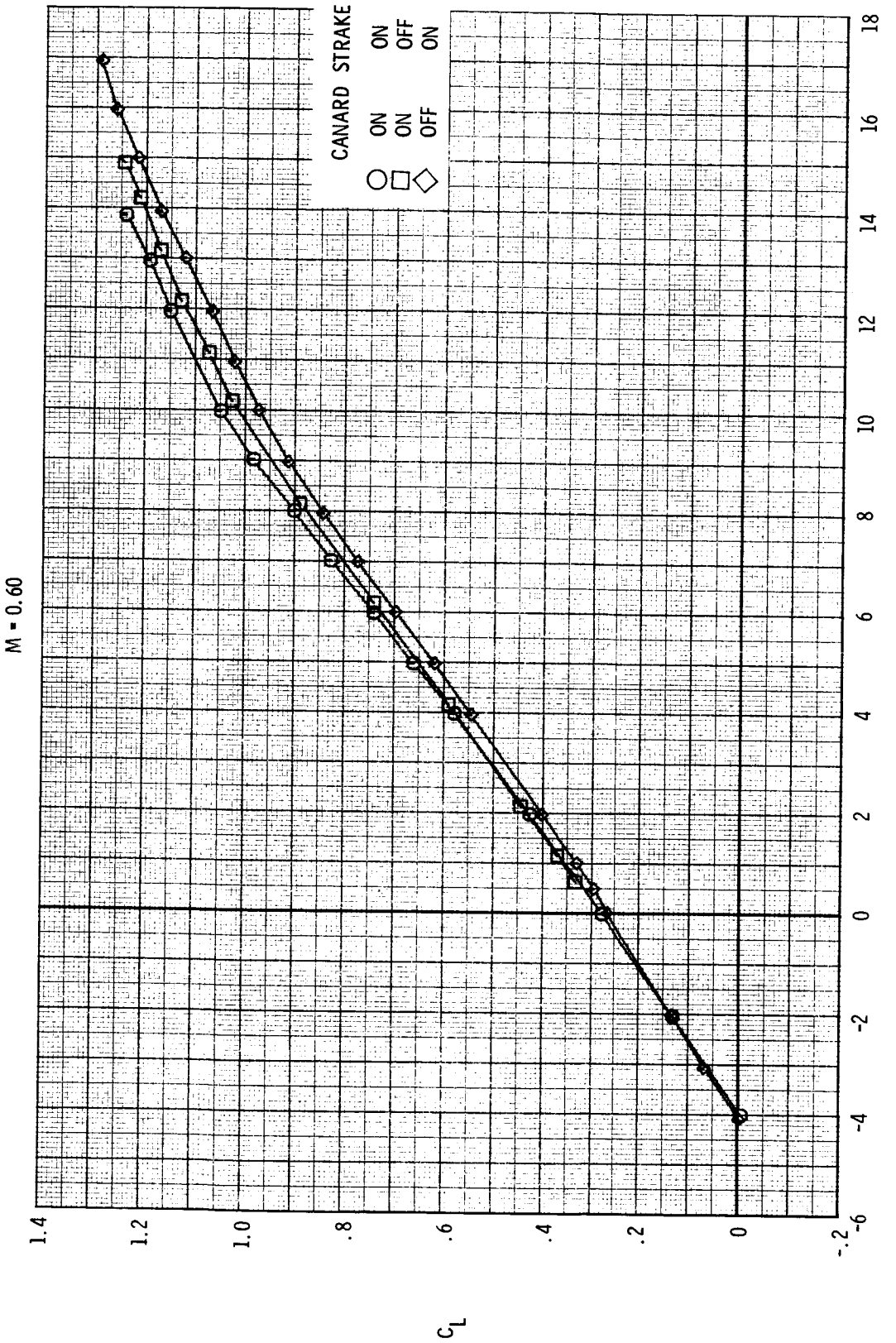

(b) Variation of C_L with α.

Figure 12.- Continued.

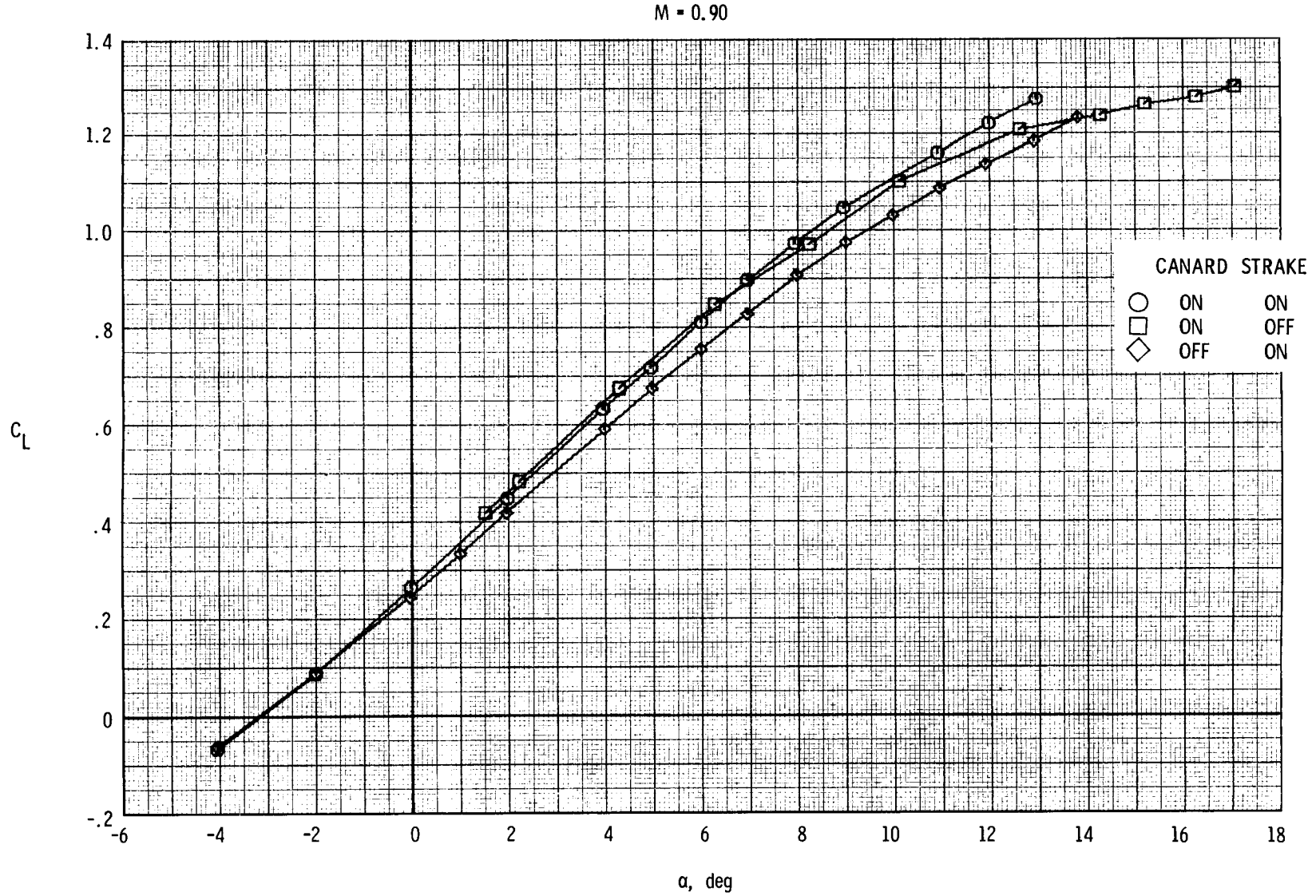

(b) Concluded.

Figure 12.- Continued.

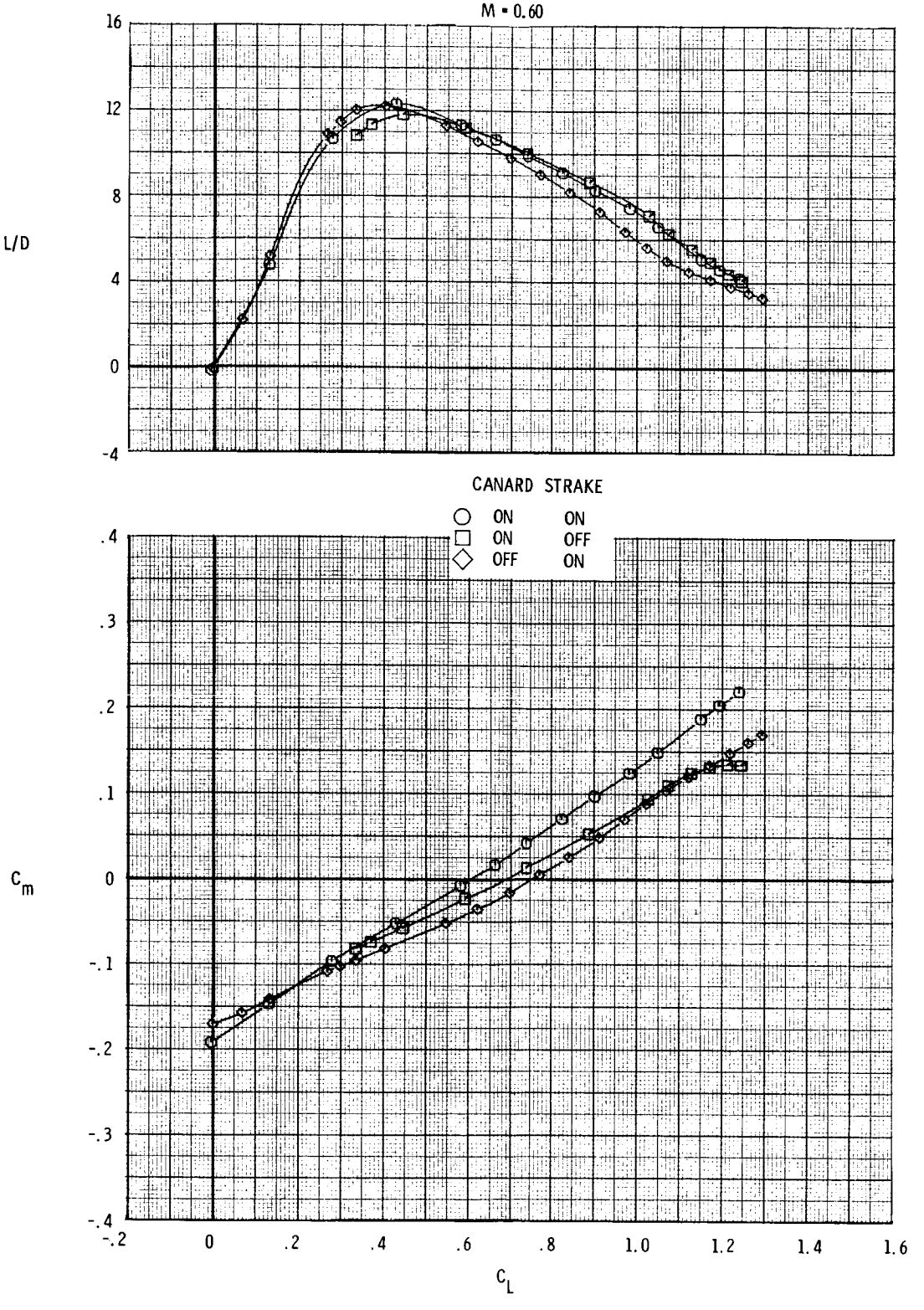

(c) Variation of L/D and C_m with C_L.

Figure 12.- Continued.

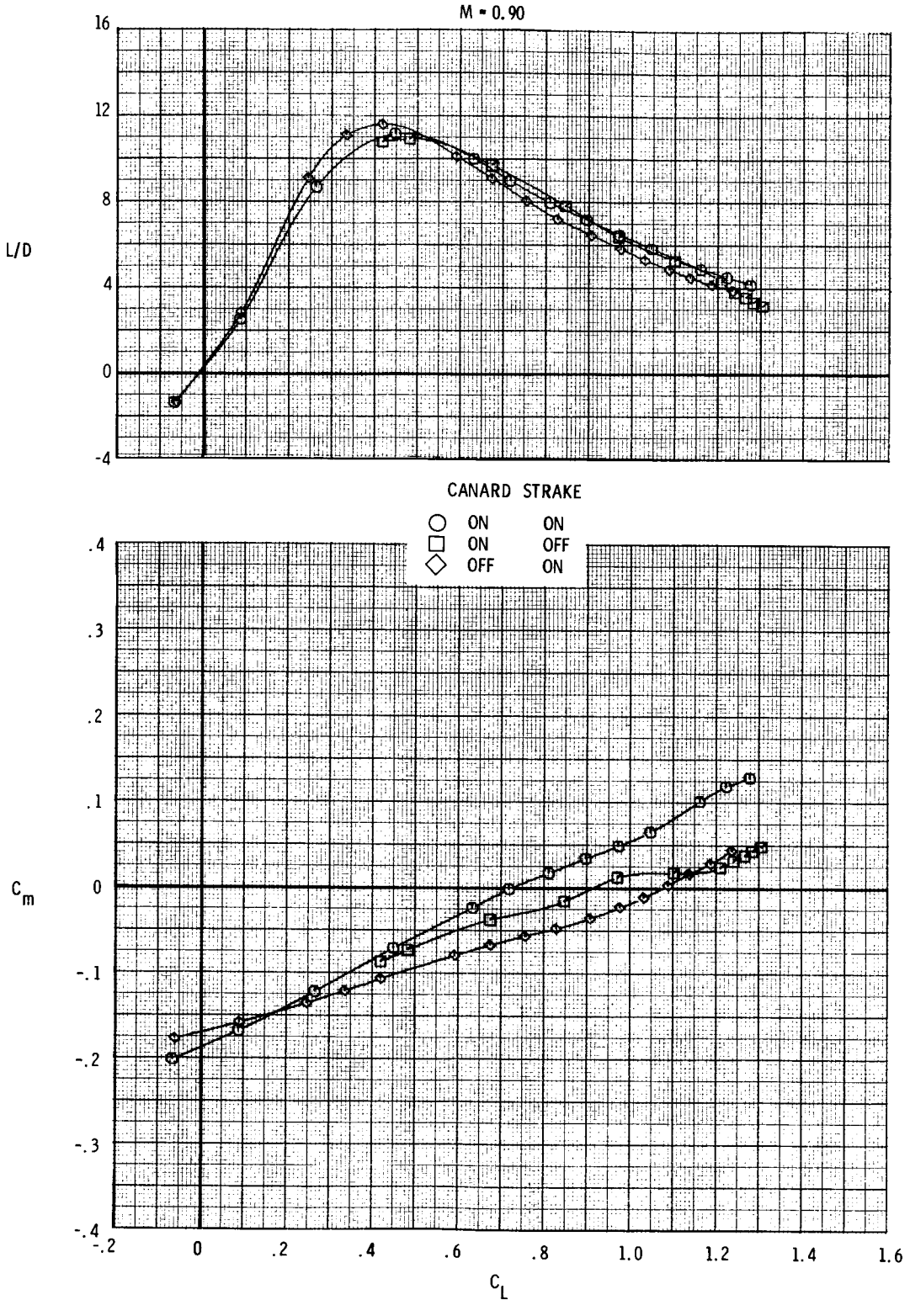

(c) Concluded.

Figure 12.- Concluded.

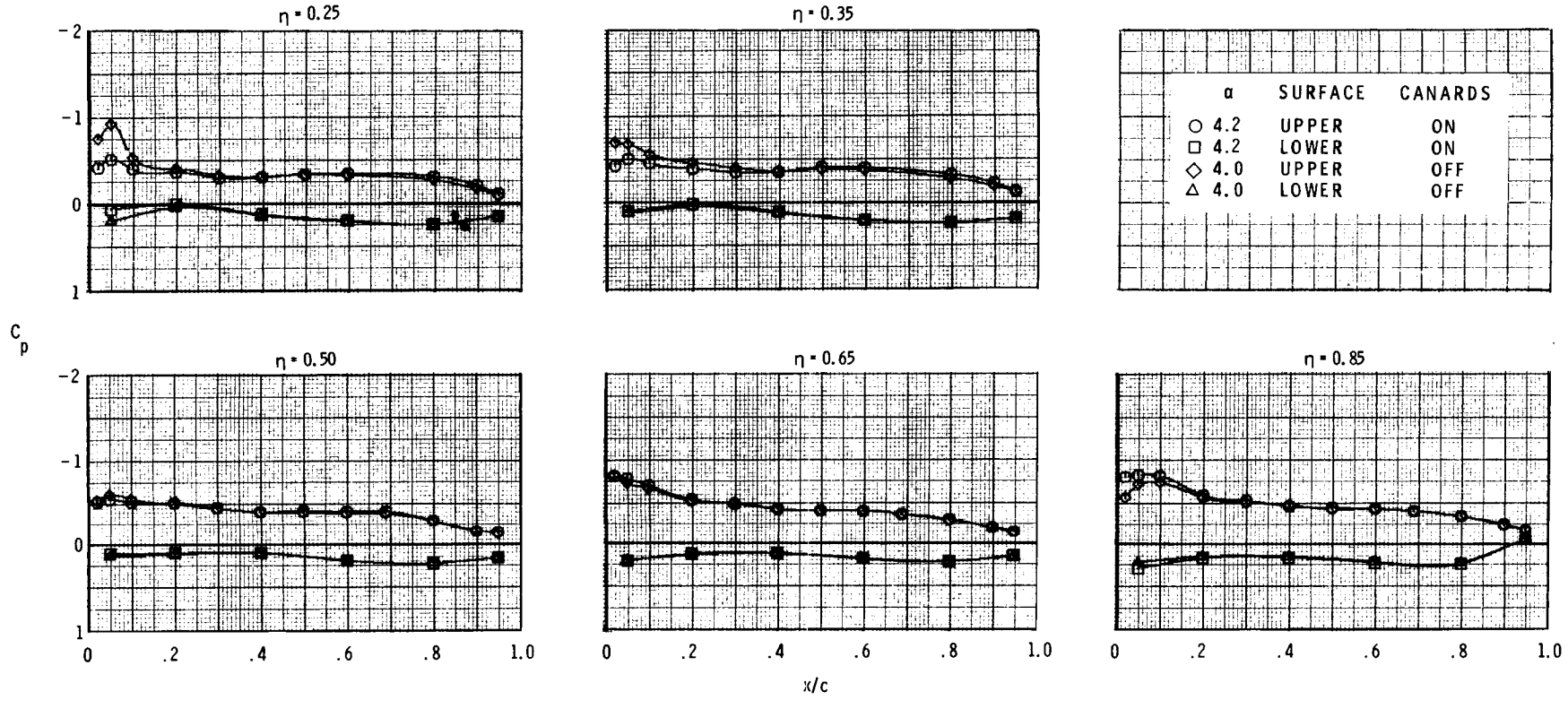

(a) M = 0.60; $\alpha \approx 4°$.

Figure 13.- Effect of canards on wing upper and lower surface pressure distributions. Strakes off; $\delta_c = 0°$; $\delta_{f,TE} = \delta_{f,LE} = 0°$.

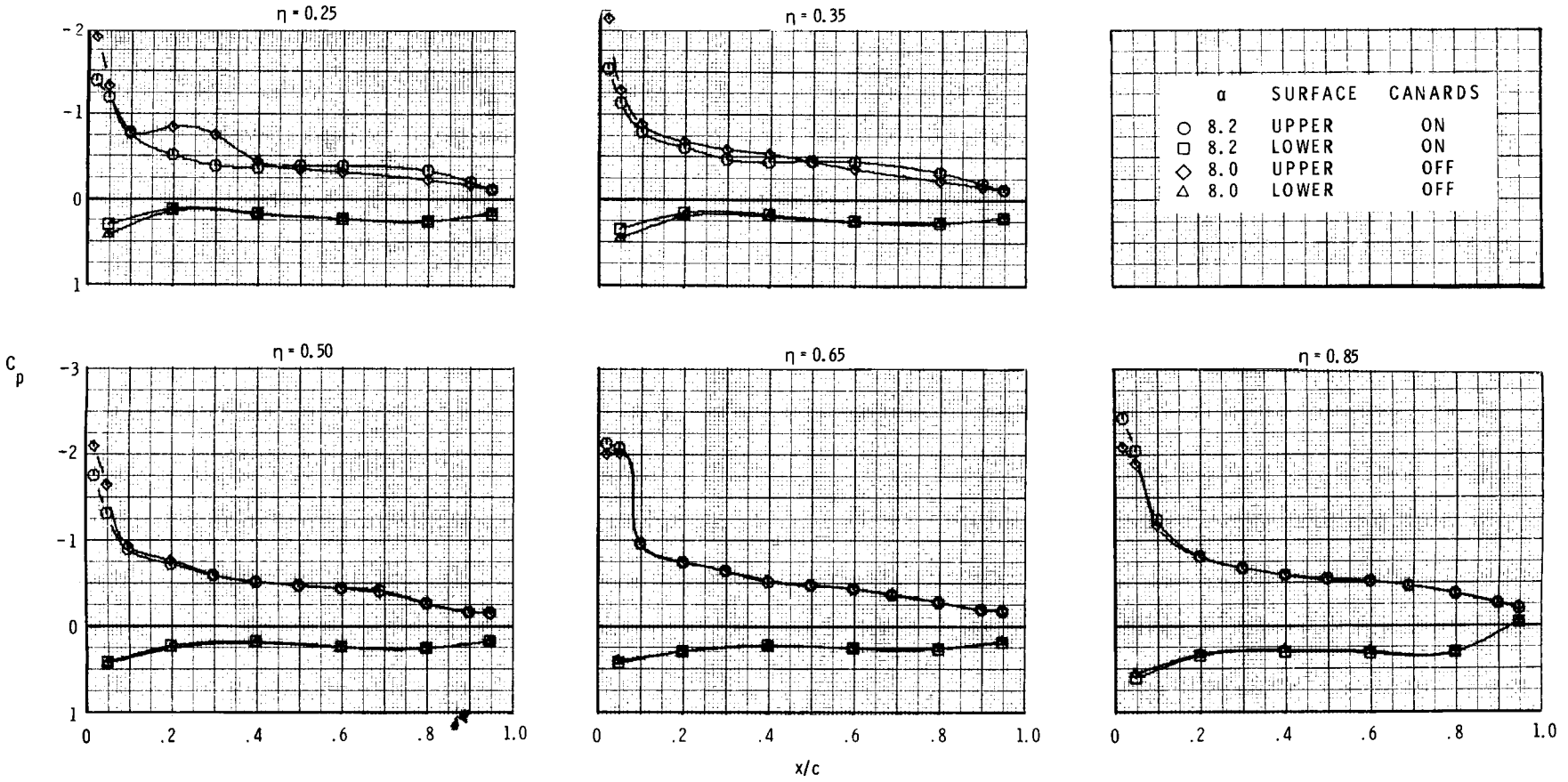

(b) M = 0.60; $\alpha \approx 8°$.

Figure 13.- Continued.

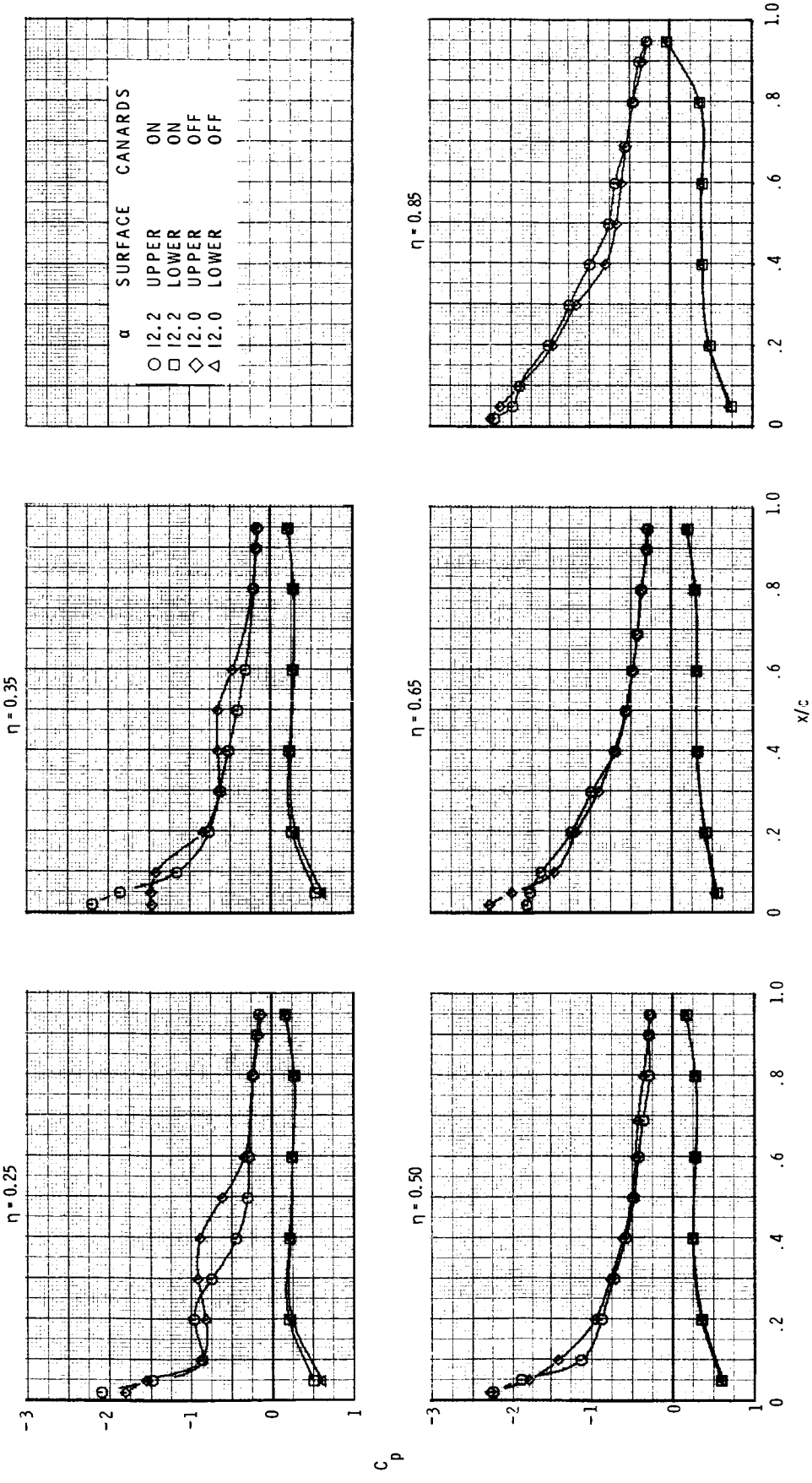

(c) M = 0.60; $\alpha \approx 12°$.

Figure 13.- Continued.

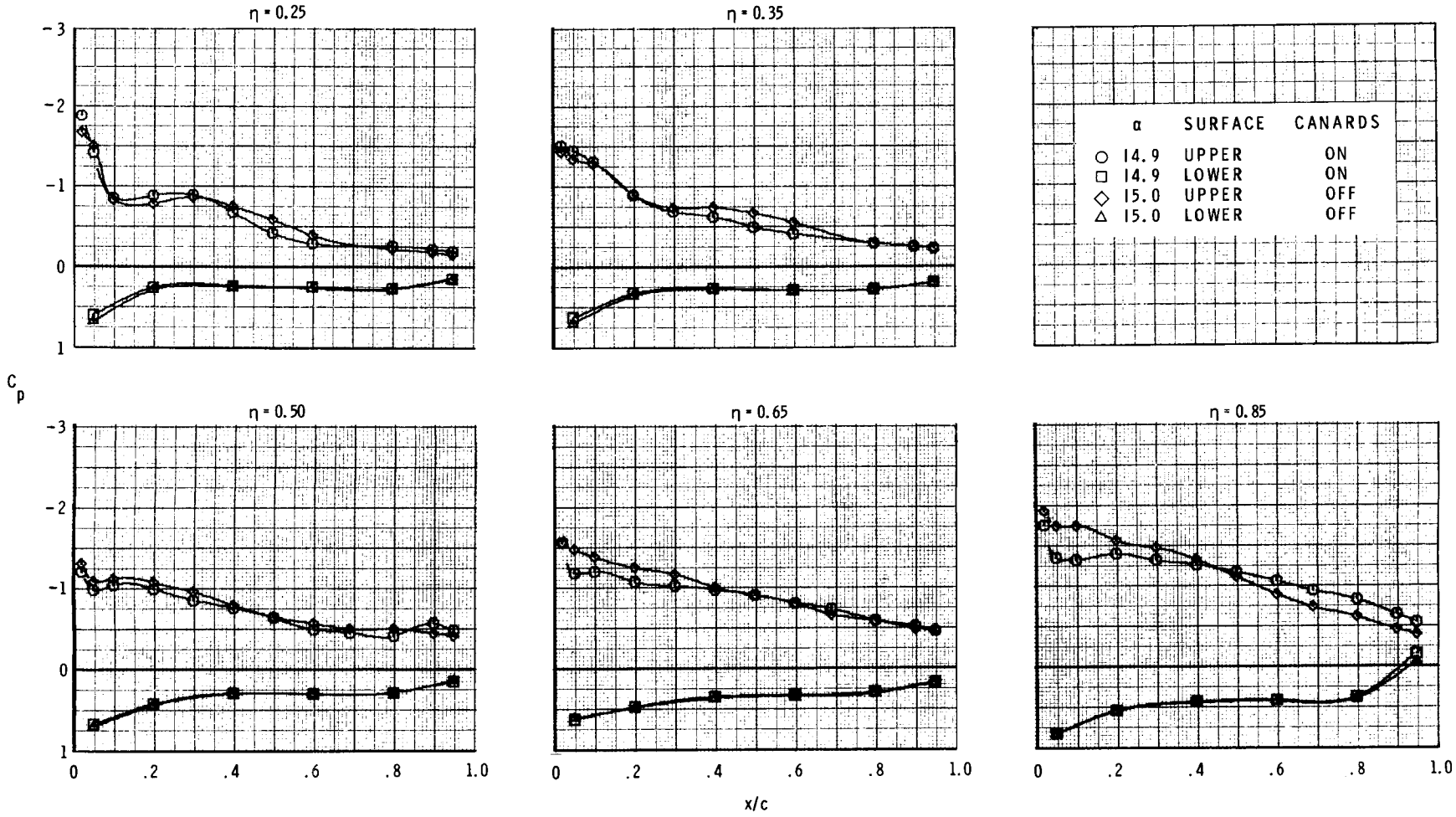

(d) M = 0.60; $\alpha \approx 15°$.

Figure 13.- Continued.

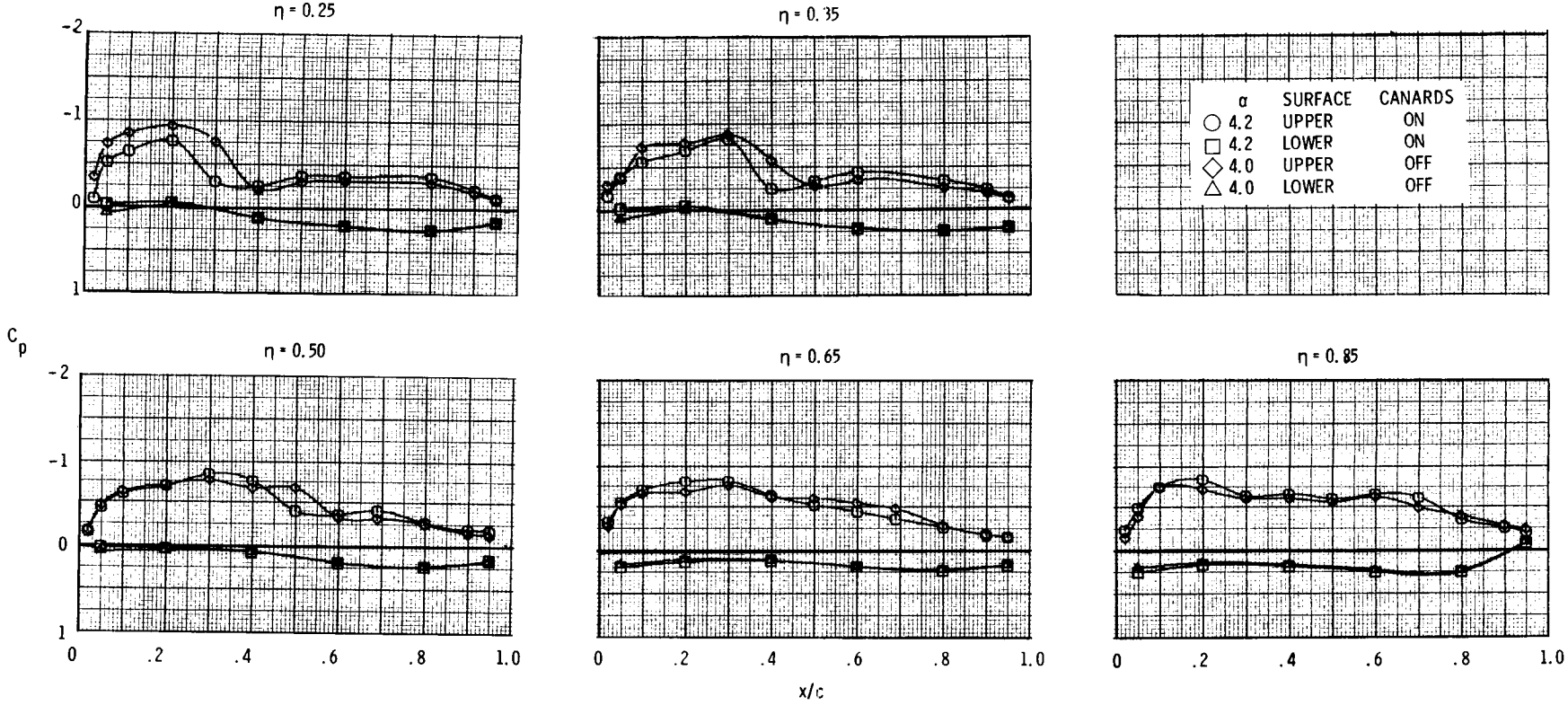

(e) M = 0.85; $\alpha \approx 4°$.

Figure 13.- Continued.

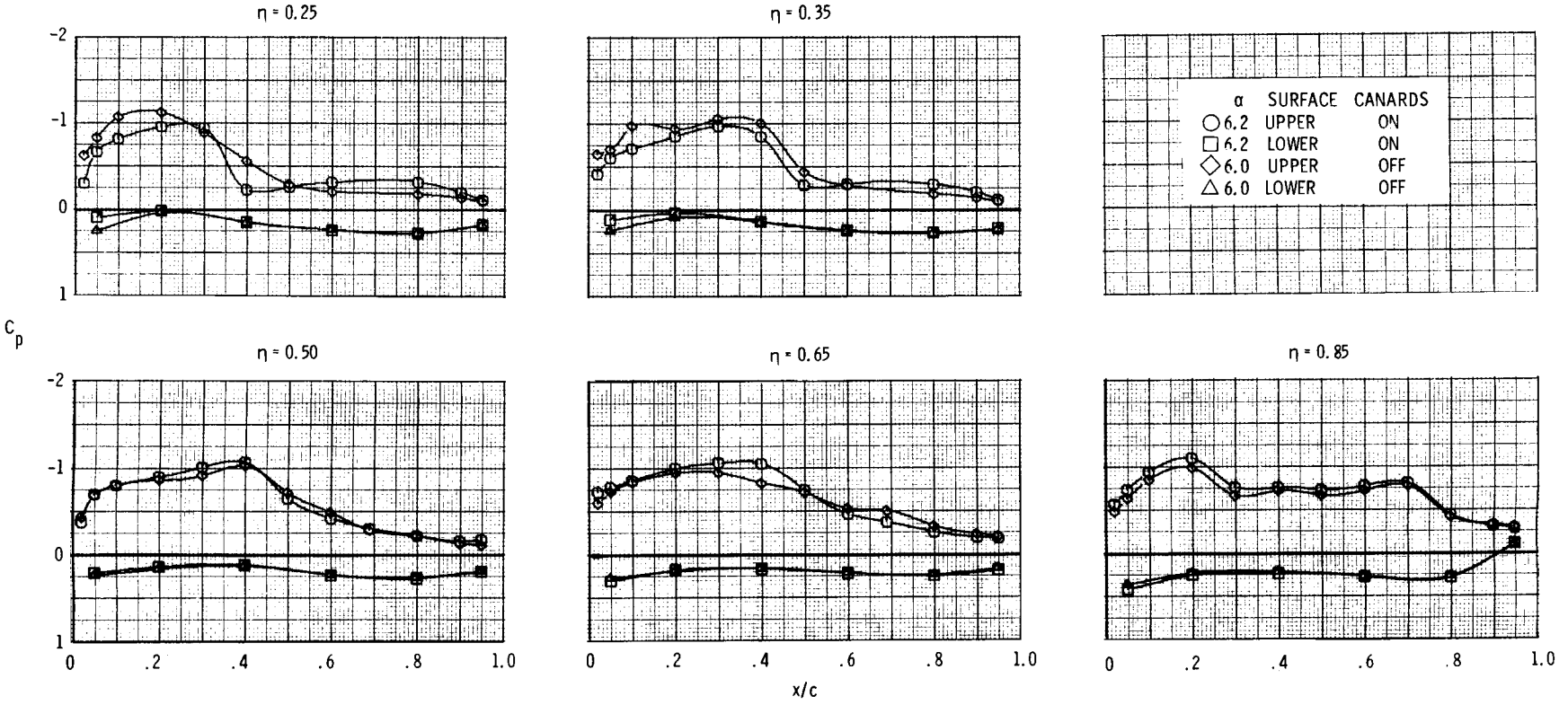

(f) M = 0.85; $\alpha \approx 6°$.

Figure 13.- Continued.

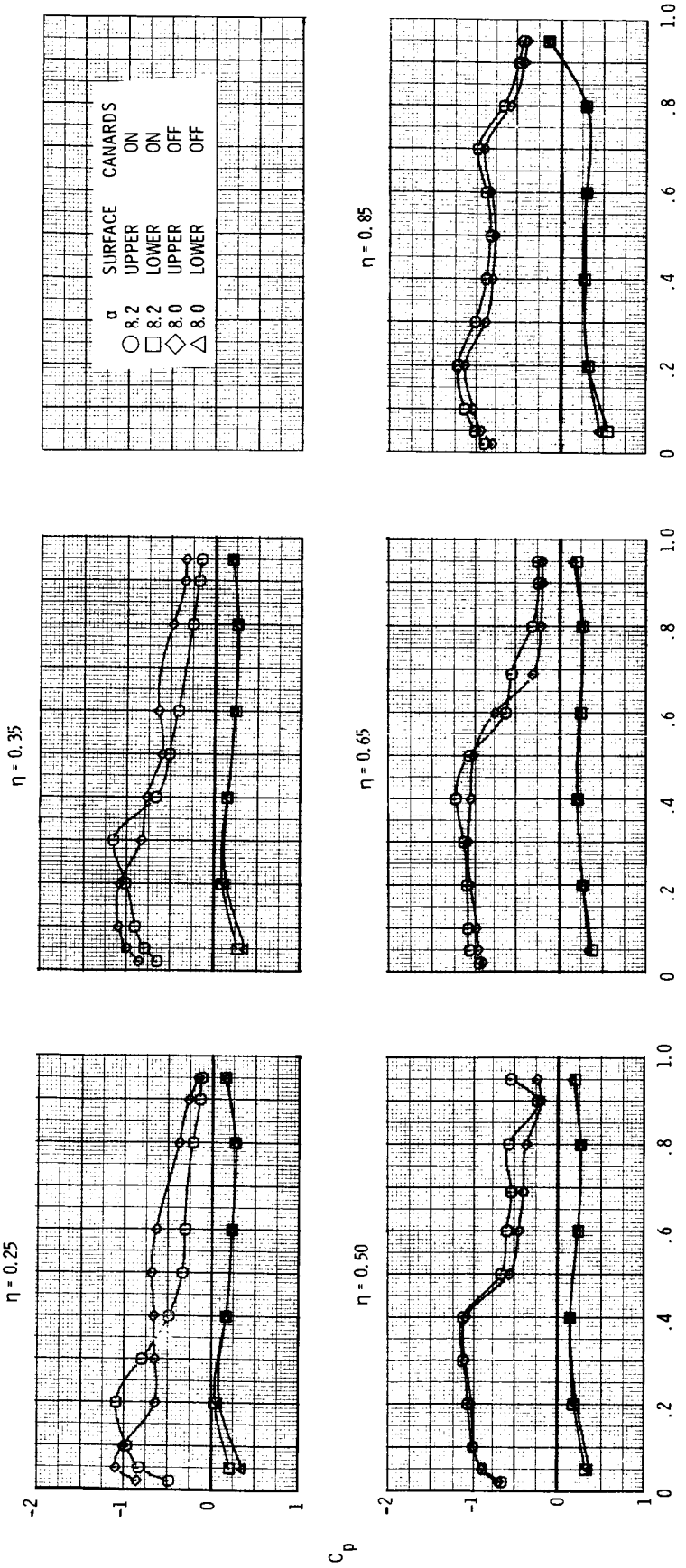

(g) M = 0.85; $\alpha \approx 8°$.

Figure 13.- Continued.

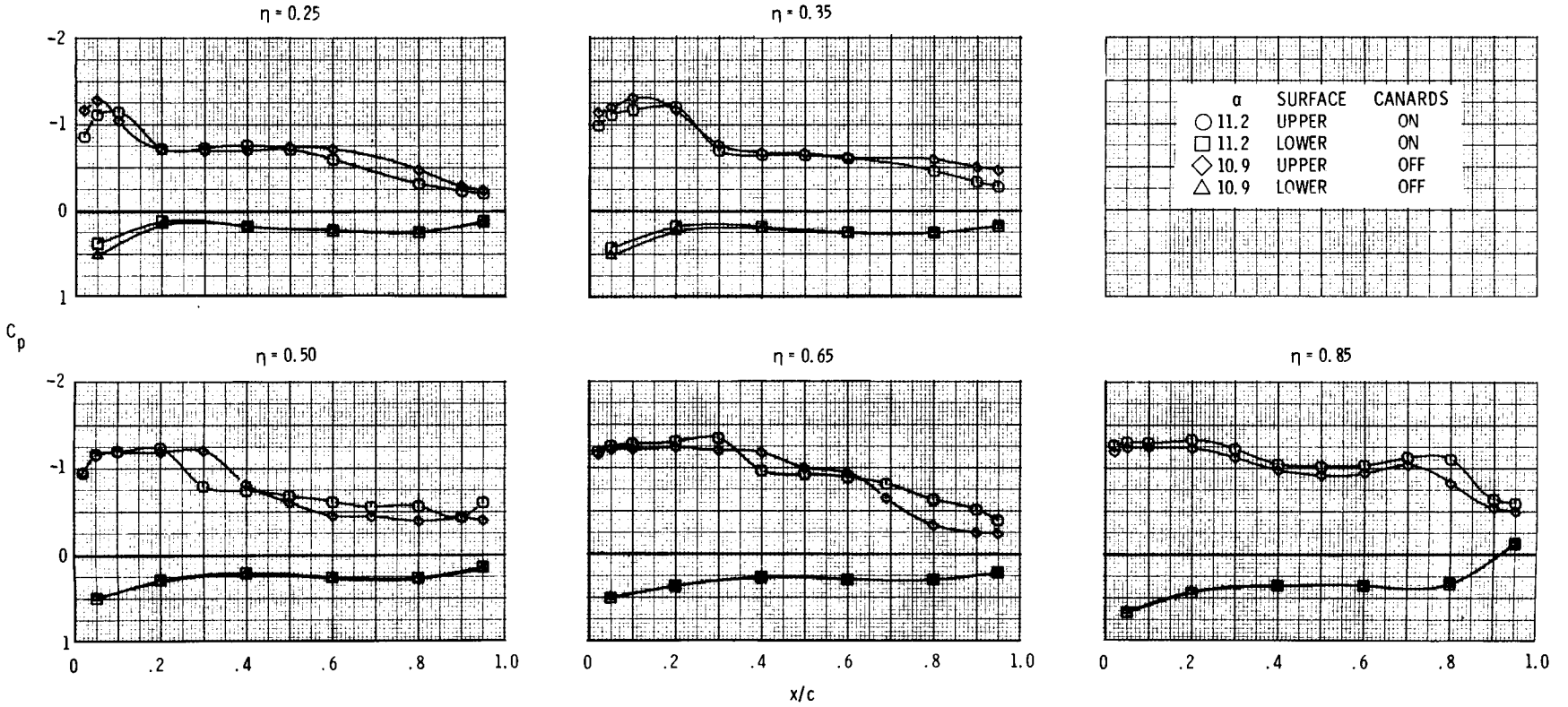

(h) M = 0.85; $\alpha \approx 11°$.

Figure 13.- Continued.

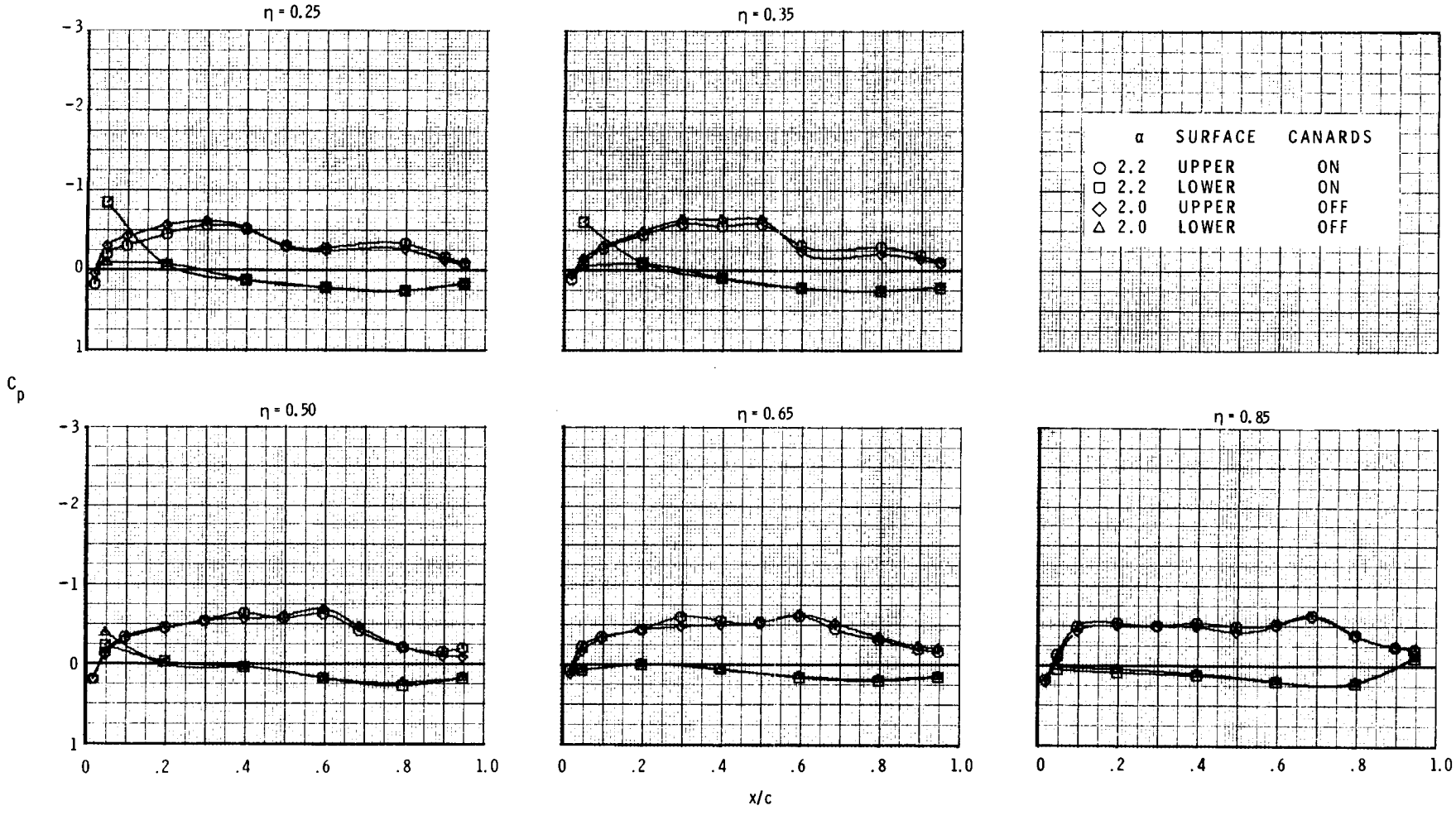

(i) M = 0.90; $\alpha \approx 2°$.

Figure 13.- Continued.

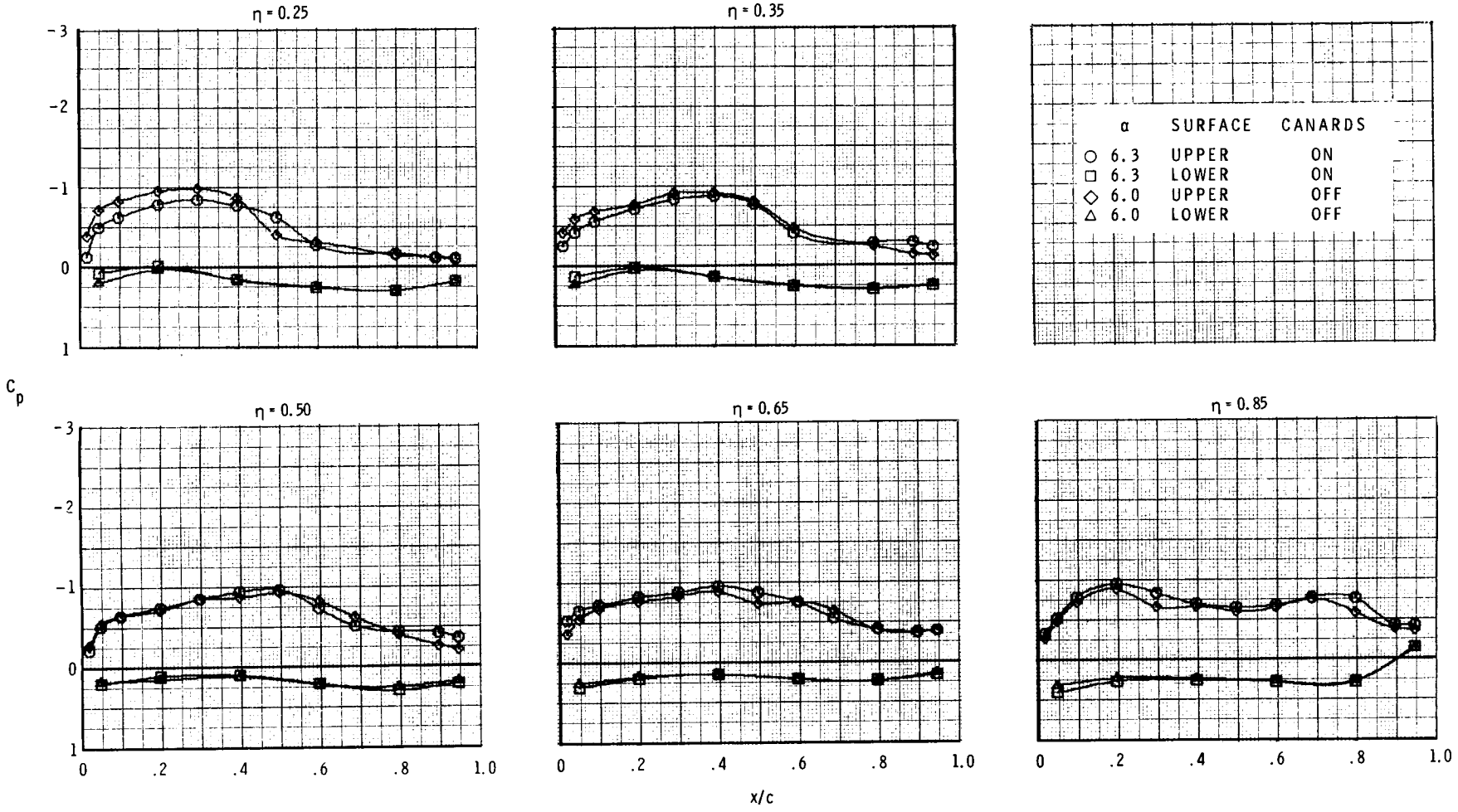

(j) M = 0.90; $\alpha \approx 6°$.

Figure 13.- Continued.

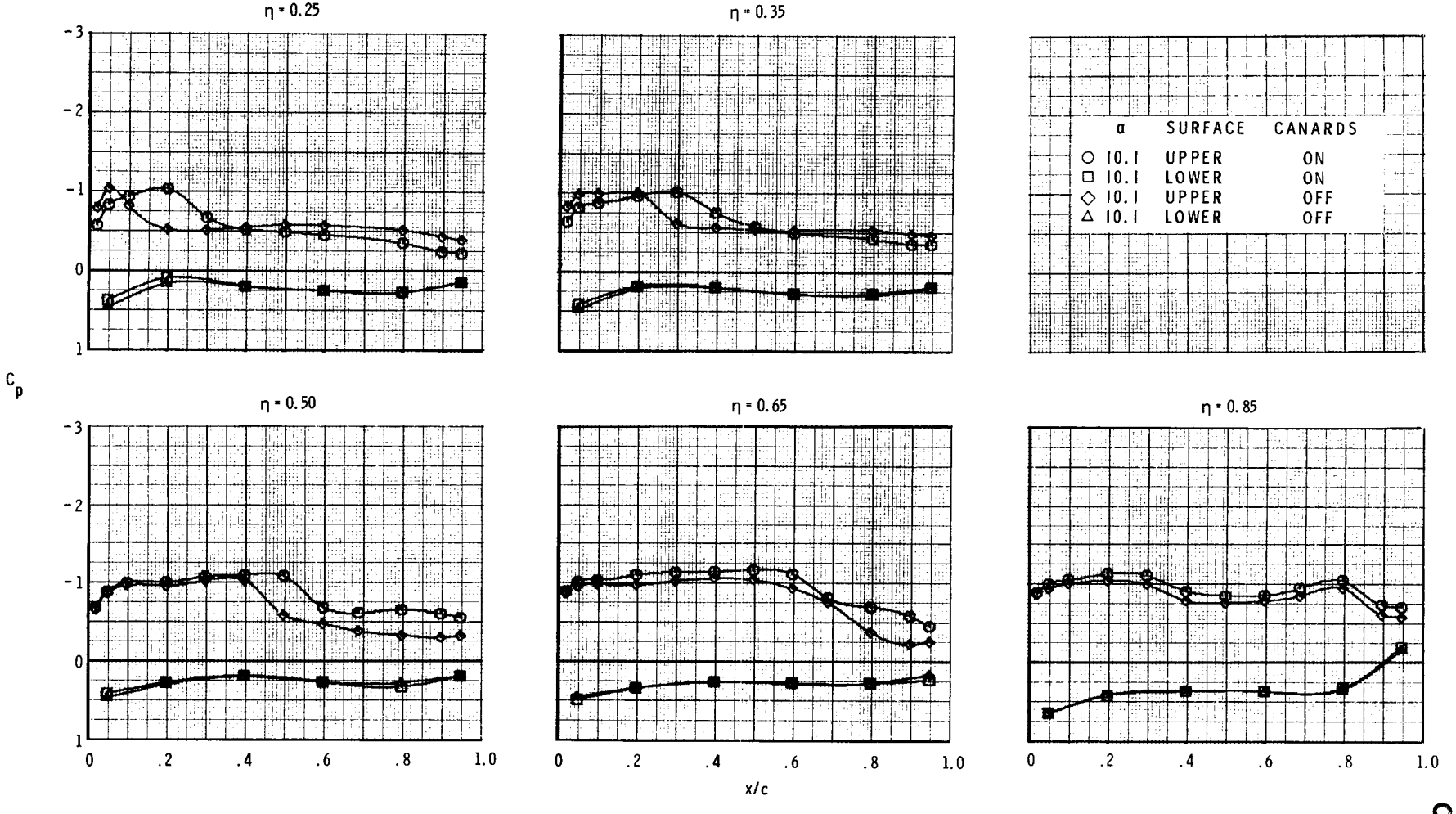

(k) M = 0.90; $\alpha \approx 10°$.

Figure 13.- Continued.

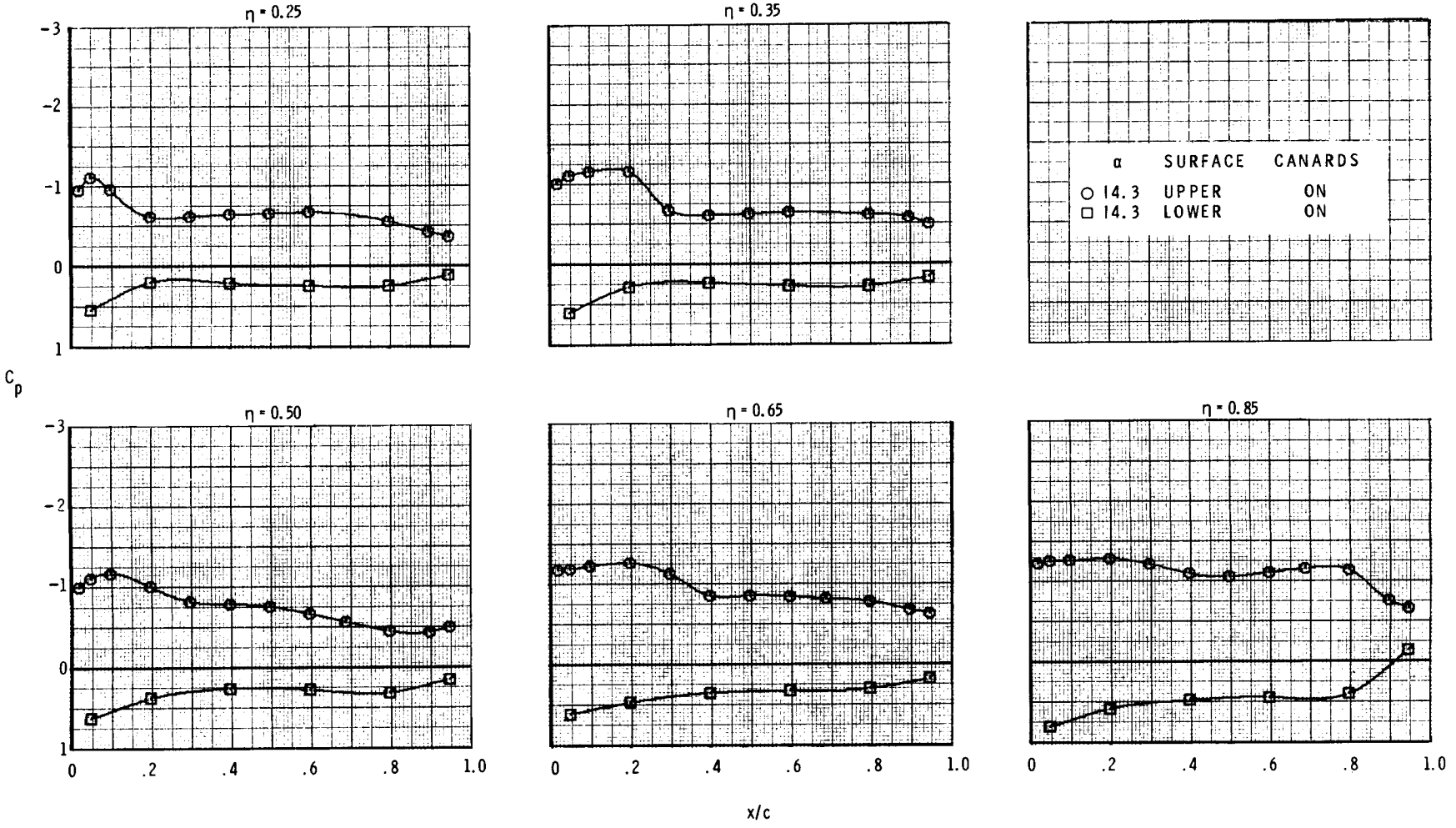

(l) M = 0.90; $\alpha \approx 14°$.

Figure 13.- Concluded.

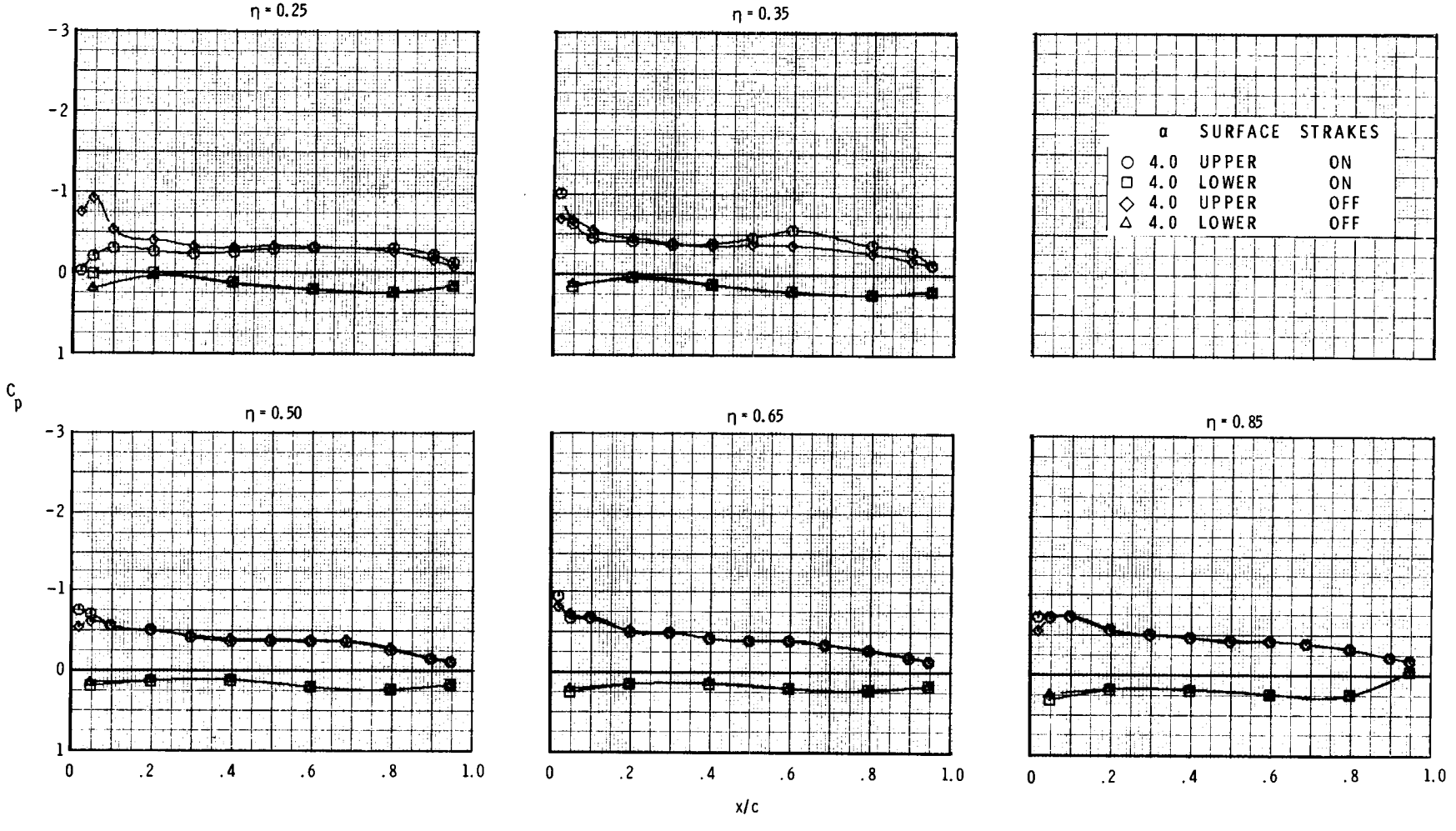

(a) M = 0.60; $\alpha \approx 4°$.

Figure 14.- Effect of strakes on wing upper and lower surface pressure distributions. Canards off; $\delta_{f,TE} = \delta_{f,LE} = 0°$.

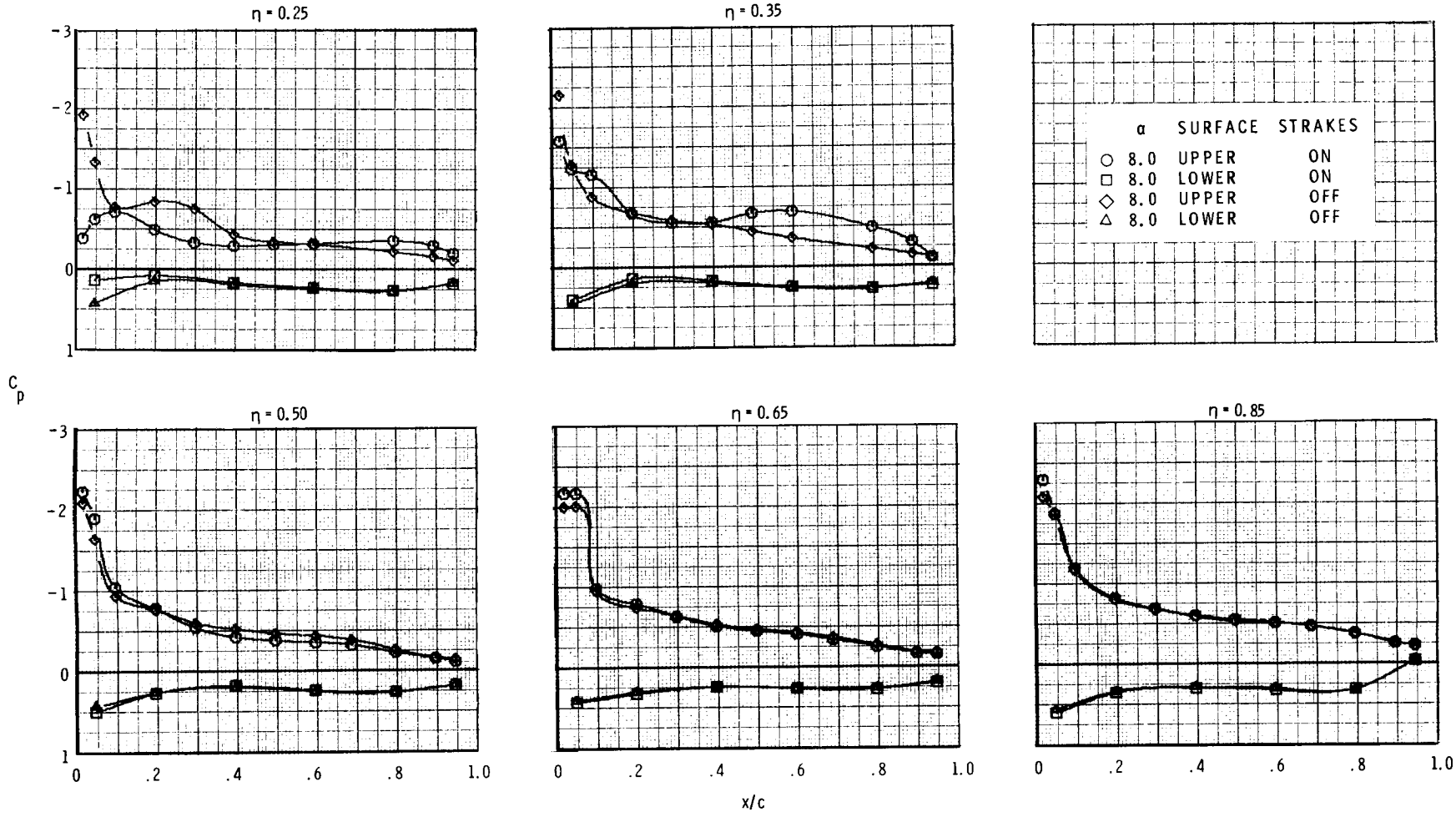

(b) M = 0.60; $\alpha \approx 8°$.

Figure 14.- Continued.

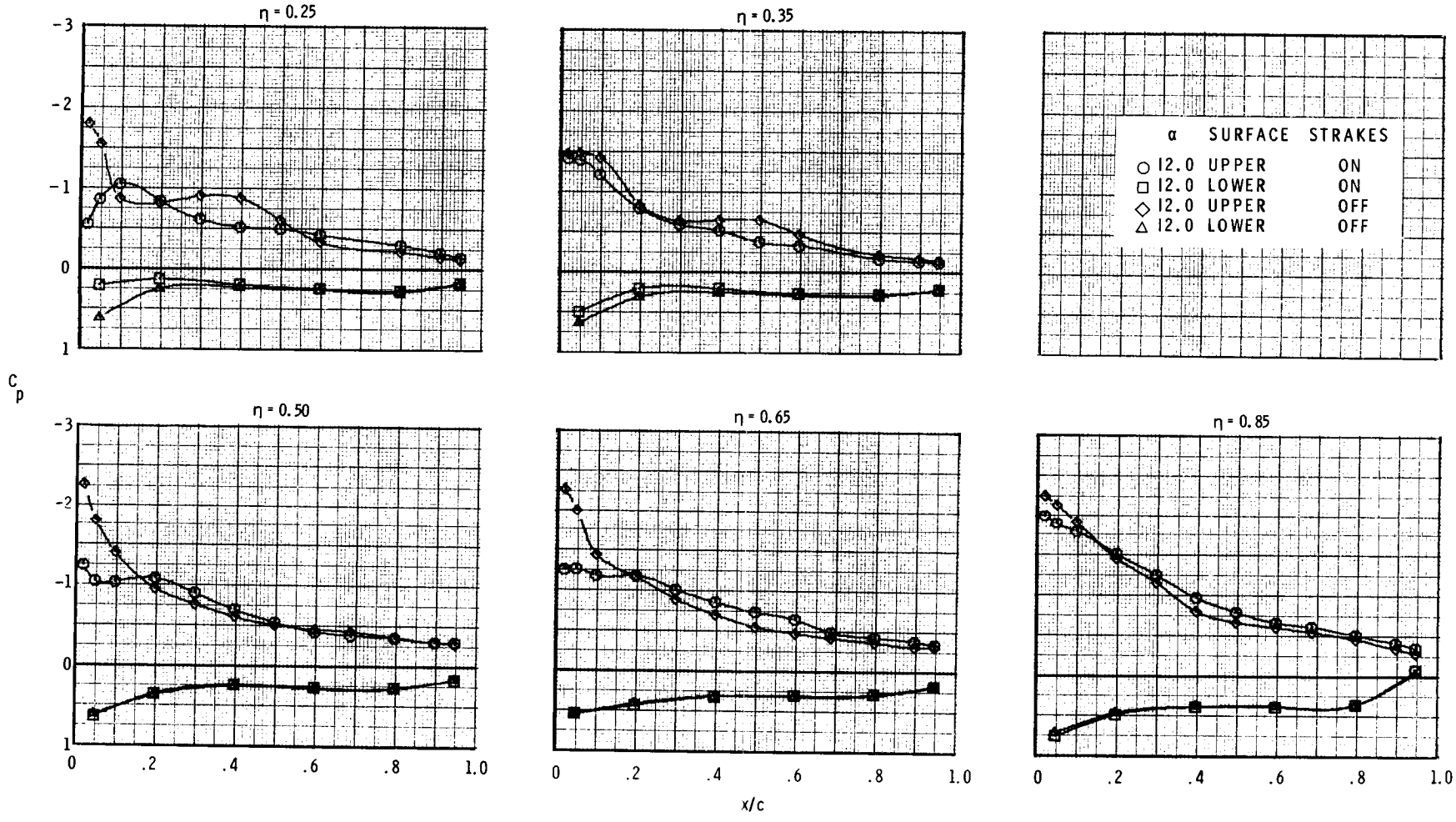

(c) M = 0.60; $\alpha \approx 12°$.

Figure 14.- Continued.

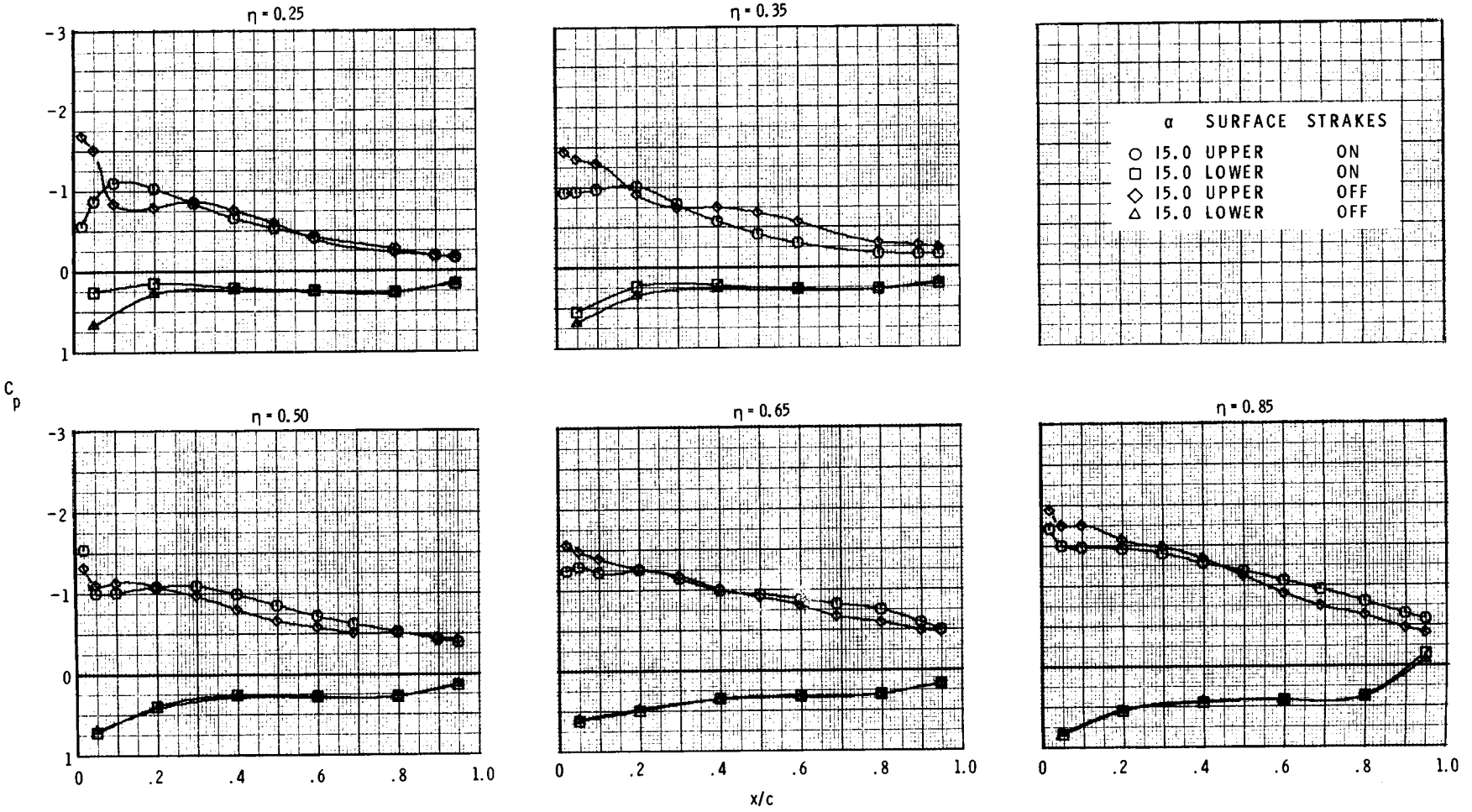

(d) M = 0.60; $\alpha \approx 15°$.

Figure 14.- Continued.

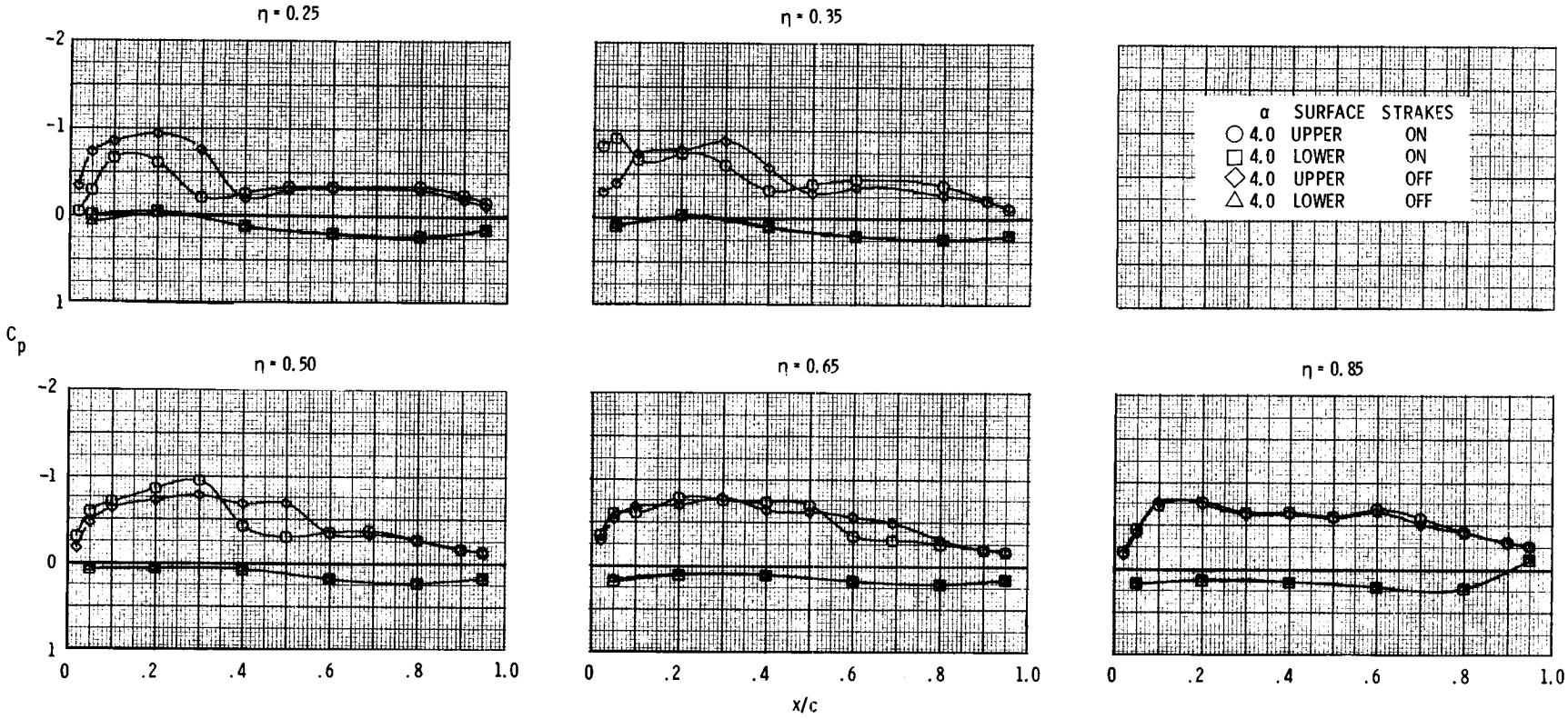

(e) M = 0.85; $\alpha \approx 4°$.

Figure 14.- Continued.

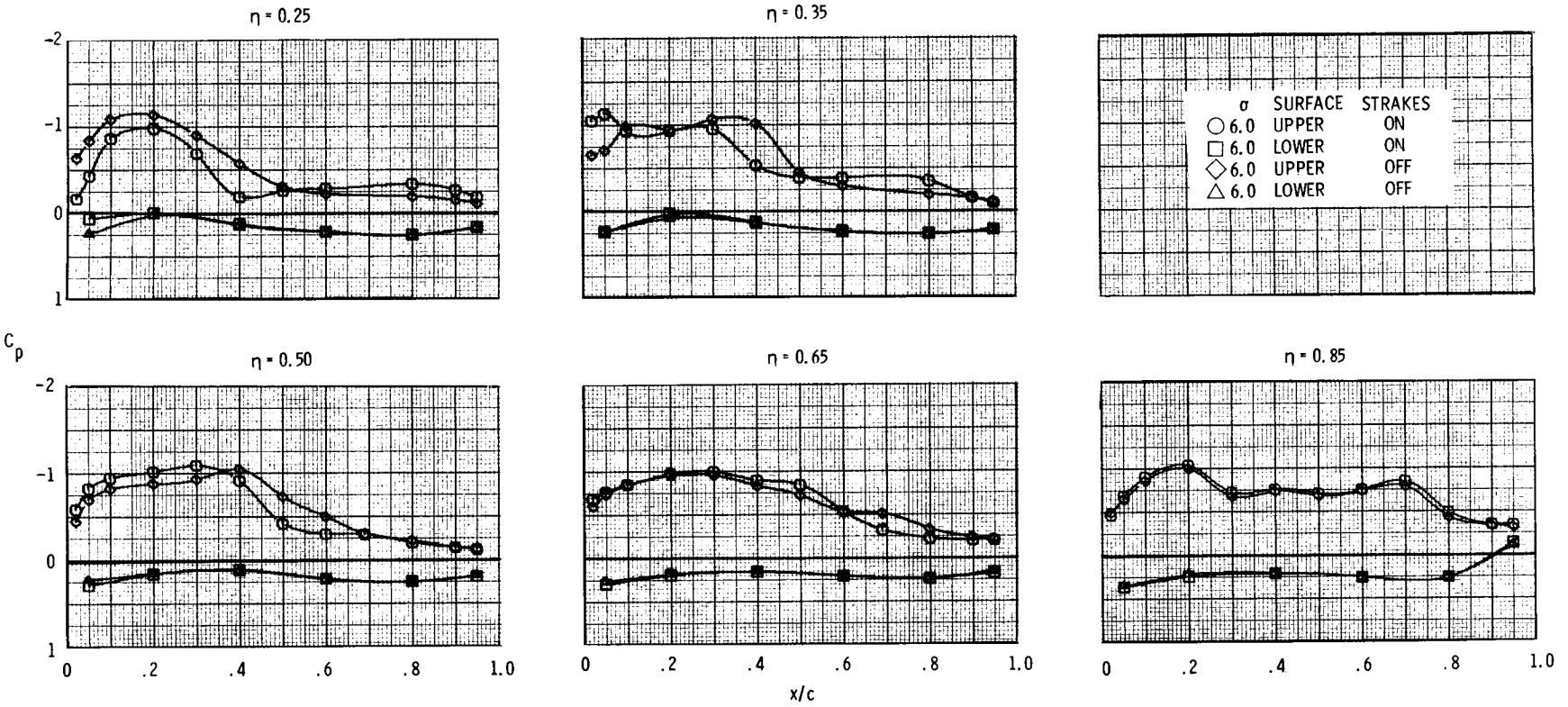

(f) M = 0.85; $\alpha \approx 6°$.

Figure 14.- Continued.

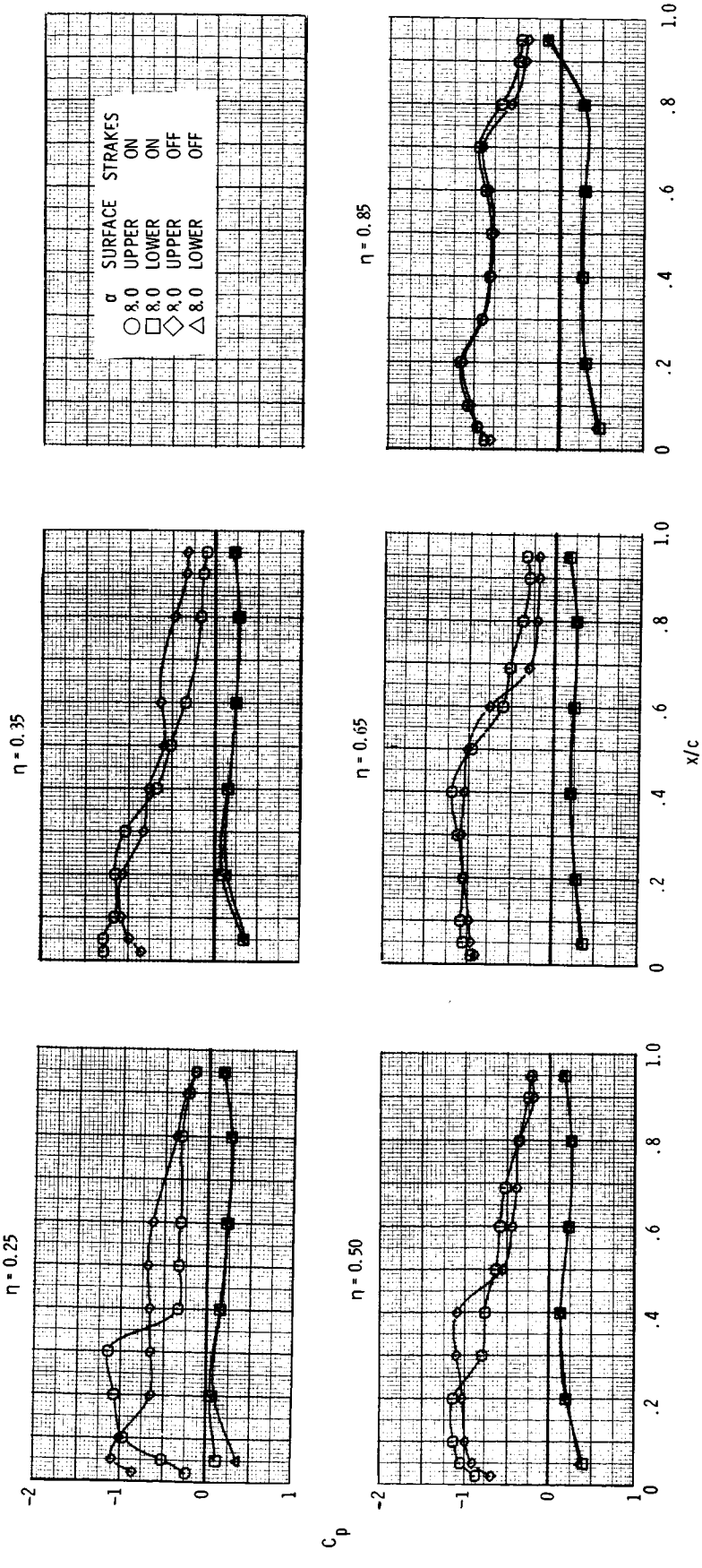

(g) M = 0.85; $\alpha \approx 8°$.

Figure 14.- Continued.

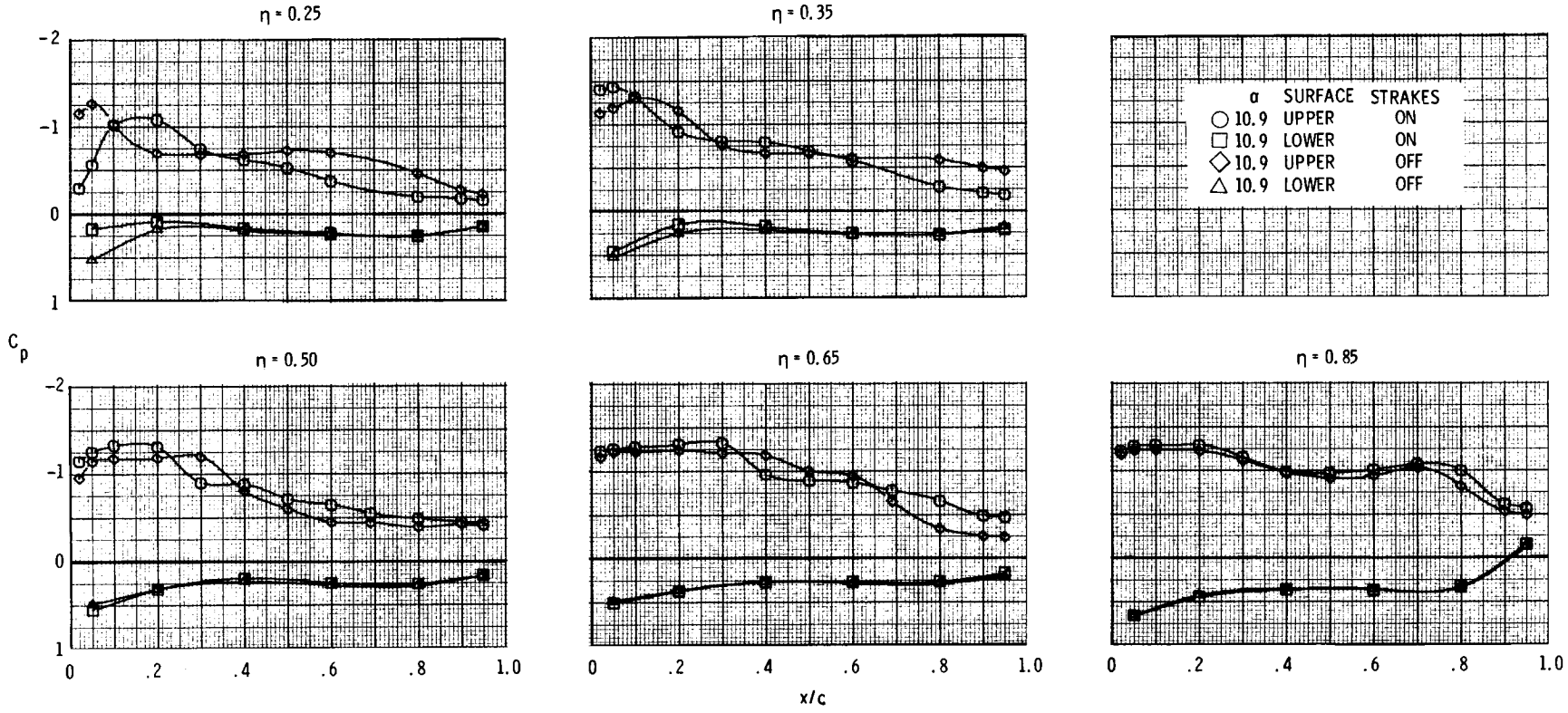

(h) M = 0.85; $\alpha \approx 11°$.

Figure 14.- Continued.

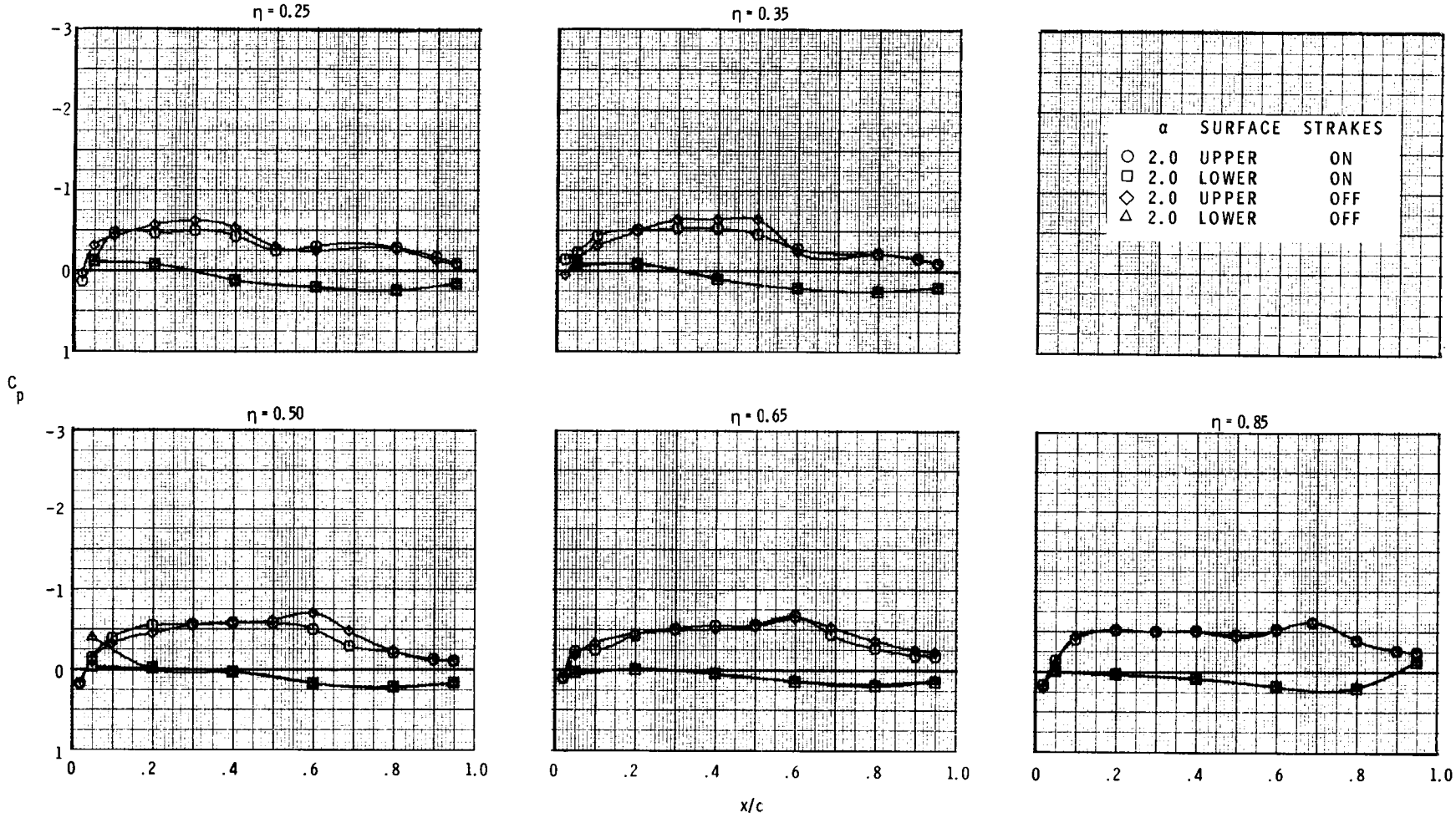

(i) M = 0.90; $\alpha \approx 2°$.

Figure 14.- Continued.

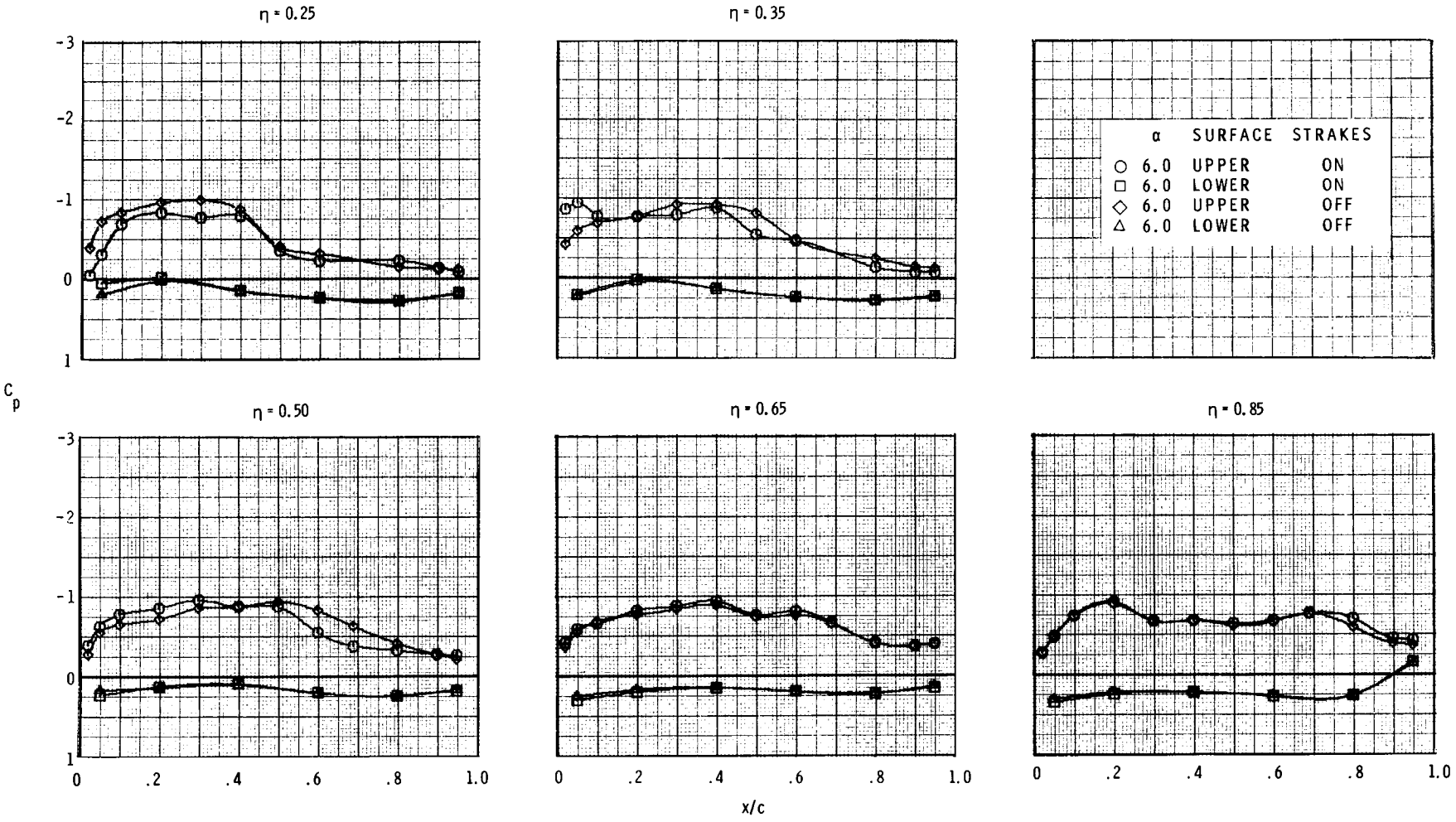

(j) M = 0.90; $\alpha \approx 6°$.

Figure 14.- Continued.

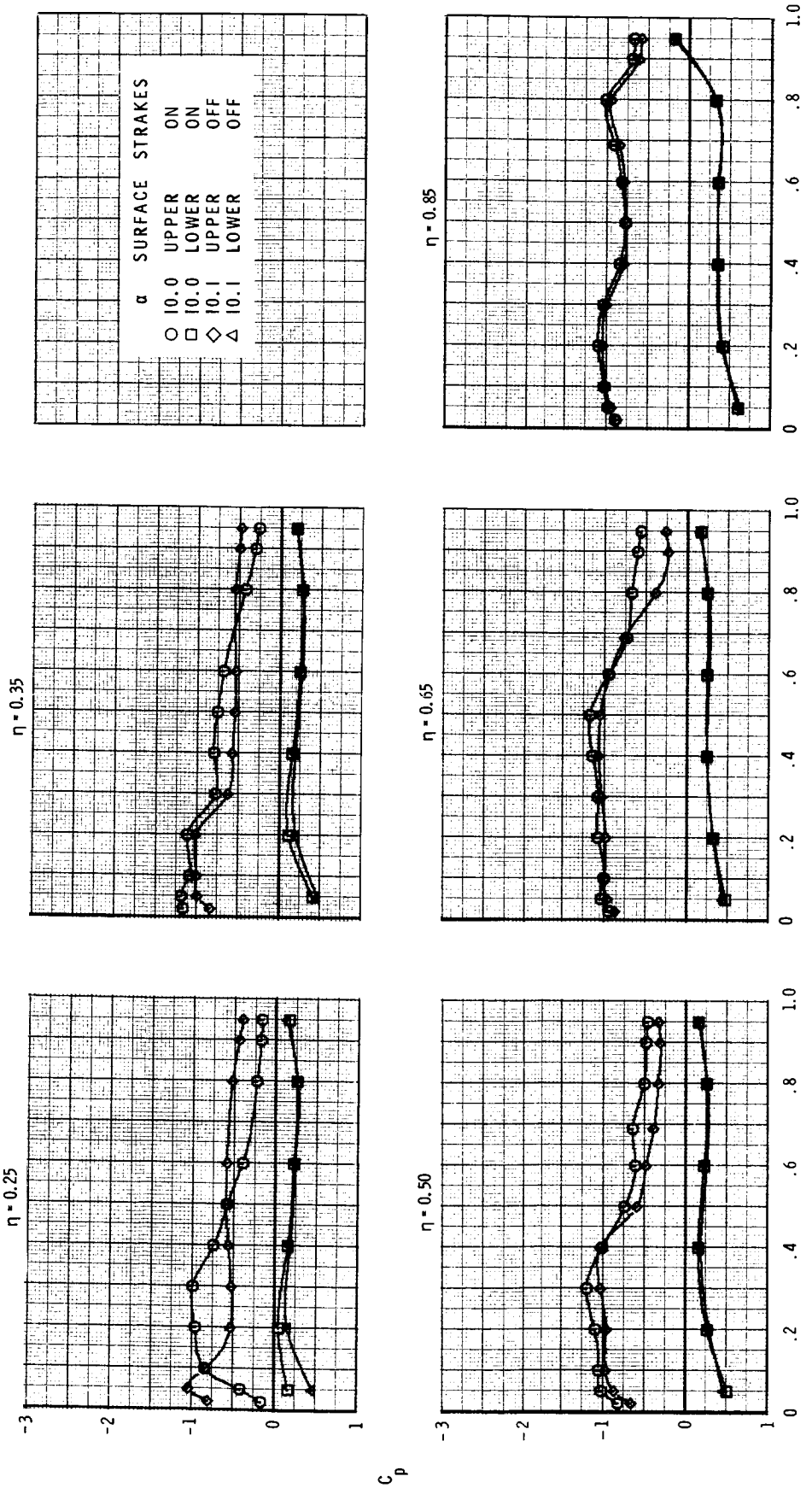

(k) M = 0.90; $\alpha \approx 10°$.

Figure 14.- Continued.

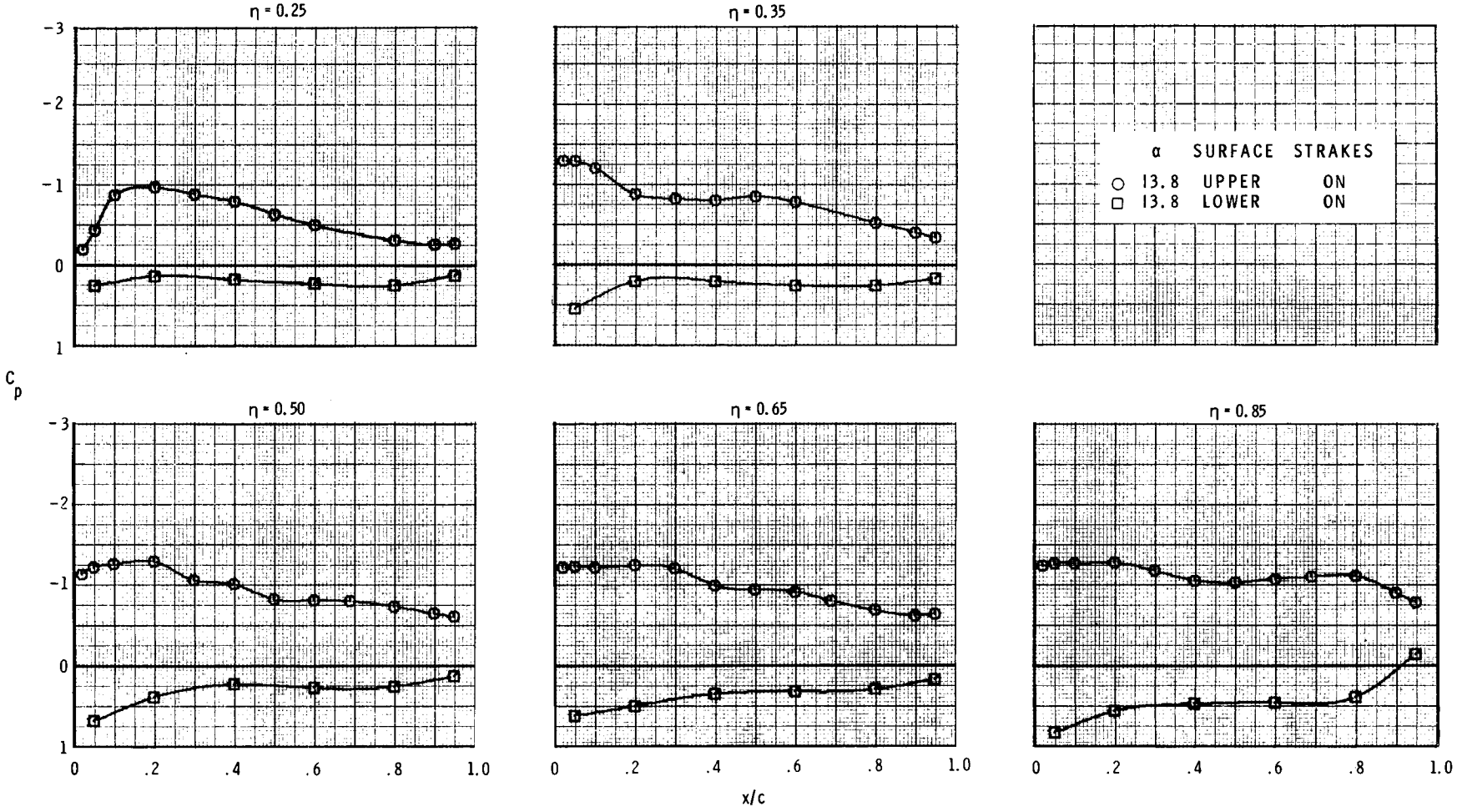

(l) M = 0.90; $\alpha \approx 14°$.

Figure 14.- Concluded.

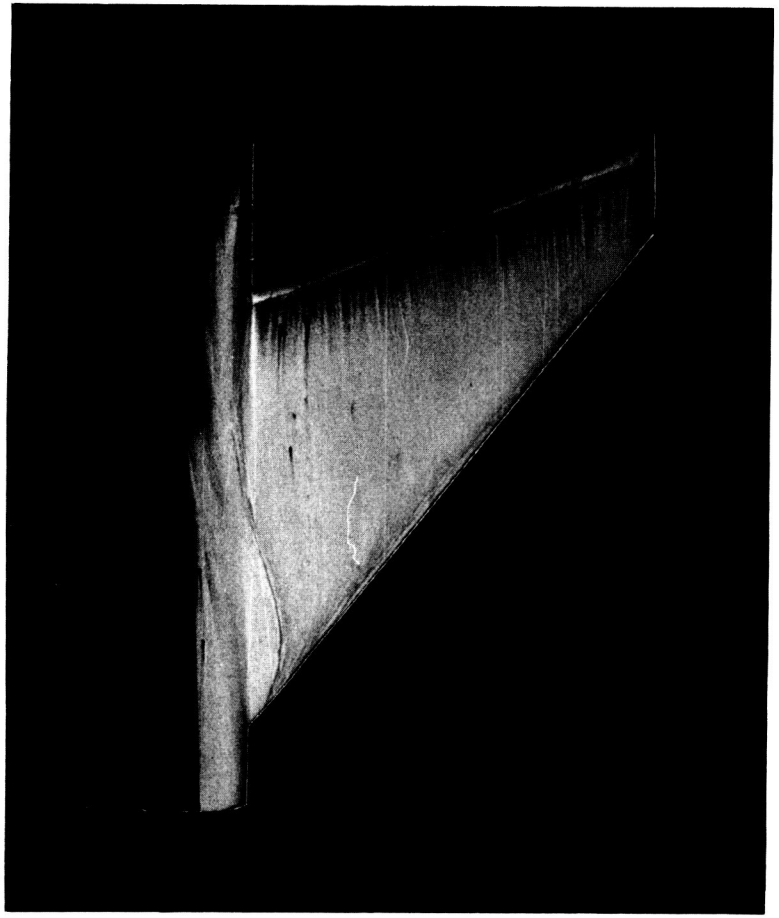

Canard off; α = 3.69°

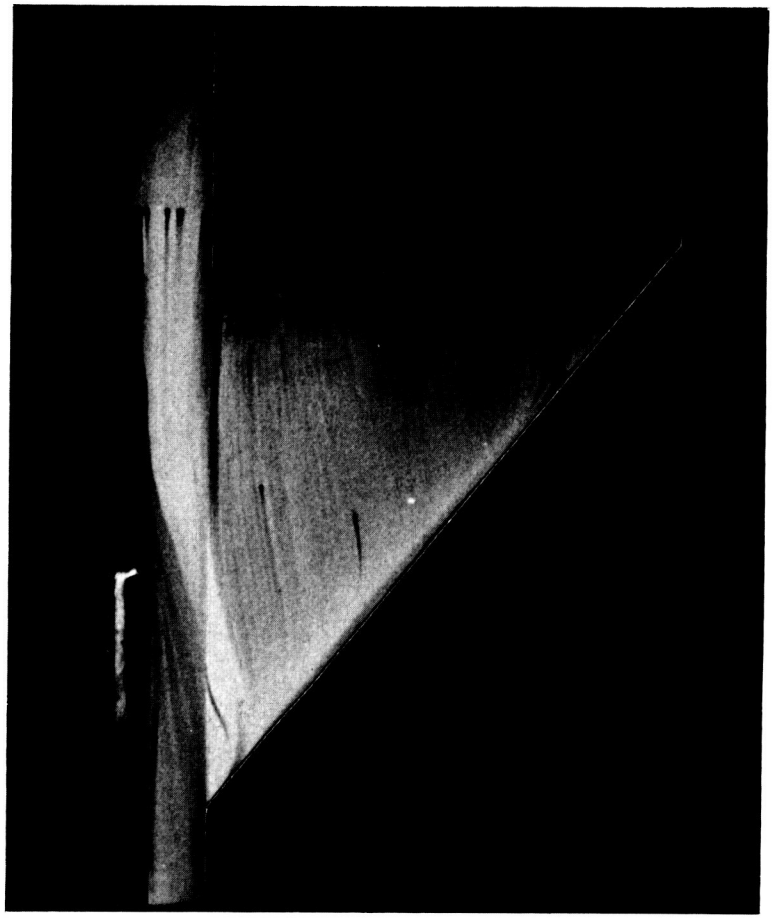

Canard on; α = 3.66°

L-86-362

(a) M = 0.60; $\alpha \approx 4°$.

Figure 15.- Upper surface oil-flow patterns with and without canards. Strakes off; $\delta_c = 0°$; $\delta_{f,TE} = \delta_{f,LE} = 0°$.

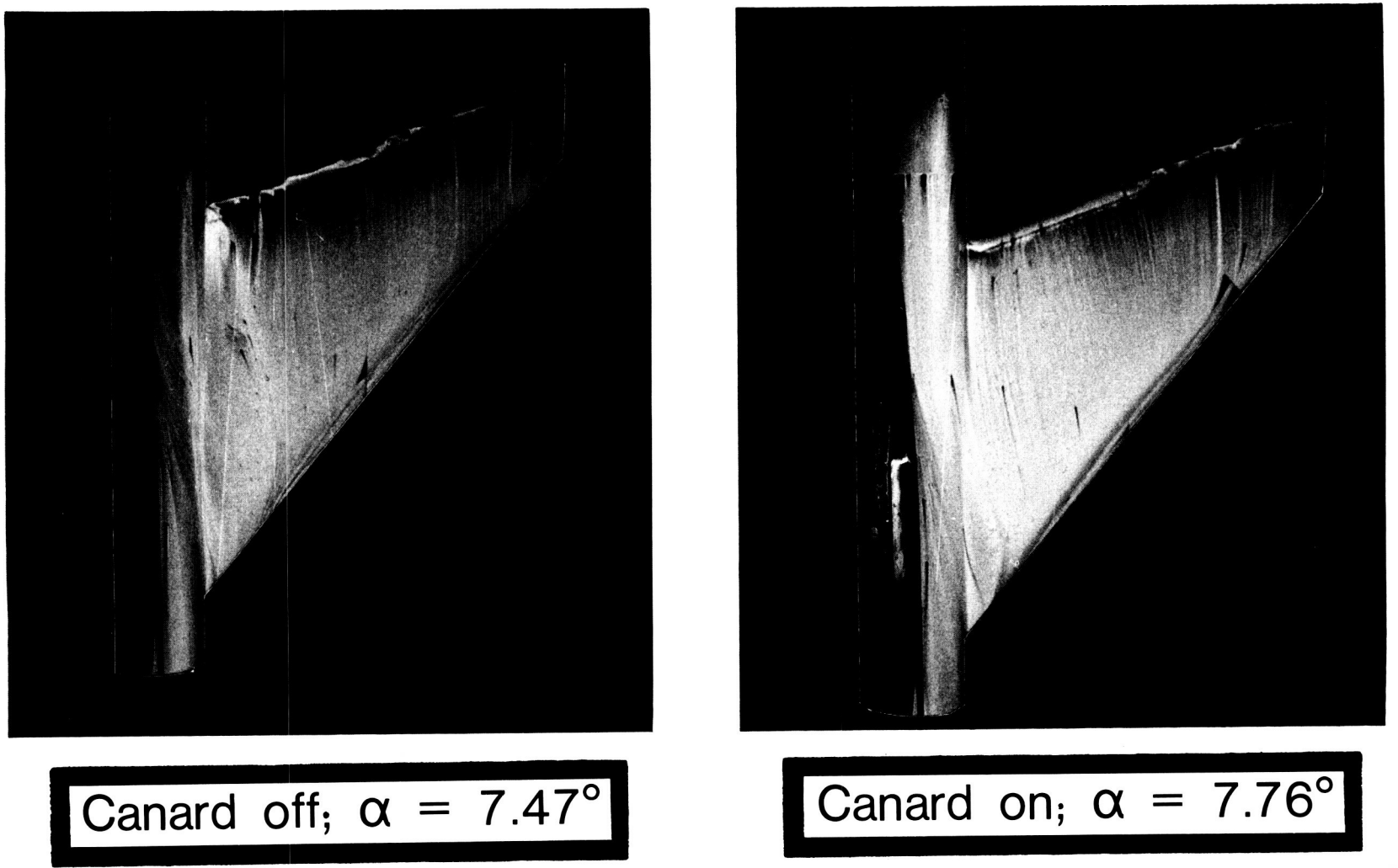

(b) M = 0.60; $\alpha \approx 7°$.

Figure 15.- Continued.

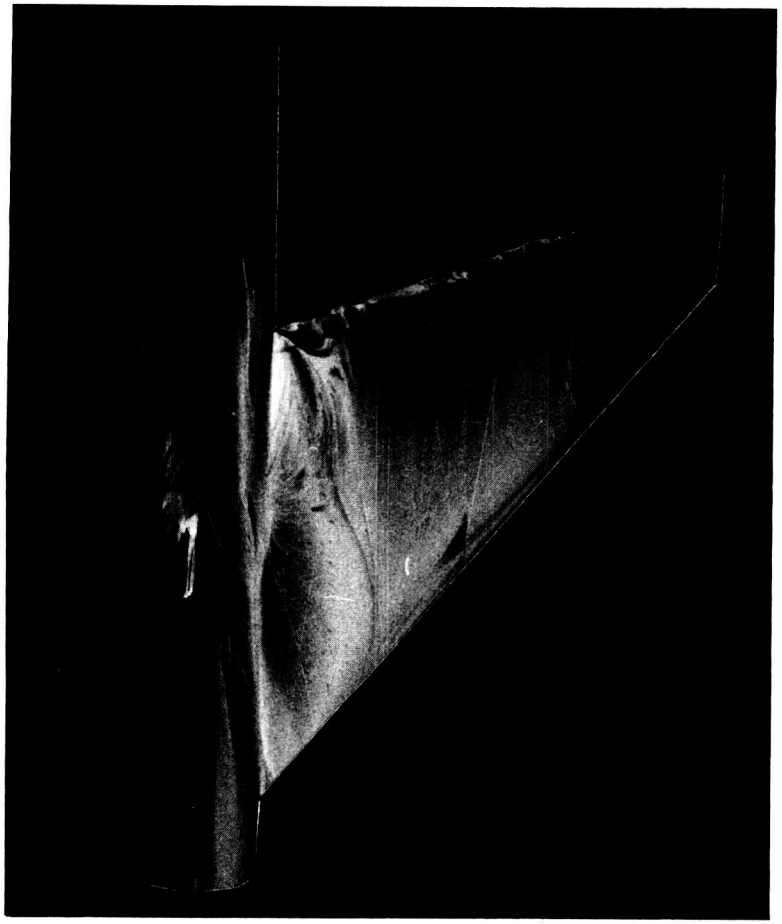

Canard off; α = 10.5°

Canard on; α = 10.75°

L-86-364

(c) M = 0.60; $\alpha \approx 11°$.

Figure 15.- Continued.

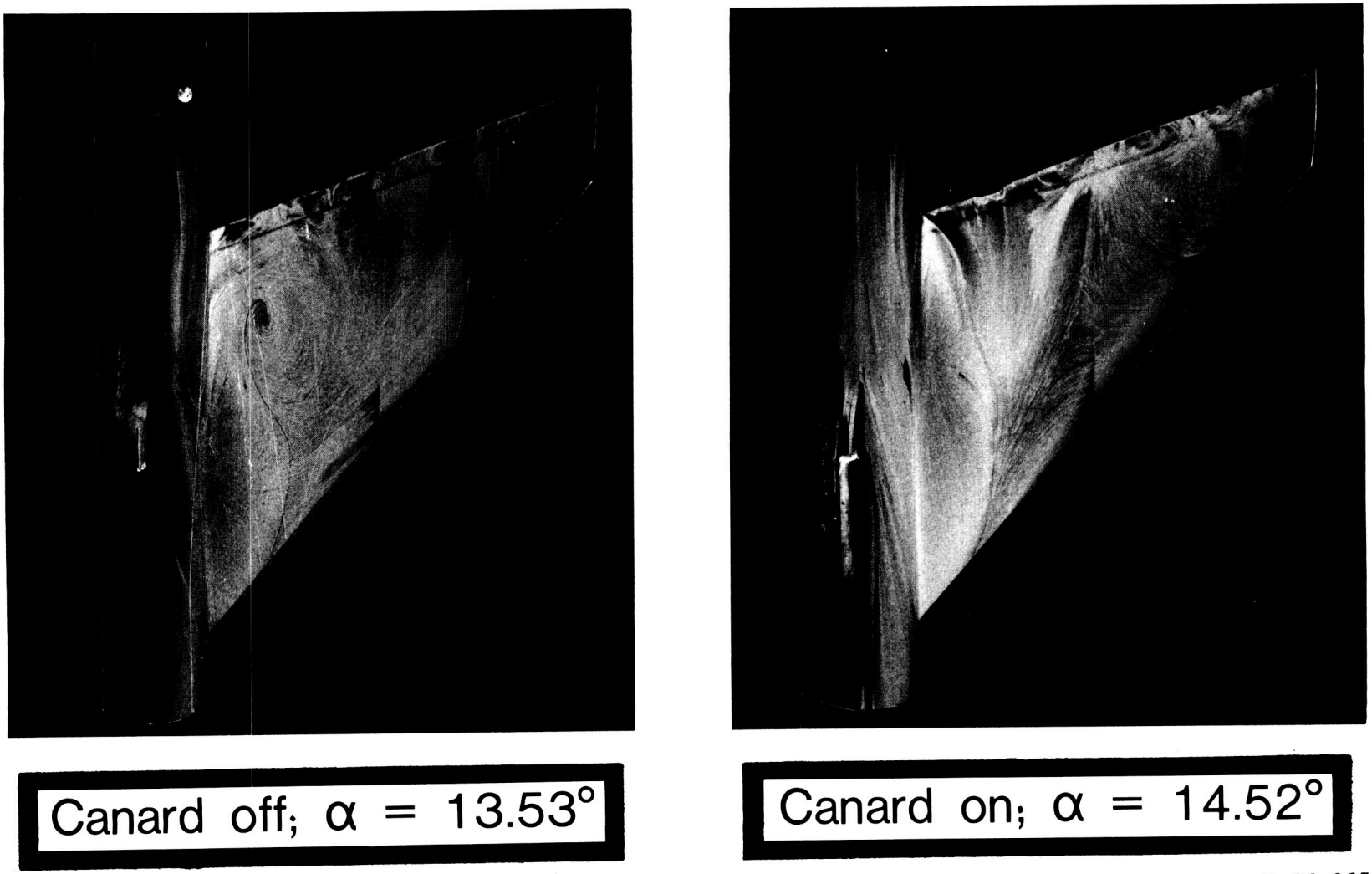

(d) M = 0.60; $\alpha \approx 14°$.

Figure 15.- Continued.

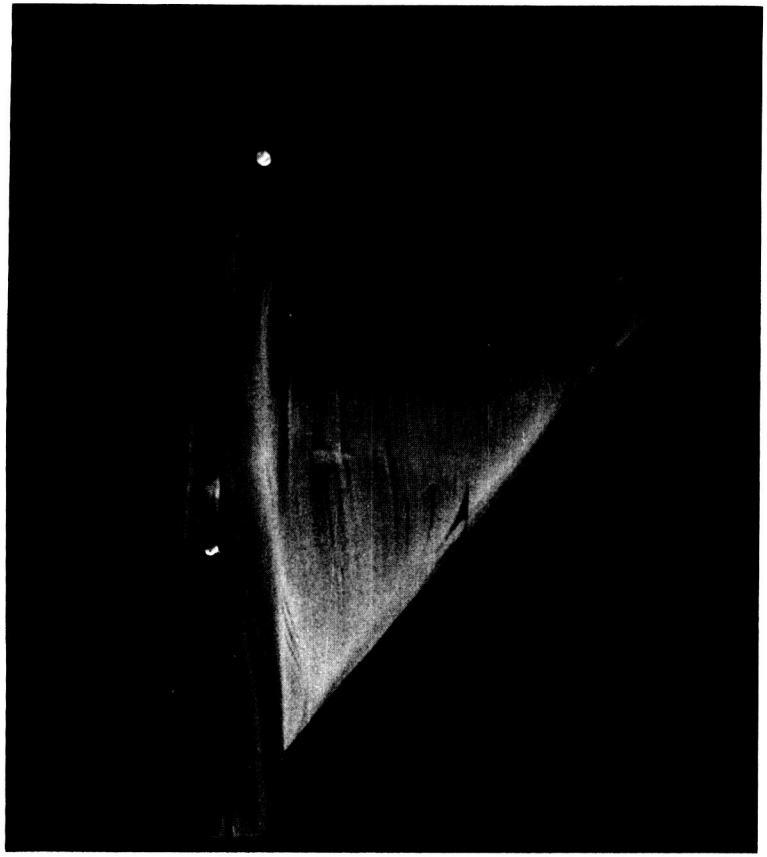

Canard off; α = 2.66°

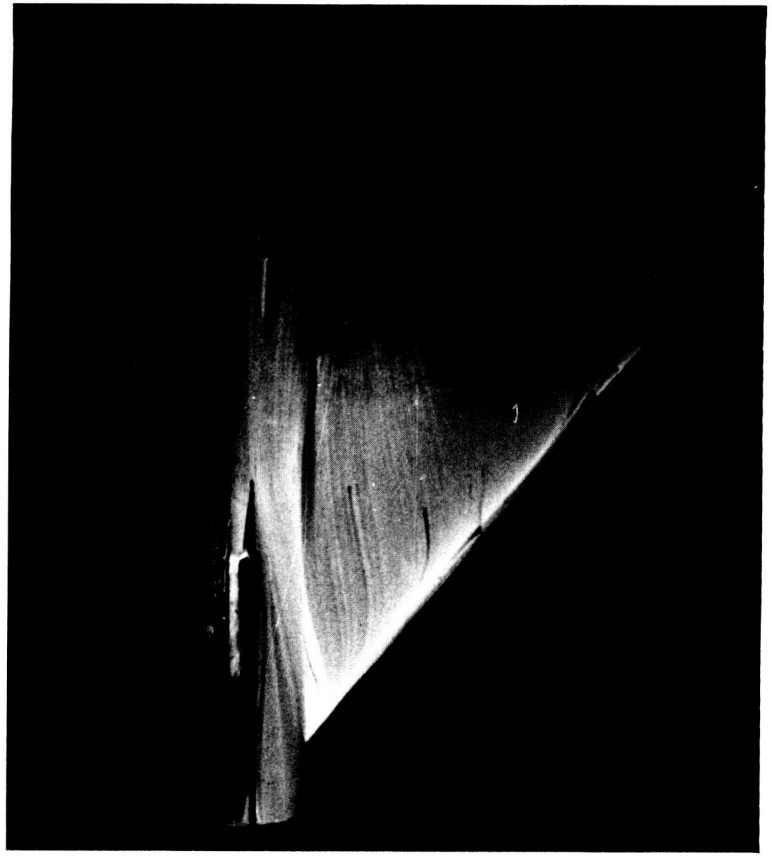

Canard on; α = 2.70°

L-86-366

(e) M = 0.85; $\alpha \approx 3°$.

Figure 15.- Continued.

Canard off; α = 6.84°

Canard on; α = 6.68°

L-86-367

(f) M = 0.85; $\alpha \approx 7°$.

Figure 15.- Continued.

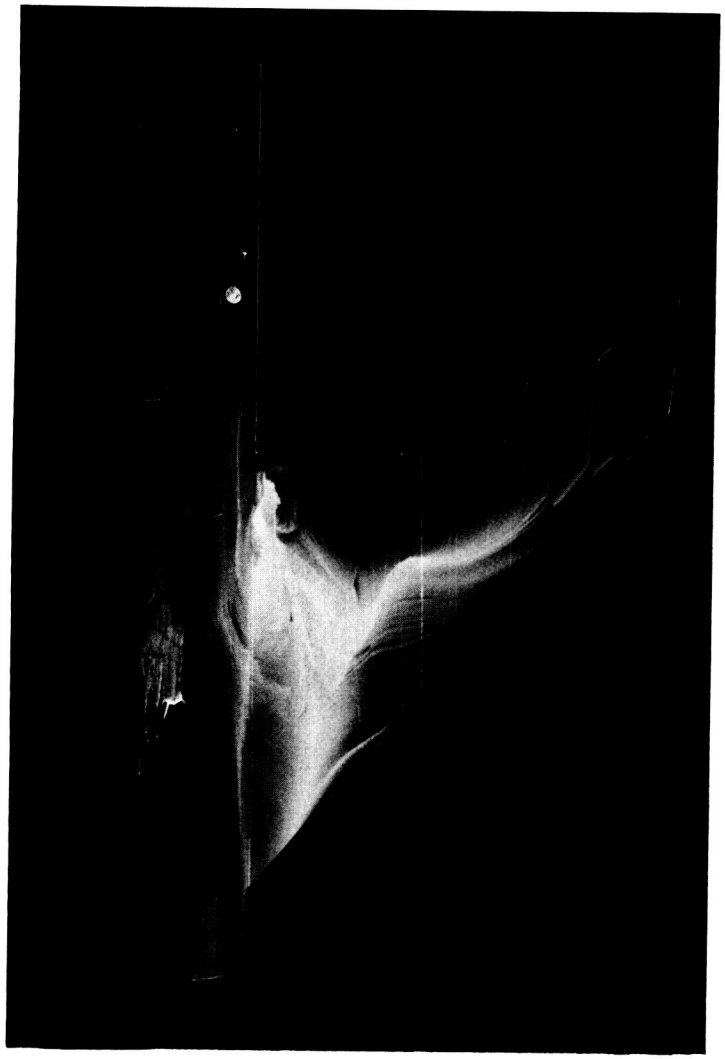

Canard off; α = 8.58°

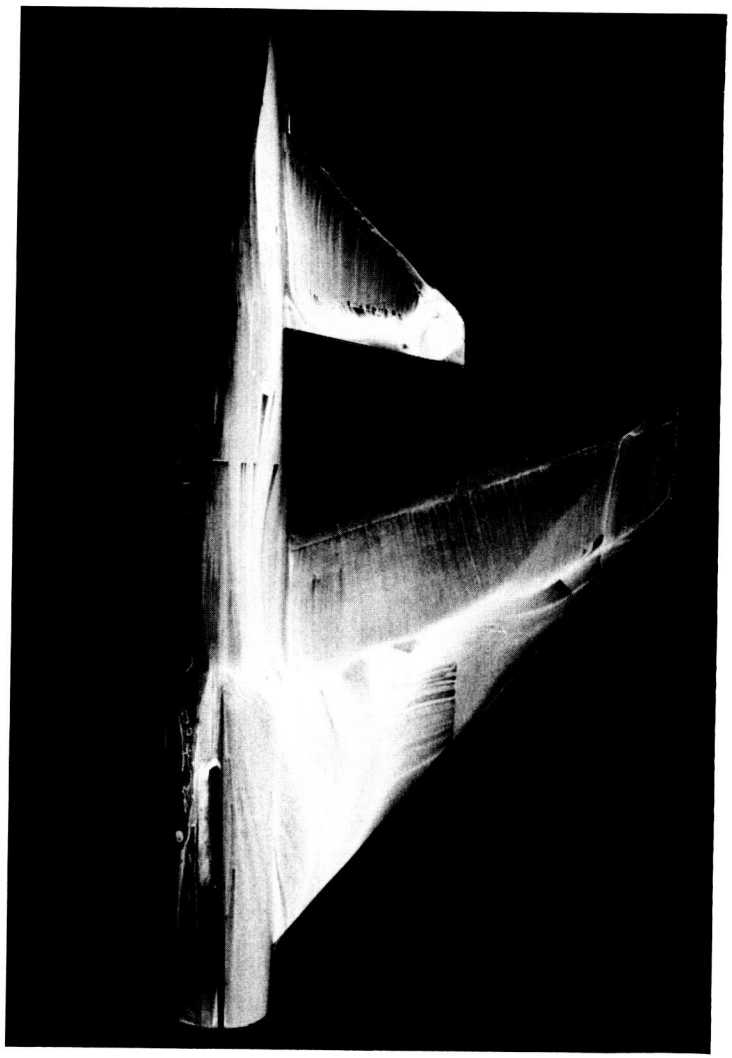

Canard on; α = 8.79°

L-86-368

(g) M = 0.85; $\alpha \approx 9°$.

Figure 15.- Continued.

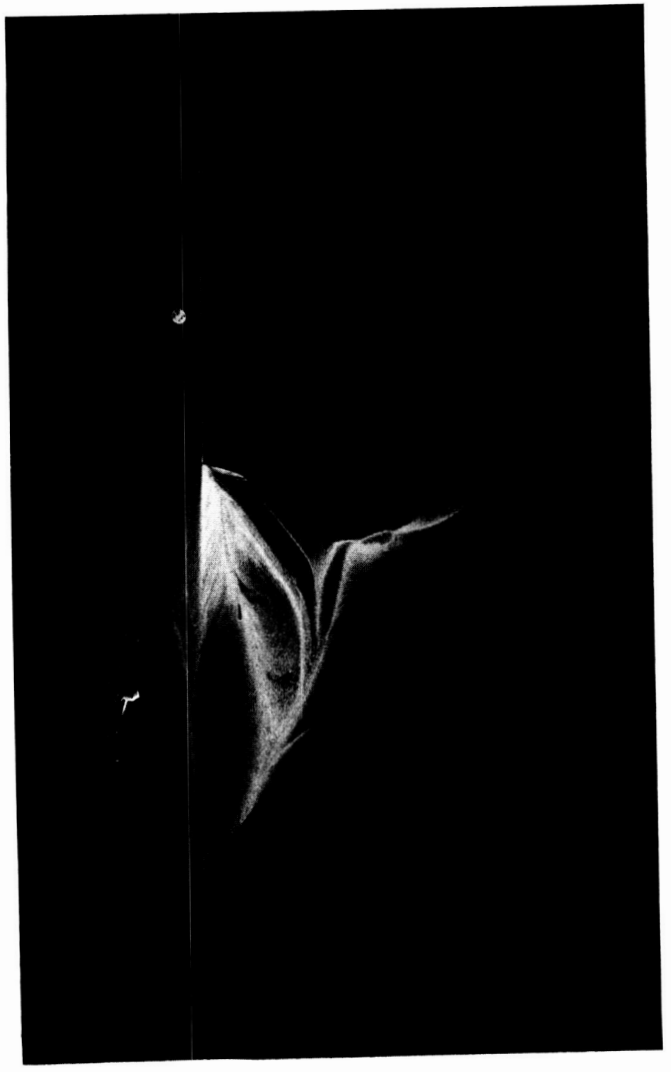

Canard off; α = 10.65°

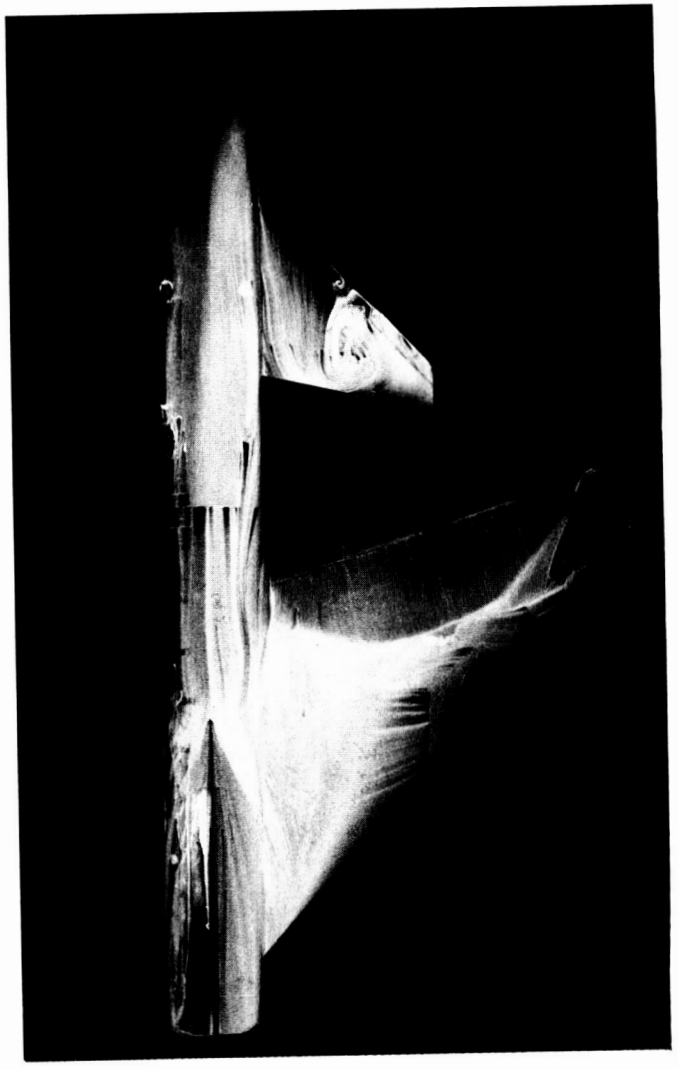

Canard on; α = 11.42°

L-86-369

(h) M = 0.85; $\alpha \approx 11°$.

Figure 15.- Continued.

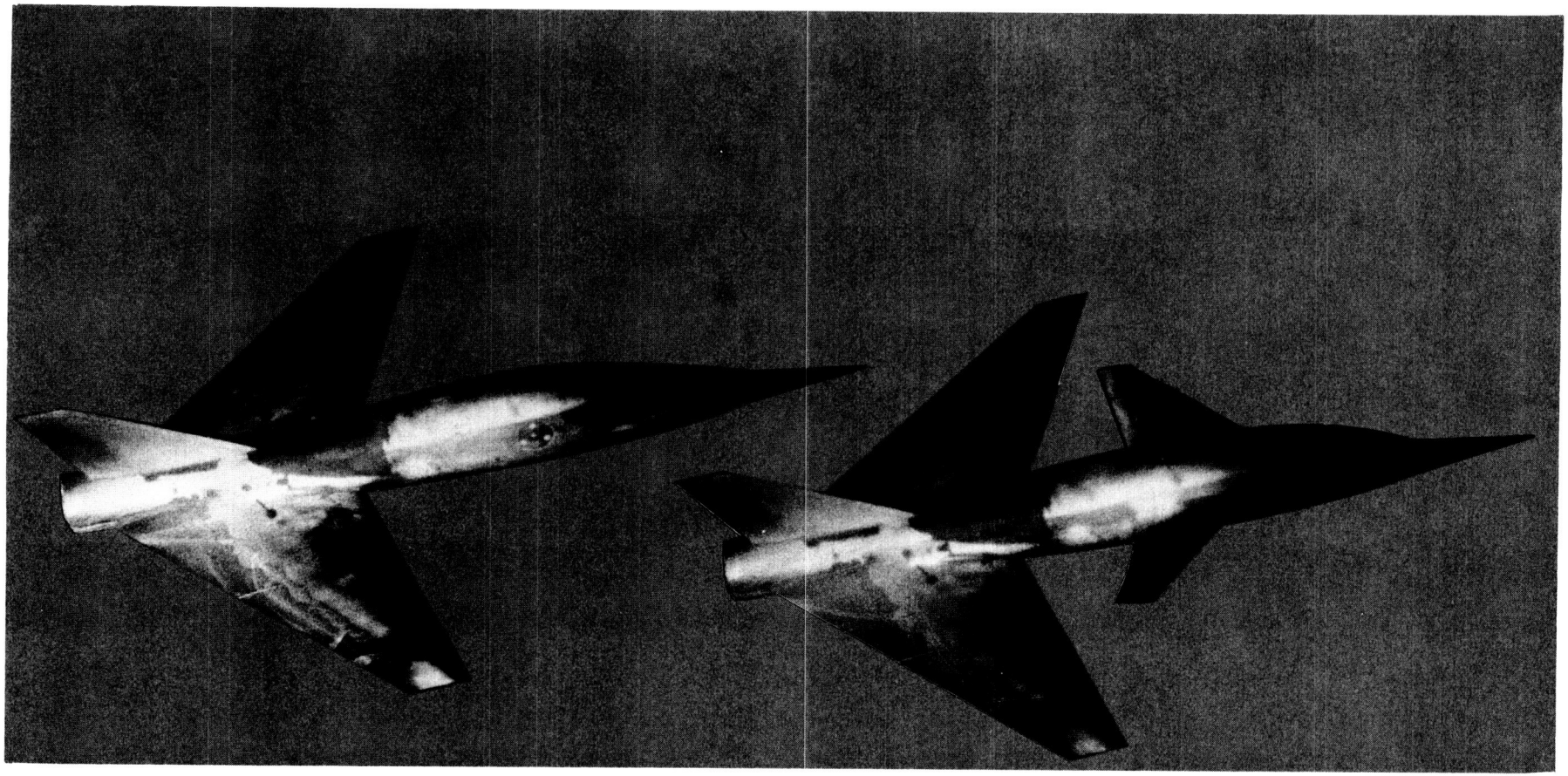

L-86-370

(i) M = 0.90; $\alpha \approx 6°$.

Figure 15.- Continued.

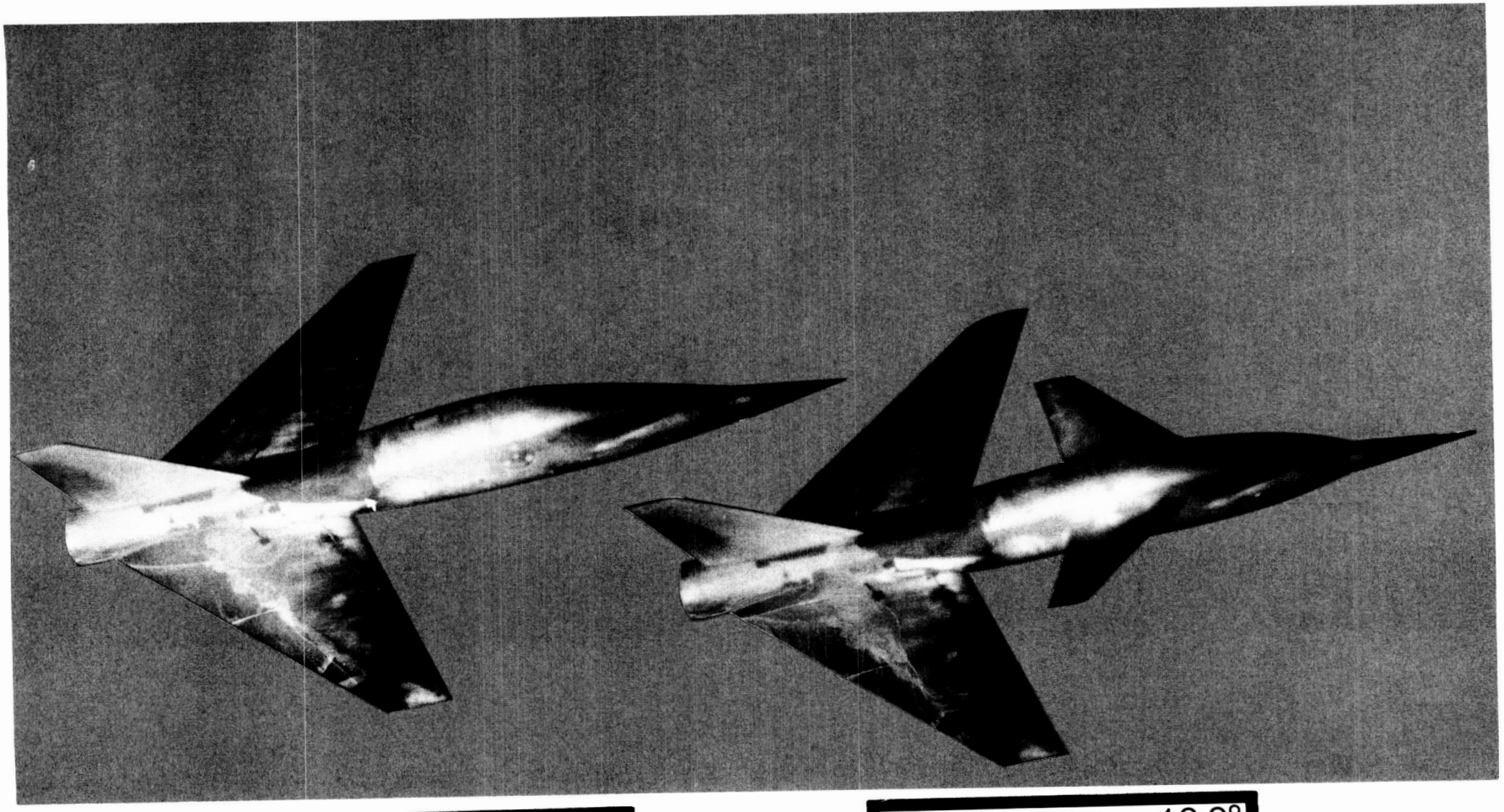

(j) M = 0.90; $\alpha \approx 10°$.

Figure 15.- Concluded.

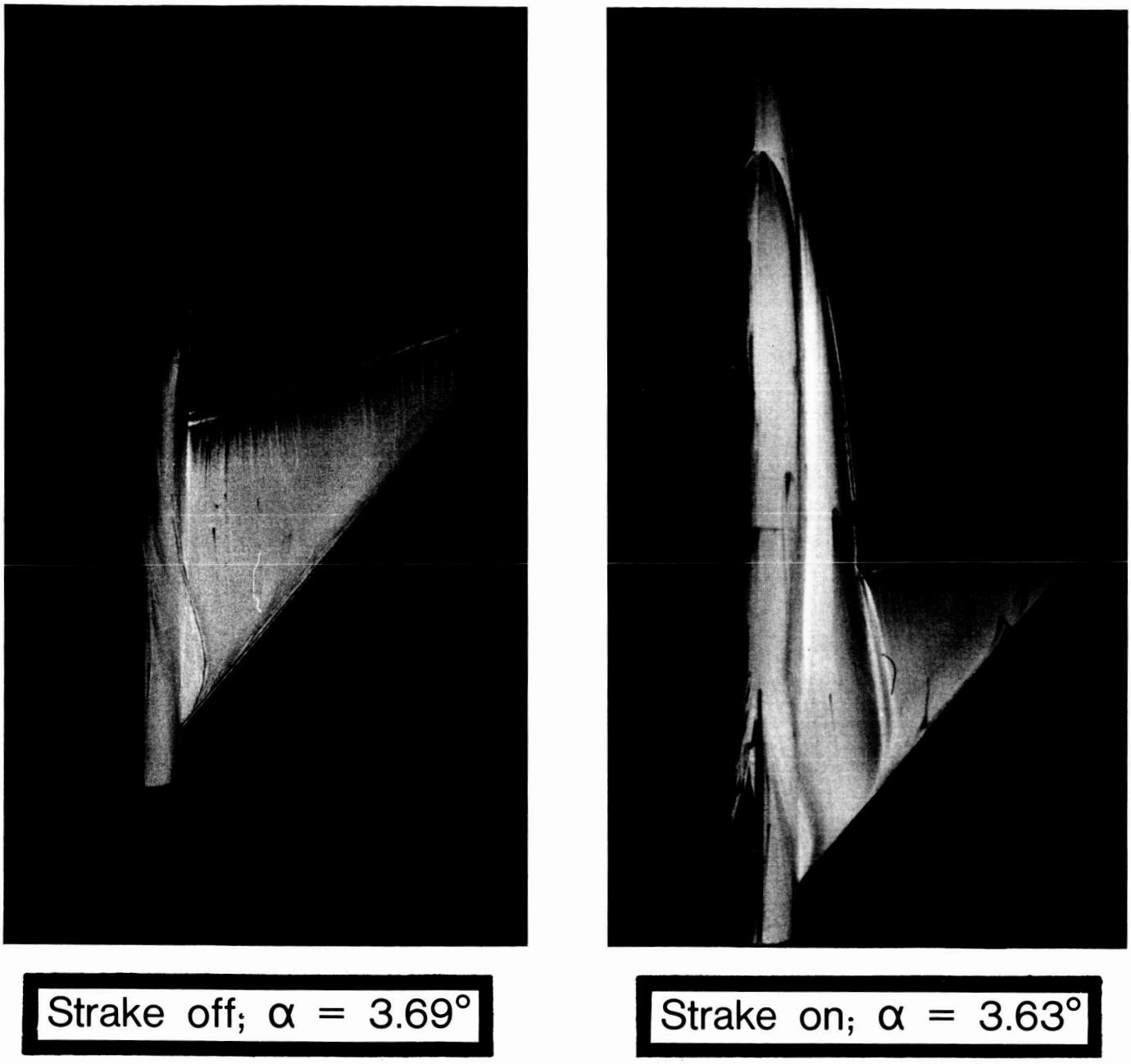

(a) M = 0.60; $\alpha \approx 4°$.

Figure 16.- Upper surface oil-flow patterns with and without strakes. Canards off; $\delta_{f,TE} = \delta_{f,LE} = 0°$.

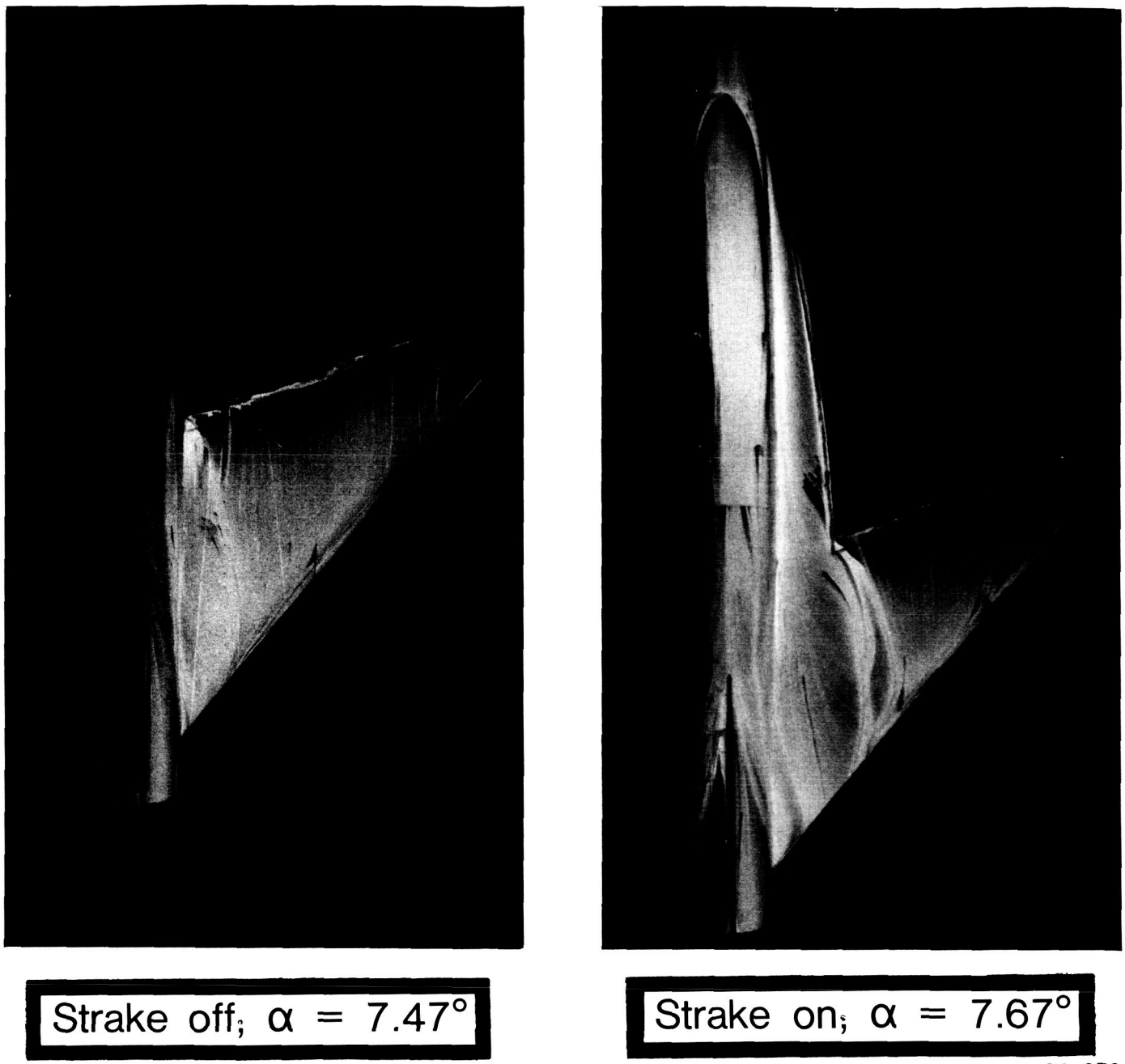

(b) M = 0.60; $\alpha \approx 7°$.

Figure 16.- Continued.

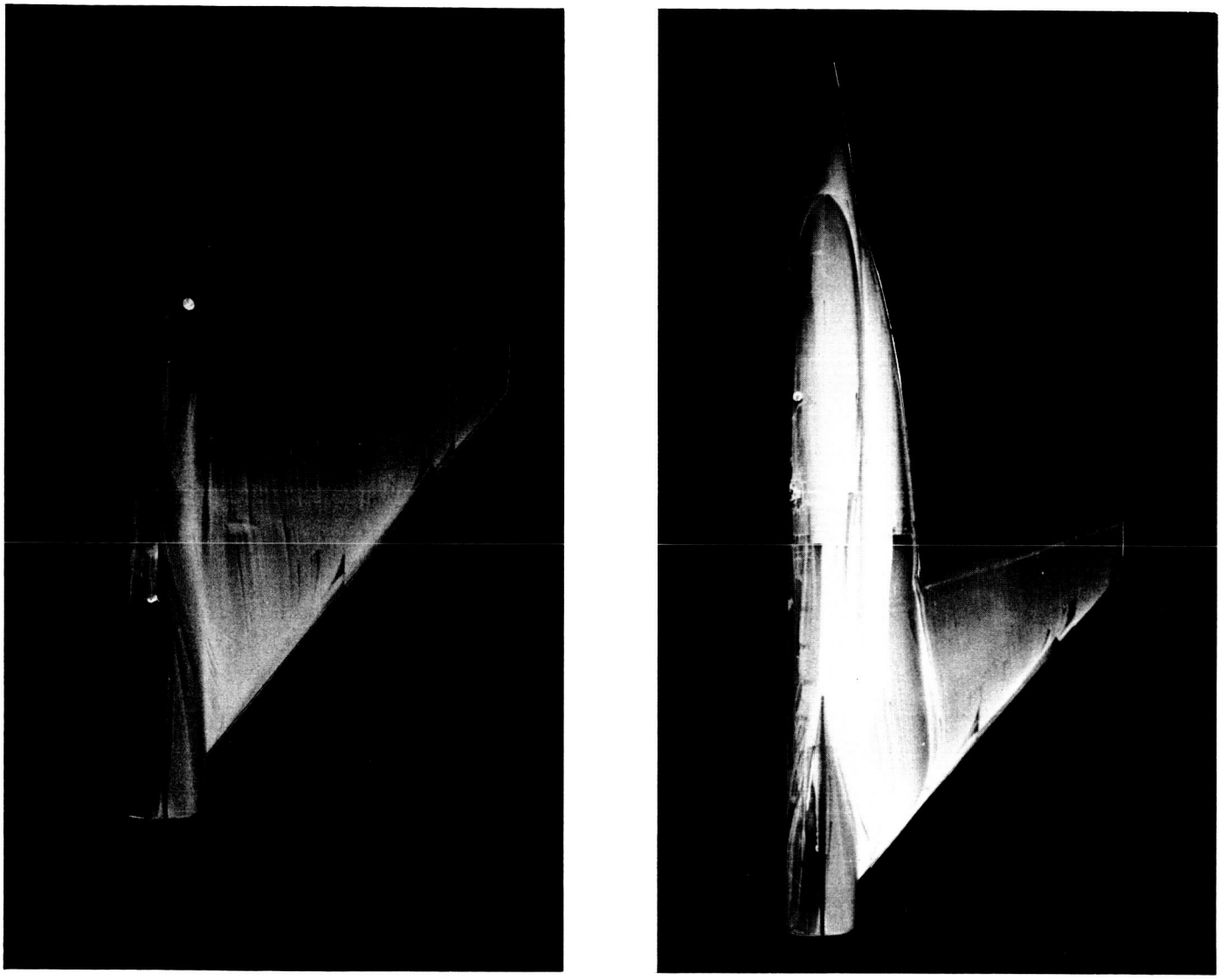

L-86-376

(e) M = 0.85; $\alpha \approx 3°$.

Figure 16.- Continued.

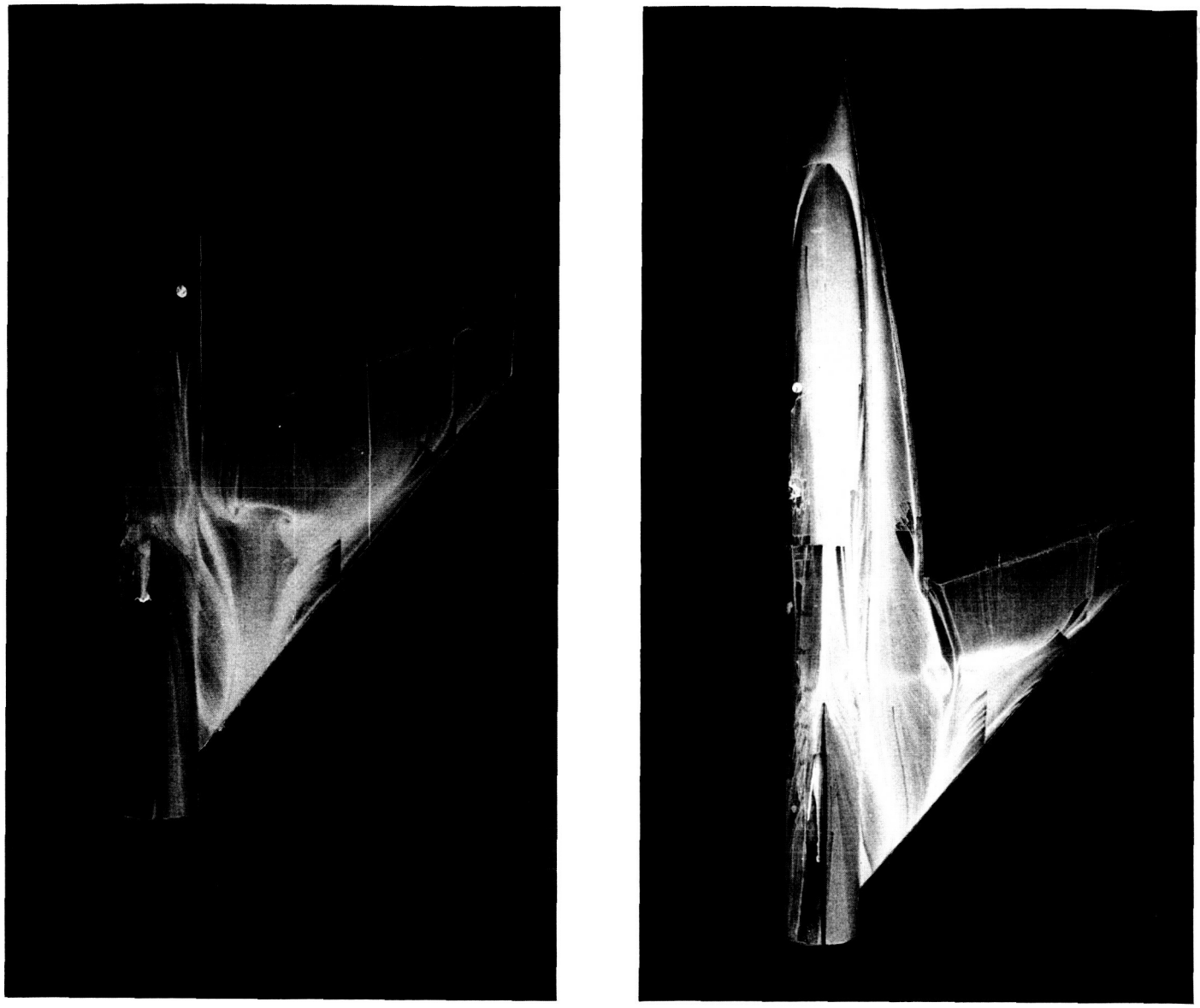

(f) M = 0.85; $\alpha \approx 7°$.

Figure 16.- Continued.

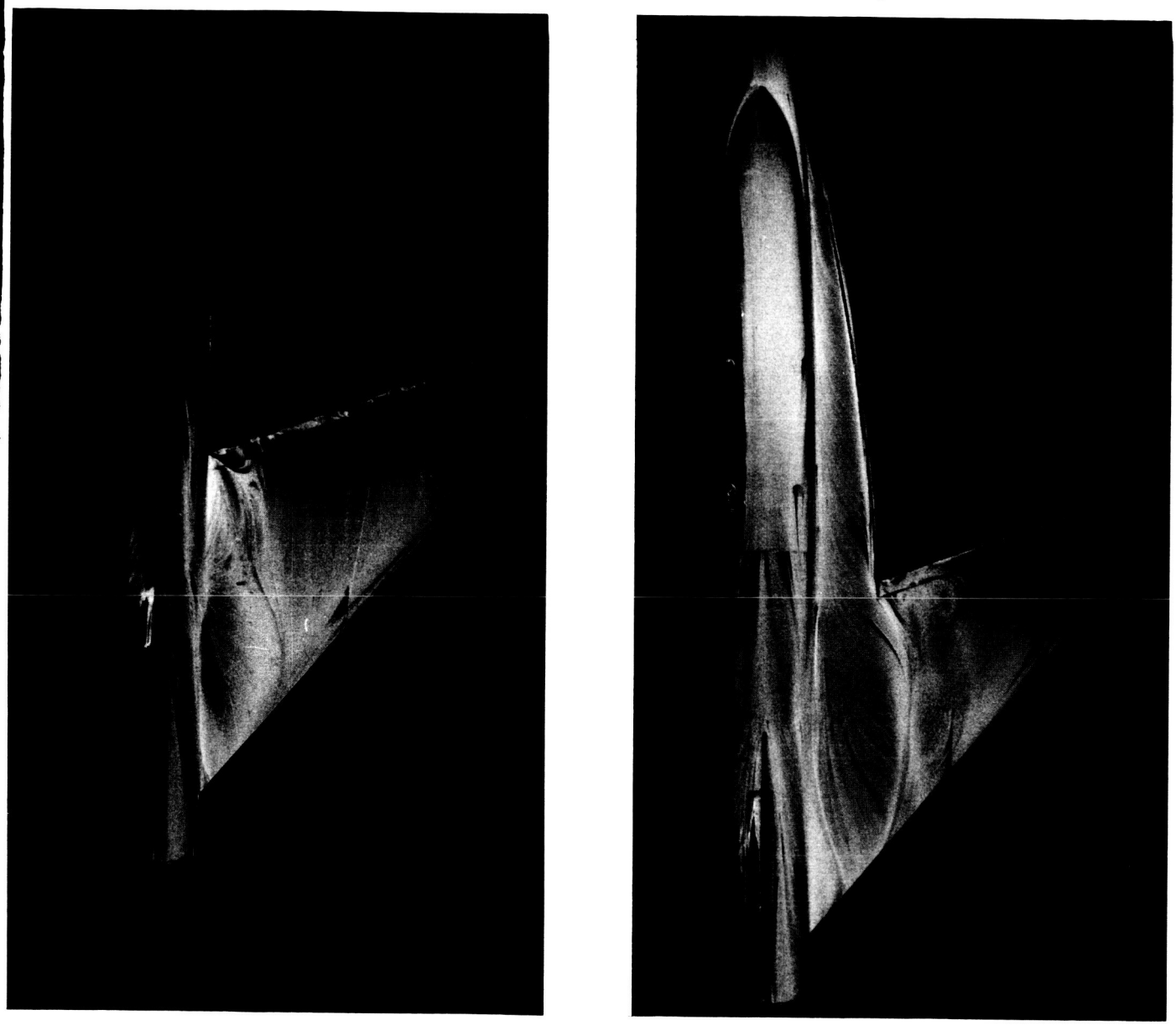

L-86-374

(c) M = 0.60; $\alpha \approx 11°$.

Figure 16.- Continued.

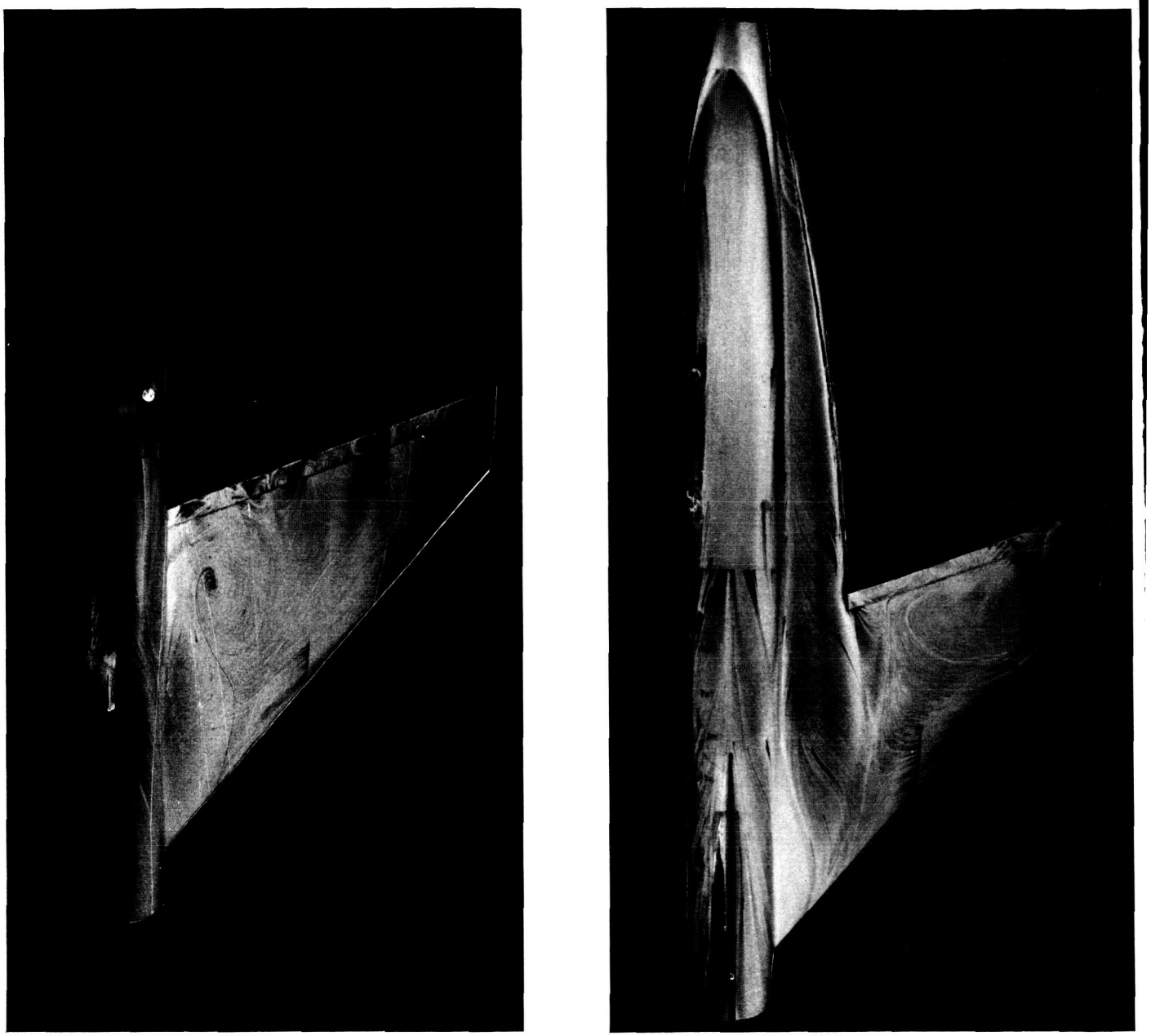

(d) M = 0.60; $\alpha \approx 14°$.

Figure 16.- Continued.

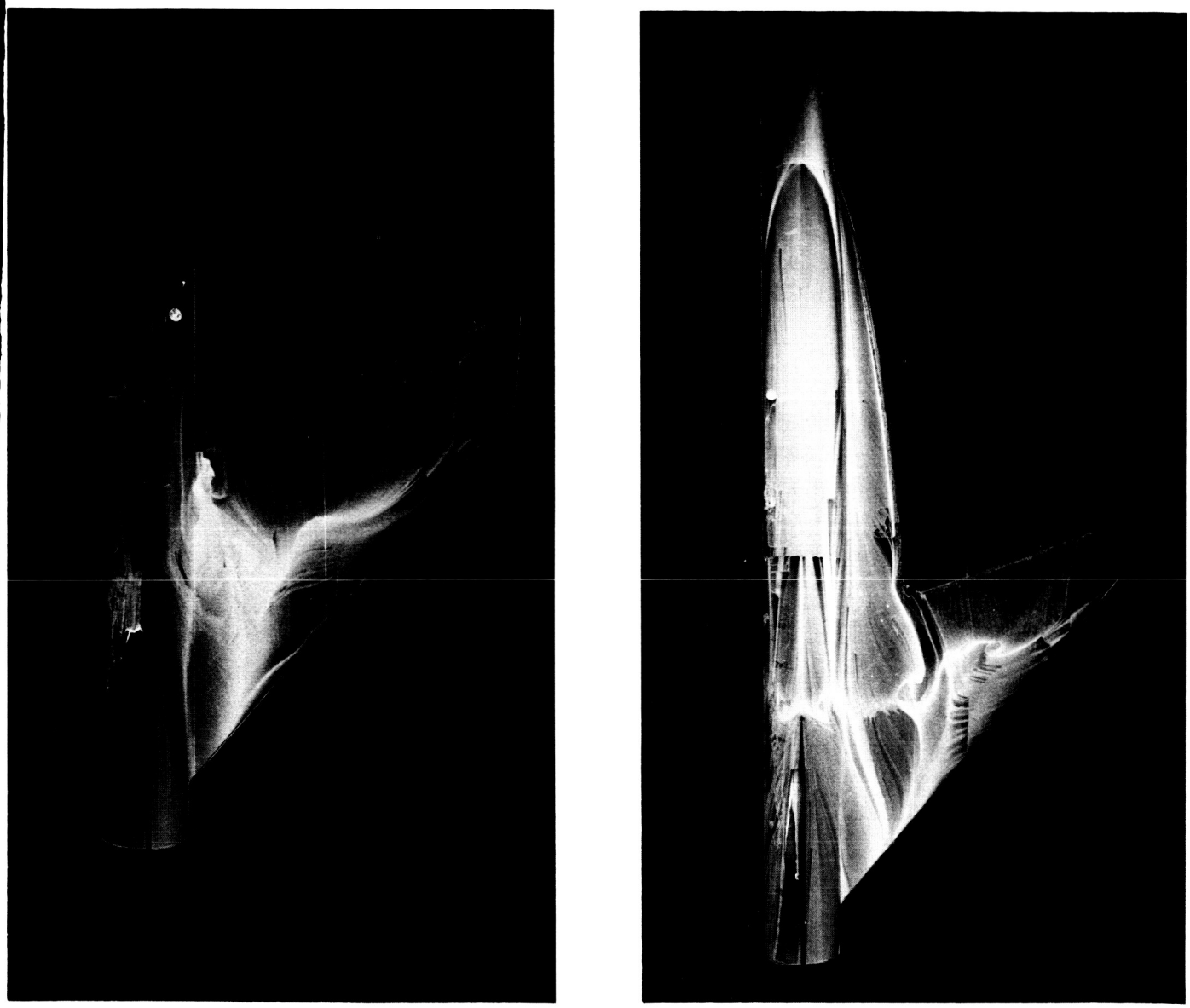

L-86-378

(g) M = 0.85; $\alpha \approx 9°$.

Figure 16.- Continued.

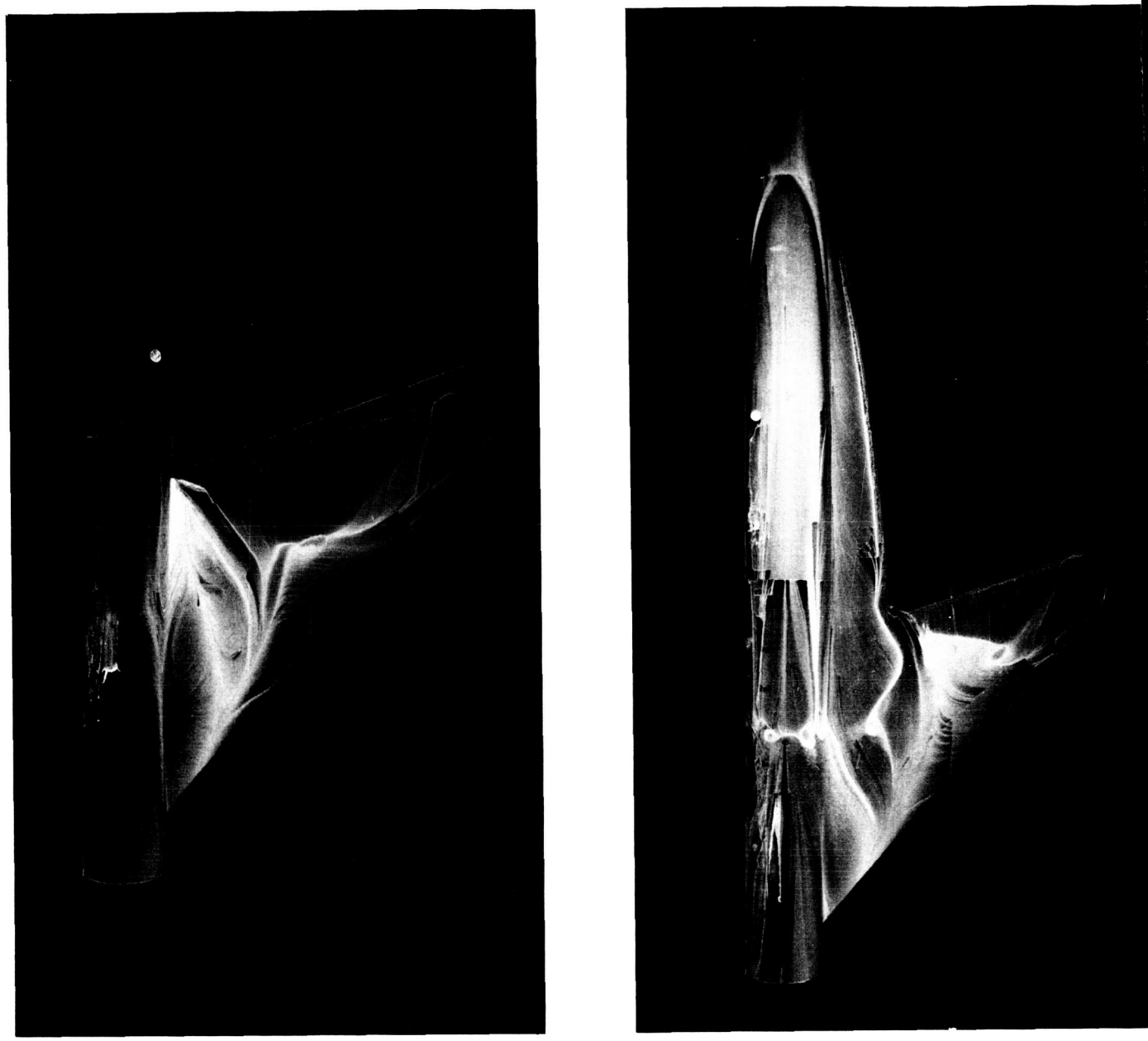

(h) M = 0.85; $\alpha \approx 11°$.

Figure 16.- Concluded.

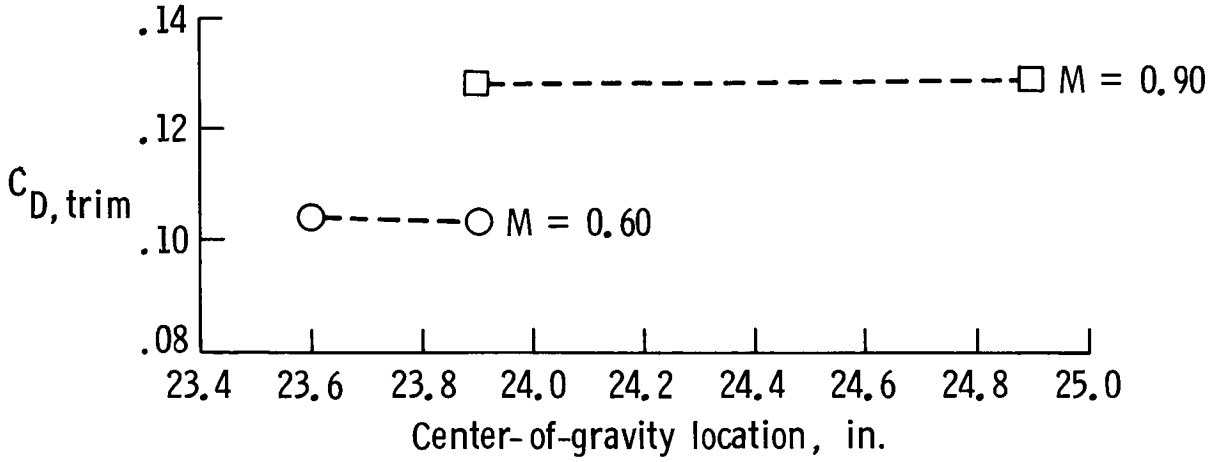

(a) Variation with center-of-gravity location.

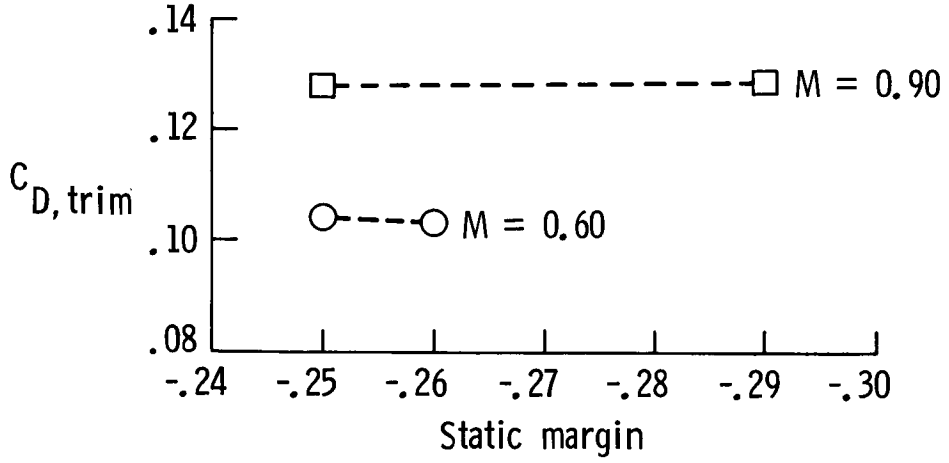

(b) Variation with static margin.

Figure 17.- Variation of trimmed drag with center-of-gravity location and static margin for C_L = 0.9. Canard on; strakes off.

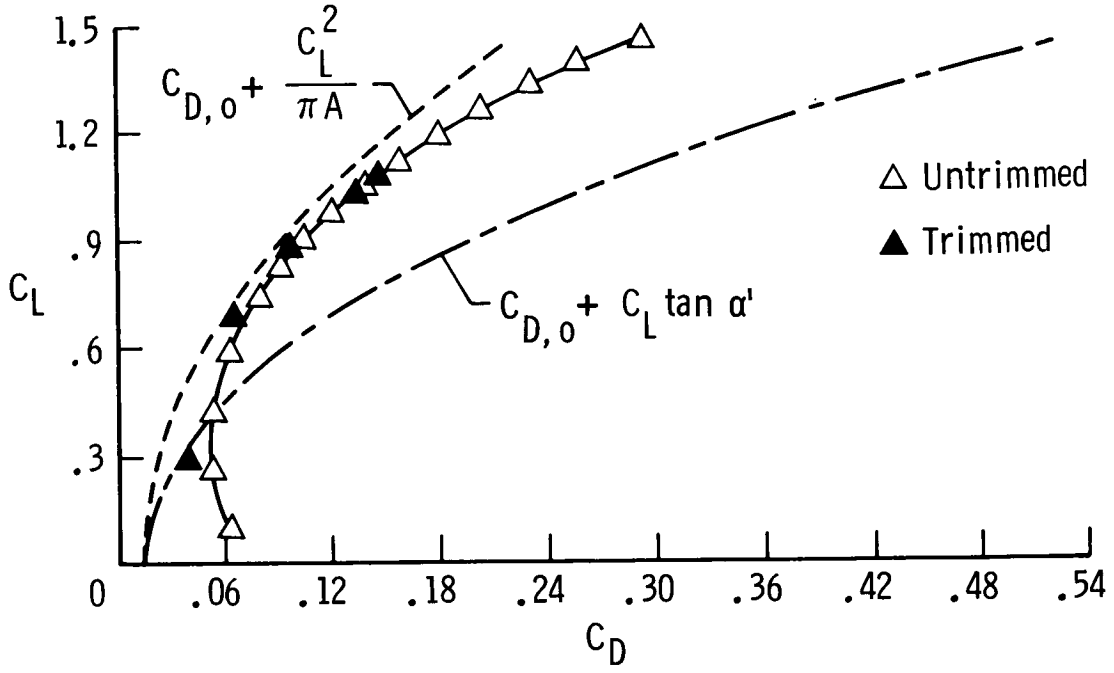

(a) M = 0.60; for untrimmed data: $\delta_c = 0°$ and $\delta_{f,TE} = \delta_{f,LE} = 10°$.

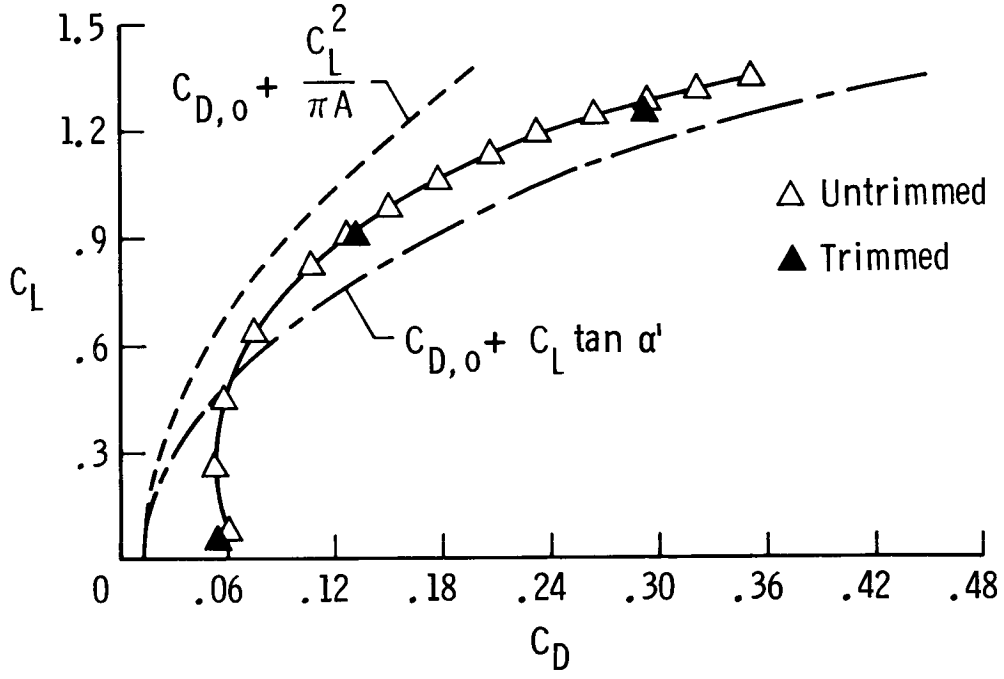

(b) M = 0.90; for untrimmed data: $\delta_c = 0°$, $\delta_{f,TE} = 10°$, and $\delta_{f,LE} = 0°$.

Figure 18.- Comparison of experimental results with ideal and zero-suction polars. Strakes off.

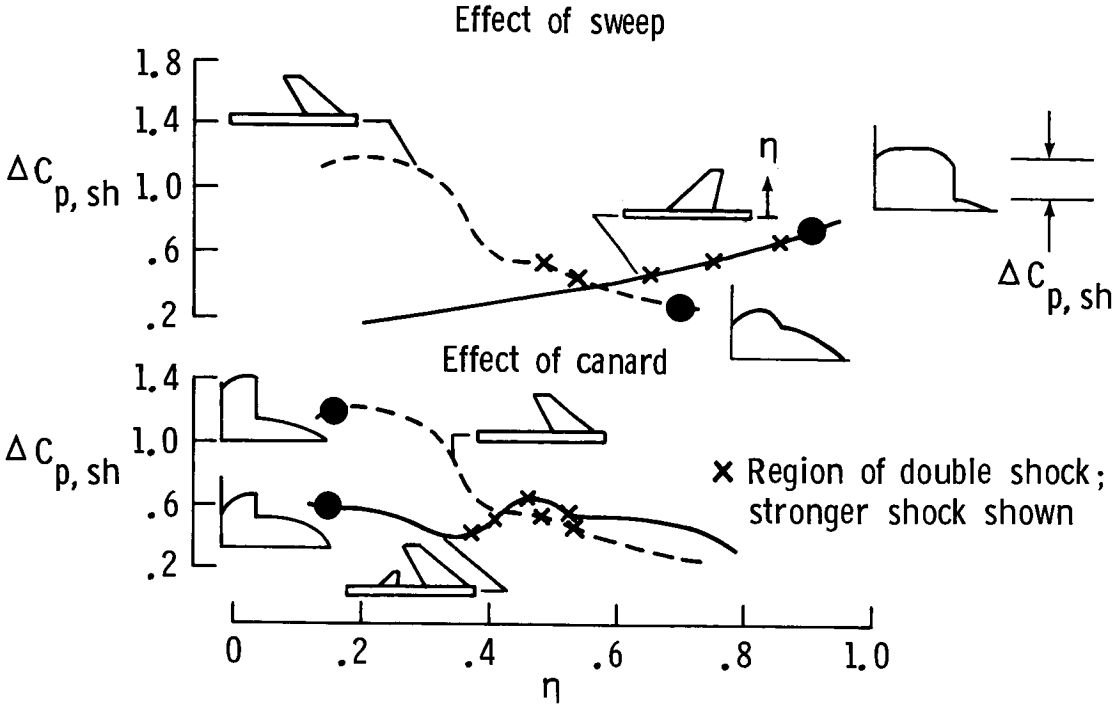

(a) Theoretical shock strength with $M = 0.85$ and $C_{L,th} = 0.7$.

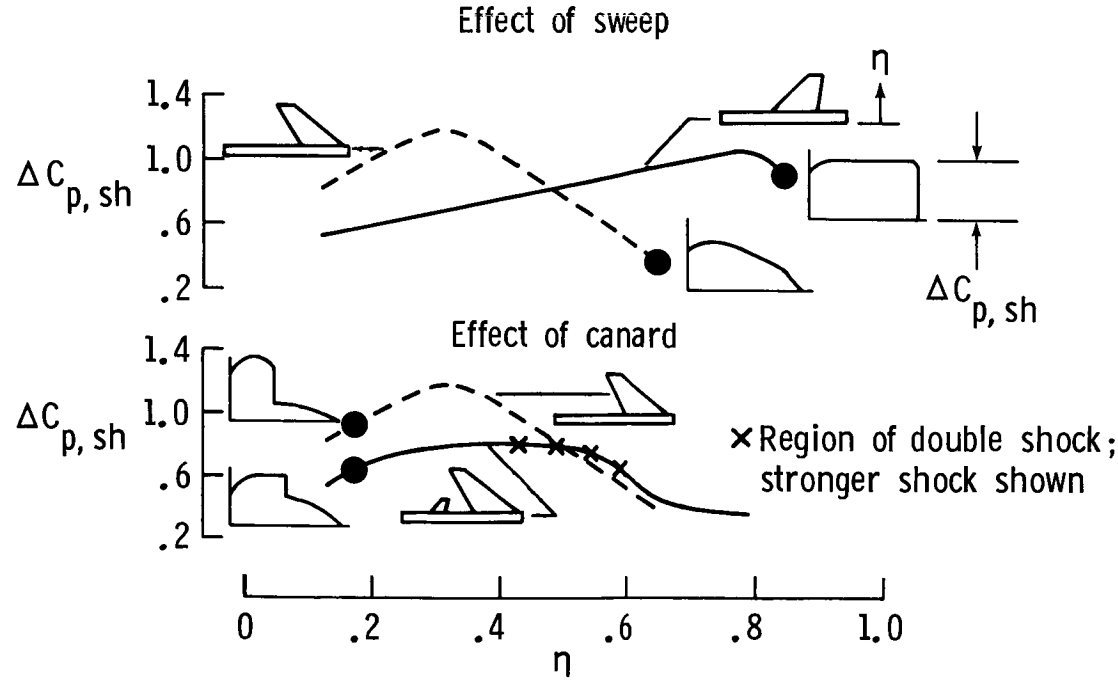

(b) Theoretical shock strength with $M = 0.90$ and $C_{L,th} = 0.7$.

Figure 19.- Spanwise variation of shock strength on forward-swept and SMF-1 aft-swept wings. Strakes off; $\delta_c = 0°$; $\delta_{f,TE} = \delta_{f,LE} = 0°$. Solid symbols show shock strength corresponding to adjacent chordwise pressure distributions.

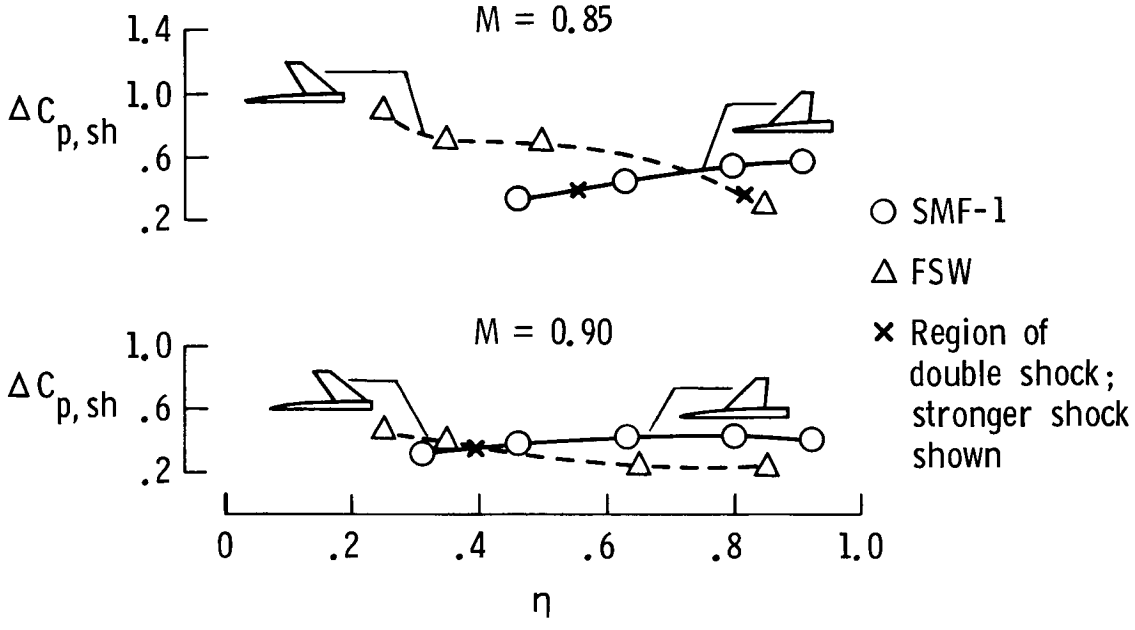

(c) Effect of sweep on experimental shock strength with $C_L = 0.7$.

Figure 19.- Concluded.

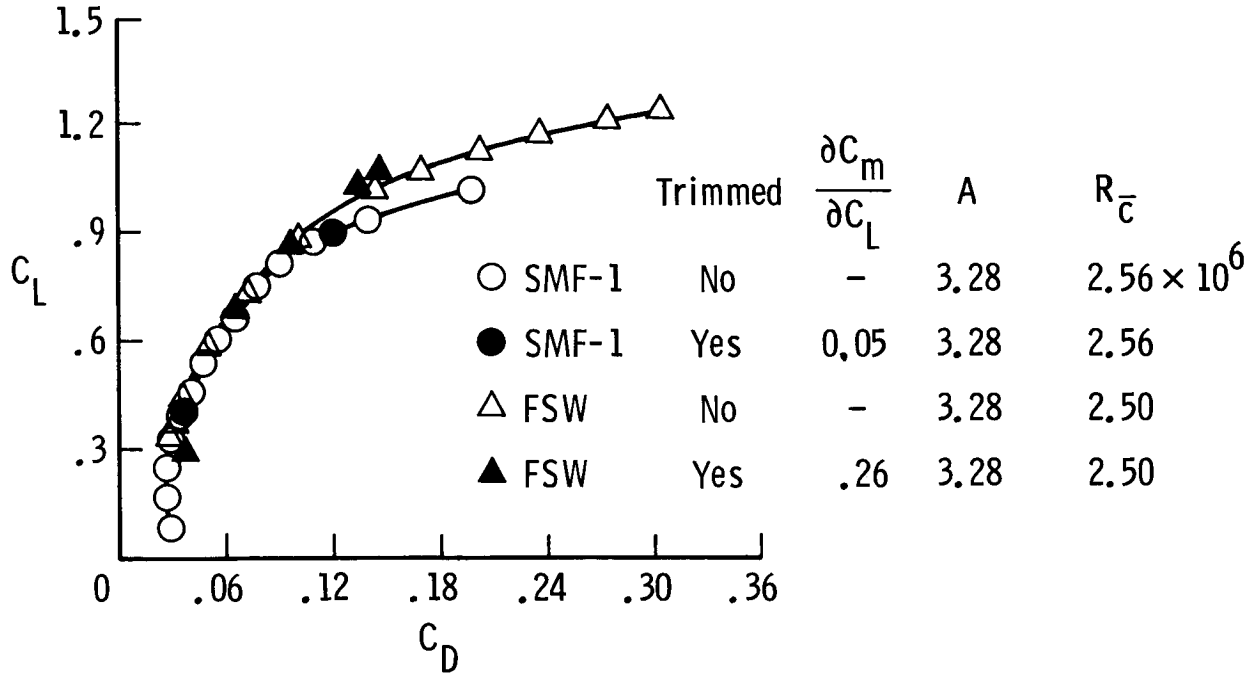

(a) M = 0.60; x_{cg} = 22.4 in. for SMF-1.

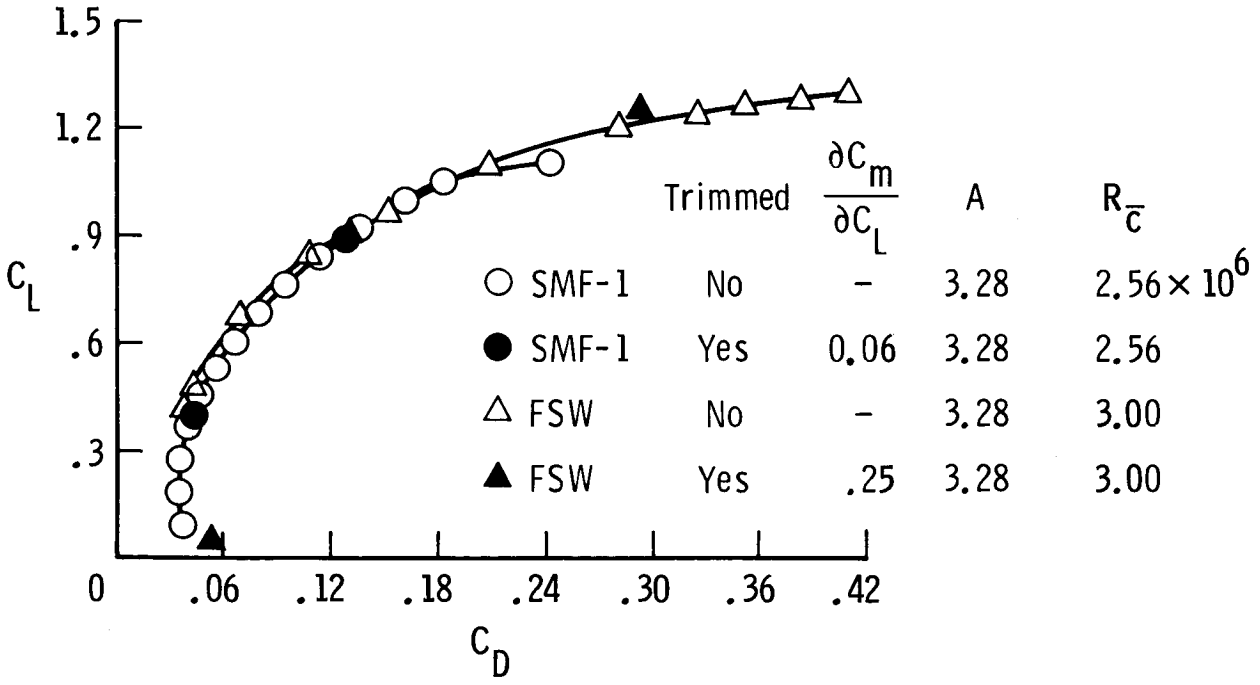

(b) M = 0.90; x_{cg} = 23.0 in. for SMF-1.

Figure 20.- Comparison of forward-swept- and SMF-1 aft-swept-wing configurations. Strakes off; for untrimmed data: $\delta_t = 0°$, $\delta_c = 0°$, and $\delta_{f,TE} = \delta_{f,LE} = 0°$.

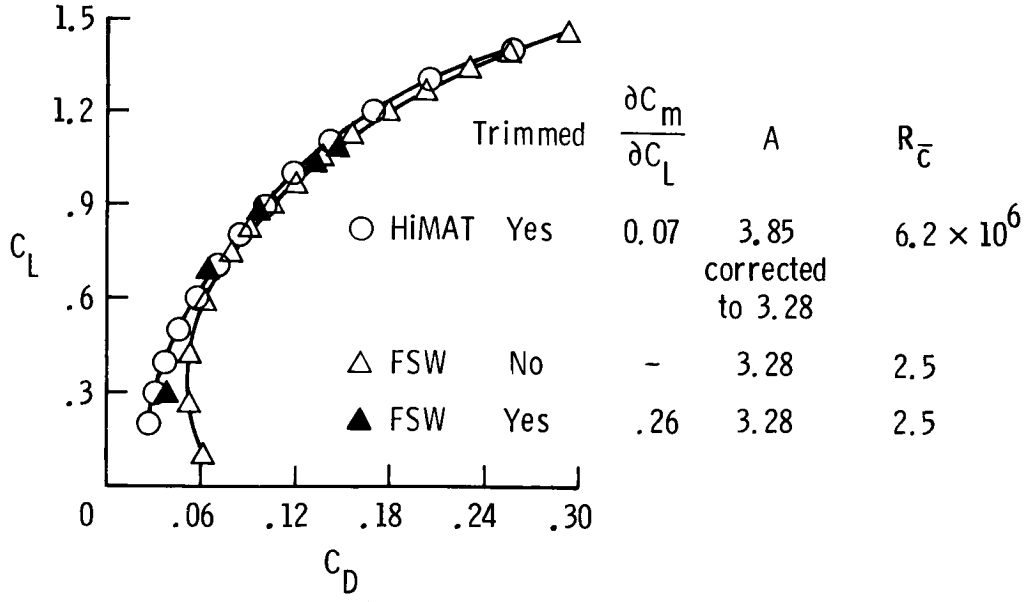

(a) Variation of C_L with C_D; M = 0.60; for FSW untrimmed data: $\delta_c = 0°$ and $\delta_{f,TE} = \delta_{f,LE} = 10°$; HiMAT maneuver configuration.

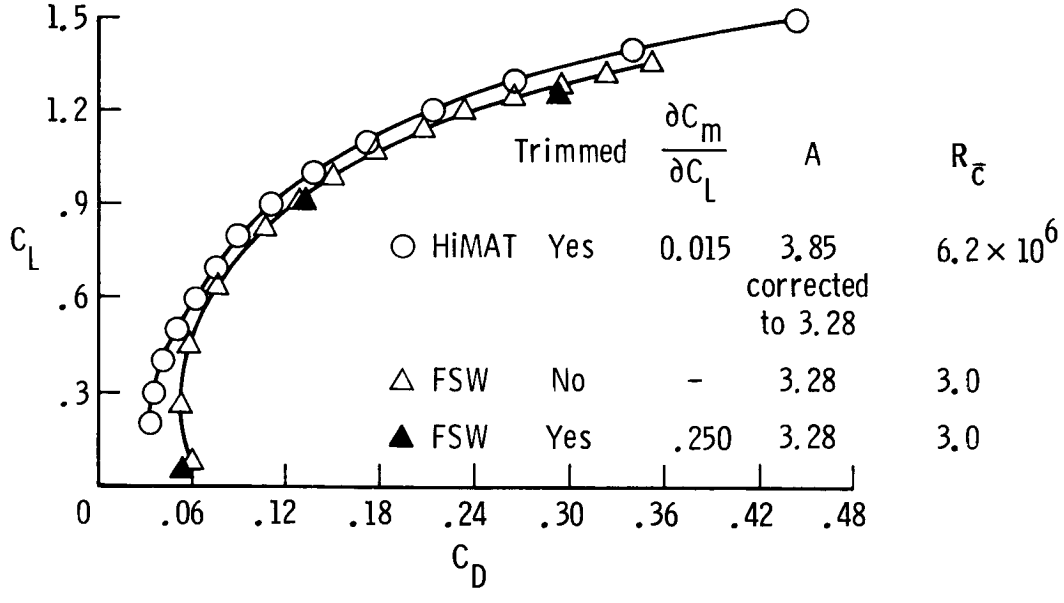

(b) Variation of C_L with C_D; M = 0.90; for FSW untrimmed data: $\delta_c = 0°$, $\delta_{f,TE} = 10°$, and $\delta_{f,LE} = 0°$; HiMAT maneuver configuration.

Figure 21.- Comparison of forward-swept-wing configuration with HiMAT configuration. Strakes off.

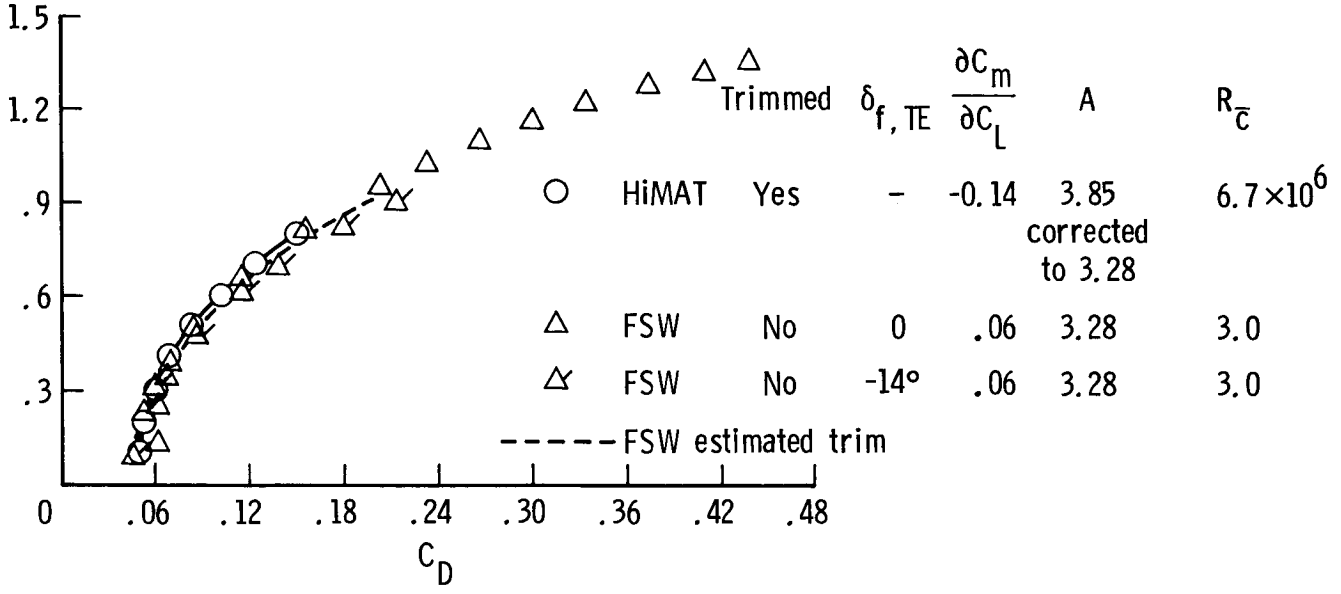

(c) Variation of C_L with C_D; M = 1.20; for FSW untrimmed data: $\delta_c = 0°$ and $\delta_{f,LE} = 0°$; HiMAT cruise configuration.

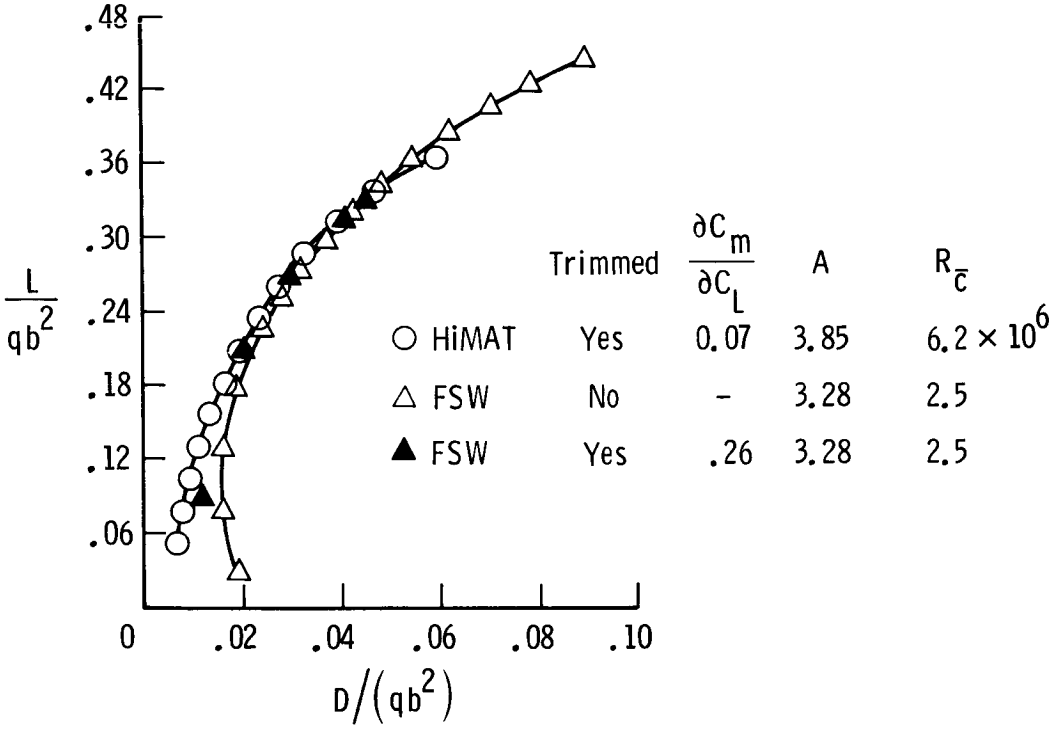

(d) Variation of L/qb^2 with $D/(qb^2)$; M = 0.60; for FSW untrimmed data: $\delta_c = 0°$ and $\delta_{f,TE} = \delta_{f,LE} = 10°$; HiMAT maneuver configuration.

Figure 21.- Continued.

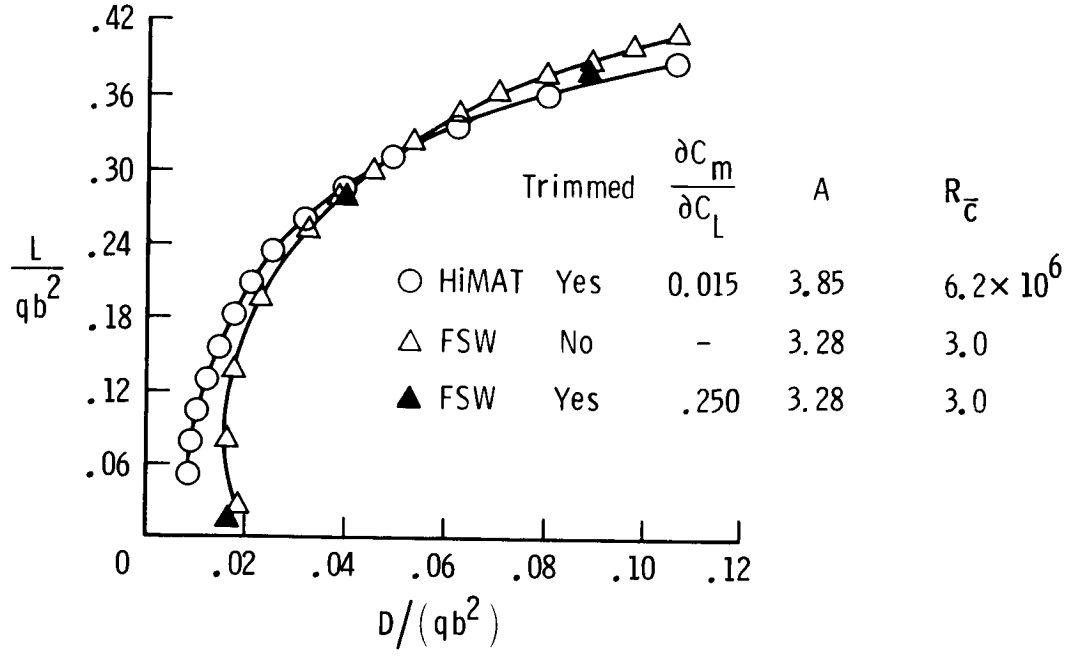

(e) Variation of L/qb^2 with $D/(qb^2)$; M = 0.90; for FSW untrimmed data: $\delta_c = 0°$, $\delta_{f,TE} = 10°$, and $\delta_{f,LE} = 0°$; HiMAT maneuver configuration.

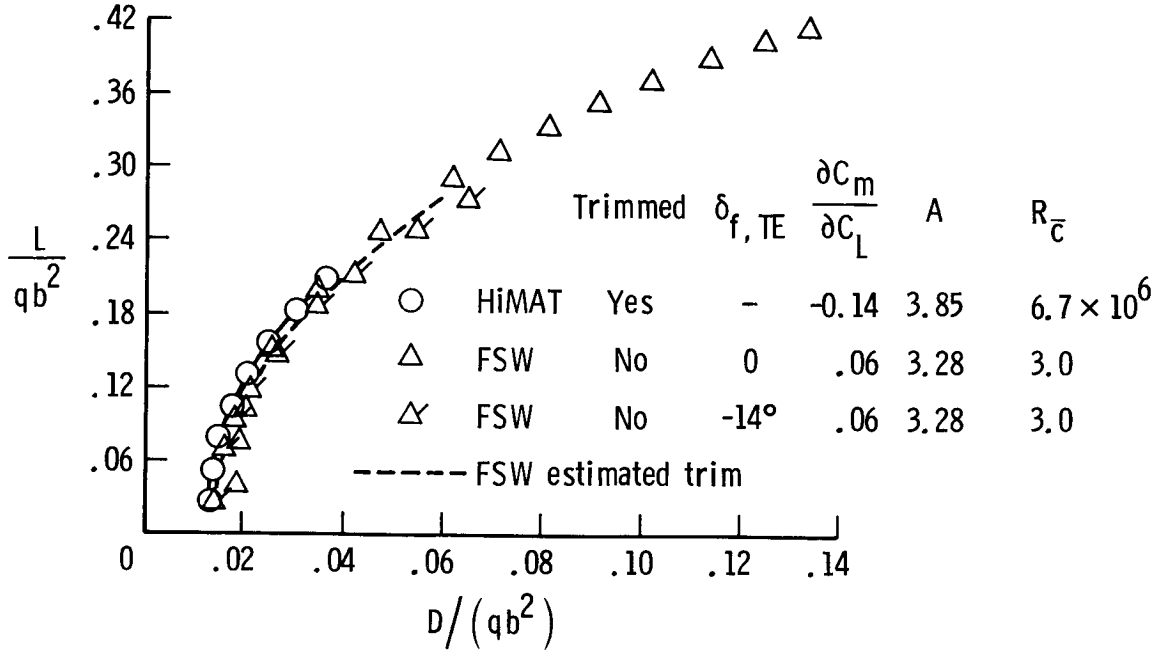

(f) Variation of L/qb^2 with $D/(qb^2)$; M = 1.20; for FSW untrimmed data: $\delta_c = 0°$ and $\delta_{f,LE} = 0°$; HiMAT cruise configuration.

Figure 21.- Concluded.

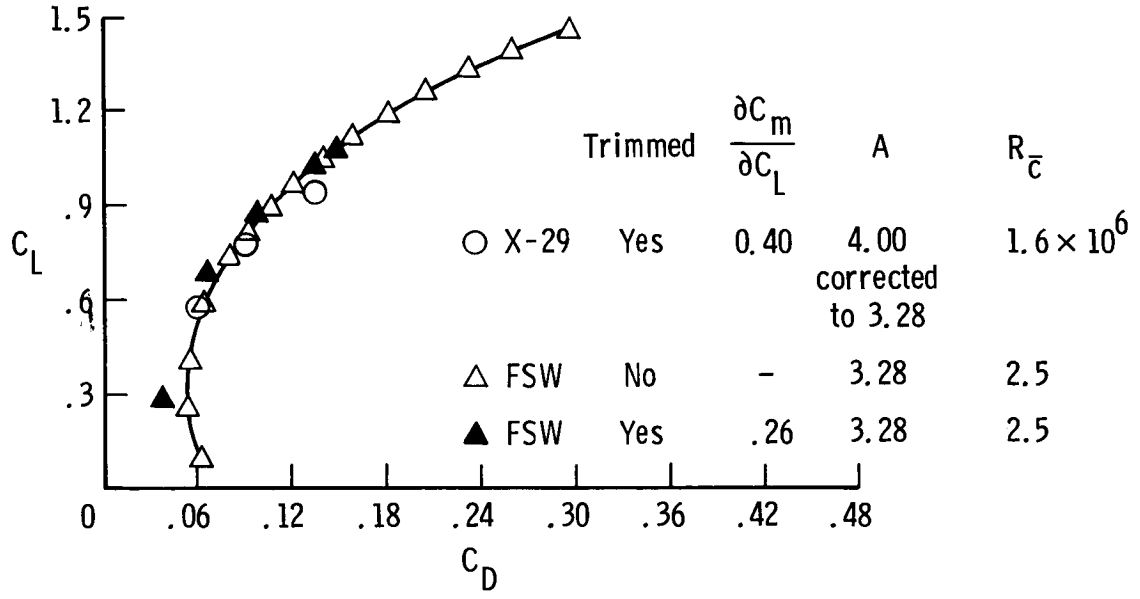

(a) Variation of C_L with C_D; M = 0.60; for FSW untrimmed data: $\delta_c = 0°$ and $\delta_{f,TE} = \delta_{f,LE} = 10°$.

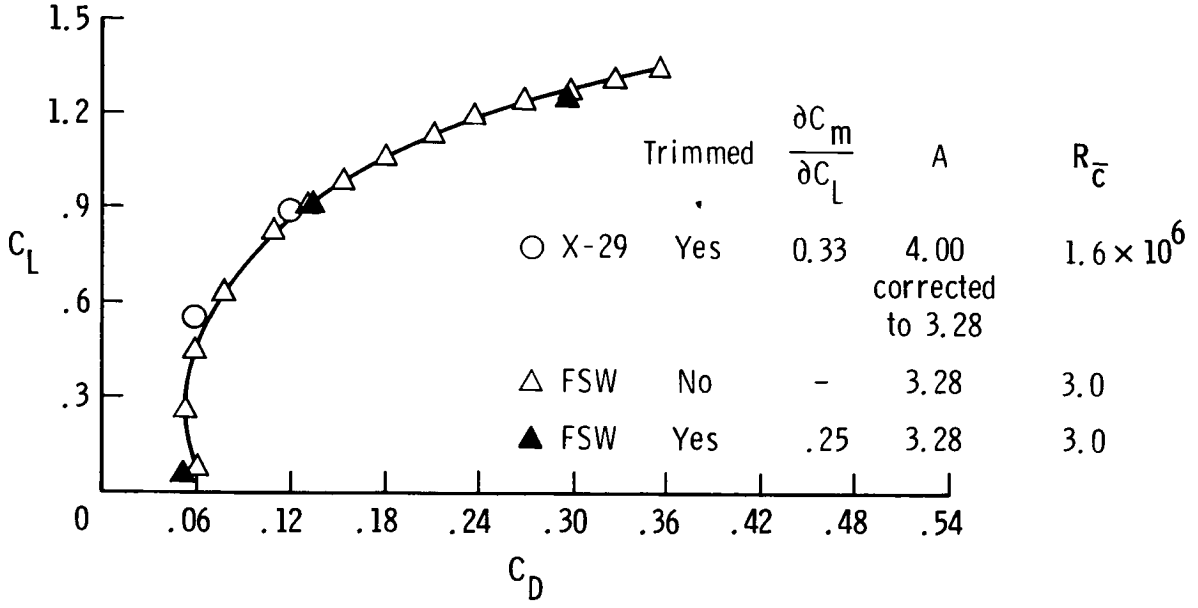

(b) Variation of C_L with C_D; M = 0.90; for FSW untrimmed data: $\delta_c = 0°$, $\delta_{f,TE} = 10°$, and $\delta_{f,LE} = 0°$.

Figure 22.- Comparison of forward-swept-wing configuration with X-29 research configuration. Strakes off.

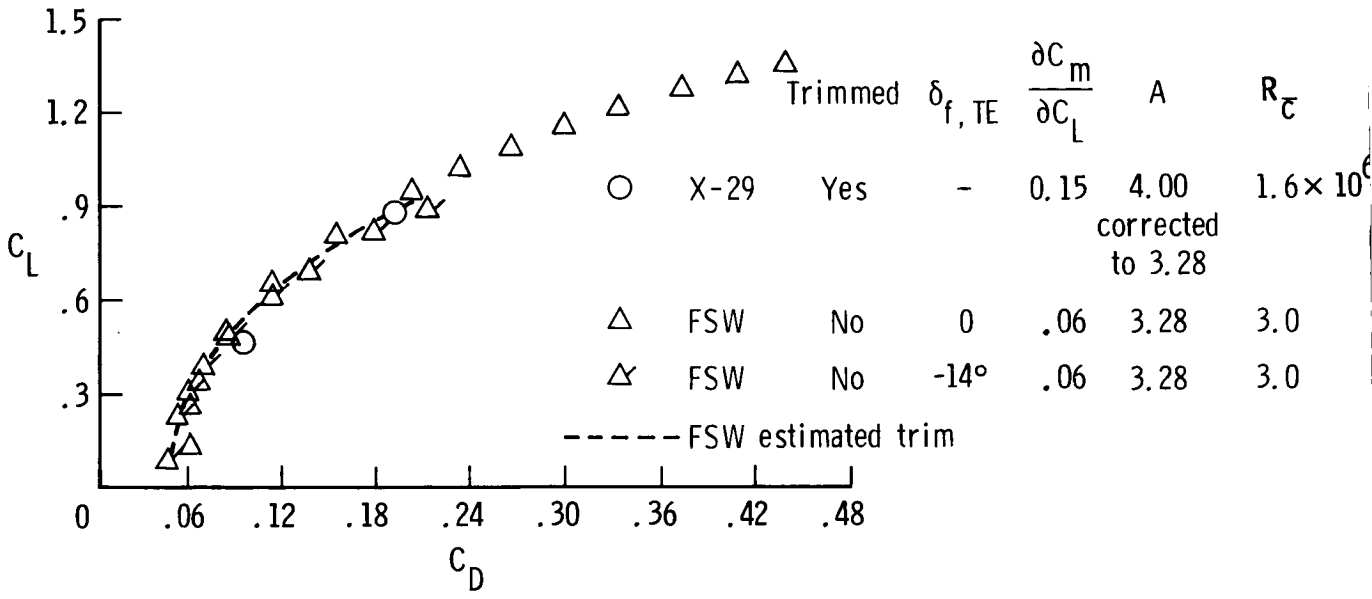

(c) Variation of C_L with C_D; M = 1.20; for FSW untrimmed data: $\delta_c = 0°$ and $\delta_{f,LE} = 0°$.

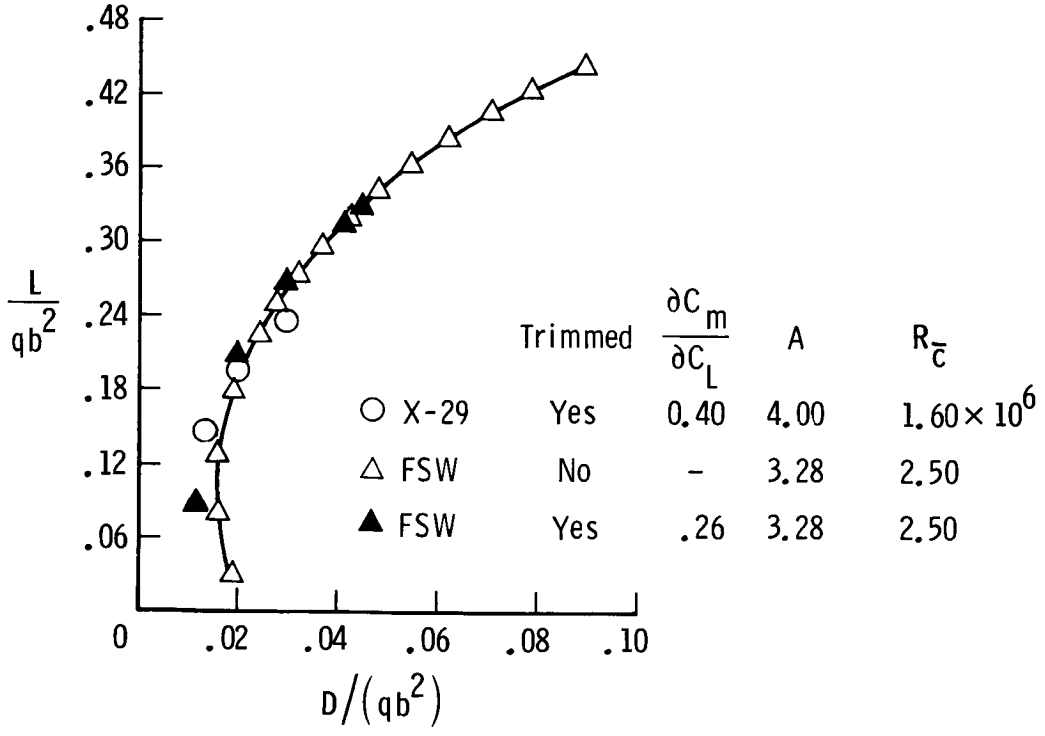

(d) Variation of L/qb^2 with $D/(qb^2)$; M = 0.60; for FSW untrimmed data: $\delta_c = 0°$ and $\delta_{f,TE} = \delta_{f,LE} = 10°$.

Figure 22.- Continued.

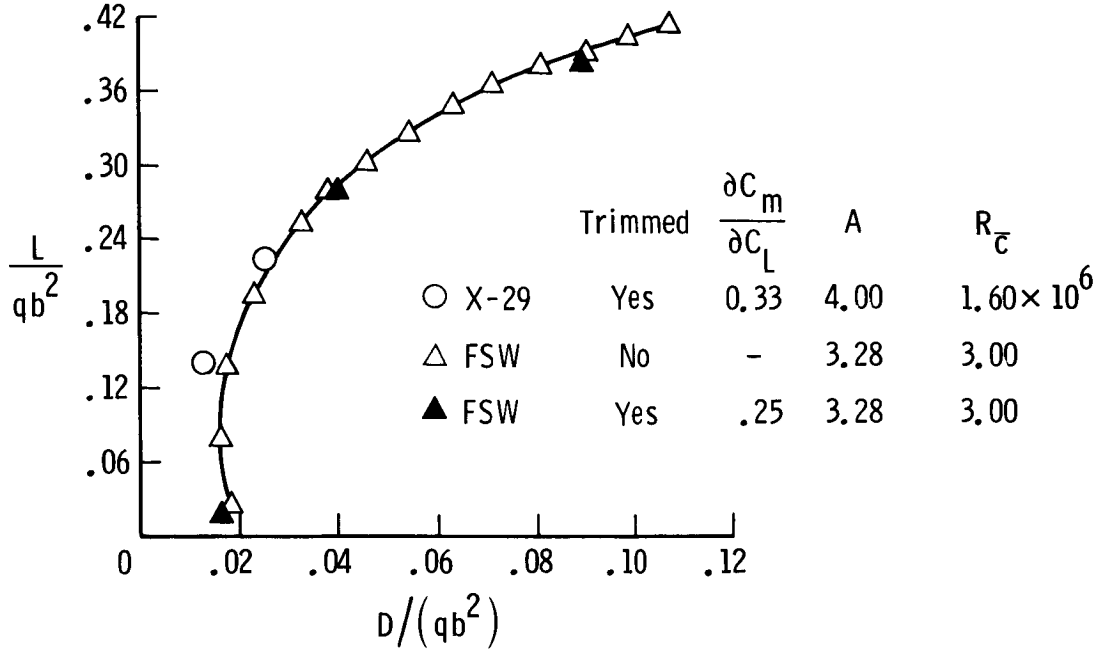

(e) Variation of L/qb^2 with $D/(qb^2)$; M = 0.90; for FSW untrimmed data: $\delta_c = 0°$, $\delta_{f,TE} = 10°$, and $\delta_{f,LE} = 0°$.

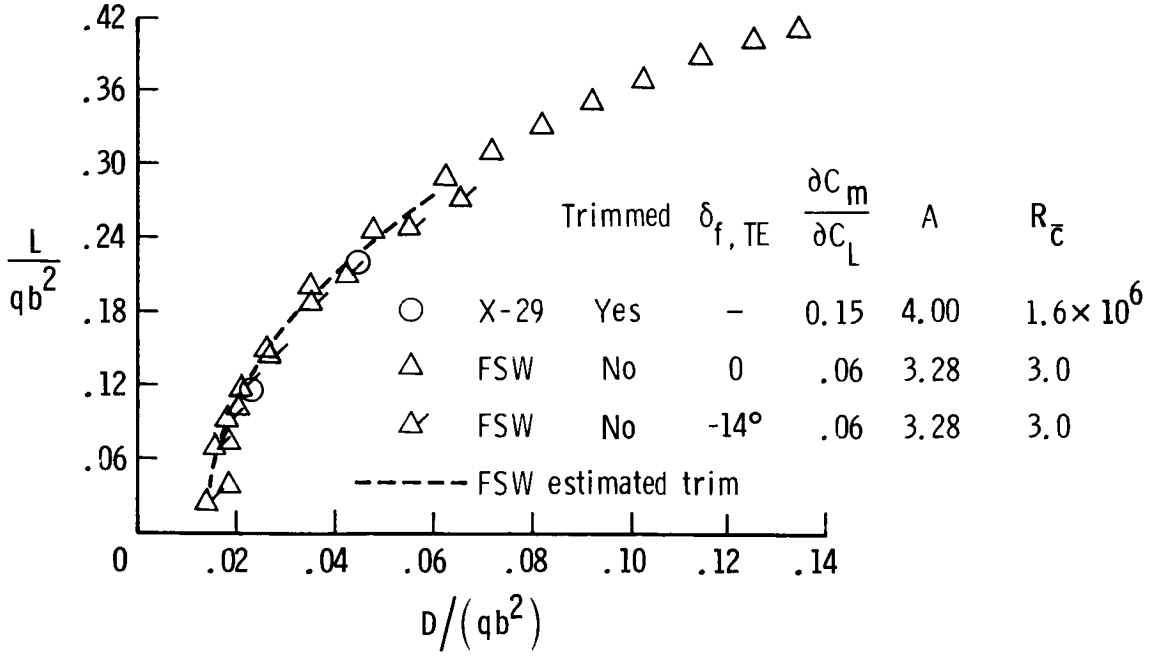

(f) Variation of L/qb^2 with $D/(qb^2)$; M = 1.20; for FSW untrimmed data: $\delta_c = 0°$ and $\delta_{f,LE} = 0°$.

Figure 22.- Concluded.

Standard Bibliographic Page

1. Report No.	2. Government Accession No.	3. Recipient's Catalog No.
NASA TP-2628		

4. Title and Subtitle	5. Report Date
Forward-Swept-Wing Configuration Designed for High Maneuverability by Use of a Transonic Computational Method	November 1986
	6. Performing Organization Code: 505-61-71-03
7. Author(s): Michael J. Mann and Charles E. Mercer	8. Performing Organization Report No.: L-16120
9. Performing Organization Name and Address: NASA Langley Research Center, Hampton, VA 23665-5225	10. Work Unit No.
	11. Contract or Grant No.
12. Sponsoring Agency Name and Address: National Aeronautics and Space Administration, Washington, DC 20546-0001	13. Type of Report and Period Covered: Technical Paper
	14. Sponsoring Agency Code

15. Supplementary Notes

16. Abstract

A transonic computational analysis method and a transonic design procedure have been used to design the wing and the canard of a forward-swept-wing fighter configuration for good transonic maneuver performance. A model of this configuration was tested in the Langley 16-Foot Transonic Tunnel. Oil-flow photographs were obtained to examine the wing flow patterns at Mach numbers from 0.60 to 0.90. The transonic theory gave a reasonably good estimate of the wing pressure distributions at transonic maneuver conditions. Comparison of the forward-swept-wing configuration with an equivalent aft-swept-wing-configuration showed that, at a Mach number of 0.90 and a lift coefficient of 0.9, the two configurations have the same trimmed drag. The forward-swept wing configuration was also found to have trimmed drag levels at transonic maneuver conditions which are comparable to those of the HiMAT (highly maneuverable aircraft technology) configuration and the X-29 forward-swept-wing research configuration. The configuration of this study was also tested with a forebody strake.

17. Key Words (Suggested by Authors(s))	18. Distribution Statement
Forward-swept wings Transonic wing design Maneuvering aerodynamics Maneuvering aircraft Transonic wings	Unclassified - Unlimited Subject Category 02

19. Security Classif.(of this report)	20. Security Classif.(of this page)	21. No. of Pages	22. Price
Unclassified	Unclassified	185	A09

For sale by the National Technical Information Service, Springfield, Virginia 22161

NASA-Langley, 1986